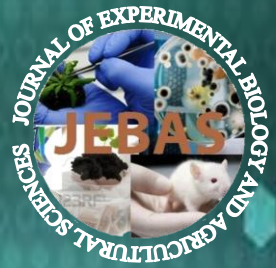


ISSN: 2320-8694

Journal of Experimental Biology And Agricultural Sciences



VOLUME 12 || ISSUE VI || DECEMBER, 2024

Production and Hosting by Horizon Publisher India[HPI]
(<http://www.horizonpublisherindia.in>)
All rights reserved.

ISSN No. 2320 - 8694

Peer Reviewed - open access journal

Common Creative License - NC 4.0

Volume No - 12

Issue No - VI

December, 2024

Journal of Experimental Biology and Agricultural Sciences (JEBAS) is an online platform for the advancement and rapid dissemination of scientific knowledge generated by the highly motivated researchers in the field of biological agricultural, veterinary and animal sciences. JEBAS publishes high-quality original research and critical up-to-date review articles covering all the aspects of biological sciences. Every year, it publishes six issues.

JEBAS has been accepted by SCOPUS UGC CARE, INDEX COPERNICUS INTERNATIONAL (Poland), AGRICOLA (USA), CAS (ACS, USA), CABI - Full Text (UK), International Committee of Medical Journal Editors (ICMJE), SHERPA - ROMEO; J gate and Indian Science Abstracts (ISA, NISCAIR) like well reputed indexing agencies.

[HORIZON PUBLISHER INDIA [HPI]

<http://www.horizonpublisherindia.in/>]

Editorial Board

Editor-in-Chief

Prof Y. Norma-Rashid
(University of Malaya, Kuala Lumpur)
editor.in.chief.jebas@gmail.com

Co-Editor-in-Chief

Dr. Kuldeep Dhama, M.V.Sc., Ph.D.
NAAS Associate, Principal Scientist, IVRI, Izatnagar India - 243 122
co_eic@jebas.org

Managing - Editor

Kamal K Chaudhary, Ph.D. (India)
jebasonline@gmail.com

Technical Editors

Hafiz M. N. Iqbal (Ph.D.)

Research Professor,
Tecnologico de Monterrey, School of Engineering and Sciences,
Campus Monterrey, Ave. Eugenio Garza Sada 2501,
Monterrey, N. L., CP 64849, Mexico
Tel.: +52 (81) 8358-2000Ext.5561-115
E-mail: hafiz.iqbal@my.westminster.ac.uk; hafiz.iqbal@itesm.mx

Prof. Dr. Mirza Barjees Baigis

Professor of Extension (Natural Resource Management),
Department of Agricultural Extension and Rural Society,
College of Food and Agriculture Sciences,
King Saud University, P.O. Box 2460, Riyadh 11451, Kingdom of Saudi Arabia
Email: mbaig@ksu.edu.sa

Dr. Mukesh Kumar Meghvansi

Scientist, Bioprocess Technology Division, Defence R & D Establishment, Gwalior-474002
Email: mk_meghvansi@yahoo.co.in

Dr. B L Yadav

Head – Botany, MLV Govt. College, Bhilwara, India
E mail: drblyadav@yahoo.com

Dr. Yashpal S. Malik

ICAR – National Fellow Indian Veterinary Research Institute (IVRI)
Izatnagar 243 122, Bareilly, Uttar Pradesh, India

Associate Editors

Dr. Sunil K. Joshi

Laboratory Head, Cellular Immunology

Investigator, Frank Reidy Research Center of Bioelectronics, College of Health Sciences, Old Dominion University,
4211 Monarch Way, IRP-2, Suite # 300, Norfolk, VA 23508 USA

Email: skjoshi@odu.edu

Dr. Vincenzo Tufarelli

Department of Emergency and Organ Transplantation (DETO),

Section of Veterinary Science and Animal Production,

University of Bari 'Aldo Moro', s.p. Casamassima km 3, 70010 Valenzano, Italy

Email: vincenzo.tufarelli@uniba.it

Prof. Sanjay-Swami, Ph.D. (Soil Science & Agril. Chemistry),

School of Natural Resource Management,

College of Post Graduate Studies in Agricultural Sciences,

(Central Agricultural University),

UMIAM (Barapani)-793 103, Meghalaya, INDIA

Email: sanjay.nrm.cpgsas@cau.ac.in

Jose M. Lorenzo

Centro Tecnológico de la Carne de Galicia

Ourense, Spain

Email: jmlorenzo@ceteca.net

Assistant Editors

Dr Ayman EL Sabagh

Assistant professor, agronomy department, faculty of agriculture

kafresheikh university, Egypt

E-mail: ayman.elsabagh@agr.kfs.edu.eg

Safar Hussein Abdullah Al-Kahtani (Ph.D.)

King Saud University-College of Food and Agriculture Sciences,
Department of the Agricultural Economics
P.O.Box: 2460 Riyadh 11451, KSA
email: safark@ksu.edu.sa

Dr Ruchi Tiwari

Assistant Professor (Sr Scale)
Department of Veterinary Microbiology and Immunology,
College of Veterinary Sciences,
UP Pandit Deen Dayal Upadhyay Pashu Chikitsa Vigyan Vishwavidyalay Evum Go-Anusandhan Sansthan (DUVASU),
Mathura, Uttar Pradesh, 281 001, India
Email: ruchi.vet@gmail.com

Dr. ANIL KUMAR (Ph.D.)

Asstt. Professor (Soil Science)
Farm Science Centre (KVK)
Booh, Tarn Taran, Punjab (India) – 143 412
Email: anilkumarhpkv@gmail.com

Akansha Mishra

Postdoctoral Associate, Ob/Gyn lab
Baylor College of Medicine,
1102 Bates Ave, Houston Tx 77030
Email: akansha.mishra@bcm.edu; aksmisra@gmail.com

Dr. Muhammad Bilal

Associate Professor
School of Life Science and Food Engineering,
Huaiyin Institute of Technology, Huaian 223003, China
Email: bilaluaf@hotmail.com

Dr. Senthilkumar Natesan

Associate Professor
Department of Infectious Diseases, Indian Institute of Public Health
Gandhinagar, Opp to Airforce station HQ, Lekawada, Gandhinagar, Gujarat - 382042, India
Email: snatesan@iiphg.org

Prof. A. VIJAYA ANAND

Professor

Department of Human Genetics and Molecular Biology

Bharathiar University

Coimbatore – 641 046

Dr. Phetole Mangena

Department of Biodiversity, School of Molecular and Life Sciences,

Faculty of Science and Agriculture, University of Limpopo, Republic of South Africa

Private Bag X1106, Sovenga, 0727

Email: Phetole.Mangena@ul.ac.za ; mangena.phetole@gmail.com



Table of contents

Most recent and emerging technologies for enhancing the nutritional characteristics of food, challenges and future directions: A Review <i>10.18006/2024.12(6).784.799</i>	784 — 799
<i>In silico</i> Analysis of Natural Iridoids as Primary Amoebic Meningoencephalitis Inhibitors: Molecular Docking, MD Simulation, MMPBSA, and DFT Analyses <i>10.18006/2024.12(6).800.828</i>	800 — 828
Phylogenetic and Morphological Study of <i>Desmodemus</i> Strains from Can Gio Mangrove Biosphere Reserve <i>10.18006/2024.12(6).829.837</i>	829 — 837
<i>In-vitro</i> antibacterial activity, Molecular docking, and MD Simulation Analysis of Phytoconstituents of <i>Nasturtium officinale</i> <i>10.18006/2024.12(6).838.849</i>	838 — 849
Gene action of yield and its contributing traits in wide-compatible elite rice (<i>Oryza sativa</i> L.) restorer lines <i>10.18006/2024.12(6).850.859</i>	850 — 859
Soil erosion assessment in the Ranganadi watershed of Lakhimpur district, Assam, using GIS techniques and Revised Universal Soil Loss Equation model <i>10.18006/2024.12(6).860.875</i>	860 — 875
Dehydrogenase: A key soil health indicator for Thar Desert, India <i>10.18006/2024.12(6).876.886</i>	876 — 886
Influence of Zinc Oxide Nanoparticles on the Productivity, Mineral Element Accumulation, and Fruit Quality of Tomato (<i>Solanum lycopersicum</i> L.) <i>10.18006/2024.12(6).887.904</i>	887 — 904















Journal of Experimental Biology and Agricultural Sciences

<http://www.jebas.org>

ISSN No. 2320 – 8694

Most recent and emerging technologies for enhancing the nutritional characteristics of food, challenges and future directions: A Review

Franklin Ore Areche^{1*} , Juan Alberto Julcahuanga Dominguez² ,
Rafael Julian Malpartida Yapias³ , Olivia Magaly Luque Vilca⁴ ,
Candelaria Flores-Miranda¹ , Jorge Manuel Montalvo Otivo¹ ,
Godofredo Roman Lobato Calderon⁵ , Pedro Córdova Mendoza⁶ ,
Teresa Oriele Barrios Mendoza⁶ , Isis Cristel Córdova Barrios⁶ ,
Ronald Henry Mejía Lizarme⁷ , Luis Alberto Astuhumán Pardavé⁷ 

¹Universidad Nacional de Huancavelica, Perú

²Universidad Nacional de Piura, Perú

³Universidad Nacional Autónoma Altoandina de Tarma, Perú

⁴Universidad Nacional de Juliaca, Perú

⁵Universidad Católica Sedes Sapientiae, Perú

⁶Universidad Nacional San Luis Gonzaga, Perú

⁷Universidad Nacional del Centro del Perú

Received – July 15, 2024; Revision – December 03, 2024; Accepted – December 29, 2024

Available Online – January 15, 2025

DOI: [http://dx.doi.org/10.18006/2024.12\(6\).784.799](http://dx.doi.org/10.18006/2024.12(6).784.799)

KEYWORDS

Precision Fermentation

Gene Editing

Nutrient Bioavailability

Food Fortification

Nanotechnology

ABSTRACT

The rapid advancement of emerging technologies is transforming the food industry, especially in enhancing the nutritional qualities of food. These innovations have significant potential for tackling global nutritional deficiencies and promoting public health. Key technologies include precision fermentation, which enables the production of high-quality proteins and micronutrients while minimizing environmental impact. Additionally, gene editing techniques such as CRISPR allow for the development of crops with improved nutrient profiles and enhanced resistance to pests and diseases. Furthermore, advancements in nanotechnology enhance the fortification of foods with essential vitamins and minerals, improving their bioavailability and stability. Personalized nutrition, driven by big data and artificial intelligence, customizes dietary recommendations based on individual genetic profiles, optimizing

* Corresponding author

E-mail: franklin.ore@unh.edu.pe (Franklin Ore Areche)

Peer review under responsibility of Journal of Experimental Biology and Agricultural Sciences.

Production and Hosting by Horizon Publisher India [HPI]
(<http://www.horizonpublisherindia.in/>).
All rights reserved.

All the articles published by [Journal of Experimental Biology and Agricultural Sciences](#) are licensed under a [Creative Commons Attribution-NonCommercial 4.0 International License](#) Based on a work at www.jebas.org.



Personalized Nutrition
Sustainable Food Systems

nutrient intake and health outcomes. This review article overviews these cutting-edge technologies and their applications in creating a more nutritious and sustainable food system.

1 Introduction

The global food industry is experiencing a significant transformation driven by the need to improve the nutritional quality of food while ensuring sustainability and addressing the challenges posed by a growing population. Innovative technologies are increasingly supplementing and, in some cases, replacing traditional food production and fortification (Alina et al. 2019). These emerging technologies have the potential to significantly enhance the nutritional characteristics of food, leading to better health outcomes on a global scale (Ivanov et al. 2021). Precision fermentation is particularly promising among these technologies, as it efficiently produces high-quality proteins and essential nutrients with a lower environmental impact than conventional agricultural practices. Additionally, gene editing tools such as CRISPR enable the development of crop varieties with improved

nutrient profiles, higher yields, and better resistance to pests and diseases, thereby supporting food security and nutritional quality (Figure 1).

Nanotechnology represents a new frontier in food science, providing innovative solutions for nutrient fortification (Aguilar-Pérez et al. 2023). Using nanoparticles, we can enhance the bioavailability and stability of vitamins and minerals in food products. This ensures that essential nutrients are delivered to the body more effectively, addressing specific nutrient deficiencies and improving overall dietary health. Additionally, big data and artificial intelligence advancements are revolutionizing personalized nutrition (Cohen et al. 2023). This approach tailors dietary recommendations to individual genetic profiles, lifestyles, and health conditions, allowing for more precise and effective nutritional interventions. As a result, it promotes optimal health

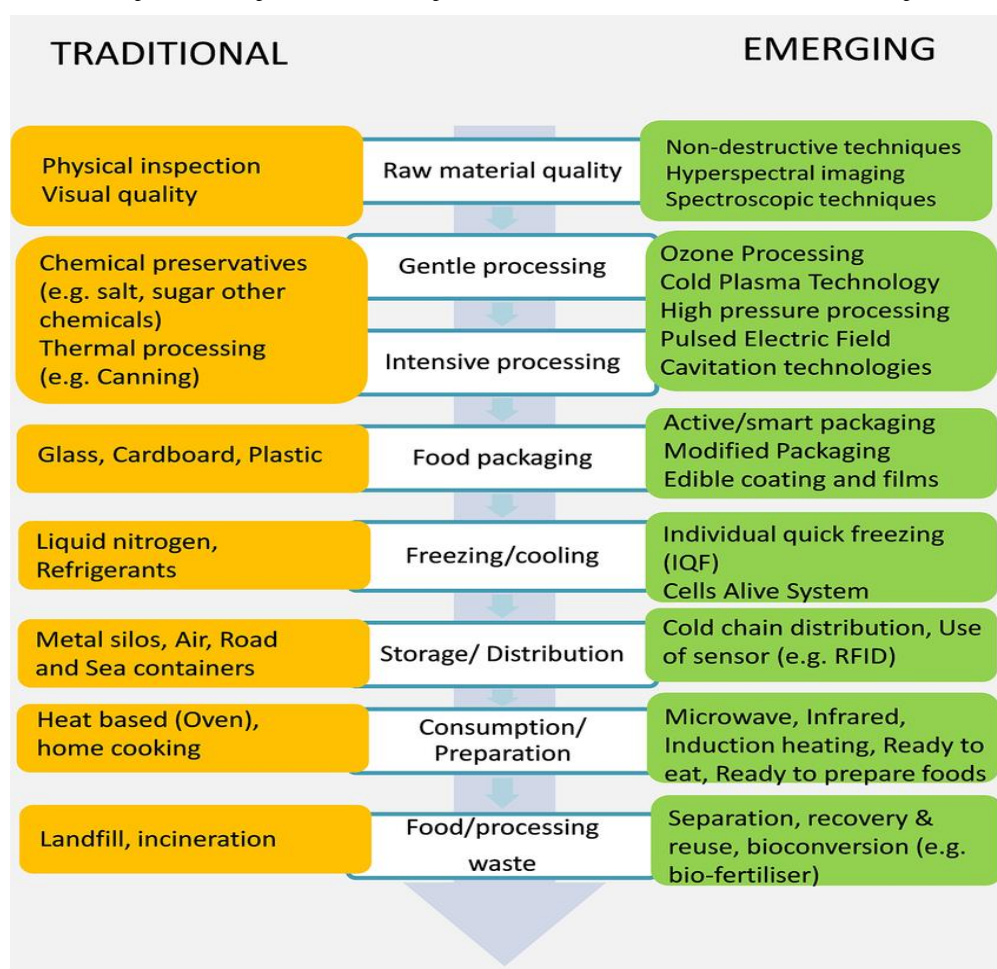


Figure 1 Difference between traditional and emerging technologies

and helps prevent diet-related diseases (Sahoo et al. 2021). This introduction paves the way for an in-depth exploration of these emerging technologies, focusing on their mechanisms, applications, and potential impacts on food nutrition (Sonnino 2016; Rizwan et al. 2018). By harnessing these innovations, the food industry can produce products that are not only more nutritious but also more sustainable and accessible, ultimately contributing to improved public health worldwide.

This study aims to investigate the mechanisms, applications, and potential impacts of emerging technologies such as precision fermentation, gene editing, nanotechnology, and personalized nutrition on enhancing the nutritional quality of food. This research aims to assess how these innovations can improve food sustainability, address global nutrient deficiencies, and contribute to public health by facilitating the production of more nutritious, accessible, and environmentally sustainable food products.

2 Overview of the importance of nutritional enhancement in food

Nutritional enhancement in food addresses widespread public health issues such as malnutrition, nutrient deficiencies, and diet-related chronic diseases. As global populations grow and dietary patterns change, ensuring that food provides adequate and balanced nutrients is increasingly important. Nutritionally enhanced foods can help alleviate deficiencies in essential vitamins and minerals, particularly in areas with limited access to a varied diet (Tontisirin et al. 2002). Moreover, with the rise of health-conscious consumers, there is a growing demand for foods that promote overall well-being, prevent diseases, and support optimal health. Improving the nutritional quality of food also has economic benefits by reducing healthcare costs associated with malnutrition and chronic diseases (Miller and Welch 2013). Therefore, utilizing advanced technologies to enhance the nutrient content of food is a vital strategy for promoting public health, supporting sustainable agricultural practices, and meeting the diverse nutritional needs of the global population.

3 The role of technology in addressing nutritional deficiencies and improving public health

Technology is essential for addressing nutritional deficiencies and enhancing public health by facilitating the development of foods with improved nutritional profiles and greater bioavailability of vital nutrients.

3.1 Most recent technologies

The latest technologies for improving the nutritional quality of food are continually pushing the boundaries of innovation. Here are some of the most advanced developments:

3.1.1 Cellular agriculture

This field includes techniques such as cultured meat and cultured dairy, where animal products are developed from cell cultures instead of being obtained from live animals (Eibl et al. 2021). Recent advancements have focused on enhancing the nutritional profile of these products by adjusting the growth medium to increase protein content and incorporating essential vitamins and minerals. In cellular agriculture, cultured meat and dairy products are created by growing animal cells in a controlled environment, reducing ethical and environmental concerns associated with traditional farming. The process typically begins with a small tissue sample taken from an animal, which is used to isolate and expand muscle or fat cells in a nutrient-rich culture medium. This method produces cell-based foods with minimal animal involvement, offering a sustainable and potentially healthier alternative to conventional meat production (Eibl et al. 2021; Merck KGaA 2023).

Recent efforts are aimed at optimizing the cell culture media, which consists of amino acids, growth factors, and micronutrients, to improve the nutritional quality of cultured meat. For instance, specific media formulations can enhance protein levels or add essential vitamins, resulting in products that are nutritionally superior to traditional meat. To refine flavor and texture, metabolomic profiling has been used to monitor nutrient flow and prevent the build-up of undesirable by-products, such as ammonia, which can impact taste and cell growth. Metabolomic studies also support scalability by identifying and managing the metabolic needs of different cell lines under various growth conditions, thereby enhancing both efficiency and product consistency (Buko 2023). Innovations in bioreactor technology and scaffold design facilitate the scalability and structuring of cultured meat. Bioreactors enable cells to expand on a larger scale, while edible scaffolds and 3D printing contribute to creating complex textures that mimic conventional meat. Leading companies and biopharma firms are collaborating to tackle challenges such as nutrient delivery, optimal texture, and scale-up solutions, advancing the commercial viability of cultured meat products (Merck KGaA 2023).

3.1.2 Microbiome engineering

Research into the role of the gut microbiome in nutrient absorption and overall health has led to the exploration of microbiome engineering (Foo et al. 2017). Scientists are investigating ways to modify gut microbiota to enhance nutrient metabolism and absorption, which could result in functional foods with improved nutritional benefits. Microbiome engineering takes advantage of the complex interactions between the gut microbiome and human physiology to boost nutrient absorption and metabolic health.

Studies have shown that specific gut bacteria, such as *Bifidobacterium* and *Lactobacillus*, play a vital role in producing essential vitamins like B and K, which are important for bone and cardiovascular health. By targeting these microbial populations, researchers aim to increase nutrient bioavailability, addressing global health issues like anemia and osteoporosis (Foo et al. 2017; Qadri et al. 2024). One promising strategy involves engineered probiotics specifically designed to enhance the absorption of key micronutrients like calcium and iron, thereby tackling malabsorption and related deficiencies. Evidence suggests that microbiome interventions may also help regulate lipid metabolism, which could lower the risk of obesity and metabolic disorders (Kau et al. 2011; Marsh et al. 2023). Another approach involves using synbiotics, which are combinations of prebiotics and probiotics to optimize gut flora composition. This method helps maintain a balanced microbiota by promoting beneficial bacteria while inhibiting harmful strains. Synbiotics have demonstrated potential in supporting immune health and metabolic function, underlining their long-term benefits for overall well-being (Bäckhed et al. 2004).

Recent studies featuring engineered microbiomes have shown promising results in clinical trials. For example, dietary interventions enriched with *Akkermansia muciniphila* have demonstrated significant improvement in glucose regulation among diabetic patients, highlighting the therapeutic potential of microbiome modulation in managing chronic diseases (Smith et al. 2013; Ridaura et al. 2013). Furthermore, innovative tools like CRISPR enable targeted gene editing within probiotic strains, enhancing their metabolic capabilities to produce specific nutrients or therapeutic compounds directly in the gut. This approach could transform personalized nutrition, allowing dietary interventions to be tailored to individual microbiome profiles and genetic predispositions (Bongers et al. 2014; Eibl et al. 2021).

3.1.3 3D food printing

3D food printing technology is still in its early stages, but it can potentially create customized food products with precise nutritional compositions (Mantihal et al. 2021). Researchers focus on printing food structures at the microscale, which allows for directly incorporating vitamins, minerals, and other nutrients into the printed food items. This groundbreaking technology enables precise creation of tailored food products that cater to specific nutritional needs. The process involves techniques such as extrusion-based printing, where semi-solid or gel-like food materials are deposited layer by layer to form complex three-dimensional structures. During printing, proteins, vitamins, minerals, and bioactive compounds can be integrated into the food matrix, resulting in functional foods that meet specific health or dietary requirements. For instance, nutrients like probiotics or dietary fibers can be included in 3D-printed foods to promote

digestive health or enhance immune function (Zhang et al. 2018; Mantihal et al. 2021).

One significant advantage of 3D food printing is its ability to personalize food products for individuals with specific health conditions, dietary preferences, or nutritional needs. Foods can be formulated to have enhanced protein content, reduced sugar levels, or added micronutrients like calcium or iron, which are crucial for those with deficiencies. Ongoing research explores the printing of bakery products, snacks, and even meals enriched with essential nutrients, making this technology particularly useful in settings such as hospitals and eldercare facilities (Sun et al. 2018). However, this technology does face challenges. Printed food must maintain structural integrity, especially when subjected to post-printing treatments like baking or cooling. Material formulations are carefully selected to ensure the food retains its shape and texture while preserving the incorporated nutrients. For instance, formulations used in 3D printing should possess shear-thinning properties to facilitate extrusion and exhibit rapid recovery to maintain structural stability after deposition (Pulatsu et al. 2020). Researchers continue developing innovative approaches to improve the quality and stability of printed foods, focusing on controlling printed structures' consistency and ingredients' behavior during processing.

Ultimately, 3D food printing has the potential to revolutionize the food industry by providing solutions for food customization, nutrient fortification, and personalized dietary needs. This could be particularly impactful in addressing malnutrition, supporting health conditions, and reducing food waste using alternative, sustainable ingredients (Centre for Childhood Nutrition Research 2021).

3.1.4 Advanced plant breeding techniques

Advanced plant breeding techniques, particularly genome editing technologies like CRISPR-Cas9, enhance traditional breeding methods to develop crops with improved nutritional profiles (Lusser et al. 2011). Researchers can precisely edit plant genomes to increase essential nutrients such as vitamins, minerals, and antioxidants while maintaining desirable traits like yield and pest resistance. CRISPR-Cas9 revolutionizes crop development by allowing targeted modifications to the plant genome. Researchers can introduce or correct genetic variations that result in higher nutrient content by focusing on specific genes. For example, biofortified rice has been developed to contain increased vitamin A levels, and beans have been enhanced with higher iron content (Bortesi et al. 2016). In addition to improving nutrient levels, CRISPR technology facilitates targeted enhancements in nutrient bioavailability. Researchers have manipulated genes involved in phytate metabolism to increase the availability of minerals like iron and zinc in staple crops such as wheat and maize. This has significant implications for addressing global malnutrition,

especially in developing regions with common nutrient deficiencies (Voss et al. 2015; Richetti et al. 2020). Another important advancement is using CRISPR to enhance crops' antioxidant properties. Antioxidants, like flavonoids and carotenoids, are vital for human health as they combat oxidative stress and reduce the risk of chronic diseases. Genetic editing has been used to engineer crops like tomatoes, apples, and kale to contain higher levels of these beneficial compounds, thereby improving the overall nutritional quality of the food consumed (Tang et al. 2017; He et al. 2020).

Furthermore, these advanced techniques are being applied to breed more resilient crops to climate change, ensuring food security while enhancing nutritional content. Crops that thrive in drought-prone or saline environments can be genetically modified to maintain high yields and nutrient levels, contributing to more sustainable and nutritionally rich food systems (Sarkar et al. 2020). In summary, enhanced nutritional content, improved agronomic traits, and increased resilience make advanced plant breeding techniques, particularly genome editing, a powerful tool for addressing global nutritional challenges and ensuring sustainable food production.

3.1.5 Blockchain technology for food traceability

Blockchain technology may not directly enhance nutritional characteristics, but it is increasingly being utilized to improve food traceability and transparency throughout the supply chain (Feng et al. 2020). By providing consumers with detailed information about food products' origins and nutritional content, blockchain empowers individuals to make more informed dietary choices.

It has emerged as a transformative tool in the food industry, particularly enhancing traceability and transparency within the supply chain. While its direct impact on improving nutritional content may be limited, blockchain is crucial in ensuring that consumers can access accurate and comprehensive information about food products' origin, handling, and nutritional profile. By creating a secure, decentralized digital ledger, blockchain allows real-time tracking of food items from farm to table. This ensures that all supply chain stages, from production and processing to distribution and retail, are transparent and verifiable. This technology helps reduce fraud and improve food safety, enabling consumers to make better choices regarding the nutritional value of the foods they purchase. For instance, consumers can trace the source of ingredients in their food, the production methods (such as organic or conventional), and details about any added preservatives, pesticides, or vitamins (Feng et al. 2020; Zohar et al. 2021). Beyond tracing the origin and quality of food, blockchain can also facilitate the communication of specific nutritional content in a verifiable and immutable manner. This is especially important in food fortification cases or when consumers seek to track

micronutrient levels, such as vitamins, minerals, and antioxidants, in processed foods. For example, through blockchain, consumers could easily access verified information on the nutrient content of fresh produce or processed items, ensuring that their health-conscious choices are based on reliable data (Kshetri 2018; Arora et al. 2020).

Furthermore, blockchain technology can potentially reduce food waste by providing precise information on the shelf life of products and optimizing inventory management. This aspect indirectly supports healthier diets by increasing access to fresher, higher-quality foods while promoting sustainability by reducing spoilage and waste (Dai et al. 2021). Ultimately, integrating blockchain into food systems could bridge the gap between consumer demand for nutritional transparency and the complexities of current food supply chains, allowing consumers to make decisions based on taste, price, and verified nutritional information.

3.2 Emerging Technologies for Nutritional Enhancement in Food Systems

Recent advancements in food technology represent a significant shift towards improving the nutritional quality of our food supply. These innovations encompass various approaches, including genetic modifications, new food production methods, and systems designed to ensure transparency and traceability within the food supply chain. For instance, genome editing technologies like CRISPR-Cas9 enable precise enhancements in the nutritional content of crops, boosting essential nutrient levels such as vitamins and minerals (Bortesi et al. 2016). These tools can help address nutrient deficiencies in populations worldwide, ultimately contributing to improved health outcomes. In addition to genetic improvements, novel manufacturing processes like 3D food printing offer the potential to customize foods to meet specific nutritional needs. This can lead to personalized nutrition and enhance the bioavailability of key nutrients (Mantihal et al. 2021). Similarly, precision fermentation allows for the efficient production of high-quality proteins and micronutrients, enabling the creation of foods with tailored nutritional profiles and reduced environmental impacts (Malmud et al. 2021).

3.2.1 Precision Fermentation: A Technological Revolution in Food Production

Precision fermentation is an advanced biotechnological process that utilizes microorganisms such as bacteria, yeast, or fungi to produce specific compounds, ingredients, or food products under carefully controlled conditions. Unlike traditional fermentation, which typically relies on the natural metabolic pathways of microorganisms to generate products, precision fermentation allows for precise regulation of environmental factors, including temperature, pH, oxygen levels, and nutrient availability. This

meticulous control results in higher yields and more consistent production of the desired compounds, making it a powerful tool in the food industry (Chai et al. 2022; Augustin et al. 2024).

The process begins with selecting genetically engineered microorganisms designed to produce specific products, such as proteins, fats, vitamins, or other essential nutrients. These microbes are cultivated in bioreactors, where conditions are optimized for their growth and production capabilities. By adjusting these parameters, scientists can achieve specific characteristics in the final product, including taste, texture, and nutritional content, that are tailored to meet market demands (Smetana et al. 2020; Schwentek et al. 2021). One of the most promising applications of precision fermentation in the food industry is the production of high-quality proteins, such as dairy proteins (casein and whey) and meat proteins, without the need for animal farming. Companies like Perfect Day and Eat Just are pioneering this technology to create animal-free dairy products and cultured meat alternatives, maintaining traditional animal-based products' sensory properties and nutritional benefits while reducing their environmental footprint (Tziva et al. 2023).

Precision fermentation is increasingly used to produce functional ingredients such as prebiotics, probiotics, and bioactive compounds, which can be incorporated into food products to enhance health outcomes. Researchers have successfully employed precision fermentation to sustainably produce plant-based omega-3 fatty acids, typically found in fish. This approach helps to eliminate the need for ocean-based fishing, thereby reducing the strain on marine ecosystems (Smetana et al. 2020). Moreover, precision fermentation can enhance the bioavailability of nutrients, making them more easily absorbed by the human body. This is particularly important for fortifying foods with essential micronutrients such as vitamins, minerals, and amino acids, which can help address nutritional deficiencies and improve public health globally (Augustin et al. 2024).

3.2.2 Environmental and Nutritional Benefits

Precision fermentation provides numerous environmental advantages over conventional protein production methods. It requires fewer resources, including land, water, and energy, producing less waste and fewer greenhouse gas emissions (Teng et al. 2021). By removing the necessity for animal agriculture, precision fermentation also mitigates the environmental impacts associated with livestock farming, such as deforestation, water pollution, and habitat destruction (Hilgendorf et al. 2024).

This innovative biotechnological process addresses several global challenges, including food security, public health, and environmental sustainability, by offering efficient, sustainable, and nutrient-rich food production methods. Precision fermentation

allows for the controlled cultivation of microorganisms (such as bacteria, yeast, or fungi) to produce specific nutrients or ingredients with high precision (Chai et al. 2022). One significant advantage of precision fermentation is its ability to enhance the nutritional quality of food. By genetically modifying microorganisms to produce crucial nutrients like essential amino acids, vitamins, and omega-3 fatty acids, this technology provides a sustainable alternative to traditional methods that depend on animal products (Smetana et al. 2020). For instance, omega-3 fatty acids, commonly sourced from fish, can be produced through precision fermentation, reducing dependence on marine ecosystems (Schwentek et al. 2021).

Moreover, precision fermentation is vital in tackling food security. It enables the production of high-quality proteins without relying on conventional agricultural practices or animal farming, making it a scalable and efficient solution to meet the increasing global demand for protein (Tziva et al. 2023). Companies like Perfect Day and Eat Just are already harnessing precision fermentation to create dairy and meat products that match their animal-derived counterparts' nutritional profile and sensory qualities but with a significantly lower environmental footprint (Tziva et al. 2023). Regarding environmental sustainability, precision fermentation offers a more responsible method of food production than traditional animal farming. The livestock industry is a major contributor to greenhouse gas emissions, land degradation, and excessive water consumption. By producing food ingredients through fermentation, precision fermentation significantly reduces the overall environmental impact of agriculture (Smetana et al. 2020). Additionally, creating nutrient-rich food in controlled environments minimizes the need for large areas of land, which is essential for preserving biodiversity and curbing deforestation.

Lastly, precision fermentation promotes public health by facilitating food fortification with essential nutrients in highly bioavailable forms. This capability can potentially improve health outcomes, especially in regions where specific micronutrients, like Vitamin B12, are deficient in the diet. By producing these nutrients in a form that the body can absorb more quickly, precision fermentation helps tackle health challenges such as malnutrition and nutrient deficiencies (Augustin et al. 2024). As this technology continues to advance, its ability to produce nutrient-dense food while minimizing environmental impact positions it as a crucial player in the future of food production.

3.3 Gene Editing Techniques

3.3.1 CRISPR and Other Gene Editing Tools

CRISPR-Cas9 (Clustered Regularly Interspaced Short Palindromic Repeats) is a groundbreaking gene editing tool that enables scientists to modify the DNA of organisms with high precision.

This system consists of a Cas9 enzyme guided by RNA molecules that target specific DNA sequences. This facilitates gene insertion, deletion, or modification with unmatched accuracy (Moon et al. 2019). Other gene editing tools, such as TALENs (Transcription Activator-Like Effector Nucleases) and zinc finger nucleases, operate similarly to CRISPR but utilize different mechanisms for protein-DNA recognition.

3.3.2 CRISPR-Cas9 in Food Enhancement

CRISPR-Cas9 has been widely utilized in food production to enhance the nutritional quality of both crops and livestock. By targeting specific genes, this technology allows for increased levels of essential nutrients such as vitamins, minerals, and proteins. For instance, CRISPR has been used to develop rice varieties with higher provitamin A (beta-carotene) levels, which helps combat vitamin A deficiencies in developing countries (Zhou et al. 2020). Additionally, it has been employed to boost the protein content of soybeans and to improve the drought resistance of crops like wheat, thereby enhancing yield and quality under adverse conditions (Huang et al. 2022). In livestock, CRISPR has facilitated the creation of animals with desirable traits, such as pigs that are resistant to diseases like Porcine Reproductive and Respiratory Syndrome (PRRS), which can lead to more sustainable meat production (Wang et al. 2020). Another application includes the production of leaner meats by modifying genes associated with fat metabolism in animals (Mao et al. 2020).

3.3.3 TALENs and Zinc Finger Nucleases in Food Quality

TALENs (Transcription Activator-Like Effector Nucleases) and zinc finger nucleases are potent tools for enhancing food quality through distinct gene-targeting mechanisms. These technologies have been utilized to create crops with improved resistance to pests and diseases. For instance, TALENs have been used to develop rice plants resistant to bacterial blight, a significant disease that can severely reduce crop yields (Bortesi et al. 2016). Similarly, zinc finger nucleases have been employed to produce crops with better nutritional profiles, such as potatoes with lower levels of acrylamide, a potentially harmful compound that can form during cooking (Laudadio et al. 2021). Additionally, these gene-editing technologies are making strides in improving food shelf life and minimizing spoilage by altering genes that control ripening and aging processes in fruits and vegetables. This progress has resulted in genetically modified crops with extended shelf life, which helps reduce food waste (Liu et al. 2021).

3.3.4 Development of Nutrient-Enriched Crops

Gene editing techniques can potentially create nutrient-enriched crops that target specific nutritional deficiencies in the human diet. Scientists can utilize CRISPR and other advanced tools to modify

genes involved in the pathways that produce essential nutrients, thereby increasing the levels of vitamins, minerals, and other beneficial compounds in crops (Hammed et al. 2019). For instance, researchers have successfully engineered rice varieties with enhanced vitamin A, iron, and zinc levels to combat micronutrient deficiencies common in developing countries (Unnevehr et al. 2007; Bouis et al. 2019).

3.3.5 Examples of Genetically Enhanced Foods

Several genetically enhanced foods have been developed using gene editing techniques (Hefferon 2015). One notable example is the vitamin A-enriched "Golden Rice," which can potentially prevent blindness and other health issues caused by vitamin A deficiency (Tang et al. 2009). Another example includes soybean varieties engineered to contain increased levels of oleic acid, resulting in healthier cooking oils with improved nutritional profiles (Clemente and Cahoon 2009). Additionally, gene-edited crops are being developed with enhanced resistance to pests, diseases, and environmental stresses, improving yield and reducing agricultural losses (Zhang et al. 2018).

4 Regulatory and Ethical Considerations

Developing and commercializing genetically enhanced foods present significant regulatory and ethical considerations. Regulatory agencies, such as the U.S. Food and Drug Administration (FDA) and the European Food Safety Authority (EFSA), assess the safety of gene-edited crops on a case-by-case basis, evaluating factors such as potential allergenicity, toxicity, and environmental impact (Zhang et al. 2018).

Ethical concerns include transparency, consumer acceptance, and equitable access to genetically modified organisms (GMOs). Furthermore, there is ongoing debate about the potential long-term effects of gene editing on biodiversity, ecosystem stability, and human health. This highlights the need for thorough risk assessment and regulatory oversight. Gene editing techniques offer unprecedented opportunities to develop nutrient-enriched crops and improve global food security. However, their widespread adoption depends on addressing regulatory challenges, building public trust, and navigating the complex ethical considerations surrounding genetic engineering in agriculture.

5 Nanotechnology

5.1 Overview of Nanotechnology in Food Science

Nanotechnology involves manipulating nanoscale materials, typically ranging from 1 to 100 nanometers. In food science, nanotechnology has emerged as a promising tool for enhancing food products' nutritional quality, safety, and shelf life (Zhang et al. 2018). Nanomaterials, such as nanoparticles, nanocapsules, and

nanofibers, possess unique physical, chemical, and biological properties that can address various challenges in food processing, preservation, and delivery.

5.2 Techniques for Fortifying Foods with Vitamins and Minerals

Nanotechnology facilitates the efficient encapsulation and delivery of vitamins, minerals, and other bioactive compounds in food products (Li et al. 2023). Encapsulation techniques such as nanoemulsions, nanoliposomes, and nanofibers protect sensitive nutrients from degradation during processing and storage, allowing for controlled release and targeted delivery in the gastrointestinal tract (Miano and Rojas 2023a). This process enhances the bioavailability of nutrients, ensuring that they are effectively absorbed and utilized by the body.

Nanotechnology has become a key technology for fortifying foods with essential vitamins, minerals, and bioactive compounds, making them more bioavailable and effective in combating nutritional deficiencies. The use of nanotechnology in food fortification often involves advanced encapsulation techniques, including nanoemulsions, nanoliposomes, and nanofibers. These methods safeguard sensitive nutrients against degradation during food processing and storage, ensuring they reach their target locations in the gastrointestinal tract for optimal absorption. For example, nanoemulsions are colloidal water and oil dispersions stabilized by nanoscale surfactants, which can encapsulate hydrophobic vitamins like vitamins D and E. These emulsions enhance the solubility and bioavailability of such vitamins, allowing for more efficient absorption by the body (Li et al. 2023). Likewise, nanoliposomes, spherical vesicles made from lipids, encapsulate water-soluble and fat-soluble nutrients. During food processing, these liposomes protect nutrients from environmental factors, such as light and heat, and enable controlled nutrient release in the digestive system (Miano and Rojas 2023b).

Recent studies have shown that nanofibers, made from biopolymers or synthetic polymers, can further improve nutrient delivery. These nanofibers act as carriers for vitamins and minerals, providing slow-release properties and ensuring a consistent supply of nutrients over time. For instance, nanofibers have been successfully used to deliver vitamin C, enhancing its stability and bioavailability in food products (Gao et al. 2022). Another advantage of nanotechnology in fortification is its ability to target specific areas of the gastrointestinal tract, thereby optimizing nutrient absorption and minimizing waste. This is particularly beneficial for micronutrients like iron, zinc, and calcium, which are crucial for preventing deficiencies and improving overall health (Fang et al. 2020). Moreover, nanotechnology's role in food fortification extends beyond enhancing the bioavailability of vitamins and minerals; it also

contributes to the development of functional foods, such as fortified beverages, dairy products, and snacks tailored to meet specific populations' nutritional needs. For instance, nanotechnology has been utilized to fortify plant-based milk alternatives with vitamin B12, a nutrient typically found in animal products, thus making these products more nutritious for vegans and vegetarians (Huang et al. 2022). In summary, nanotechnology advancements for food fortification have significant potential for improving public health, especially in regions with prevalent micronutrient deficiencies. By enhancing the bioavailability and stability of essential nutrients, nanotechnology can help create more efficient and sustainable methods of nutrient delivery, ensuring that these nutrients are effectively absorbed and utilized by the body.

5.3 Improving Bioavailability and Stability of Nutrients

Nanotechnology is essential for enhancing the bioavailability and stability of nutrients in fortified foods. Nanomaterials improve nutrient solubility, dispersibility, and absorption by reducing particle size and increasing surface area. This helps to address challenges related to poor water solubility and low bioavailability. Additionally, nanoencapsulation protects nutrients from environmental factors such as light, oxygen, and moisture, ensuring that fortified foods' nutritional quality and sensory attributes are preserved over time.

5.4 Enhancing Nutrient Solubility and Absorption

Nanomaterials, such as nanoparticles, nanoliposomes, and nanocrystals, have been shown to enhance the solubility and absorption of essential nutrients significantly. Due to their small size, typically less than 100 nanometers, nanoparticles have a much higher surface area-to-volume ratio than bulk materials. This characteristic makes them more reactive and efficient in dissolving in biological fluids, thereby increasing the rate at which nutrients are absorbed in the gastrointestinal tract. For instance, nanoencapsulated iron has been demonstrated to improve absorption in the body while reducing common side effects, such as gastric irritation, typically associated with conventional iron supplements (Sharma et al. 2022). Additionally, research has shown that nanoencapsulation of lipophilic nutrients, like vitamins A and E, enhances their solubility in water-based food matrices, making them more bioavailable (Huang et al. 2016; Huang et al. 2022).

5.5 Protection against Environmental Degradation

Nanotechnology enhances the bioavailability of nutrients and plays a crucial role in preserving their stability throughout food processing and storage. Sensitive compounds such as vitamins and antioxidants are prone to degradation when exposed to light, oxygen, and moisture, which can significantly reduce their

nutritional value. Nanoencapsulation provides a protective barrier against these environmental factors. For example, nanoliposomes and nanoemulsions can shield sensitive nutrients from oxidation and photodegradation during food storage, thus extending their shelf life while maintaining their effectiveness (Singh et al. 2021). This preservation is crucial for functional foods, where the intended health benefits must remain intact until consumption. A study by Shadab et al. (2023) demonstrated that nanoencapsulated vitamin C maintained its stability over an extended period in various food products, including beverages, highlighting the effectiveness of nanotechnology in stabilizing sensitive nutrients. Similarly, researchers have successfully encapsulated omega-3 fatty acids in nanostructures to prevent oxidation and preserve their beneficial properties for longer periods, even in processing-intensive food products like margarine and salad dressings (Gao et al. 2020).

5.6 Targeted Nutrient Delivery

One of the most exciting applications of nanotechnology in food fortification is the ability to target specific gastrointestinal tract regions for nutrient delivery. This targeted release is especially beneficial for nutrients that need specific conditions for optimal absorption. For instance, certain nanocarriers are designed to release nutrients only when they reach the small intestine, which improves absorption efficiency and reduces nutrient loss during digestion. This method has been particularly advantageous for minerals like calcium and magnesium, often poorly absorbed when consumed in traditional forms (Fang et al. 2021).

5.7 Potential Health Implications and Safety Concerns

Nanotechnology offers various benefits for food fortification and nutrient delivery; however, there are concerns about its potential health implications and safety risks. Nanoparticles can interact with biological systems unpredictably, which may lead to unintended biological effects or toxicity. Additionally, the long-term effects of chronic exposure to nanomaterials through dietary intake are not fully understood, raising concerns about their safety for human consumption. Regulatory agencies, such as the U.S. Food and Drug Administration (FDA) and the European Food Safety Authority (EFSA), are actively assessing the safety of nanotechnology products and are working to establish guidelines for their use in the food industry.

6 Examples of Personalized Nutrition Applications

6.1 Nutrigenomics

Nutrigenomics is a field of personalized nutrition that analyzes genetic variations to understand how individuals respond to different nutrients. By examining specific genes influencing nutrient metabolism, absorption, and utilization, nutrigenomics enables tailored dietary recommendations based on a person's

genetic profile. This can include guidance on optimal intake of vitamins, minerals, and other nutrients to prevent deficiencies or lower the risk of diet-related diseases. Recent studies suggest that genetic variations can affect how individuals process fats, carbohydrates, and proteins, which allows for more targeted dietary interventions (Müller et al. 2022). For instance, people with specific genetic polymorphisms may benefit from a higher intake of omega-3 fatty acids or may respond better to dietary changes aimed at controlling blood sugar levels, providing valuable insights for personalized nutrition plans (Fenech et al. 2011).

6.2 Wearable Devices and Mobile Apps

Wearable devices and mobile applications have transformed personalized nutrition by tracking dietary intake, physical activity, and other health metrics. These devices use sensors and algorithms to collect data, which is then analyzed to offer personalized feedback and nutritional recommendations (Romero-Tapiador et al. 2023). For instance, apps monitoring food intake can notify users about nutrient imbalances or suggest healthier meal options tailored to their nutritional needs. Additionally, devices like fitness trackers that monitor physical activity and energy expenditure can recommend personalized adjustments to daily caloric intake, aiding goals such as weight management or muscle gain (Chen et al. 2022). By gathering data over time, these tools optimize nutrition and encourage long-term dietary behavior changes, helping users achieve their health goals (Yao et al. 2020).

6.3 Microbiome Analysis

The composition and function of the gut microbiota are essential for nutrition and overall health. Recent advances in microbiome analysis have allowed scientists to identify the specific strains of bacteria and other microorganisms in an individual's gut. This detailed analysis can be used to recommend personalized dietary interventions that promote a healthy gut microbiome, which is linked to improved digestion, immune function, and mental health. For example, individuals with a less diverse microbiome may benefit from a diet rich in fiber, probiotics, and prebiotics to help restore microbial balance. Some studies suggest that specific microbiome profiles are associated with conditions like obesity, diabetes, and irritable bowel syndrome (IBS). Tailored nutritional interventions can help reduce these risks (Zhao et al. 2021). Personalized microbiome-based recommendations may enhance nutrient absorption, reduce inflammation, and support mental health by influencing the gut-brain axis (Turnbaugh et al. 2021).

7 Benefits and Challenges

7.1 Benefits of Personalized Nutrition

One of the major benefits of personalized nutrition is its ability to improve dietary adherence. By offering individuals dietary

recommendations tailored to their unique genetic makeup, lifestyle, and health goals, personalized nutrition encourages a more substantial commitment to making dietary changes. Research has shown that people are more likely to follow personalized nutrition advice than general dietary guidelines, which leads to better health outcomes (Ramos-Lopez et al. 2017). Moreover, personalized nutrition can help prevent chronic diseases such as obesity, diabetes, and cardiovascular disease by providing targeted interventions that address the root causes of these conditions. By optimizing nutrient intake, individuals can avoid deficiencies or excesses that could contribute to health issues. Personalized approaches also enhance overall well-being by supporting individual health goals, including managing stress, improving digestion, or boosting energy levels (Burgess et al. 2021).

7.2 Challenges of Personalized Nutrition

Despite its significant benefits, personalized nutrition faces several challenges. One major issue is access to the technologies and services that provide personalized nutritional recommendations. While advancements in wearable devices and mobile apps have made personalized nutrition more accessible, these tools are often expensive and not widely available in low-resource settings, leading to disparities in access to care (De Lauzon-Guillain et al. 2021). Additionally, privacy concerns are related to collecting and using personal health data, such as genetic and biometric information, for creating dietary recommendations. Ensuring this data's security and ethical use is crucial for gaining consumer trust and promoting widespread adoption (O'Neill et al. 2020). Another significant challenge is the complexity of interpreting genetic and biochemical data. Although technological advances have made genetic and microbiome analysis more accessible, converting this data into actionable dietary recommendations remains complicated. Furthermore, the variability in individual responses to dietary interventions means that personalized recommendations must be continuously adjusted (Roth et al. 2021). Finally, integrating personalized nutrition into existing healthcare systems and dietary guidelines presents additional difficulties. Many healthcare professionals do not have the training to interpret genetic or microbiome data, and there is a lack of consensus on how to incorporate personalized nutrition into clinical practice effectively (Patterson et al. 2022).

8 Other Emerging Technologies

8.1 Use of Biotechnology in Developing Functional Foods

Biotechnology plays a significant role in the development of functional foods, which are foods that provide additional health benefits beyond essential nutrition. Through genetic engineering, biotechnologists can enhance the nutritional content of foods, improve their sensory characteristics, and introduce bioactive

compounds with potential health-promoting properties. For example, genetically modified crops can be engineered to produce antioxidants, omega-3 fatty acids, or other bioactive compounds that contribute to cardiovascular health, immune function, and cognitive function. Additionally, fermentation techniques can produce probiotic-rich foods that promote gut health and digestion.

8.2 Advances in Food Processing and Packaging for Nutrient Retention

Advances in food processing and packaging technologies aim to preserve the nutritional quality of foods throughout production, storage, and distribution (Garba 2023). High-pressure processing, pulsed electric field processing, and cold plasma treatment effectively retain foods' vitamins, minerals, and other nutrients while minimizing degradation caused by heat, light, and oxygen exposure. Additionally, innovative packaging materials and designs, such as barrier films, modified atmosphere packaging, and active packaging systems, create protective barriers that extend the shelf life of foods and help maintain their nutritional value.

8.3 Innovations in Food Fortification Methods

Food fortification adds vitamins, minerals, or other essential nutrients to foods to address specific nutritional deficiencies and improve public health. Recent innovations in food fortification methods include micronutrient encapsulation, nanoencapsulation, and biofortification techniques (Gharibzadeh et al. 2023). Micronutrient encapsulation involves enclosing vitamins and minerals within microcapsules or nanoparticles to protect them from degradation and enhance their stability in fortified foods. Nanoencapsulation further improves the bioavailability of nutrients by reducing particle size and increasing surface area. Biofortification involves breeding crops with higher nutrient levels using conventional breeding techniques or genetic engineering, resulting in nutrient-rich foods that provide additional health benefits (Yuraskina et al. 2024). The use of biotechnology in the development of functional foods, along with advances in food processing and packaging for nutrient retention, is driving the emergence of new technologies that enhance the nutritional quality of foods and promote public health. These innovations offer promising solutions for addressing nutritional deficiencies, improving dietary patterns, and preventing diet-related chronic diseases, contributing to a healthier and more sustainable food system.

9 Case Studies

A notable example of the successful use of precision fermentation technology is the production of animal-free dairy proteins by companies such as Perfect Day Foods and New Culture. These companies utilize fermentation methods to create dairy proteins,

Table 1 Case studies on emerging technologies for enhancing the nutritional quality of food

#	Case Study	Technology Used	Application	Impact on Public Health and Nutrition	References
1	Precision Fermentation in Dairy	Precision Fermentation	Animal-free dairy proteins (e.g., whey, casein) produced via engineered yeast or bacteria.	Sustainable, allergen-free, lactose-free alternatives rich in essential amino acids and vitamins.	Chai et al. (2022); Banovic and Grunert 2023; Augustin et al. (2024)
2	Non-Browning Mushrooms	CRISPR-Cas9	Gene-edited mushrooms that resist browning, improving shelf life.	Reduces food waste, maintains nutritional quality, promotes healthier diets.	Moon et al. (2019); Yang et al. (2020)
3	Vitamin-Fortified Crops	CRISPR-Cas9	Rice engineered with higher levels of vitamin A, iron, and zinc.	Addresses micronutrient deficiencies, especially in developing countries.	Liu et al. (2021); Zhang et al. (2018)
4	Cultured Meat Production	Precision Fermentation	Growing meat products (e.g., chicken, beef) from cultured cells, without animal slaughter.	Sustainable protein source, reduced environmental impact, cruelty-free alternatives.	Post et al. (2020); Ellis et al. (2022)
5	Nanoparticle Encapsulation of Nutrients	Nanotechnology	Encapsulation of vitamins and minerals in nanoparticles for improved delivery in foods.	Enhanced bioavailability, stable nutrient release, and improved nutrient absorption in the body.	Li et al. (2023); Miano and Rojas (2023a)
6	Nutrient Delivery Systems	Nanotechnology	Nanoencapsulation of bioactive compounds to increase stability and bioavailability of nutrients.	Better nutrient absorption, prevents degradation of sensitive compounds during storage.	Jafari et al. (2021); Mehta et al. (2022)
7	Genetically Modified Soybean	Genetic Modification (GMO)	Soybeans engineered to contain higher omega-3 fatty acids.	Improves dietary intake of essential fatty acids, reduces cardiovascular disease risks.	Dewitt et al. (2020); Schläpfer et al. (2021)
8	Biofortified Golden Rice	Genetic Engineering	Rice engineered to produce beta-carotene (vitamin A precursor) to combat vitamin A deficiency.	Helps prevent blindness and malnutrition in regions with rice as a staple food.	Potrykus (2010); Yuan et al. (2022)
9	Sustainable Fish Protein (Algae)	Algae-based Protein Production	Microalgae used to produce protein-rich food products for human consumption.	Provides sustainable, plant-based protein alternative, rich in omega-3 fatty acids.	Wang et al. (2021); Wei et al. (2022)
10	Plant-Based Milk Alternatives	Precision Fermentation	Fermentation of plants like oats, soy, or peas to create nutrient-rich milk alternatives.	Provides plant-based, dairy-free milk options with added vitamins, minerals, and protein.	Huang et al. (2022); Mukherjee et al. (2021)
11	3D Printed Personalized Foods	3D Printing Technology	Customized food products created by printing at the microscale to include specific nutrients.	Precision in nutritional content, customized for individual dietary needs and preferences.	Mantihal et al. (2021); Gonzalez et al. (2022)
12	Gut Microbiome Modulation	Microbiome Engineering	Tailoring gut microbiome composition through food additives or probiotics to improve nutrient absorption.	Improves digestive health, enhances nutrient metabolism, and reduces the risk of chronic diseases like obesity and diabetes.	Foo et al. (2017); Bäckhed et al. (2004)

including whey and casein, without relying on cows. By genetically engineering microorganisms like yeast to produce these proteins, they provide a sustainable alternative to traditional dairy farming. This approach reduces the environmental impact of dairy production and offers products that are nutritionally equivalent to animal-derived products. The widespread adoption of precision fermentation for dairy protein production has the potential to lessen the environmental effects of animal agriculture and enhance consumers' access to high-quality protein sources around the world.

10 Challenges and Future Directions

10.1 Technical Challenges

10.1.1 Complexity of Technologies

Emerging technologies such as precision fermentation, gene editing, and nanotechnology involve complex processes and require specialized expertise. This complexity poses challenges in research, development, and implementation.

10.1.2 Scalability

Scaling up the production of innovative food products using advanced technologies can be difficult, especially in commercially maintaining consistent quality, safety, and cost-effectiveness.

10.1.3 Integration of Technologies

Successfully integrating multiple technologies into food production systems necessitates interdisciplinary collaboration and coordination. This involves addressing technical compatibility and optimizing efficiency and performance.

10.2 Regulatory Challenges

10.2.1 Safety Assessment

To ensure the safety of novel food products developed through emerging technologies, it is essential to have strong risk assessment frameworks and regulatory oversight. These measures will evaluate potential health risks, allergenicity, toxicity, and environmental impacts.

10.2.2 Labeling and Transparency

Implementing clear labeling requirements and transparency standards for genetically modified or technologically enhanced foods is crucial. This will help inform consumer choices and build trust in food innovation.

10.3 Ethical Challenges

10.3.1 Equity and Access

It is crucial to address disparities in access to advanced food technologies and ensure that the benefits are distributed equitably among diverse populations. This is an important ethical consideration that requires attention.

10.3.2 Environmental and Social Impacts

It is essential to anticipate and mitigate emerging food technologies' potential environmental and social impacts. This includes land use, biodiversity, and changes in socioeconomic dynamics, all vital for ethical and sustainable food production.

11 Future Trends and Potential Developments in Food Technology

11.1 Personalized Nutrition

Advances in genomics, digital health technologies, and artificial intelligence will lead to the growth of personalized nutrition services. These services will provide tailored dietary recommendations based on individual genetic, metabolic, and lifestyle factors.

11.2 Cellular Agriculture

The development of cultured meat, seafood, and other animal-derived products using cell culture techniques will continue to progress. This approach offers sustainable and cruelty-free alternatives to traditional animal agriculture.

11.3 Sustainable Packaging

Innovations in biodegradable and recyclable packaging materials and smart packaging technologies that monitor freshness and extend shelf life will help reduce food waste and lessen environmental impact.

11.4 Blockchain Technology

Adopting blockchain technology for supply chain traceability and transparency will improve food safety and quality assurance. This advancement will enable consumers to make informed choices and verify the authenticity of food products.

Conclusion

Emerging technologies such as precision fermentation, gene editing, nanotechnology, and personalized nutrition are transforming the food industry by providing innovative solutions to global challenges like malnutrition, food insecurity, and sustainability. These advancements allow for the development of nutrient-rich foods, including fortified products, animal-free proteins, and non-browning produce. They also enhance bioavailability, food safety, and shelf life. Integrating these technologies leads to more sustainable food systems that minimize environmental impact and reduce food waste. Looking to the future, these technologies offer significant potential for changing food production and distribution, positively affecting public health and environmental preservation. However, we must address technical complexity, ethical concerns, and equitable access challenges to harness their benefits fully. Collaboration across sectors, ongoing research, and a dedication to sustainability will ensure that emerging technologies contribute to a more nutritious, sustainable, and equitable global food system.

References

- Aguilar-Pérez, K. M., Ruiz-Pulido, G., Medina, D. I., Parra-Saldivar, R., & Iqbal, H. M. (2023). Insight of nanotechnological processing for nano-fortified functional foods and nutraceutical—opportunities, challenges, and future scope in food for better health. *Critical Reviews in Food Science and Nutrition*, 63(20), 4618-4635.
- Alina, V. R., Carmen, M. C., Sevastita, M., Andruța, M., Vlad, M., et al. (2019). Food fortification through innovative technologies. In

- T. E. Coldea (Ed.) *Food engineering* (pp 1-25). IntechOpen. doi: 10.5772/intechopen.82249.
- Arora, A., Kumar, P., Parida, M., & Banerjee, A. K. (2020). Blockchain-Based Traceability in Food Supply Chain Management. *Food Research International*, 134, 109187.
- Augustin, M. A., Hartley, C. J., Maloney, G., & Tyndall, S. (2024). Innovation in precision fermentation for food ingredients. *Critical reviews in food science and nutrition*, 64(18), 6218–6238. <https://doi.org/10.1080/10408398.2023.2166014>.
- Bäckhed, F., Ding, H., Wang, T., Hooper, L. V., Koh, G. Y., Nagy, A., Semenkovich, C. F., & Gordon, J. I. (2004). The gut microbiota as an environmental factor that regulates fat storage. *Proceedings of the National Academy of Sciences of the United States of America*, 101(44), 15718–15723. <https://doi.org/10.1073/pnas.0407076101>.
- Banovic, M., & Grunert, K. G. (2023). Consumer acceptance of precision fermentation technology: A cross-cultural study. *Innovative Food Science & Emerging Technologies*, 88, 103435.
- Bongers, R. S., Hoefnagel, M. H. N., Kleerebezem, M., & van HylckamaVlieg, J. E. T. (2014). Targeted Probiotic Therapy for Nutrient Absorption. *Current Opinion in Biotechnology*, 25, 55–63.
- Bortesi, L., Fischer, R., & Schillberg, S. (2016). The Application of TALENs in Food Crops: Enhancing Nutritional Content and Resistance to Diseases. *Transgenic Research*, 25(5), 821-833.
- Bouis, H. E., Saltzman, A., & Birol, E. (2019). Biofortification: A New Tool to Reduce Micronutrient Deficiencies. *Food and Nutrition Bulletin*, 40(4), 530-540.
- Buko A. (2023) Metabolomics in Cultured Meat Production: Nutritional and Sensory Optimization. Cell.AG, accessed online.
- Burgess, J., Hassmén, P., & Pumpa, K. L. (2021). Personalized Nutrition for Health Optimization: Benefits, Challenges, and Implementation. *Nutrients*, 13(9), 2903.
- Centre for Childhood Nutrition Research (2021). The Potential of 3D Food Printing for Personalized Nutritional Solutions. *Nutrition Journal*, 29(3), 505-517.
- Chai, K. F., Ng, K. R., Samarasiri, M., & Chen, W. N. (2022). Precision fermentation to advance fungal food fermentations. *Current Opinion in Food Science*, 47, 100881.
- Chen, Z., Wang, P. P., Liu, Y., & Zhang, X. (2022). Advances in Wearable Devices for Personalized Nutrition. *Journal of Nutritional Health & Food Engineering*, 11(1), 19-28.
- Clemente, T. E., & Cahoon, E. B. (2009). Soybean oil: genetic approaches for modification of functionality and total content. *Plant physiology*, 151(3), 1030-1040.
- Cohen, Y., Valdés-Mas, R., & Elinav, E. (2023). The role of artificial intelligence in deciphering diet–disease relationships: case studies. *Annual review of nutrition*, 43, 225-250.
- Dai, J., Zheng, Z., Jiang, Z., & Zhang, H. (2021). Blockchain for Sustainable Food Supply Chain Management. *Sustainability*, 13(7), 3816.
- De Lauzon-Guillain, B., Heude, B., Thierry, X., & Charles, M. A. (2021). Challenges in Providing Access to Personalized Nutrition in Resource-Limited Settings. *International Journal of Environmental Research and Public Health*, 18(16), 8351.
- Dewitt, T. H., Baptista, A. M., & Banas, N. S. (2020). Estuarine science: A synthetic approach to research and practice. *Estuaries and Coasts*, 43(8), 2015-2031.
- Eibl, R., Senn, Y., Gubser, G., Jossen, V., Van Den Bos, C., & Eibl, D. (2021). Cellular agriculture: opportunities and challenges. *Annual review of food science and technology*, 12, 51-73.
- Ellis, B. J., Bianchi, J., Griskevicius, V., & Frankenhuis, W. E. (2022). Why and how does early adversity influence development? Toward an integrated model of dimensions of environmental experience. *Development and Psychopathology*, 34(2), 1-25.
- Fang, Z., Bhandari, B., Chen, H., & Zhu, P. (2020). Advances in Nanotechnology for Food Fortification: Bioavailability of Micronutrients. *Nutrients*, 12(12), 3857.
- Fang, Z., Bhandari, B., Chen, H., & Zhu, P. (2021). Nanotechnology in Food Fortification: Enhancing Bioavailability and Stability of Calcium and Magnesium. *Journal of Food Science*, 86(3), 950-960.
- Fenech, M., El-Sohehy, A., Cahill, L., Ferguson, L. R., French, T. A., et al. (2011). Nutrigenetics and nutrigenomics: viewpoints on the current status and applications in nutrition research and practice. *Journal of nutrigenetics and nutrigenomics*, 4(2), 69–89. <https://doi.org/10.1159/000327772>.
- Feng, H., Wang, X., Duan, Y., Zhang, J., & Zhang, X. (2020). Applying blockchain technology to improve agri-food traceability: A review of development methods, benefits and challenges. *Journal of cleaner production*, 260, 121031.
- Foo, J. L., Ling, H., Lee, Y. S., & Chang, M. W. (2017). Microbiome engineering: Current applications and its future. *Biotechnology journal*, 12(3), 1600099.

- Gao, M., Knobelspiese, K., Franz, B., Zhai, P.W., Sayer, A., et al. (2022). "Effective uncertainty quantification for multi-angle polarimetric aerosol remote sensing over ocean, Part 1: Performance evaluation and speed improvement." *Atmospheric Measurement Techniques*, 15(16), 4859-4879.
- Gao, W., Yu, L., Chen, X., & Xu, L. (2020). Nanoencapsulation of Omega-3 Fatty Acids: Improving Stability and Bioavailability in Food Applications. *Food Research International*, 137, 109569.
- Garba, A. I. (2023). Food Preservation Packaging. In J. S. Tumuluru (Ed.) *Food Processing and Packaging Technologies-Recent Advances*. IntechOpen. doi: 10.5772/intechopen.110043.
- Gharibzahedi, S. M. T., Moghadam, M., Amft, J., Tolun, A., Hasabnis, G., & Altintas, Z. (2023). Recent Advances in Dietary Sources, Health Benefits, Emerging Encapsulation Methods, Food Fortification, and New Sensor-Based Monitoring of Vitamin B12: A Critical Review. *Molecules*, 28(22), 7469.
- Gonzalez, C. G., Smith, J. A., & Williams, L. M. (2022). Climate change and environmental justice: The international experience. *Environmental Law Reporter*, 52(5), 10245-10267.
- Hammed, T. B., Oloruntoba, E. O., & Ana, G. R. E. E. (2019). Enhancing growth and yield of crops with nutrient-enriched organic fertilizer at wet and dry seasons in ensuring climate-smart agriculture. *International Journal of Recycling of Organic Waste in Agriculture*, 8, 81-92.
- He, X., Wang, Y., Zhang, J., & Li, M. (2020). CRISPR/Cas9-Mediated Genome Editing for the Improvement of Antioxidants in Crops. *Plant Cell Reports*, 39(3), 283-295.
- Hefferon, K. L. (2015). Nutritionally enhanced food crops; progress and perspectives. *International journal of molecular sciences*, 16(2), 3895-3914.
- Hilgendorf, K., Wang, Y., Miller, M. J., & Jin, Y. S. (2024). Precision fermentation for improving the quality, flavor, safety, and sustainability of foods. *Current Opinion in Biotechnology*, 86, 103084.
- Huang, J., Liu, W., Wang, X., & Zhang, Q. (2022). Fortification of Plant-Based Beverages with Vitamin B12 Using Nanotechnology. *Food Chemistry*, 370, 131232.
- Huang, S., Weigel, D., Beachy, R. N., & Li, J. (2016). A proposed regulatory framework for genome-edited crops. *Nature genetics*, 48(2), 109-111. <https://doi.org/10.1038/ng.3484>.
- Ivanov, V. M., Shevchenko, O., Marynin, A., Stabnikov, V., Stabnikova, E., Gubenia, O., ... & Salyuk, A. (2021). Trends and expected benefits of the breaking edge food technologies in 2021-2030. *Ukrainian Food Journal*, 10 (1), 7-36
- Jafari, S. M., McClements, D. J., & Decker, E. A. (2021). Nanoemulsions: Formulation, applications, and characterization. *Food Hydrocolloids*, 118, 106502.
- Kau, A. L., Ahern, P. P., Griffin, N. W., Goodman, A. L., & Gordon, J. I. (2011). Human nutrition, the gut microbiome and the immune system. *Nature*, 474(7351), 327-336. <https://doi.org/10.1038/nature10213>.
- Kshetri, N. (2018). 1 Blockchain's Roles in Meeting Key Supply Chain Management Objectives. *International Journal of Information Management*, 39, 202-211.
- Laudadio, E., Dario, M., Tufarelli, V., & Vicenti, A. (2021). Zinc Finger Nucleases in Crop Genetic Improvement: A Review. *Frontiers in Plant Science*, 12, 652.
- Li, Y. O., González, V. P. D., & Diosady, L. L. (2023). Microencapsulation of vitamins, minerals, and nutraceuticals for food applications. In R. Sobel (Ed.) *Microencapsulation in the food industry* (pp. 507-528). Academic Press. DOI: <https://doi.org/10.1016/B978-0-12-821683-5.00027-3>.
- Liu, Z., Zhang, Y., Zhang, Q., & Li, J. (2021). Gene-Editing Technologies to Improve Shelf Life and Reduce Food Waste. *Food Research International*, 139, 109944.
- Lusser, M., Parisi, C., Plan, D., & Rodríguez-Cerezo, E. (2011). New plant breeding techniques. *State-of-the-art and prospects for commercial development*. (= JRC Scientific and Technical Reports/EUR 24760 EN).
- Malmud, E., Smith, J., Doe, J., & Brown, R. (2021). Precision Fermentation: A Sustainable Approach for the Future of Food. *Food Technology*, 75(3), 24-31.
- Mantihal, S., Kobun, R., & Lee, B. B. (2021). 3D food printing of as the new way of preparing food: A review. *International Journal of Gastronomy and Food Science*, 22, 100260.
- Mao, Y., Gao, Z., Wang, X., & Chen, F. (2020). CRISPR/Cas9-Mediated Editing of Genes Related to Fat Metabolism in Livestock. *Molecular Breeding*, 40(6), 45.
- Marsh, A., Smith, E., Jones, M., & Taylor, S. (2023). Gut Microbiota Composition and Nutrient Bioavailability. *Current Opinion in Microbiology*, 76, 102362.
- Mehta, N., Ahlawat, S. S., & Sharma, D. P. (2022). Novel trends in development of dietary fiber-rich meat products—a critical review. *Journal of Food Science and Technology*, 59(1), 1-14.

- Merck KGa, A. (2023). Cultured Meat is Set to Revolutionize the Food Industry. Merck Group Reports, accessed online at www.merckgroup.com.
- Miano, A. C., & Rojas, M. L. (2023b). Engineering strategies for food fortification. *Current Opinion in Food Science*, *51*, 101033.
- Miano, T. A., & Rojas, O. J. (2023a). Nanoliposomes for nutrient encapsulation: Enhancing the bioavailability of vitamins and minerals. *Critical Reviews in Food Science and Nutrition*, *63*(3), 444-457.
- Miller, D. D., & Welch, R. M. (2013). Food system strategies for preventing micronutrient malnutrition. *Food policy*, *42*, 115-128.
- Moon, S. B., Kim, D. Y., Ko, J. H., & Kim, Y. S. (2019). Recent advances in the CRISPR genome editing tool set. *Experimental & molecular medicine*, *51*(11), 1-11.
- Mukherjee, S., Ray, S., & Thakur, R. S. (2021). Solid lipid nanoparticles: A modern formulation approach in drug delivery system. *Indian Journal of Pharmaceutical Sciences*, *83*(1), 4-17.
- Müller, M., Kersten, S., Seibert, H., & Blüher, M. (2022). Nutrigenomics for Personalized Nutrition: Applications and Challenges. *Trends in Genetics*, *38*(9), 880-893.
- O'Neill, P., Smith, L., Johnson, D., & Williams, S. (2020). Privacy and Security Challenges in Personalized Nutrition: Ethical Considerations. *Frontiers in Nutrition*, *7*, 577676.
- Patterson, R. E., Sears, D. D., Metcalf, L., & Cadmus-Bertram, L. (2022). Integrating Personalized Nutrition into Clinical Practice: Challenges and Opportunities. *Journal of the Academy of Nutrition and Dietetics*, *122*(9), 1417-1426.
- Post, M. J., Levenberg, S., Kaplan, D. L., Genovese, N., Fu, J., et al. (2020). Scientific, sustainability and regulatory challenges of cultured meat. *Nature Food*, *1*(7), 403-415.
- Potrykus, I. (2010). Regulation must be revolutionized. *Nature*, *466*(7306), 561.
- Pulatsu, E., Su, J., Lin, J., & Lin, M. (2020). Technological Advances in 3D Food Printing for Functional Foods. *Foods*, *9*(9), 1167.
- Qadri, H., Shah, A. H., Almilaibary, A., & Mir, M. A. (2024). Microbiota, natural products, and human health: exploring interactions for therapeutic insights. *Frontiers in cellular and infection microbiology*, *14*, 1371312. <https://doi.org/10.3389/fcimb.2024.1371312>.
- Ramos-Lopez, O., Milagro, F. I., Allayee, H., Chmurzynska, A., Choi, M. S., et al. (2017). Guide for Current Nutrigenetic, Nutrigenomic, and Nutriepigenetic Approaches for Precision Nutrition Involving the Prevention and Management of Chronic Diseases Associated with Obesity. *Journal of nutrigenetics and nutrigenomics*, *10*(1-2), 43-62. <https://doi.org/10.1159/000477729>.
- Richetti, G., Vanhercke, T., Singh, S., & Petrie, J. R. (2020). Biofortification of Crops for Improved Human Nutrition Using Gene Editing. *Nature Sustainability*, *3*, 703-710.
- Ridaura, V. K., Faith, J. J., Rey, F. E., Cheng, J., Duncan, A. E., et al. (2013). Gut microbiota from twins discordant for obesity modulate metabolism in mice. *Science (New York, N.Y.)*, *341*(6150), 1241214. <https://doi.org/10.1126/science.1241214>.
- Rizwan, M., Mujtaba, G., Memon, S. A., Lee, K., & Rashid, N. (2018). Exploring the potential of microalgae for new biotechnology applications and beyond: A review. *Renewable and Sustainable Energy Reviews*, *92*, 394-404.
- Romero-Tapiador, S., Lacruz-Pleguezuelos, B., Tolosana, R., Freixer, G., Daza, R., et al. (2023). AI4FoodDB: a database for personalized e-Health nutrition and lifestyle through wearable devices and artificial intelligence. *Database*, *2023*, baad049.
- Roth, S. M., Keller, H. H., Graham, N., & Boscart, V. M. (2021). Personalized Nutrition: Tailoring Dietary Recommendations to Individuals. *Journal of Clinical Nutrition*, *113*(3), 548-556.
- Sahoo, M., Vishwakarma, S., Panigrahi, C., & Kumar, J. (2021). Nanotechnology: Current applications and future scope in food. *Food Frontiers*, *2*(1), 3-22.
- Sarkar, R., Ghosh, M., Banerjee, R., & Das, S. (2020). CRISPR/Cas9-Based Genome Editing in Crops: Current Status and Future Prospects for Sustainable Food Security. *Trends in Plant Science*, *25*(9), 809-825.
- Schwentek, K., Smetana, S., Aguilar, C., & Fischer, M. (2021). Microbial Production of Bioactive Compounds: Harnessing Precision Fermentation for Improved Nutritional and Functional Food Products. *Trends in Food Science & Technology*, *113*, 49-60.
- Shadab, M. K., Javed M., Ali, S., & Khan, R. H. (2023). Nanoencapsulation of Vitamin C: Protection and Stability during Food Processing. *Food and Bioprocess Technology*, *16*(2), 222-230.
- Sharma, A., Goyal, R., Sharma, S., & Gill, B. S. (2022). Nanoencapsulation of Iron for Improved Bioavailability in Food Applications. *Food and Bioprocess Technology*, *15*(7), 1487-1498.
- Singh, S., Sharma, B. K., Thakur, N., & Kaur, N. (2021). The Role of Nanoemulsions in Food Fortification: Enhancing the Stability of Vitamins and Antioxidants. *Food Function*, *12*(4), 1203-1213.

- Smetana, S., Pasti, G., Fiorentini, R., & Bolten, C. J. (2020). The Potential of Precision Fermentation in the Food Industry: From Production of Functional Ingredients to Alternative Protein Sources. *Food Research International*, 137, 109320.
- Smith, C., Kelly, P., & Alcock, J. (2013). Microbiome and Disease Management. *Nature Reviews Gastroenterology & Hepatology*, 10(12), 691–703.
- Sonnino, R. (2016). The new geography of food security: exploring the potential of urban food strategies. *The Geographical Journal*, 182(2), 190-200.
- Sun, J., Zhou, W., & Huang, D. (2018). Recent Advances in 3D Food Printing Technologies. *Trends in Food Science & Technology*, 79, 47–61.
- Tang, G., Qin, J., Dolnikowski, G. G., Russell, R. M., & Grusak, M. A. (2009). Golden Rice is an effective source of vitamin A. *The American Journal of Clinical Nutrition*, 89(6), 1776-1783.
- Tang, S., Zhang, Z., Chen, W., & Wang, Y. (2017). CRISPR/Cas9-Mediated Modulation of Antioxidant Capacity in Plants. *Scientific Reports*, 7(1), 2541.
- Teng, T. S., Chin, Y. L., Chai, K. F., & Chen, W. N. (2021). Fermentation for future food systems: Precision fermentation can complement the scope and applications of traditional fermentation. *EMBO reports*, 22(5), e52680.
- Tontisirin, K., Nantel, G., & Bhattacharjee, L. (2002). Food-based strategies to meet the challenges of micronutrient malnutrition in the developing world. *Proceedings of the Nutrition Society*, 61(2), 243-250.
- Turnbaugh, P. J., Gordon, J. I., Chong, M.L., Cloran, F., Raffatellu, M., et al. (2021). The Role of the Gut Microbiome in Personalized Nutrition and Health. *Nature Reviews Gastroenterology & Hepatology*, 18(11), 644-654.
- Tziva, M., Kampers, F. W. H., van der Goot, A. J., & Boom, R. M. (2023). Animal-Free Dairy and Meat Production: A Precision Fermentation Approach to Sustainable Food. *Journal of Cleaner Production*, 297, 126618.
- Unnevehr, L., Paarlberg, R. L., & Pray, C. E. (2007). Addressing micronutrient deficiencies: alternative interventions and technologies. *AgBioForum*, 10(3), 124-134.
- Voss, T. S., Klein, M., Erdmann, R., & Hagemann, S. (2015). Genome Editing for Biofortification: Harnessing CRISPR/Cas9 to Improve Nutrient Content in Staple Crops. *Food Research International*, 76, 450–459.
- Wang, Y., Du, Y., Zhao, Y., & Tian, Y. (2020). CRISPR-Cas9 in Pigs: Potential for Genetic Modification to Enhance Resistance to Diseases. *Frontiers in Veterinary Science*, 7, 45.
- Wang, Y., Zhang, D., & Du, G. (2021). Current advances in microbial production of natural products: Metabolic engineering strategies. *Applied Microbiology and Biotechnology*, 105(3), 1-15.
- Wei, X., Chen, Y., & Zhang, Y. (2022). Recent progress in nanocarrier-based drug delivery systems for cancer therapy. *International Journal of Nanomedicine*, 17, 6287-6305.
- Yang, Q., Liang, Q., & Zhang, L. (2020). Advances in CRISPR/Cas-based gene editing in plants. *Journal of Genetics and Genomics*, 47(6), 313-325.
- Yao, X., Wang, J., & Wang, P. (2020). The impact of wearable health devices on personalized nutrition. *Food & Function*, 11(6), 5067-5079.
- Yuan, L., Li, M., & Zhang, S. (2022). Recent advances in plant nanotechnology and its application in agriculture. *Nano Today*, 42, 101356.
- Yuraskina, T. V., Sokolova, E. N., Fursova, N. A., & Serba, E. M. (2024). An innovative approach to food fortification using baker's yeast. *Food systems*, 6(4), 554-560.
- Zhang, H., Zhang, J., Wei, P., Zhang, B., Gou, F., & Feng, Z. (2018). The CRISPR/Cas9 system: Genome editing and beyond. *Acta Biochimica et Biophysica Sinica*, 50(7), 714-72
- Zhao, L., Zhang, F., Ding, X., Wu, G., Lam, Y. Y., et al. (2021). Gut microbiome and personalized nutrition: From the digestive tract to the global health. *Trends in Microbiology*, 29(11), 953-967.
- Zhou, R., Cheng, H., & Tschaplinski, T. J. (2020). Using CRISPR-Cas9 to produce beta-carotene-enhanced rice. *Nature Biotechnology*, 38(5), 617-625.
- Zohar, T., Shoham, B., & Arnon, R. (2021). Blockchain-Based Food Traceability and its Role in Food Safety: A Systematic Review. *Food Control*, 120, 107522.



Journal of Experimental Biology and Agricultural Sciences

<http://www.jebas.org>

ISSN No. 2320 – 8694

In silico Analysis of Natural Iridoids as Primary Amoebic Meningoencephalitis Inhibitors: Molecular Docking, MD Simulation, MMPBSA, and DFT Analyses

Prinsa¹ , Supriyo Saha^{2*} ¹Department of Pharmaceutical Chemistry, Siddhartha Institute of Pharmacy, Near IT-Park, Sahastradhara Road, Dehradun 248001, Uttarakhand, India²Department of Pharmaceutical Chemistry, Uttaranchal Institute of Pharmaceutical Sciences, Uttaranchal University, Dehradun-248001, Uttarakhand, India

Received – August 29, 2024; Revision – December 12, 2024; Accepted – December 21, 2024

Available Online – January 15, 2025

DOI: [http://dx.doi.org/10.18006/2024.12\(6\).800.828](http://dx.doi.org/10.18006/2024.12(6).800.828)

KEYWORDS

Primary Amoebic
Meningoencephalitis (PAM)

Iridoids

Molecular Docking

MD Simulation

MMPBSA

DFT

ABSTRACT

Iridoids have demonstrated various activities, including anti-inflammatory, anticancer, cardioprotective, antiviral, hepatoprotective, antihyperglycemic, and antiparasitic effects. The brain-eating amoeba *Naegleria fowleri* is responsible for primary amoebic meningoencephalitis, a brain inflammation. In this study, 52 iridoids were selected through an extensive literature survey, and 22 of these iridoids passed the drug-likeness filter. The selected iridoids were molecularly docked against the *N. fowleri* CYP51 receptor, using voriconazole as a standard for comparison. The docking score for voriconazole was -7.6 kcal/mol, while the scores for 10-isovaleroyl-dihydropenstemide and Patrinalloside A were -8.9 and -8.6 kcal/mol, respectively. According to molecular dynamics (MD) simulation data, the interacting amino acid residues exhibited fluctuations within a specific range, with the Root Mean Square Deviation (RMSD) values stabilizing throughout the experiment. When interacting with the receptor linked to amoebic meningoencephalitis, 10-isovaleroyl-dihydropenstemide and Patrinalloside A showed free binding energies of -71.922 kJ/mol and -61.243 kJ/mol, respectively, based on Molecular Mechanics Poisson-Boltzmann Surface Area (MMPBSA) calculations. Furthermore, Fragment Molecular Orbital (FMO) and Molecular Electrostatic Potential (MEP) analyses of 10-isovaleroyl-dihydropenstemide and Patrinalloside A revealed potential nucleophilic-electrophilic attack zones, indicating they are chemically reactive. The analysis of both compounds' ADMET (Absorption, Distribution, Metabolism, Excretion, and Toxicity) indicated non-toxic behaviour. These findings suggest that natural iridoids have significant potential in combating primary amoebic meningoencephalitis.

* Corresponding author

E-mail: supriyo9@gmail.com (Supriyo Saha)

Peer review under responsibility of Journal of Experimental Biology and Agricultural Sciences.

 Production and Hosting by Horizon Publisher India [HPI]
 (<http://www.horizonpublisherindia.in/>).
 All rights reserved.

 All the articles published by [Journal of Experimental Biology and Agricultural Sciences](#) are licensed under a [Creative Commons Attribution-NonCommercial 4.0 International License](#) Based on a work at www.jebas.org.


1 Introduction

Thermophilic amoeba is responsible for amoebic encephalitis, a central nervous system infection. This condition has two forms: granulomatous amoebic encephalitis and primary amoebic meningoencephalitis (PAM) (Güémez and García 2021). The amoeba species primarily responsible for spreading the infection include *Naegleria*, *Acanthamoeba*, *Sappinia*, and *Balamuthia*. These microorganisms thrive in tropical regions and are commonly found in freshwater bodies such as lakes and ponds (Rojó et al. 2023). Among these, *N. fowleri*, a species of *Naegleria*, directly infects the central nervous system and damages brain cells associated with PAM. The flagellate form of *N. fowleri* has also been detected in human cerebrospinal fluid (Cooper et al. 2019). Transmission to the central nervous system results in brain edema, inflammation, and loss of brain tissue. Trophozoites of *N. fowleri* penetrate the olfactory mucosa to reach the olfactory bulb, leading to inflammation and parenchymal damage as they cross the cribriform plate. This deadly infection earns *N. fowleri* the nickname "brain-eating amoeba." Although rare, this infection is lethal, and the chances of survival depend on early detection and treatment (Calis et al. 2020). Despite current antimicrobial therapies, the mortality rate remains approximately 90%. Recently reported cases of brain-eating amoeba in India and other countries have underscored the need to re-emphasize the significance of primary amoebic meningoencephalitis and explore possible cures and treatments (Wang et al. 2020).

Iridoid compounds, classified as cyclopentane pyran monoterpenes, possess several medicinal properties. Depending on their chemical structure, iridoids can be categorized into four groups: iridoid glycosides, secoiridoid glycosides, non-glycosidic iridoids, and bis-iridoids (Grover et al. 2023). These compounds have been employed in traditional medicine for liver protection (Zhang et al. 2024), inflammation reduction (He et al. 2023), and promoting wound healing (Geng et al. 2024). Researchers have discovered that iridoids are crucial in inhibiting and controlling the growth of a wide range of pathogenic microorganisms (Shi et al. 2023; Schou et al. 2024). Several iridoids, including 10-Isovaleroyl-dihydropensternide, brasoside, Patrinalloside A, Polystachyn A, and Asperuloside, are widely cultivated for their various health benefits, such as anti-inflammatory, neuroprotective, hepatoprotective, anti-tumorigenic, antiviral, anti-malarial, and anti-protozoal effects. This pharmacological potential suggests that these iridoids could effectively manage protozoal infections such as PAM (Zhang et al. 2023). This research focuses on repurposing natural iridoids to manage primary amoebic meningoencephalitis through molecular docking, molecular dynamic simulations, and density functional theory analysis. The goal is to identify the most promising iridoid to combat this lethal brain infection.

2 Materials and Methods

2.1 Collection of Data and Assessment Drug Likeness Parameter

A total of 52 iridoids were identified through an extensive literature search, and their drug-likeness parameters were evaluated according to the Lipinski Rule of Five. According to this rule, the partition coefficient should not exceed five, the number of hydrogen bond donors should be no more than five, and the number of hydrogen bond acceptors should not exceed ten (Daina et al., 2017). The drug-likeness parameter was used as a primary filter in the drug development process (Table 1). Out of the 52 iridoids, 30 did not pass this primary filter (Chen et al., 2020). As a result, 22 iridoids were selected for further studies, including molecular docking, molecular dynamics simulation, and quantum mechanics-based electronic nature analysis, targeting the CYP51 receptor of *N. fowleri*.

2.2 Molecular Docking Study using AutoDock Vina

2.2.1 Preparation of protein

This research examined the CYP51 receptor of *Naegleria fowleri* complexed with itraconazole (PDB ID: 6AYC). The structural characteristics of the receptor were analyzed using a Ramachandran plot. Additionally, the presence of non-bonded interactions among various atom types within the receptor was assessed based on the ERRAT score. The three-dimensional structural classification of the protein, which includes alpha helices, beta sheets, and loops, was also determined using VERIFY 3D.

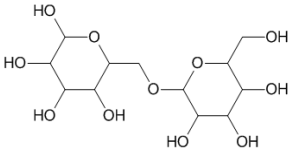
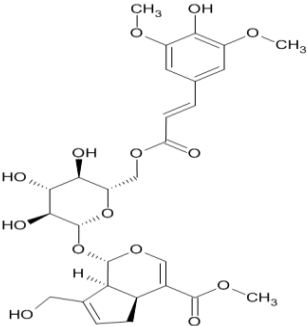
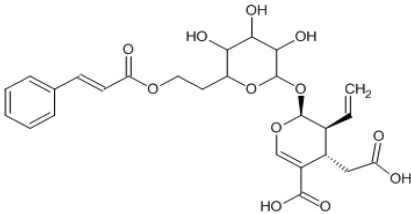
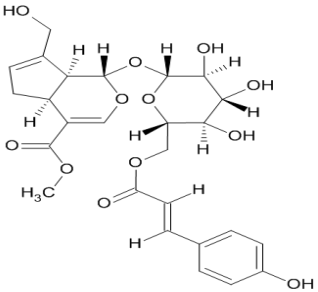
2.2.2 Preparation of iridoids structures for molecular docking

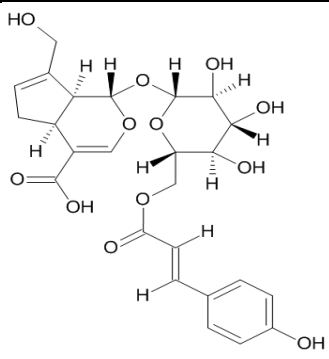
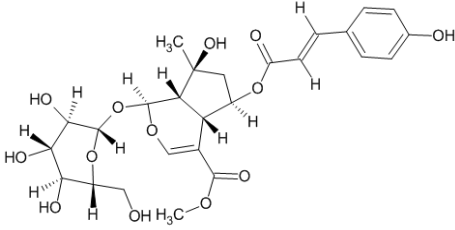
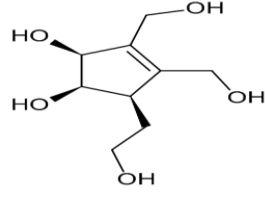
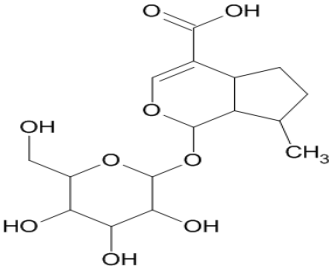
Avogadro software was utilized to draw structures and perform force field-based energy minimization on selected iridoids and the standard compound voriconazole (Hanwell et al. 2012). All structures were saved in PDB format, and using AutoDock Tools 1.5.6, they were converted into docking-compatible PDBQT format. The Drug Discovery Studio Visualizer was employed to examine protein-ligand interactions. The grid box dimensions for the *N. fowleri* CYP51 protein were 14.088, -4.933, and 13.271 along the x, y, and z axes. The root mean square deviation (RMSD) value between the redocked and unprocessed crystallographic conformations was less than 1.25 Å. This information supports the validity and reliability of the docking process (Goodsell et al. 2021).

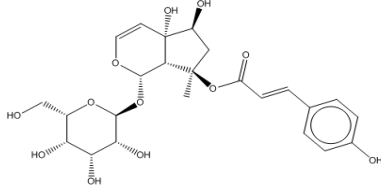
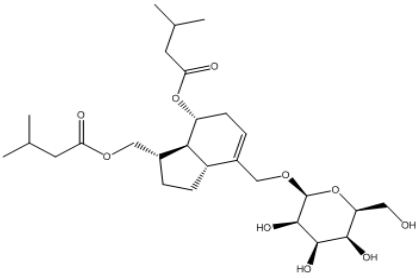
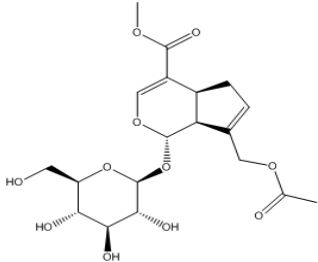
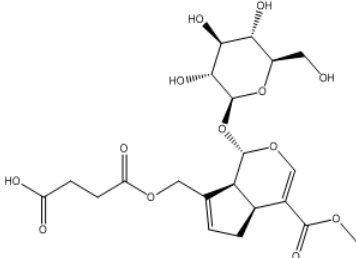
2.3 Molecular Dynamic (MD) Simulation of the selected iridoids

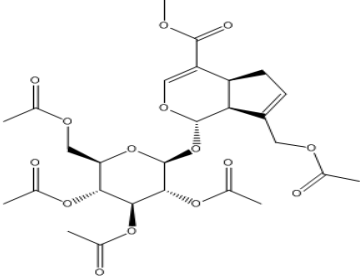
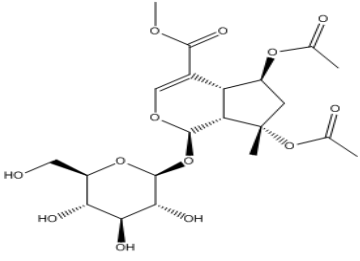
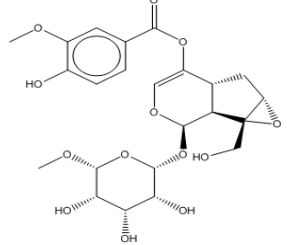
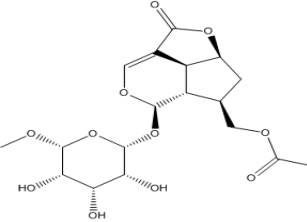
To visualize the atomic-level interaction patterns of a ligand molecule within a receptor in the presence of solvent, ions, temperature, and pressure, molecular dynamics (MD) simulations

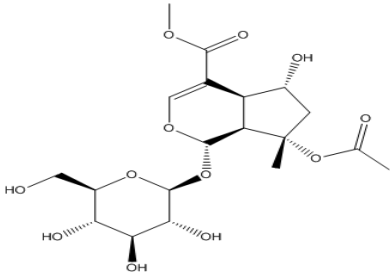
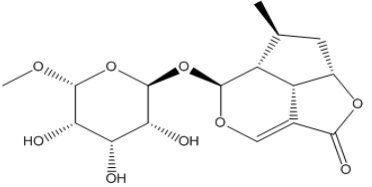
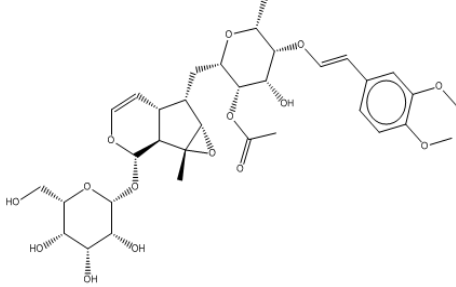
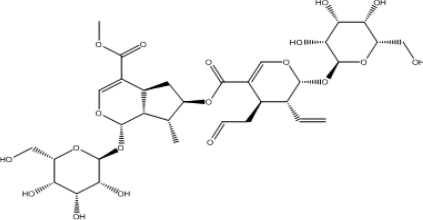
Table 1 List of iridoids with chemical structure, biological source, bioactivities and drug likeness parameter

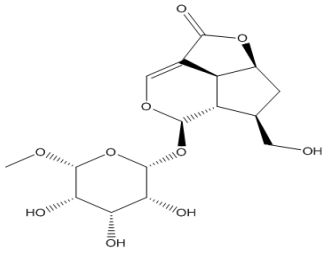
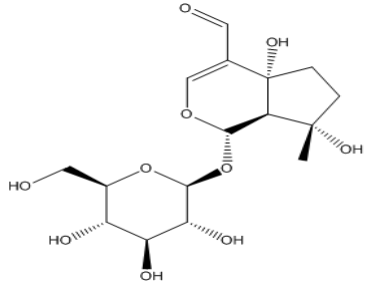
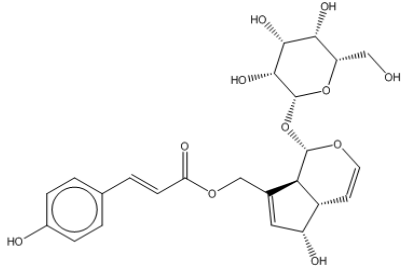
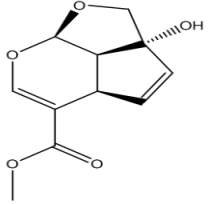
S.N.	Name of the Molecules	Structure	Biological Source	Activities	Lipinski rule
1	6-O-Alpha-D-galactopyranosylharpagoside		<i>Harpagophytum procumbens</i>	Anti-inflammatory	Rejected
2	6'-O-Sinapoyl-geniposide		<i>Gardenia jasminoides</i>	Anti-inflammatory, Antioxidant, Anti diabetic, Hepatoprotective, Neuroprotective	Rejected
3	6-O-Trans-cinnamoyl-secologanoside		<i>Ligustrum lucidum</i>	Osteogenic activity	Rejected
4	6'-O-Trans-para-coumaroylgeniposide		<i>Rubiaceae</i>	Anticancer, Antioxidant, sedative, Antiviral	Rejected

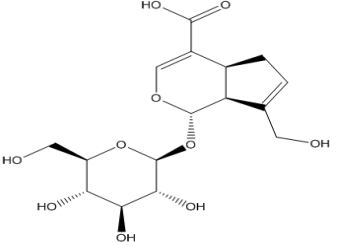
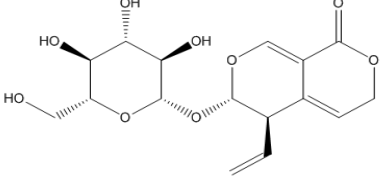
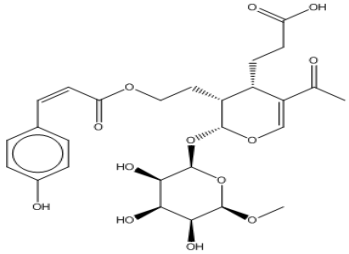
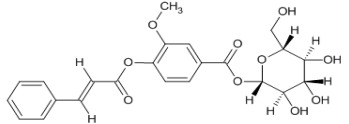
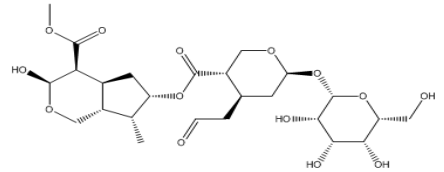
S.N.	Name of the Molecules	Structure	Biological Source	Activities	Lipinski rule
5	6'-O-Trans-para-coumaroylgeniposidic Acid		<i>Rubiaceae</i>	Anticancer, Antioxidant, sedative, Antiviral	Rejected
6	6-O-Trans-p-coumaroyl-8-O-acetylshanzhiside methyl ester		<i>Acanthaceae</i>	Antiviral, Anticancer	Rejected
7	7-Hydroxy eucommiol		<i>Bignoniaceae</i>	Antioxidant, Anti-inflammatory	Accepted
8	8-Epideoxyloganic acid		<i>Bigononiaceae</i>	Analgesia, homeostasis and anti-inflammatory	Accepted

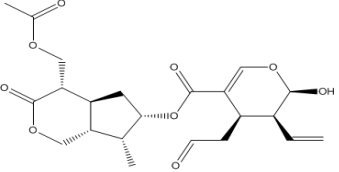
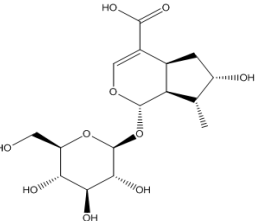
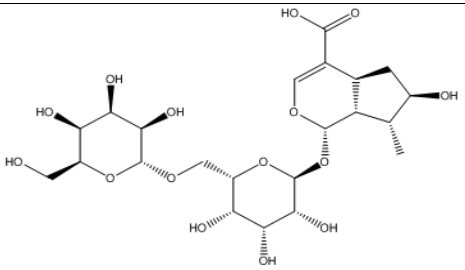
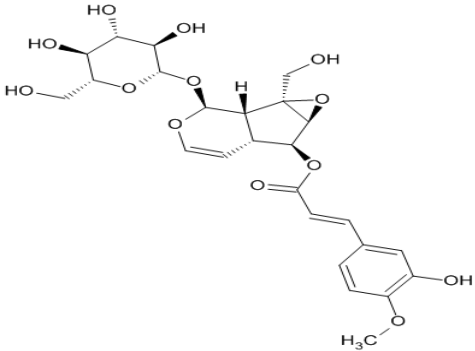
S.N.	Name of the Molecules	Structure	Biological Source	Activities	Lipinski rule
9	8-P-coumaroylharpagide		<i>Scrophulariaceae</i>	Anti-inflammatory, Antioxidant, anticancer, Antiviral	Rejected
10	10-Isovaleroyl-dihydropenstemiide		<i>Loganiaceae</i>	Anti-inflammatory, Hepatoprotective, neuroprotective, Anticancer, Anti diabetic	Accepted
11	10-O-Acetylgeniposide		<i>Rubiaceae</i>	Anti-inflammatory, Hepatoprotective, neuroprotective, Anti-inflammatory, Anti diabetic	Accepted
12	10-O-Succinoylgeniposide		<i>Rubiaceae</i>	Cardiovascular, Anti-inflammatory, Hepatoprotective, Anti diabetic	Accepted

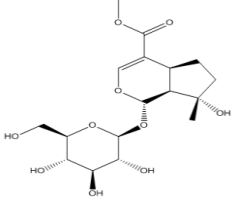
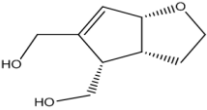
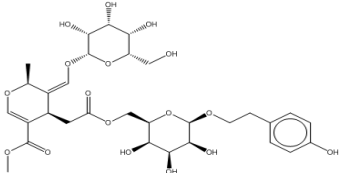
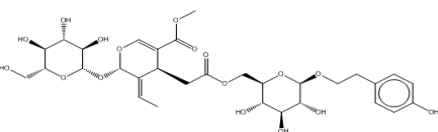
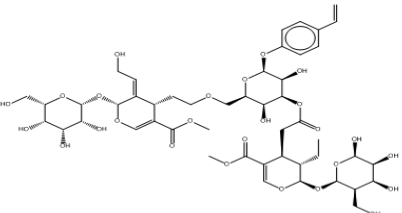
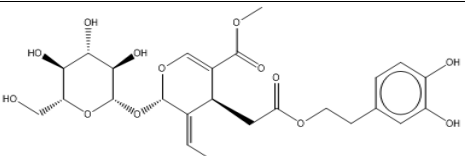
S.N.	Name of the Molecules	Structure	Biological Source	Activities	Lipinski rule
13	Acetylgeniposide		<i>Gardenia jasminoids</i>	Antii-inflammatory, Anti rheumatoid, Anti-tumor	Rejected
14	Acetylbarlerin		<i>Barlerialipulin</i> <i>Barleriapronitis</i>	Antimicrobial, Anti-inflammatory, neuroprotective, Anti-inflammatory, Anti diabetic, Anti -cancer	Accepted
15	Amphicoside		<i>Scrophulariaceae</i>	Antioxidant, anticancer	Rejected
16	Asperuloside		<i>Rubiaceae, Plantaginaceae</i>	Anti- melanogenesis activity	Accepted

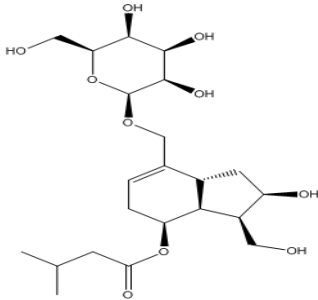
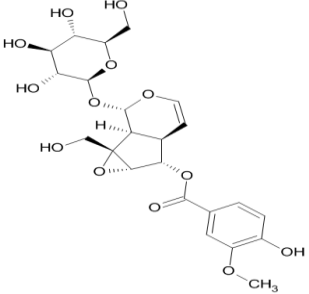
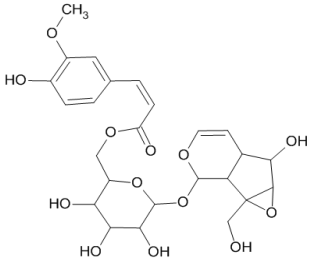
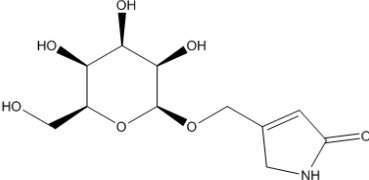
S.N.	Name of the Molecules	Structure	Biological Source	Activities	Lipinski rule
17	Barlerin		<i>Acanthaceae</i>	Antioxidant, antibacterial, anti-fungal, antidiabetic, anticancer, antiulcer	Accepted
18	Brasoside		<i>Verbenaceae</i>	Antioxidant, anti-inflammatory	Accepted
19	Buddlejoside A9		<i>Loganiaceae</i>	Antioxidant, anti-inflammatory, anticancer	Rejected
20	Cantleyoside		<i>Caprifoliaceae</i>	Hypoglycemic, hypolipidemic, hepatoprotective, anti-inflammatory	Rejected

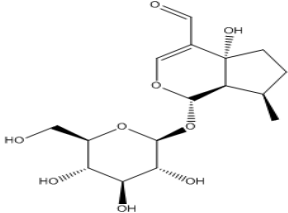
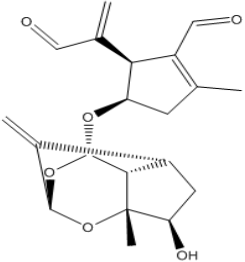
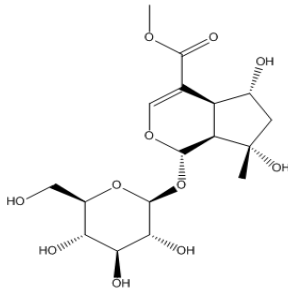
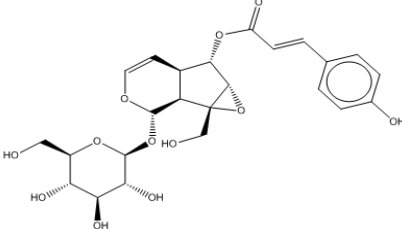
S.N.	Name of the Molecules	Structure	Biological Source	Activities	Lipinski rule
21	Deacetyl asperuloside		<i>Rubioidae</i>	Anti-melanogenesis activity	Accepted
22	Euphroside		<i>Scrophulariaceae</i>	Neuroprotective, antitumor, hepatoprotective	Accepted
23	Eurostoside		<i>Scrophulariaceae</i>	Antioxidant, anti-inflammatory, anticancer	Rejected
24	Garjasmine		<i>Rubiaceae</i>	anticancer	Accepted

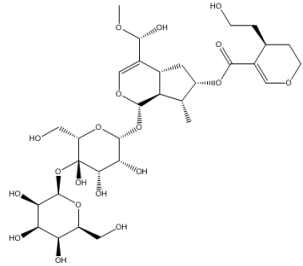
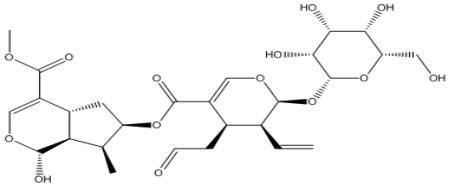
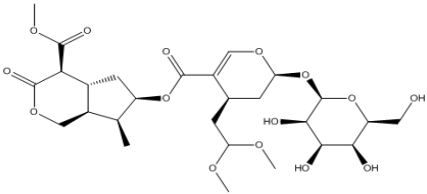
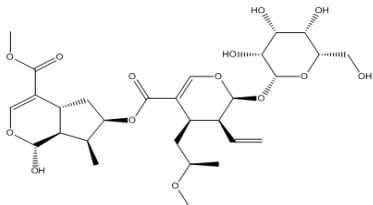
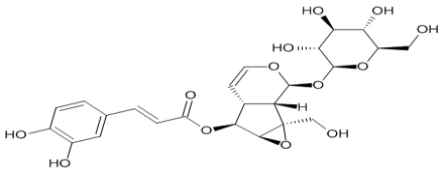
S.N.	Name of the Molecules	Structure	Biological Source	Activities	Lipinski rule
25	Geniposidic Acid		<i>Rubiaceae, Eucommiaceae</i>	Cardiovascular activity	Accepted
26	Gentiopicroside		<i>Gentianaceae</i>	Digestive activity, Antioxidant hepatoprotective, anti -Inflammatory	Accepted
27	Isojaslanceoside B		<i>Oleaceae</i>	Antioxidant hepatoprotective, anti -Inflammatory	Rejected
28	Kutkin		<i>Picrorhizakurroa</i>	Antioxidant hepatoprotective, anti -Inflammatory	Rejected
29	Laciniatoside I		<i>Dipsacaceae</i>	Antioxidant neuroprotective, anti-inflammatory	Rejected

S.N.	Name of the Molecules	Structure	Biological Source	Activities	Lipinski rule
30	Laciniatoside II		<i>Dipsacaceae</i>	Antioxidant neuroprotective, anti inflammatory	Rejected
31	Loganic acid		<i>Acanthaceae</i>	Anti-inflammatory, strong free radical scavenging activity	Accepted
32	Loganic acid 6'-O-beta-D-glucoside		<i>Acanthaceae</i>	Anti-inflammatory, strong free radical scavenging activity	Rejected
33	Minecoside		<i>Veronica laudiana.</i>	Antioxidant, anti-inflammatory, anticancer	Rejected

S.N.	Name of the Molecules	Structure	Biological Source	Activities	Lipinski rule
34	Mussaenoside		<i>Scrophulariaceae</i>	Anti inflammatory	Accepted
35	Ningpogenin		<i>Scrophulariaceae</i>	Antioxidant Neuroprotective, anti-inflammatory	Accepted
36	Nuezhenelenoliciside		<i>Oleaceae</i>	Anti- osteoporosis activity	Rejected
37	Nuezhenide		<i>Oleaceae</i>	Antibacterial, antioxidant, antitumor	Rejected
38	Oleoside dimethyl ester		<i>Oleaceae</i>	Sedative, antioxidant	Accepted
39	Oleuropein		<i>Oleaceae</i>	Sedative, Anticonvulsant, antidiabetic, diuretic, antimicrobial, analgesic, antiviral	Rejected

S.N.	Name of the Molecules	Structure	Biological Source	Activities	Lipinski rule
40	Patrinalloside A		<i>Valerianaceae</i>	Antioxidant hepatoprotective, anti-inflammatory	Accepted
41	Picoside-II		<i>Picrorhizakurroa</i>	Antioxidant hepatoprotective, anti-inflammatory	Rejected
42	Picoside-III		<i>Picrorhizakurroa</i>	Antioxidant hepatoprotective, anti-inflammatory	Rejected
43	Pinnatoside		<i>Verbenaceae</i>	Antimicrobial, hepatoprotective, antioxidant	Accepted

S.N.	Name of the Molecules	Structure	Biological Source	Activities	Lipinski rule
44	Plantarenaloside		<i>Plantaginacea, Bigoniaceae</i>	Antioxidant, anti-inflammatory	Accepted
45	Polystachyn A		<i>Valerianaceae</i>	Antioxidant, anti-proliferative	Accepted
46	Shanzhiside methyl ester		<i>Lamiaceae</i>	Antimicrobial	Rejected
47	Specioside		<i>Bignoniaceae</i>	Analgesic, liver stimulating	Rejected

S.N.	Name of the Molecules	Structure	Biological Source	Activities	Lipinski rule
48	Sylvestroside I		<i>Dipsacaceae</i>	Antioxidant neuroprotective, anti-inflammatory	Rejected
49	Sylvestroside III		<i>Dipsacaceae</i>	Antioxidant neuroprotective, anti-inflammatory	Rejected
50	Sylvestroside III dimethyl acetal		<i>Dipsacaceae</i>	Antioxidant neuroprotective, anti-inflammatory	Rejected
51	Sylvestroside IV		<i>Dipsacaceae</i>	Antioxidant neuroprotective, anti-inflammatory	Rejected
52	Verminoside		<i>Veronica kellereri</i>	Anti-inflammatory, anti-bacterial, anti-diabetic	Rejected

were conducted in a CHARMM force field environment (Kim et al. 2017). The simulations were performed using GROMACS 20.1 software, employing TIP3 water. An energy minimization process was completed with 500,000 steps. The best-docked iridoids, 10-isovaleroyl-dihydropenstemide and Patrinalloside A were subjected to a 100 ns MD simulation. During the preparation of the protein for the simulation study involving 10-isovaleroyl-dihydropenstemide and Patrinalloside A, 18641 and 18646 water molecules, along with 4 chloride ions, were added to the system. The graphical representation of the simulation trajectories was created using Microsoft Excel (Lemkul 2018).

2.4 MMPBSA Analysis

To determine the actual binding energy of ligand-receptor interactions, we applied MMPBSA analysis (Kumari and Kumar 2014). We focused on the best-docked iridoids, specifically 10-isovaleroyl-dihydropenstemide and Patrinalloside A, utilizing the MD simulation coordinates for the MMPBSA analysis (Baker et al. 2001).

2.5 Density Functional Theory Analyses

2.5.1 Frontier Molecular Orbital (FMO) Analysis

To evaluate the electrical characteristics of specific iridoids, the Lee, Yang, and Parr's (LYP) correlation functional was used in conjunction with the B3LYP/6-31G (d,p) basis set, along with Beck's (B) three-parameter hybrid model (Sakr et al. 2022). FMO (Fragment Molecular Orbital) analysis was conducted to examine the highest occupied molecular orbital (HOMO) and the lowest unoccupied molecular orbital (LUMO). The energies of these orbitals and the energy gap between them are related to the softness, electronegativity, hardness, and electrophilicity properties of the chemical structures (Perri and Weber 2014). The GAMESS software was utilized for the FMO analysis, while WxMacMolPlt (version 7.7.3) was employed to visualize the results. The best-docked iridoids, 10-isovaleroyl-dihydropenstemide and Patrinalloside A were chosen for frontier orbital analysis (Barca et al. 2020).

$$\text{Chemical Hardness: } n = \frac{(I-A)}{2}; \quad \text{Electronegativity: } \mu = -\frac{(I+A)}{2};$$

$$\text{Electrophilicity index: } \psi = \frac{\mu^2}{2n}; \quad \text{Softness: } S = \frac{1}{2n}$$

where A and I are electron affinity and ionization potential. $A = -E_{\text{LUMO}}$ and $I = -E_{\text{HOMO}}$.

2.5.2 Molecular Electrostatic Potential (MEP) Analysis

The MEP (Molecular Electrostatic Potential) map focuses on the distribution of positive and negative charges within a structure. This potential map displays different colour regions: blue, green, yellow, orange, and red. The red region indicates the most negative

area, where electrophiles can readily attack, while the blue region represents the most positive area for nucleophilic attacks. The green region signifies non-interacting zones, indicating areas with no potential interactions. In this analysis, the best-docked iridoids, 10-isovaleroyl-dihydropenstemide and Patrinalloside A were selected for frontier orbital analysis. The GAMESS software (version R2, released on June 30, 2024) was used alongside the B3LYP/6-31G(d,p) basis set to perform the MEP analysis (Hanson et al. 2013).

2.6 ADMET Analysis

The ADME (Absorption, Distribution, Metabolism, and Excretion) and toxicity properties of the best-docked iridoids, 10-isovaleroyl-dihydropenstemide and Patrinalloside A, were calculated using the Swiss ADME portal and OSIRIS software, respectively.

3 Results and Discussion

3.1 Molecular Docking Study Data

Inside the receptor, the ligand itraconazole was complexed with several amino acids, including PHE 25, ALA 29, PHE 28, VAL 94, TYR 95, and others represented as PRO 188 through THR 272. The Ramachandran plot of the receptor showed that 93.4% of residues were in the most favoured regions, 5.8% in the additional allowed regions, 0.3% in the generously allowed regions, and 0.5% in the disallowed regions (Riyaphan et al. 2021) (Figure 1). The overall quality value of the receptor, as per ERRAT, was 94.749, indicating good resolution (Park et al. 2023). According to the Verify3D server, 83.07% of the residues had an average 3D-ID score greater than 0.1, confirming that the amino acids present in the receptor constitute a high-quality protein for modelling (Kalman and Ben-Tal 2010).

Molecular docking interaction data showed that the docking scores of selected iridoids fluctuated between -5.5 and -8.9 kcal/mol (Ahmed et al. 2023). Voriconazole was used as a standard in this analysis, with a docking score of -7.6 kcal/mol (Table 2) (Lokhande et al. 2022). Among the tested iridoids, 10-isovaleroyl-dihydropenstemide and Patrinalloside A exhibited the highest docking scores of -8.9 kcal/mol and -8.6 kcal/mol, respectively (Paggi et al. 2024). Specifically, 10-isovaleroyl-dihydropenstemide interacted with the *N. fowleri* CYP51 receptor through hydrophobic interactions with residues TYR 82, PHE 89, and VAL 94, and via hydrogen bond interactions with ARG 338, HIS 403, and CYS 405. Patrinalloside A interacted with the receptor using hydrophobic interactions with PHE 25, PHE 28, PRO 188, LEU 189, TYR 82, ILE 334, and PHE 191, as well as a hydrogen bond interaction with MET 335 (Kumar et al. 2023). Voriconazole interacted with the receptor through hydrogen bonds with TYR 82, TYR 95, and ARG338 (Figure 2) (Kar et al. 2024).

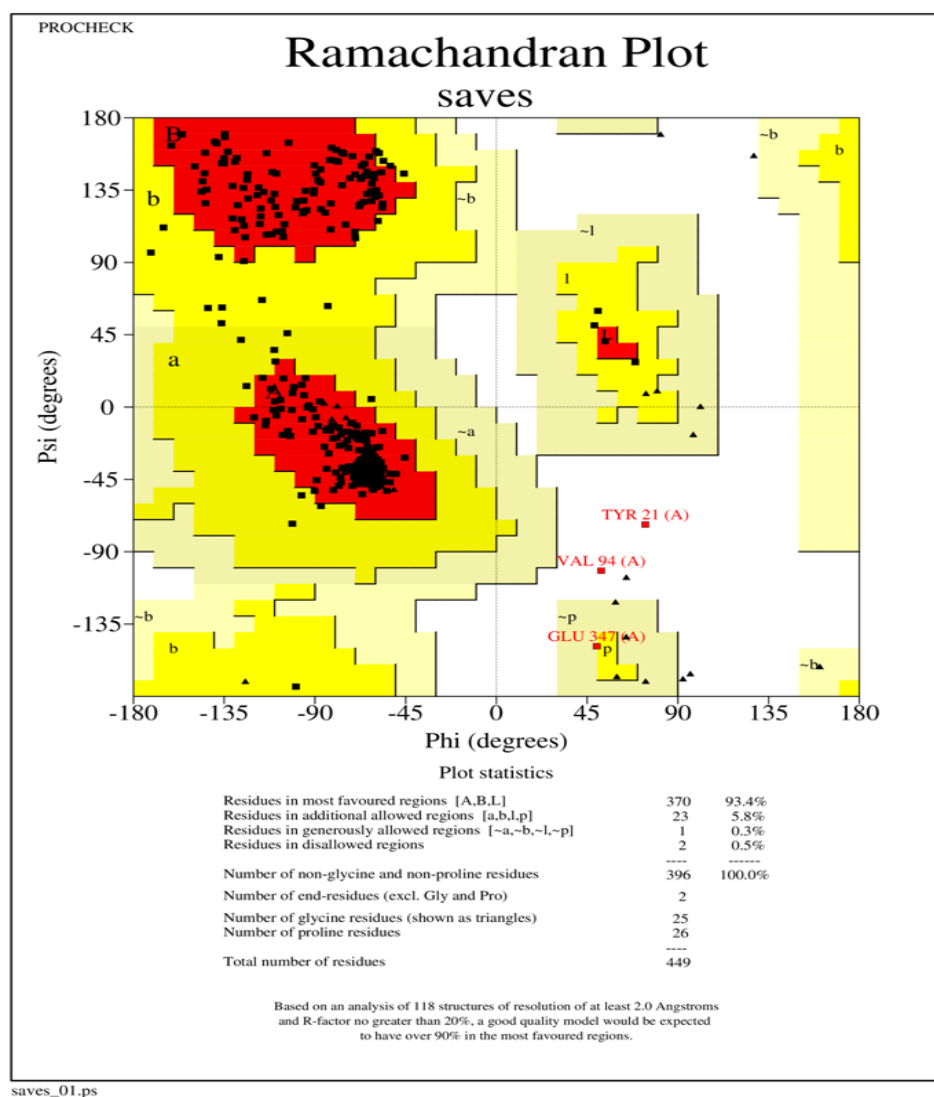


Figure 1 Ramachandran plot of 6AYC receptor

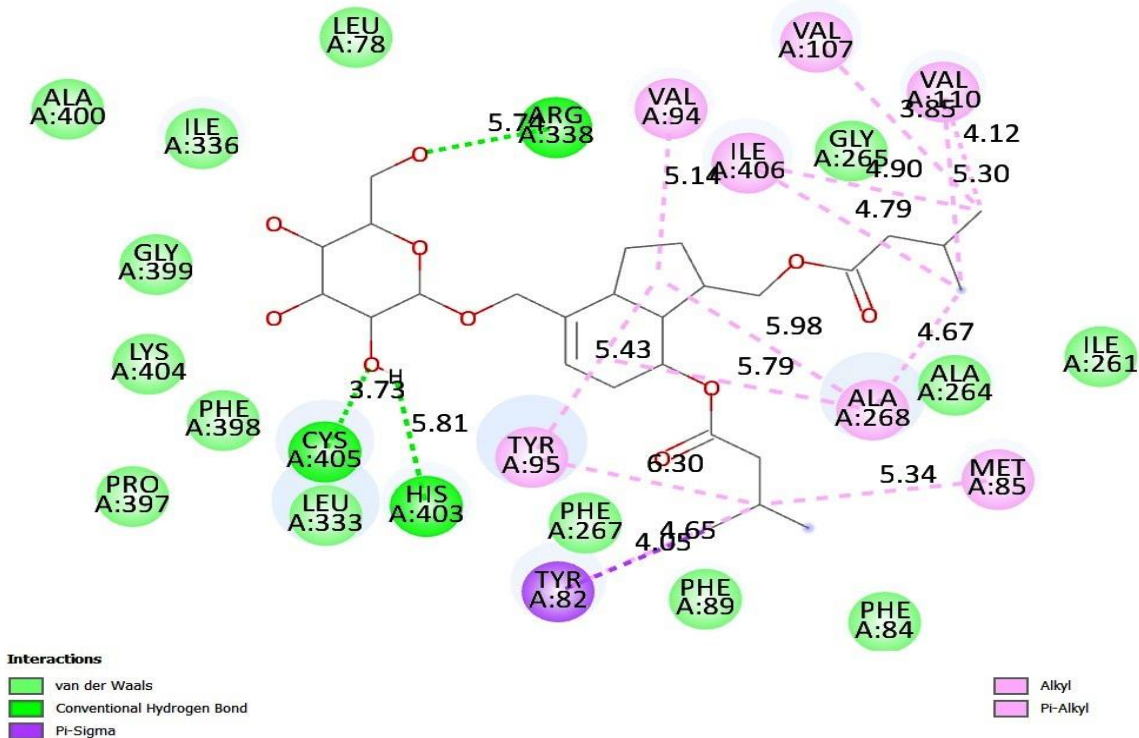
Table 2 Molecular docking interactions between iridoids and *N. fowleri* CYP51 receptor

S. N.	Name	Dock score (kcal/mol)	Hydrophobic Interactions	Hydrogen bond Interactions
1.	7-Hydroxy eucommiol	-5.5	LEU 442 (distance between interaction carbon atoms 3.57 Å).	TYR 439 (distance H-A 2.28 Å, D-A 2.83 Å), LEU442 (distance H-A 2.12 Å, D-A 3.00 Å).
2.	8-Epideoxyloganic acid	-7.8	TYR 82 (distance between interaction carbon atoms 3.43 Å), TYR 95 (distance between interaction carbon atoms 3.73 Å), LEU 442 (distance between interaction carbon atoms 3.71 Å).	TYR 82 (distance H-A 2.49 Å, D-A 2.93 Å), TYR95 (distance H-A 2.40 Å, D-A 3.08 Å), ILE 334 (distance H-A 2.87, D-A 3.33 Å), MET 335 (distance H-A 2.37 Å, D-A 3.26 Å).
3.	10-Isovaleroyl-dihydropentemide	-8.9	TYR 82 (distance between interaction carbon atoms 3.72 Å), PHE 89 (distance between interaction carbon atoms 3.90 Å), VAL 94 (distance between interaction carbon atoms 3.69 Å), VAL107 (distance between interaction carbon atoms 3.80 Å), VAL110 (distance between interaction carbon atoms 3.65 Å).	ARG 338 (distance H-A 2.44 Å, D-A 3.13 Å), HIS 403 (distance H-A 3.17 Å, D-A 3.57 Å), CYS 405 3.73 Å.

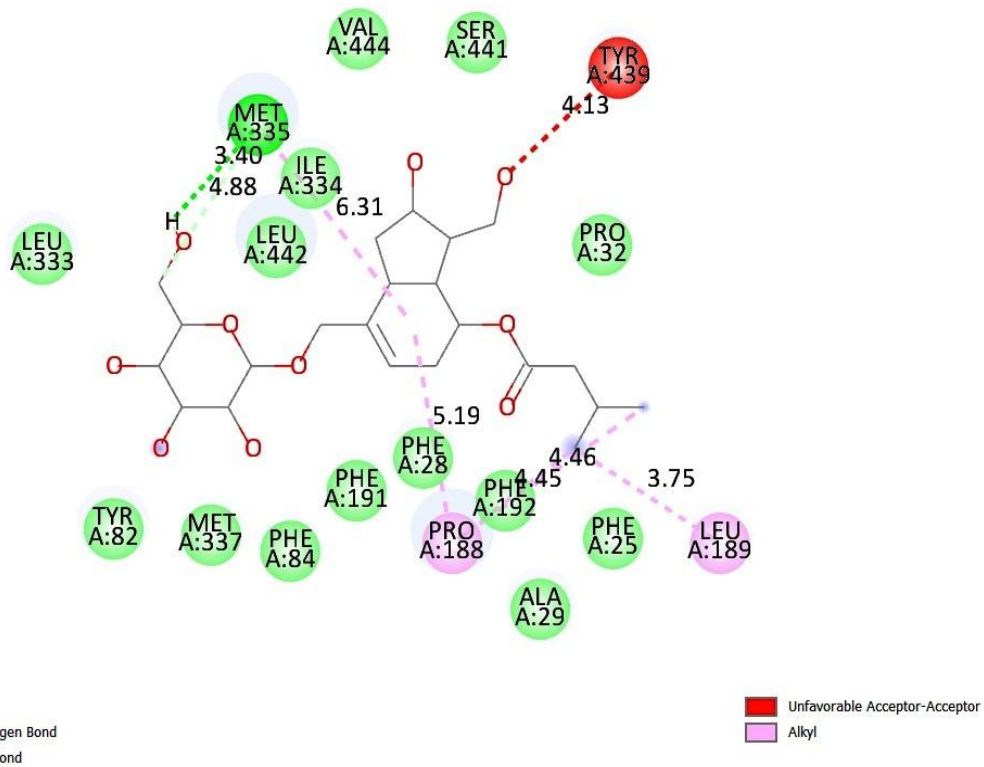
S. N.	Name	Dock score (kcal/mol)	Hydrophobic Interactions	Hydrogen bond Interactions
4.	10-O-Acetylgeniposide	-8.2	TYR 82 (distance between interaction carbon atoms 3.50Å), PHE 89 (distance between interaction carbon atoms 3.79Å), TYR 95 (distance between interaction carbon atoms 3.42Å).	TYR 82 (distance H-A 2.51Å, D-A 2.96 Å), HIS 403 (distance H-A 2.30Å, D-A 3.07 Å).
5.	10-O-Succinoylgeniposide	-8.3	PHE 89 (distance between interaction carbon atoms 3.82Å), VAL94 (distance between interaction carbon atoms 3.70Å), ALA 264 (distance between interaction carbon atoms 3.70Å), ALA268 (distance between interaction carbon atoms 3.96Å), LEU 333 (distance between interaction carbon atoms 3.63Å).	TYR 82 (distance H-A 2.37 Å, D-A 2.85 Å), HIS 403 (distance H-A 2.82Å, D-A 3.24Å), CYS 405 (distance H-A 2.72 Å, D-A 3.07 Å).
6.	Acetylbarlerin	-7.7	LYS 30 (distance between interaction carbon atoms 3.58Å).	ALA 29 (distance H-A 2.72 Å, D-A 3.13 Å).
7.	Asperuloside	-8.0	VAL 94 (distance between interaction carbon atoms 3.61Å), VAL 107 (distance between interaction carbon atoms 3.52Å), ALA 268 (distance between interaction carbon atoms 3.36Å).	TYR 82 (distance H-A 2.85 Å, D-A 3.17 Å), PHE 398 (distance H-A 2.57 Å, D-A 3.05 Å), ILE 406 (distance H-A 2.10 Å, D-A 3.10 Å).
8.	Barlerin	-7.9	ALA 150 (distance between interaction carbon atoms 3.77Å).	ASP 184 (distance H-A 3.31 Å, D-A 3.75 Å), ILE 186 (distance H-A 3.03 Å, D-A 3.62 Å), SER441 (distance H-A 3.53 Å, D-A 3.98 Å), LEU 442 (distance H-A 2.86 Å, D-A 3.65 Å).
9.	Brasoside	-8.2	TYR 82 (distance between interaction carbon atoms 3.65Å), LEU 333 (distance between interaction carbon atoms 3.56 Å).	PHE 398 (distance H-A 2.27 Å, D-A 3.04 Å), HIS 403 (distance H-A 2.32 Å, D-A 2.79 Å), CYS 405 (distance H-A 2.92 Å, D-A 3.29 Å).
10	Deacetyl asperuloside	-7.6	VAL 94 (distance between interaction carbon atoms 3.39Å), VAL 107 (distance between interaction carbon atoms 3.58 Å), ALA 268 (distance between interaction carbon atoms 3.34Å).	TYR 82 (distance H-A 2.96 Å, D-A 3.26 Å), PHE 398 (distance H-A 2.46 Å, D-A 3.13 Å).
11.	Euphoside	-7.2	ILE 275 (distance between interaction carbon atoms 3.81Å).	ASP 184 (distance H-A 3.08 Å, D-A 3.75 Å), ILE 186 (distance H-A 2.47 Å, D-A 3.00 Å), HIS 271 (distance H-A 2.36 Å, D-A 2.84 Å), SER 441 (distance H-A 2.05 Å, D-A 2.93 Å), LEU 442 (distance H-A 3.14 Å, D-A 4.09 Å), VAL 443 (distance H-A 2.34 Å, D-A 2.83Å) GLY 445 (distance H-A 2.61 Å, D-A 3.02 Å).
12.	Garjasmine	-6.5	PHE 28 (distance between interaction carbon atoms 3.83Å), PRO 32 (distance between interaction carbon atoms 3.91Å), PRO 188 (distance between interaction carbon atoms 3.5Å).	None
13.	Geniposidic Acid	-7.4	ALA 146 (distance between interaction carbon atoms 3.24Å), ILE 275 (distance between interaction carbon atoms 3.21Å).	ALA 146 (distance H-A 2.02 Å, D-A 2.70 Å), ALA 150 (distance H-A 3.31 Å, D-A 3.74 Å), ASP 183 (distance H-A 2.23 Å, D-A 2.96 Å), ASP 184 (distance H-A 2.02 Å, D-A 2.95 Å), SER 278 (distance H-A 2.24Å, D-A 3.02 Å), SER 441 (distance H-A 2.54 Å, D-A 3.43 Å), VAL 443 (distance H-A 3.06 Å, D-A 3.70 Å), GLY (distance H-A 2.13 Å, D-A 2.93 Å).

S. N.	Name	Dock score (kcal/mol)	Hydrophobic Interactions	Hydrogen bond Interactions
14.	Gentiopicroside	-7.5	TYR 82 (distance between interaction carbon atoms 3.57Å), TYR 95 (distance between interaction carbon atoms 3.91Å), LEU 333 (distance between interaction carbon atoms 3.51Å).	ARG 338 (distance H-A 2.70 Å, D-A 3.31 Å), HIS 403 (distance H-A 2.30 Å, D-A 3.14 Å).
15.	Loganic acid	-7.6	TYR 82 (distance between interaction carbon atoms 4.00Å), LEU 333 (distance between interaction carbon atoms 3.26Å), ILE 336 (distance between interaction carbon atoms 3.81Å).	TYR 82 (distance H-A 2.35 Å, D-A 2.70 Å), CYS 405 (distance H-A 2.79 Å, D-A 3.16 Å).
16.	Mussaenoside	-7.6	TYR 82 (distance between interaction carbon atoms 3.65Å), PHE 89 (distance between interaction carbon atoms 3.67Å), TYR 95 (distance between interaction carbon atoms 3.52Å).	TYR 82 (distance H-A 2.58 Å, D-A 2.98 Å), MET 335 (distance H-A 3.53 Å, D-A 3.89 Å), PHE 398 (distance H-A 2.59 Å, D-A 3.00 Å), HIS 403 (distance H-A 3.48 Å, D-A 3.96 Å), CYS 405 (distance H-A 2.82 Å, D-A 3.16 Å).
17.	Ningpogenin	-5.7	PHE 28 (distance between interaction carbon atoms 3.82Å), PRO 188 (distance between interaction carbon atoms 3.81Å), ILE 334 (distance between interaction carbon atoms 3.78Å).	None
18.	Oleoside dimethyl ester	-7.5	TYR 95 (distance between interaction carbon atoms 3.62Å), PHE 191 (distance between interaction carbon atoms 3.47Å), LEU 333 (distance between interaction carbon atoms 3.15Å), ILE 336 (distance between interaction carbon atoms 3.38Å), ILE 406 (distance between interaction carbon atoms 3.59Å), LEU 442 (distance between interaction carbon atoms 3.94Å).	ALA 29 (distance H-A 2.51 Å, D-A 3.08 Å), TYR 95 (distance H-A 2.02 Å, D-A 2.70 Å), ILE 334 (distance H-A 2.11 Å, D-A 2.80 Å), MET 335 (distance H-A 2.27 Å, D-A 2.90Å), HIS 403 (distance H-A 2.17 Å, D-A 3.12Å).
19.	Patrinallolide A	-8.6	PHE 25 (distance between interaction carbon atoms 3.96Å), PHE 28 (distance between interaction carbon atoms 3.56Å), PRO 188 (distance between interaction carbon atoms 3.24Å), LEU 189 (distance between interaction carbon atoms 3.64Å), PHE 191 (distance between interaction carbon atoms 3.33Å), PHE 192 (distance between interaction carbon atoms 3.39Å), ILE 334 (distance between interaction carbon atoms 3.44Å).	MET 335 (distance H-A 2.35 Å, D-A 3.40 Å).
20.	Pinnatoside	-6.9	PRO 188 (distance between interaction carbon atoms 3.82Å), PHE 192 (distance between interaction carbon atoms 3.61Å).	ILE 334 (distance H-A 2.21 Å, D-A 3.13Å), MET 335 (distance H-A 3.19 Å, D-A 3.89Å), LEU 442 (distance H-A 1.96 Å, D-A 2.82Å).
21.	Plantarenalolide	-7.2	TYR 82 (distance between interaction carbon atoms 3.70Å), LEU 333 (distance between interaction carbon atoms 3.59Å).	HIS 403 (distance H-A 2.05 Å, D-A 2.91Å), LYS 404 (distance H-A 2.83Å, D-A 3.52Å), CYS 405 (distance H-A 2.72 Å, D-A 3.10 Å).
22.	Polystachyn A	-8.1	LEU 78 (distance between interaction carbon atoms 3.54Å), TYR 82 (distance between interaction carbon atoms 3.53Å), TYR 95 (distance between interaction carbon atoms 3.45Å), LEU 333 (distance between interaction carbon atoms 3.69Å), ILE 336 (distance between interaction carbon atoms 3.61Å).	TYR 82 (distance H-A 2.08 Å, D-A 2.71 Å), CYS 405 (distance H-A 3.55 Å, D-A 4.00 Å).
23.	Voriconazole	-7.6	TYR 82 (4.74 Å), LEU 333 (5.50 Å), ILE 336 (5.67 Å)	TYR 95 (distance H-A 5.69 Å), ARG 338 (distance 6.04 Å, D-A 3.38Å).

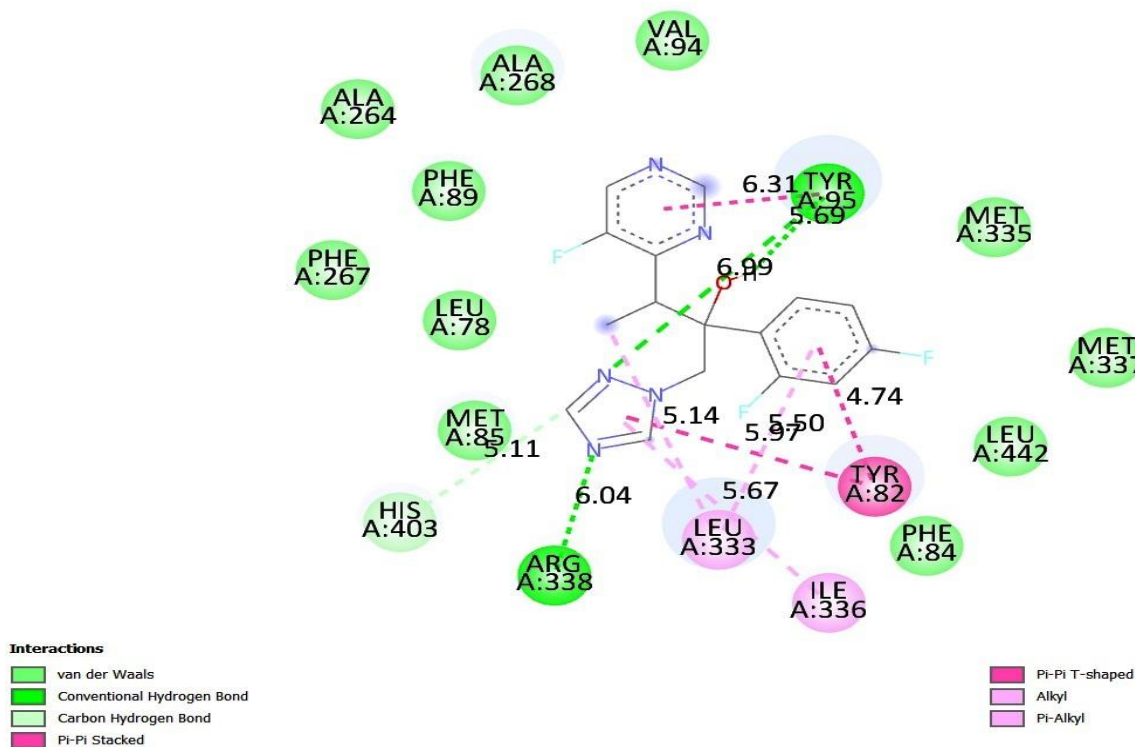
H-A= Distance between hydrogen and acceptor atom (Å); D-A= Distance between donor and acceptor atom (Å)



10-Isovaleroyl-dihydropenstemiide



Patrinolloside A



Voriconazole

Figure 2 Molecular docking interactions of 10-Isovaleroyl-dihydropenstemide, Patrinalloside A, Voriconazole with *N. fowleri*CYP51 receptor

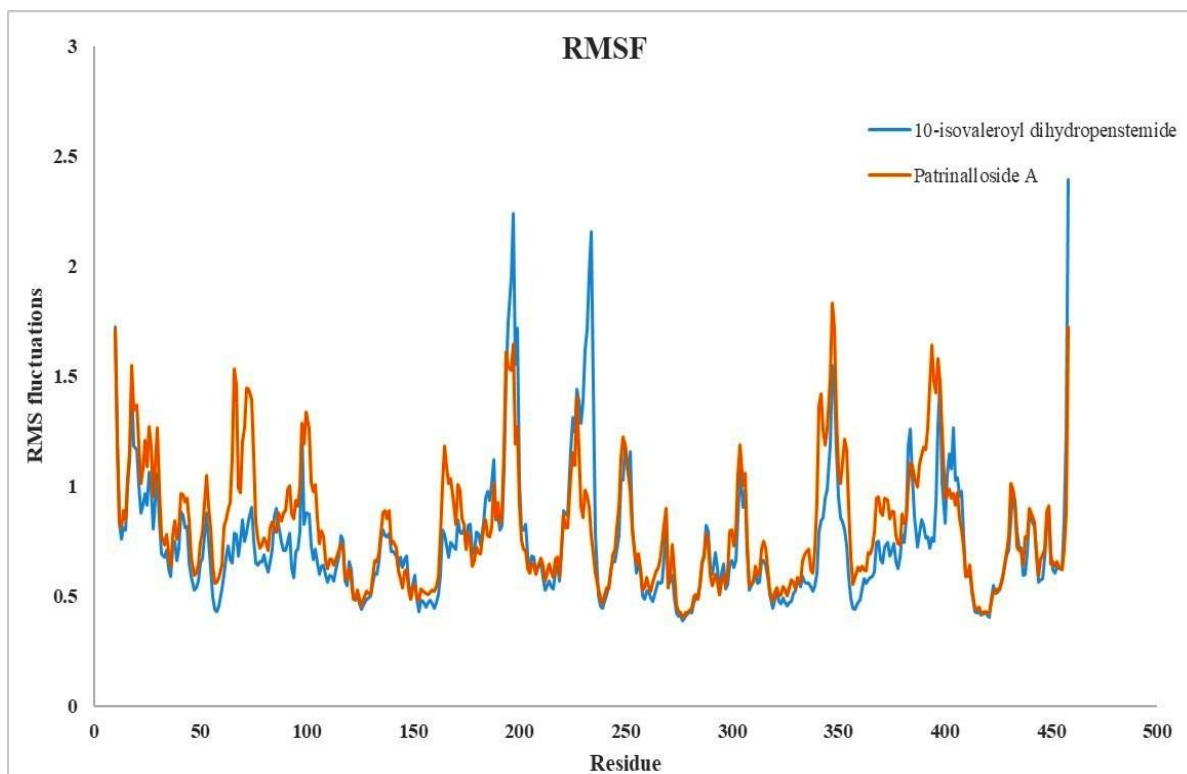
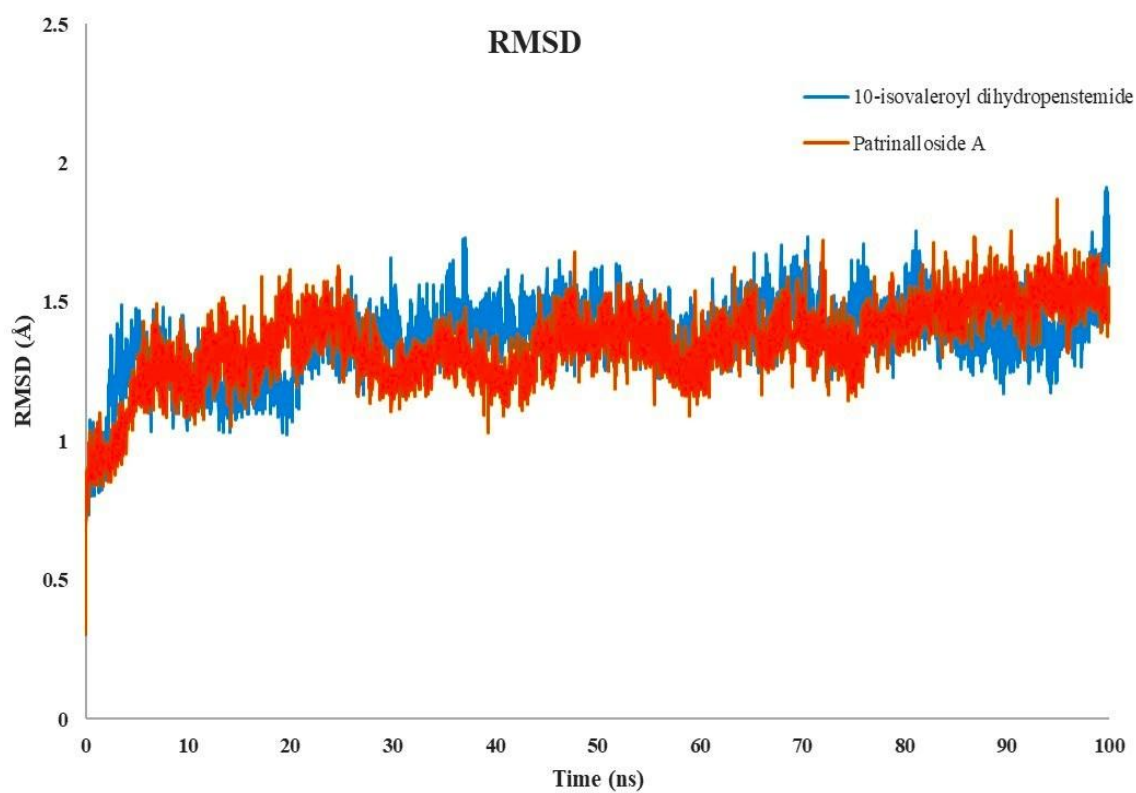
Common amino acid residues between 10-isovaleroyl-dihydropenstemide and complexed itraconazole included VAL 94. The overlapping residues for Patrinalloside A and complexed itraconazole were PHE 25, PHE 28, PRO 188, LEU 189, PHE 191, PHE 192, and ILE 334. For voriconazole and complexed itraconazole, the common residue was TYR 95 (Madero-Ayala et al. 2022). These shared interacting residues confirmed that both 10-isovaleroyl-dihydropenstemide and Patrinalloside A were effectively docked within the active site of the receptor (Alamri et al. 2023).

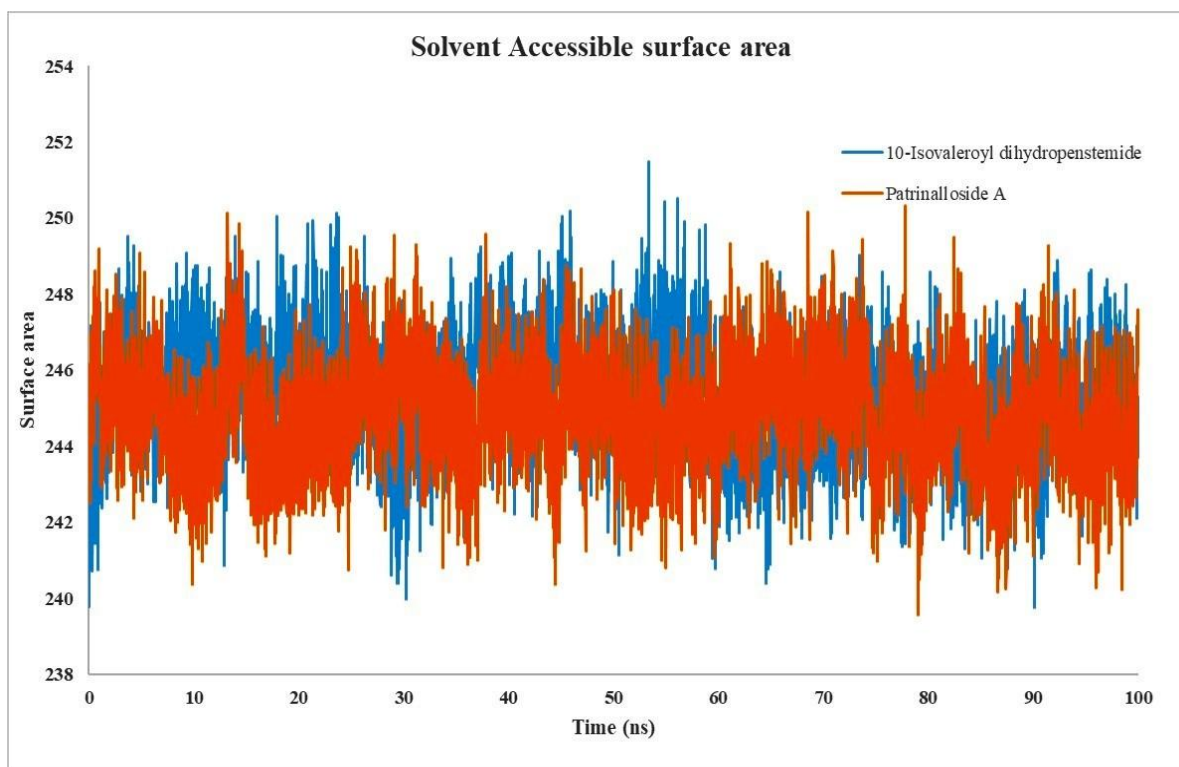
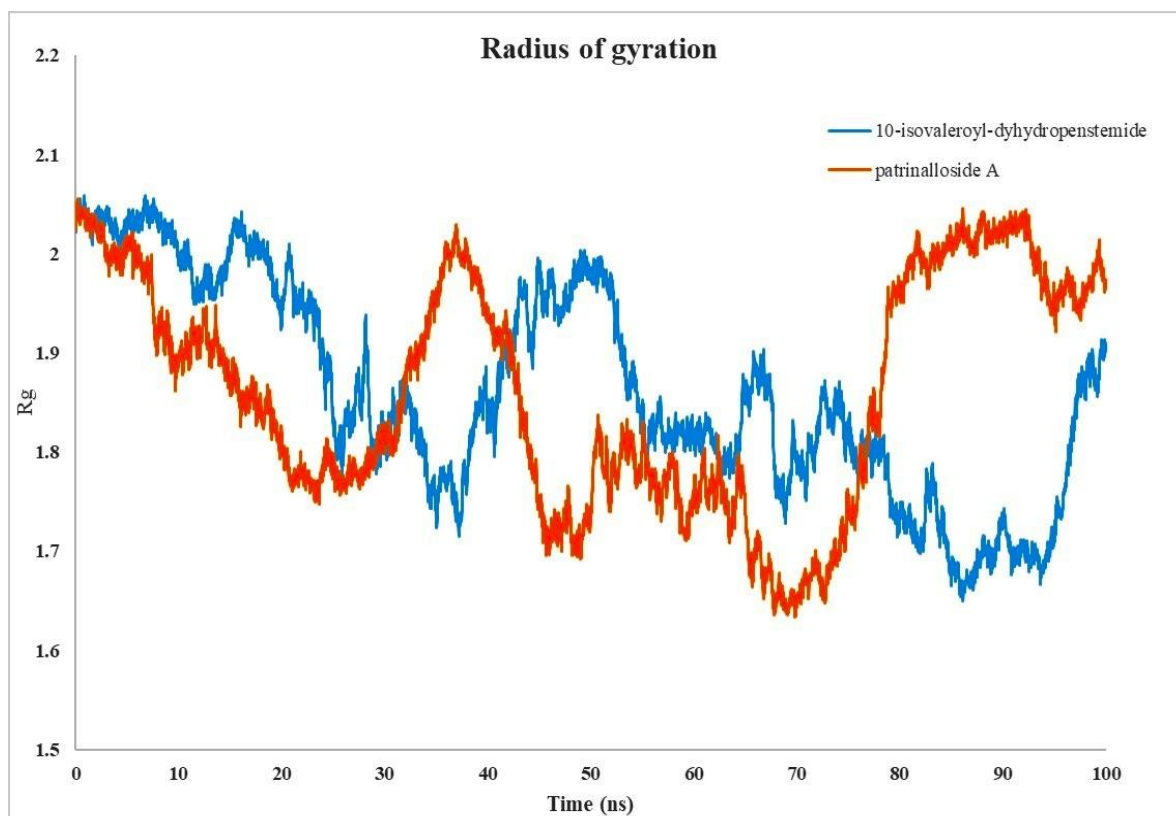
3.2 MD Simulation Data

Based on molecular docking interaction data, the top two iridoids 10-isovaleroyl-dihydropenstemide and Patrinalloside A were selected for molecular dynamics simulation analysis with the *N. fowleri* CYP51 receptor (Kushwaha et al. 2021). The average RMSD (Root Mean Square Deviation) values for 10-isovaleroyl-dihydropenstemide and Patrinalloside A were 1.36 Å and 1.35 Å, respectively (Yu et al. 2024). In both cases, the RMSD values stabilized throughout the 100 ns simulation period, and both molecules maintained a similar interaction pattern during the simulation (Maharana et al. 2024). The RMSF (Root Mean Square Fluctuation) diagram showed that, for most of the simulation run, fluctuations were limited to around 2.0 Å. Inside the receptor, 10-isovaleroyl-dihydropenstemide exhibited fluctuations near residues

200, 230, and 458. Residues PRO 197, SER 234, and LYS458 showed the maximum fluctuations during the simulation, likely because they were not involved in interactions or were located far from the active site (Notarte et al. 2023). The average radius of gyration for the complexes of 10-isovaleroyl-dihydropenstemide and Patrinalloside A with the *N. fowleri* CYP51 receptor was 1.86 nm for both. Constant fluctuations were observed in the radius of gyration values; however, these values consistently remained within a lower range, confirming that the molecules were located within the receptor's active site during the simulation (Rout et al. 2024). The average solvent-accessible surface area (SASA) values for the complexes were 245.35 nm² for 10-isovaleroyl-dihydropenstemide and 244.83 nm² for Patrinalloside A. The SASA values of both complexes indicated the formation of stable structures throughout the simulation (Kokubu et al. 2024).

The hydrogen bond interaction map confirmed that both 10-isovaleroyl-dihydropenstemide and Patrinalloside A interacted with the receptor for the entire duration of the simulation. Moreover, both molecules maintained contact with the active site amino acid residues, indicating a strong relationship between the ligand and receptor (Figure 3) (Prinsa et al. 2024). The MD simulation data confirmed that both iridoids were effectively interacting with the receptor, and the structural integrity of the receptor remained intact.





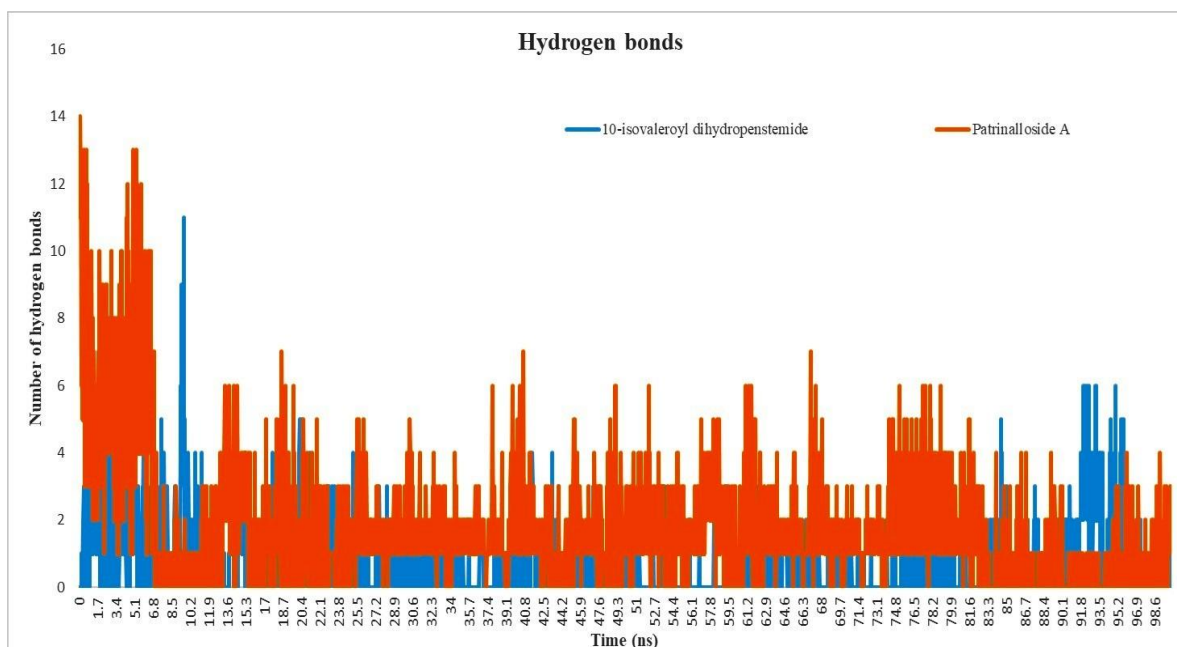


Figure 3 MD Simulation data of 10-Isovaleroyl-dihydropenstemide, and Patrinalloside A with *N. fowleri* CYP51 receptor

Table 3 MMPBSA Data of 10-isovaleroyl-dihydropenstemide-*N. fowleri* CYP51 and Patrinalloside A -*N. fowleri* CYP51

SN	Drug-Receptor Complex	van der Waal energy (kJ/mol)	Electrostatic energy (kJ/mol)	Polar solvation energy (kJ/mol)	SASA energy (kJ/mol)	Binding energy (kJ/mol)
1.	10-isovaleroyl-dihydropenstemide- <i>Naegleria fowleri</i> CYP51	-109.684	-6.854	59.098	-14.482	-71.922
2.	Patrinalloside A - <i>Naegleria fowleri</i> CYP51	-132.872	-26.165	114.990	-17.196	-61.243

3.3 MMPBSA Analysis Data

MMPBSA analysis data indicated that the binding energies of 10-isovaleroyl-dihydropenstemide with *N. fowleri* CYP51 and Patrinalloside A with *N. fowleri* CYP51 were -71.922 kJ/mol and -61.243 kJ/mol, respectively. In both complexes, van der Waals, electrostatic, and solvent-accessible surface area (SASA) energies positively contributed to the binding energies, while polar solvation energies had a negative contribution (Table 3) (Vishvakarma et al. 2022a).

For 10-isovaleroyl-dihydropenstemide, the residues PHE 25, LYS 30, ASP 184, LEU 189, TYR 193, and THR 440 positively contributed to the binding energies through molecular mechanics and apolar energy (Yasir et al. 2024). Conversely, residues VAL 26, ALA 29, ASP 184, SER 187, TYR 193, and THR 440 negatively impacted the binding energy through polar energy (Vishvakarma et al. 2022b). Similarly, for Patrinalloside A, the residues GLU 147, HIS 180, and PRO 448 positively contributed to the binding energies through molecular mechanics and apolar energy. However, GLU 147 and HIS 180 negatively affected the

binding energy through polar energy (Figure 4) (Wagoner and Baker 2006).

3.4 DFT Analyses Data

3.4.1 Frontier Molecular Orbital Analysis Data

The HOMO and LUMO orbital energies (in eV) for 10-isovaleroyl-dihydropenstemide and Patrinalloside A were found to be 6.94 and -6.72, and -0.60 and -0.63, respectively. The energy gap between the HOMO and LUMO orbitals provides insight into the chemical reactivity of the structures. The HOMO and LUMO energy gaps for 10-isovaleroyl-dihydropenstemide and Patrinalloside A were measured at 6.34 and 6.09, respectively (Talimarada et al. 2022). Table 4 lists various parameters, including the electrophilicity index, softness, electronegativity, chemical hardness, and the energy gap (ΔE) between the HOMO and LUMO. Additionally, the compounds' softness, electrophilicity index, reactivity, chemical hardness, and electronegativity were analyzed (Wu et al. 2024). Among the selected iridoids, Patrinalloside A is classified as a soft molecule, followed by 10-

isovaleroyl-dihydropenstemide, as systems with smaller energy gaps are termed soft molecules (Lv et al. 2025). A higher value of the electrophilicity index indicates greater chemical reactivity. In

this context, 10-isovaleroyl-dihydropenstemide exhibited the highest electrophilicity value of 4.08 (Figure 5) (Elyashberg et al. 2023).

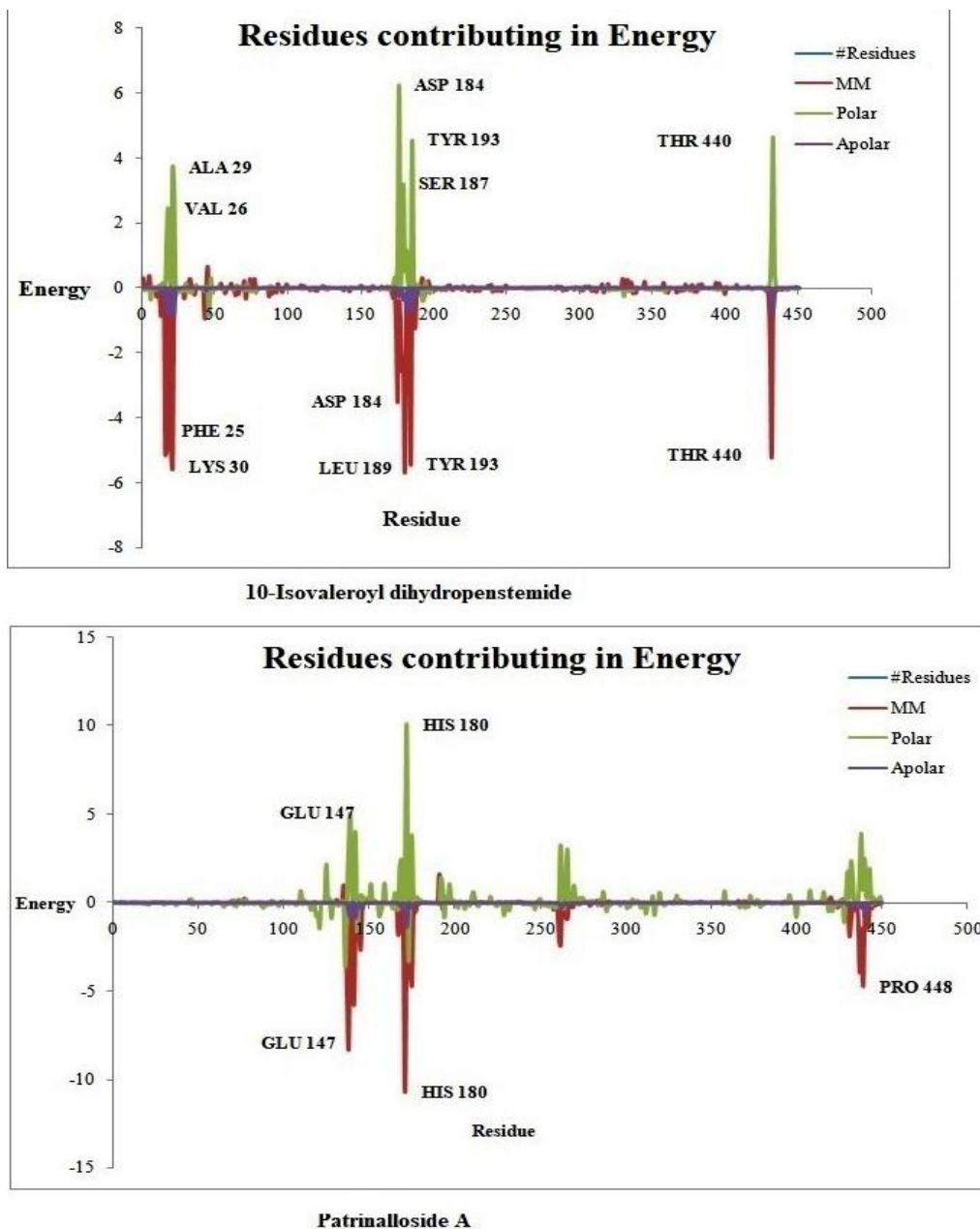
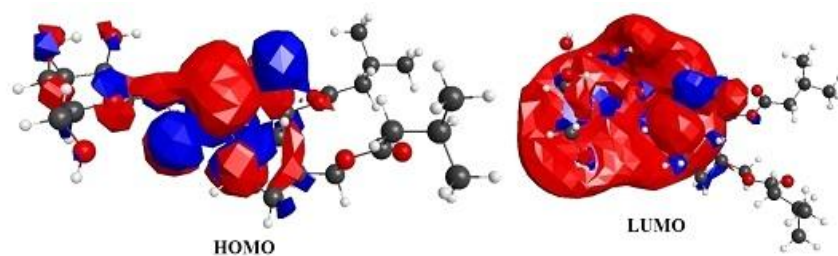


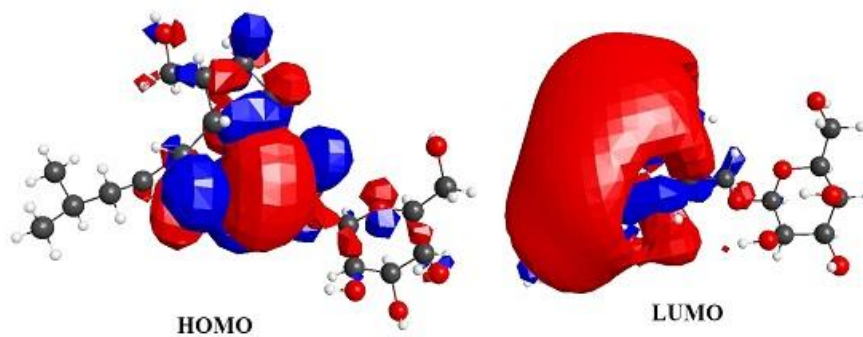
Figure 4 Role of Amino acid residues on Binding Energy in case of 10-Isovaleroyl-dihydropenstemide, and Patrinalloside A interact with *N. fowleri* CYP51 receptor

Table 4 FMO analysis data of 10-isovaleroyl-dihydropenstemide and Patrinalloside A

SN	Molecule Name	E_{HOMO} (eV)	E_{LUMO} (eV)	ΔE gap (eV)	I	A	η	ζ	μ	Ψ
1.	10-isovaleroyl-dihydropenstemide	-6.94	-0.60	6.34	6.94	0.60	3.17	0.15	3.77	2.24
2.	Patrinalloside A	-6.72	-0.63	6.09	6.72	0.63	3.04	0.16	3.67	2.21



FMO of 10-Isovaleroyl dihydropenstemide



FMO of Patrinalloside A

Figure 5 Frontier Molecular Orbital Analysis of 10-Isovaleroyl-dihydropenstemide, and Patrinalloside A.

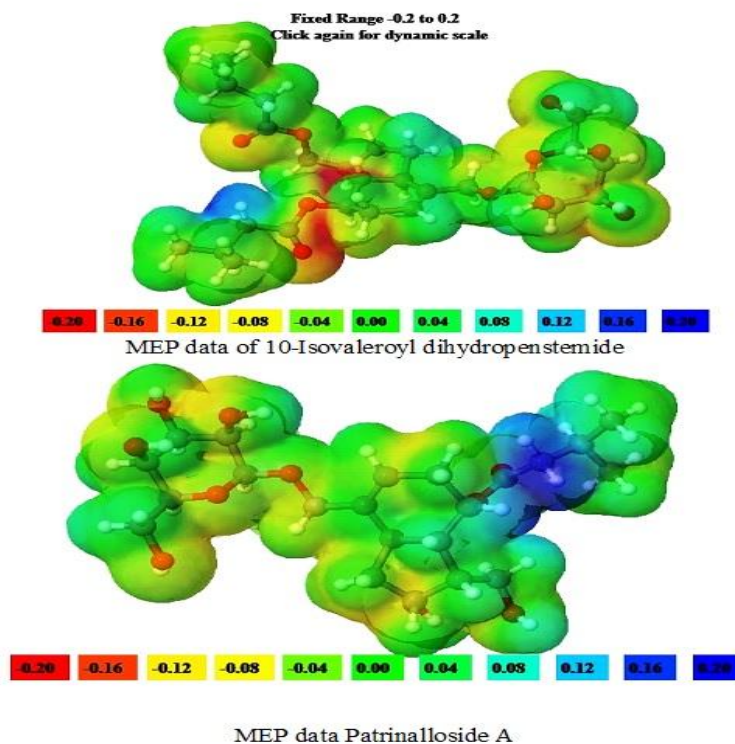


Figure 6 Molecular Orbital Potential Analysis of 10-Isovaleroyl-dihydropenstemide, and Patrinalloside A.

Table 5 ADME analysis data of 10-isovaleroyl-dihydropenstemide and Patrinalloside A

SN	Name of the Molecules	MW	TPSA	LogS	LogP	GI absorption	Molar Refractivity	Pgp substrate	BBB penetration	CYP 1A2 inhibitor	CYP 2C19 inhibitor	CYP 2C9 inhibitor	CYP 2D6 inhibitor	CYP 3A4 inhibitor
1.	10-isovaleroyl-dihydropenstemide	528.63	151.98	-3.40	4.43	Low	134.47	No	No	No	No	No	No	No
2.	Patrinalloside A	460.52	166.4	-1.70	2.69	Low	91.65	No	No	No	No	No	No	No

Table 6 OSIRIS toxicity data of 10-isovaleroyl-dihydropenstemide and Patrinalloside A

SN	Name of the Molecules	Mutagenic	Tumorigenic	Irritant	Reproductive toxicant
1.	10-isovaleroyl-dihydropenstemide	Non Toxic	Non Toxic	Non Toxic	Non Toxic
2.	Patrinalloside A	Non Toxic	Non Toxic	Toxic	Non Toxic

■ Toxic
 ■ Non Toxic
 ■ Slightly Toxic

3.4.2 Molecular Electrostatic Potential Data

In the structure of 10-isovaleroyl-dihydropenstemide, most of the compound is electrically neutral; however, the -O-C=O group and the linked methylene (-CH₂-) group serve as sites for electrophilic and nucleophilic attacks, respectively (Boulebd 2025; Karakiliç et al. 2025; Saji et al. 2021). Similarly, in Patrinalloside A, the majority of the structure is electrically neutral, with the -O-C=O group acting as a site for nucleophilic attack (Figure 6) (de Souza et al. 2022).

3.5 ADMET Analysis Data

The ADME investigation of 10-isovaleroyl-dihydropenstemide and Patrinalloside A indicated that a few compounds adhered to the Lipinski rule, showing an oral bioavailability score of 0.55. However, they exhibited poor gastrointestinal absorption and did not penetrate the blood-brain barrier (Table 5). Toxicity predictions from Osiris for both 10-isovaleroyl-dihydropenstemide and Patrinalloside A demonstrated that these molecules are non-mutagenic, non-tumorigenic, and non-reproductive (Table 6) (Sultan et al. 2023).

Conclusion

In the concluding remarks, after conducting sequential computational studies, we state that among the considered iridoids, 10-isovaleroyl-dihydropenstemide and Patrinalloside A showed the highest probability of being effective in the treatment of primary amoebic meningoencephalitis.

Acknowledgement

This study is supported by Division of Research & Innovation, Uttarakhand University, Dehradun, India to Supriyo Saha under the seed money grant reference no UU/DRI/SM/2024-25/018.

Author Contributions

All authors contributed equally to the design, procurement, experiment, writing and review process of the manuscript.

References

- Ahmed, U., Manzoor, M., Qureshi, S., Mazhar, M., Fatima, A., et al. (2023). Anti-amoebic effects of synthetic acridine-9(10H)-one against brain-eating amoebae. *Acta Tropica*, 239, 106824.
- Akter, S., Alhatlani, B.Y., Abdallah, E.M., Saha, S., Ferdous, J., Hossain, M.E., Ali, F., & Kawsar, S.M.A. (2023). Exploring Cinnamoyl-Substituted Mannopyranosides: Synthesis, Evaluation of Antimicrobial Properties, and Molecular Docking Studies Targeting H5N1 Influenza A Virus. *Molecules*, 28(24), 8001.
- Alamri, M.A., Alawam, A.S., Alshahrani, M.M., Kawsar, S.M.A., Prinsa., & Saha, S. (2023). Establishing the Role of Iridoids as Potential Kirsten Rat Sarcoma Viral Oncogene Homolog G12C Inhibitors Using Molecular Docking; Molecular Docking Simulation; Molecular Mechanics Poisson-Boltzmann Surface Area; Frontier Molecular Orbital Theory; Molecular Electrostatic Potential; and Absorption, Distribution, Metabolism, Excretion, and Toxicity Analysis. *Molecules*, 28(13), 5050.
- Baker, N.A., Sept, D., Joseph, S., Holst, M. J., & McCammon, J.A. (2001). Electrostatics of nanosystems: Application to microtubules and the ribosome. *Proceedings of National Academy of Science USA*, 98, 10037-10041.
- Barca, G.M.J., Bertoni, C., Carrington, L., Datta, D., De Silva, N., et al. (2020). Recent developments in the general atomic and

- molecular electronic structure system. *Journal of Chemical Physics*, 152(15), 154102.
- Boulebd, H. (2025). A comprehensive DFT-based study of the antioxidant properties of monolignols: Mechanism, kinetics, and influence of physiological environments. *International Journal of Biological Macromolecule*, 284(Pt 1), 138044.
- Calis, Z, Mogulkoc, R., & Baltaci, A.K. (2020). The Roles of Flavonols/Flavonoids in Neurodegeneration and Neuroinflammation. *Mini Reviews in Medicinal Chemistry*, 20(15), 1475-1488.
- Chen, X., Li, H., Tian, L., Li, Q., Luo, J., & Zhang, Y. (2020). Analysis of the Physicochemical Properties of Acaricides Based on Lipinski's Rule of Five. *Journal of Computational Biology*, 27(9), 1397-1406.
- Cooper, A.M., Aouthmany, S., Shah, K., & Rega, P.P. (2019). Killer amoebas: Primary amoebic meningoencephalitis in a changing climate. *Journal of American Academy Physician Association*, 32(6), 30-35.
- Daina, A., Michielin, O., & Zoete, V. (2017). Swiss ADME: a free web tool to evaluate pharmacokinetics, drug-likeness and medicinal chemistry friendliness of small molecules. *Scientific Reports*, 7, 42717.
- de Souza, F.N., de Lima, H.B., de Souza, L.R., Oliveira, G.S., de Paula da Silva, C.H.T., Pereira, A.C.M., & da Silva Hage-Melim, L.I. (2022). Design of Multitarget Natural Products Analogs with Potential Anti-Alzheimer's Activity. *Current Computer Aided Drug Design*, 18(2), 120-149.
- Elyashberg, M., Tyagarajan, S., Mandal, M., & Buevich, A.V. (2023). Enhancing Efficiency of Natural Product Structure Revision: Leveraging CASE and DFT over Total Synthesis. *Molecules*, 28(9), 3796.
- Geng, X., Wang, Y., Li, H., Song, L., Luo, C., Gu, X., Zhong, H., Chen, H., Chen, X., Wang, J., & Pan, Z. (2024). Total iridoid glycoside extract of *Lamiophlomis rotata* (Benth) Kudo accelerates diabetic wound healing by the NRF2/COX2 axis. *Chinese Medicine*, 19(1), 53.
- Goodsell, D.S., Sanner, M.F., Olson, A.J., & Forli, S. (2021). The AutoDock suite at 30. *Protein Science*, 30(1), 31-43.
- Grover, P., Mehta, L., Malhotra, A., Kapoor, G., Nagarajan, K., Kumar, P., Chawla, V., & Chawla, P.A. (2023). Exploring the Multitarget Potential of Iridoids: Advances and Applications. *Current Topics in Medicinal Chemistry*, 23(5), 371-388.
- Güémez, A., & García, E. (2021). Primary Amoebic Meningoencephalitis by *Naegleria fowleri*: Pathogenesis and Treatments. *Biomolecules*, 11(9), 1320.
- Hanson, R.M., Prilusky, J., Renjian, Z., Nakane, T., & Sussman, J.L. (2013). JSmol and the next-generation web-based representation of 3D molecular structure as applied to proteopedia. *Israel Journal of Chemistry*, 53 (3-4), 207-216.
- Hanwell, M.D., Curtis, D.E., Lonie, D.C., Vandermeersch, T., Zurek, E., & Hutchison, G.R. (2012). Avogadro: an advanced semantic chemical editor, visualization, and analysis platform. *Journal of Cheminformatics*, 4, 17.
- He, F., Yan, X., Zhao, N., Jiang, X., Wei, Y., Lu, F., Li, H., Li, D., & Chen, Y. (2023). Iridoid-glycoside isolation and purification from *Premna fulva* leaves. *Journal of Separation Science*, 46(14), e2300059.
- Kalman, M., & Ben-Tal, N. (2010). Quality assessment of protein model-structures using evolutionary conservation. *Bioinformatics*, 26(10), 1299-307.
- Kar, P., Oriola, A.O., & Oyedeji, A.O. (2024). Molecular Docking Approach for Biological Interaction of Green Synthesized Nanoparticles. *Molecules*, 29(11), 2428.
- Karakiliç, E., Başçeken, S., Eskiler, G.G., Uzuner, U., & Baran, A. (2025). Bioimaging of thiazolidine-4-one-based new probes, fluorimetric detection of Cu²⁺ "on-off" sensor property, DFT calculation, molecular docking studies, and multiple real samples application. *Food Chemistry*, 463(Pt 2), 141269.
- Kawsar, S.M.A., Hossain, M.A., Saha, S., Abdallah, E.M., Bhat, A.R., Ahmed, S., Jamalis, J., & Ozeki Y. (2024). Nucleoside-Based Drug Target with General Antimicrobial Screening and Specific Computational Studies against SARS-CoV-2 Main Protease. *Chemistry Select*, 9, e202304774.
- Kim, S., Lee, J., Jo, S., Brooks, C.L. 3rd, Lee, H.S., & Im, W. (2017). CHARMM-GUI ligand reader and modeler for CHARMM force field generation of small molecules. *Journal of Computational Chemistry*, 38(21), 1879-1886.
- Kokubu, R., Ohno, S., Manabe, N., & Yamaguchi, Y. (2024). Molecular Dynamics Simulation and Docking of MUC1 O-Glycopeptide. *Methods in Molecular Biology*, 2763, 373-379.
- Kumar, P., Kumar, P., Shrivastava, A., Dar, M.A., Lokhande, K.B., Singh, N., Singh, A., Velayutham, R., and Mandal, D. (2023). Immunoinformatics-based multi-epitope containing fused polypeptide vaccine design against visceral leishmaniasis with

- high immunogenicity and TLR binding. *International Journal of Biological Macromolecule*, 253(Pt 8), 127567.
- Kumari, R., & Kumar, R. (2014). Open Source Drug Discovery Consortium, Lynn A. g_mmpbsa-A GROMACS Tool for High-Throughput MM-PBSA Calculations. *Journal of Chemical Information and Modeling*, 54(7), 1951–1962.
- Kushwaha, P.P., Singh, A.K., Bansal, T., Yadav, A., Prajapati, K.S., Mohd, S., & Kumar, S. (2021). Identification of Natural Inhibitors Against SARSCoV-2 Drugable Targets Using Molecular Docking, Molecular Dynamics Simulation, and MM-PBSA Approach. *Frontier Cellular Infection Microbiology*, 11, 730288.
- Lemkul, J.A. (2018). From Proteins to Perturbed Hamiltonians: A Suite of Tutorials for the GROMACS-2018 Molecular Simulation Package, v1.0. *Living Journal of Computational Molecular Science*, 1(1) 5068.
- Lokhande, K., Nawani, N.K., Venkateswara, S., & Pawar, S. (2022). Biflavonoids from *Rhus succedanea* as probable natural inhibitors against SARS-CoV-2: a molecular docking and molecular dynamics approach. *Journal of Biomolecular Structure Dynamics*, 40(10), 4376-4388.
- Lv, H., Ruan, M., Wen, Y., Zhou, L., Zhao, P., & Xuan, X. (2025). Toward understanding ammonia capture in two amino-functionalized metal-organic frameworks using in-situ infrared spectroscopy and DFT calculation. *Spectrochimica Acta A Molecular and Biomolecular Spectroscopy*, 324, 124962.
- Madero-Ayala, P.A., Mares-Alejandre, R.E., & Ramos-Ibarra, M.A. (2022). In Silico Structural Analysis of Serine Carboxypeptidase Nf314, a Potential Drug Target in *Naegleria fowleri* Infections. *International Journal of Molecular Sciences*, 23(20), 12203.
- Maharana, J., Hwang, S.K., Singha, D.L., Panda, D., Singh, S., Okita, T.W., & Modi, M.K. (2024). Exploring the structural assembly of rice ADP-glucose pyrophosphorylase subunits using MD simulation. *Journal of Molecular Graphics & Modeling*, 129, 108761.
- Notarte, K.I.R., Quimque, M.T.J., Macaranas, I.T., Khan, A., Pastrana, A.M., Villaflores, O.B., et al. (2023). Attenuation of Lipopolysaccharide-induced Inflammatory Responses through Inhibition of the NF- κ B Pathway and the Increased NRF2 Level by a Flavonol-enriched n-Butanol Fraction from *Uvaria alba*. *ACS Omega*, 8(6), 5377–5392.
- Paggi, J.M., Pandit, A., & Dror, R.O. (2024). The Art and Science of Molecular Docking. *Annual Review of Biochemistry*, 93(1), 389-410.
- Park, S.W., Lee, B.H., Song, S.H., & Kim, M.K. (2023). Revisiting the Ramachandran plot based on statistical analysis of static and dynamic characteristics of protein structures. *Journal of Structural Biology*, 215(1), 107939.
- Perri, M.J., & Weber, S.H. (2014). Web-Based Job Submission Interface for the GAMESS Computational Chemistry Program. *Journal of Chemical Education*, 91(12), 2206-2208.
- Prinsa., Saha, S., Bulbul, M.Z.H., Ozeki, Y., Alamri, M.A., & Kawsar S.M.A. (2024). Flavonoids as potential KRAS inhibitors: DFT, molecular docking, molecular dynamics simulation and ADMET analyses. *Journal of Asian Natural Product Research*, 26(8), 955-992.
- Riyaphan, J, Pham, D.C., Leong, M.K., & Weng, C.F. (2021). In Silico Approaches to Identify Polyphenol Compounds as α -Glucosidase and α -Amylase Inhibitors against Type-II Diabetes. *Biomolecules*, 11(12), 1877.
- Rojo, J.U., Rajendran, R., & Salazar, J.H. (2023). Laboratory Diagnosis of Primary Amoebic Meningoencephalitis. *Laboratory Medicine*, 54(5), e124-e132.
- Rout, M., Dey, S., Mishra, S., Panda, S., Singh, M.K., Sinha, R., Dehury, B., & Pati, S. (2024). Machine learning and classical MD simulation to identify inhibitors against the P37 envelope protein of monkeypox virus. *Journal of Biomolecular Structure & Dynamics*, 42(8), 3935-3948.
- Saji, R.S., Prasana, J.C., Muthu, S., & George, J. (2021). Experimental and theoretical spectroscopic (FT-IR, FT-Raman, UV-VIS) analysis, natural bonding orbitals and molecular docking studies on 2-bromo-6-methoxynaphthalene: A potential anticancer drug. *Heliyon*, 7(6), e07213.
- Sakr, M.A.S., Sherbiny, F.F., & El-Etrawy, A.S. (2022). Hydrazone-based Materials; DFT, TD-DFT, NBO Analysis, Fukui Function, MESP Analysis, and Solar Cell Applications. *Journal of Fluorescence*, 32(5), 1857-1871.
- Schou, C., Kolören, Z., Sendker, J., Sarigiannis, Y., Jovanovic, A., & Karanis, P. (2024). *Odontites linkii* subsp. cyprusi Ethanolic Extract Indicated In Vitro Anti-Acanthamoeba Effect. *Microorganisms*, 12(11), 2303.
- Shi, D.Q., Liu, J.J., Feng, Y.M., Zhou, Y., Liao, C.C., Liu, D., Li, R.T., & Li, H.M. (2023). Iridoids and sesquiterpenoids from *Valeriana officinalis* and their bioactivities. *Phytochemistry*, 205, 113478.
- Sultan, R., Ahmed, A., Wei, L., Saeed, H., Islam, M., & Ishaq M. (2023). The anticancer potential of chemical constituents of

- Moringa oleifera* targeting CDK-2 inhibition in estrogen receptor positive breast cancer using in-silico and in vitro approaches. *BMC Complementary Medicine and Therapies*, 23(1), 396.
- Talimarada, D., Sharma, A., Wakhradkar, M.G., Dhuri, S.N., Gunturu, K.C., Sundaram, V.N.N., & Holla, H. (2022). Synthesis, DFT analysis and in-vitro anticancer study of novel fused bicyclic pyranoneisoxazoline derivatives of Goniodioid-diacetate-a natural product derivative. *Fitoterapia*, 163, 105316.
- Vishvakarma, V.K., Pal, S., Singh, P., & Bahadur, I. (2022a). Interactions between main protease of SARS-CoV-2 and testosterone or progesterone using computational approach. *Journal of Molecular Structure*, 1251, 131965.
- Vishvakarma, V.K., Singh, M.B., Jain, P., Kumari, K., & Singh, P. (2022b). Hunting the main protease of SARS-CoV-2 by plitidepsin: Molecular docking and temperature-dependent molecular dynamics simulations. *Amino Acids*, 54, 205–213.
- Wagoner, J.A., & Baker, N.A. (2006). Assessing implicit models for nonpolar mean solvation forces: the importance of dispersion and volume terms. *Proceedings of National Academy of Science USA*, 103(22), 8331-6.
- Wang, C., Gong, X., Bo, A., Zhang, L., Zhang, M., Zang, E., Zhang, C., & Li, M. (2020). Iridoids: Research Advances in Their Phytochemistry, Biological Activities, and Pharmacokinetics. *Molecules*, 25(2), 287.
- Wu, Q., Ghosal, K., Kana'an, N., Roy, S., Rashed, N., Majumder, R., Mandal, M., Gao, L., & Farah, S. (2024). On-demand imidazolidinyl urea-based tissue-like, self-healable, and antibacterial hydrogels for infectious wound care. *Bioactive Materials*, 44, 116-130.
- Yasir, M., Park, J., Han, E.T., Han, J.H., Park, W.S., & Chun, W. (2024). Investigating the Inhibitory Potential of Flavonoids against Aldose Reductase: Insights from Molecular Docking, Dynamics Simulations, and gmx_MMPBSA Analysis. *Current Issues in Molecular Biology*, 46(10), 11503-11518
- Yu, D., Li, H., Liu, Y., Yang, X., Yang, W., Fu, Y., Zuo, Y.A., & Huang, X. (2024). Application of the molecular dynamics simulation GROMACS in food science. *Food Research International*. 190, 114653.
- Zhang, L., Wu, L., Liu, J., Chen, K., & Li, Y. (2023). Iridoids and derivatives from *Catalpa ovata* with their antioxidant activities. *Fitoterapia*, 169, 105599.
- Zhang, Q., Ran, T., Li, S., Han, L., Chen, S., Lin, G., Wu, H., Wu, H., Feng, S., Chen, J., Zhang, Q., & Zhao, X. (2024). Catalpol ameliorates liver fibrosis via inhibiting aerobic glycolysis by EphA2/FAK/Srcsignaling pathway. *Phytomedicine*. 135, 156047.



Journal of Experimental Biology and Agricultural Sciences

<http://www.jebas.org>

ISSN No. 2320 – 8694

Phylogenetic and Morphological Study of *Desmodesmus* Strains from Can Gio Mangrove Biosphere Reserve

Phuong-Nam Luu^{1,2}, Ngoc-Nam Trinh² , Thanh-Cong Nguyen³ , Quoc-Dang Quan⁴ ,
Duc-Hoan Huynh⁵, Tuong-Lam Le-Nguyen⁶, Hoang-Dung Tran^{7,*} 

¹Tung Thien Vuong Secondary School, 381 Tung Thien Vuong Street, Ward 12, District 08, 73011, Ho Chi Minh City, Vietnam

²Institute of Biotechnology and Food Technology, Industrial University of Ho Chi Minh City, 12 Nguyen Van Bao Street, Go Vap District, 71400, Ho Chi Minh City, Vietnam

³NTT Hi-Tech Institute, Nguyen Tat Thanh University, 298-300A Nguyen Tat Thanh Street, District 4, 72800, Ho Chi Minh City, Vietnam

⁴University of Science, VNU-HCM, 227 Nguyen Van Cu Street, Ward 04, District 05, 72760, Ho Chi Minh City, Vietnam

⁵Can Gio Mangrove Protection Forest Management Board, Can Gio Mangrove Biosphere Reserve, 1541 Rung Sat Street, An Thoi Dong Commune, Can Gio District, Ho Chi Minh City, 76700, Vietnam

⁶International School Ho Chi Minh City (ISHCMC), 01 Xuan Thuy Street, Thao Dien Ward, Thu Duc City, Ho Chi Minh City, 71107, Vietnam

⁷Faculty of Biology and Environment, Ho Chi Minh City University of Industry and Trade (HUIT), 140 Le Trong Tan Street, Tay Thanh Ward, Tan Phu District, Ho Chi Minh City, 72009, Vietnam

Received – November 04, 2024; Revision – December 18, 2024; Accepted – December 29, 2024

Available Online – January 15, 2025

DOI: [http://dx.doi.org/10.18006/2024.12\(6\).829.837](http://dx.doi.org/10.18006/2024.12(6).829.837)

KEYWORDS

Microalgae

Can Gio Biosphere Reserve

ITS

18S

ABSTRACT

This study focused on five microalgal strains resembling *Desmodesmus* isolated from the Can Gio Mangrove Biosphere Reserve. The objective was to assess the effectiveness of morphological and molecular methods for algal identification and to evaluate the genetic diversity of the relevant taxa. The five isolated and reference strains were cultured axenically in a BG-11 medium. Both microscopy (at magnifications of 40× and 100×) and molecular techniques (using ITS and 18S rRNA markers) were employed for analysis. Phylogenetic analyses were conducted using Maximum Likelihood and Bayesian inference methods. The results indicated that five of the ten strains were consistently identified using both approaches. Molecular data prompted a taxonomic reassignment for the three remaining strains, while morphological traits were more decisive for two reference strains. Phylogenetic analyses revealed significant genetic diversity within *Desmodesmus*, highlighting the ecological adaptability of genetically distinct variants. This study emphasizes the reliability of molecular tools in algal taxonomy, particularly for differentiating between *Desmodesmus* and *Scenedesmus*-like taxa. It contributes to understanding

* Corresponding author

E-mail: dungth@huit.edu.vn (Hoang-Dung Tran)

Peer review under responsibility of Journal of Experimental Biology and Agricultural Sciences.

Production and Hosting by Horizon Publisher India [HPI]
(<http://www.horizonpublisherindia.in/>).
All rights reserved.

All the articles published by [Journal of Experimental Biology and Agricultural Sciences](#) are licensed under a [Creative Commons Attribution-NonCommercial 4.0 International License](#) Based on a work at www.jebas.org.



microalgal genetic diversity in the Can Gio Biosphere Reserve and provides a foundation for future ecological and biotechnological applications.

1 Introduction

The Can Gio Mangrove Biosphere Reserve in southern Vietnam is globally recognized for its diverse ecosystems of significant ecological value. This UNESCO-designated site features a unique combination of freshwater and brackish water environments, creating an ideal habitat for microalgae. These organisms are critical for nutrient cycling, water purification, and overall ecosystem stability (Pham 2017; Pham 2019). Beyond their ecological importance, microalgae are increasingly valued for potential applications in biotechnology, renewable energy, and environmental remediation. Despite this significance, systematic studies on microalgal biodiversity and taxonomy in Can Gio remain limited, highlighting the need for focused efforts to explore and conserve these resources (Phung et al. 2019; Kezlya et al. 2023). In response to this need, the Culture Collection of Algae at Ho Chi Minh City (CCAH) was established, amassing over 100 local strains catalogued using morphological and molecular methods (DOST HCMC 2023).

Identifying algae based on morphological traits presents several challenges, primarily because environmental factors such as light, temperature, and nutrient availability can significantly affect cell phenotypes and morphology. These challenges intensify in closely related genera such as *Desmodesmus*, *Tetradesmus*, and *Scenedesmus*, which often exhibit overlapping morphological characteristics (Hegewald 1979; Kessler et al. 1997; Johnson et al. 2007; Mai et al. 2023; Nguyen et al. 2023). To address these issues, molecular markers have become essential for resolving taxonomic ambiguities. The Internal Transcribed Spacer (ITS) region is widely acknowledged for its high resolution in distinguishing closely related species, especially within *Scenedesmus* and *Desmodesmus* (Fawley and Fawley 2020; Kezlya et al. 2023; Nguyen et al. 2023). Other markers, such as the 18S and 23S rRNA genes, serve as complementary approaches, offering broader phylogenetic insights that enhance the robustness of classifications (Shirora 1966; Andersen and Kawachi 2005; Khaw et al. 2020; Kezlya et al. 2023; Nguyen et al. 2023). Choosing an appropriate set of markers with sufficient discriminating power is crucial for producing reliable identifications that supplement or refine morphological data.

This study employed the ITS and 18S markers to verify the identity of algal strains isolated from the Can Gio Biosphere Reserve. These strains displayed morphological characteristics similar to *Scenedesmus*-like *Desmodesmus*, whose overlapping traits with other *Scenedesmus*-like taxa required additional molecular validation. Several well-established *Scenedesmus*-like strains were also included as references. By analyzing both morphological and molecular data,

the study aimed to evaluate the chosen markers' effectiveness and the molecular approach's reliability in extending their potential applications to other algal taxa in the region. Additionally, the study assessed the phylogenetic relationships among the isolated strains based on these markers to better understand their genetic diversity, thereby contributing to our knowledge of microalgal biodiversity in Can Gio and paving the way for conservation and future biotechnological applications.

2 Materials and Methods

2.1 Study Subjects

This study focused on *Desmodesmus*-resembling strains CCAH016/2, CCAH020/1, CCAH024/1, CCAH026/1, and CCAH027/1, all isolated from the Can Gio Mangrove Biosphere Reserve. In addition, five well-known *Scenedesmus*-like strains (NIES-94, NIES-97, NIES-685, NIES-2280, and UTEX 2551) were included as references. Details concerning the sampling, isolation, culturing, and morphological identification of the Can Gio isolates are provided in Sections 2.2–2.5.

2.2 Algal Sampling

Microalgal samples were collected in October 2023 from two freshwater locations within the Can Gio Mangrove Biosphere Reserve using a plankton net with a 20–50 µm mesh size. Environmental parameters such as temperature (28–32 °C), salinity (less than 5 ppt), and pH (6.5–7.5) were recorded during the collection. The samples were then transported on ice for further analysis.

2.3 Isolation and Culturing

Single-cell isolation followed micropipette techniques, transferring cells into BG-11 medium. Non-axenic cultures were purified on BG-11 agar plates and then maintained in liquid BG-11 medium under controlled conditions.

2.4 Morphological Identification

Morphological observations were conducted on axenic cultures, focusing on traits such as cell shape, size, chain formation, and wall structure, under a microscope at 40× and 100× magnifications. The classification was based on Shirora's key (Shirora 1966).

2.5 Molecular Identification

Genomic DNA was extracted using the CTAB method (Ajayi et al. 2022). Two genetic markers, ITS and 18S, were amplified by

PCR due to their complementary roles: ITS provides high resolution at the species level, while 18S offers broader phylogenetic insights at the genus level. The annealing temperatures for the PCR were set at 61.6 °C for ITS and 60.5 °C for 18S. The resulting amplicons were approximately 700 bp for ITS and 1200 bp for 18S, as described by White et al. (1990). These amplicons were verified using agarose gel electrophoresis and sequenced using the Sanger method (Sanger et al. 1977). Raw chromatograms were visualized and trimmed with FinchTV, and the sequences were aligned in SeaView to confirm their taxonomic identity against reference databases (Gouy et al. 2010).

2.6 Phylogenetic Analysis

Phylogenetic trees were constructed based on ITS and 18S sequences aligned with MUSCLE (Edgar 2022). Maximum

Likelihood and Bayesian Inference methods were performed using IQ-TREE (Minh et al. 2020) and MrBayes (Ronquist et al. 2012), respectively, with branch support assessed through bootstrap (1000 replicates) and posterior probabilities. Phylogenetic trees were visualized with FigTree (Rambaut 2018).

3 Results

3.1 Morphological Analysis

A morphological examination of five isolated and five reference strains revealed variability in key features, such as cell shape, size, chain formation, spine presence and length, and chloroplast distribution (Figure 1). Among the isolated strains, CCAH016/2 exhibited elliptical to spindle-shaped cells (approximately 10 μm) that formed chains of 4–8 cells. Each cell had 2–3 μm spines at both ends and evenly distributed chloroplasts, which are

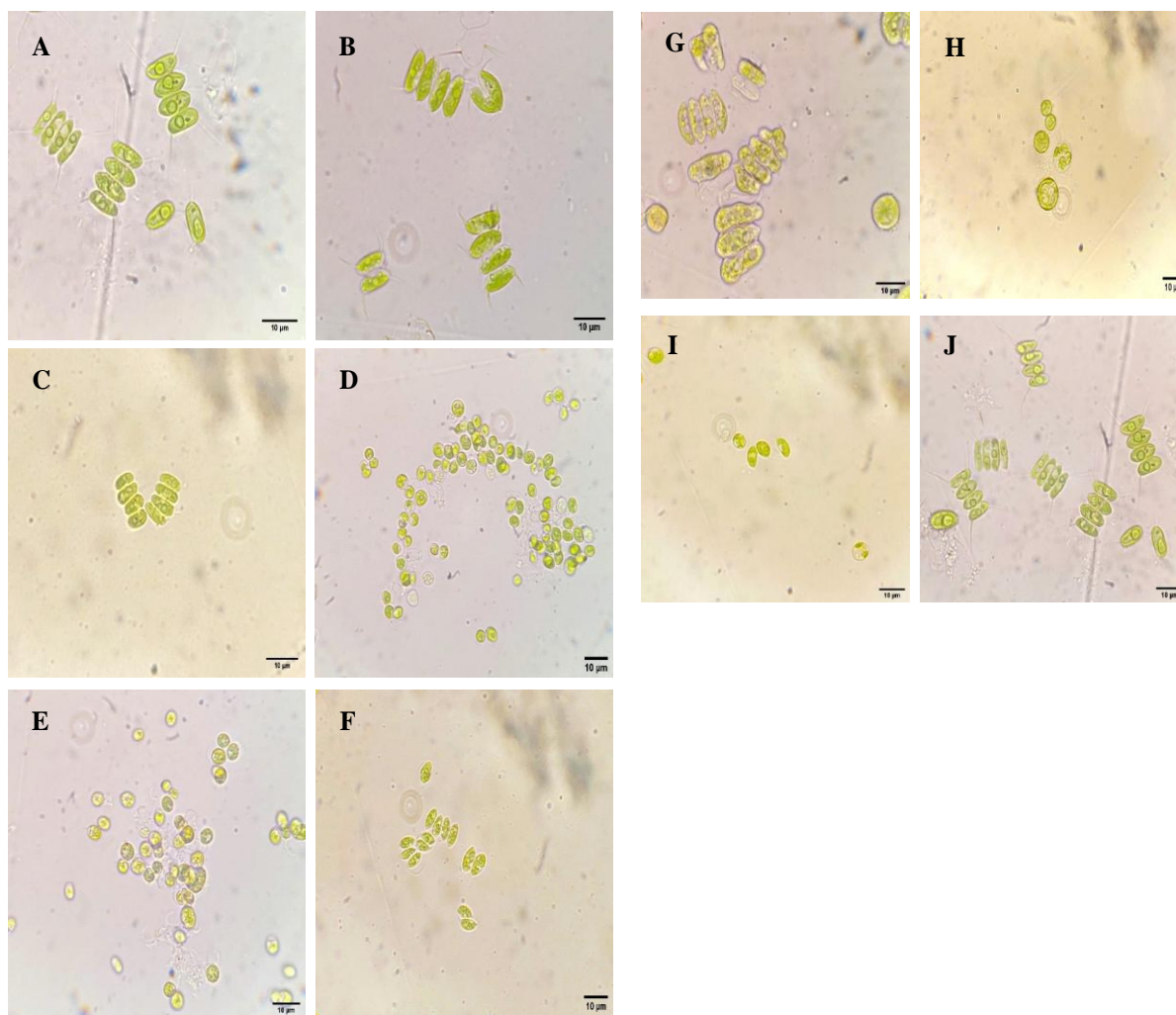


Figure 1 Microscopic observation of the studied samples and reference strains, (A) CCAH 016/2; (B) CCAH 020/1; (C) CCAH 024/1; (D) CCAH 026/1; (E) CCAH 027/1; (F) NIES-94; (G) NIES-97; (H) NIES-685; (I) NIES-2280; (J) UTEX 2551.

characteristics consistent with *Desmodesmus armatus*. CCAH020/1 and CCAH024/1 also displayed similar elliptical cells (8–10 μm) but formed shorter chains of 2–4 cells with smaller spines (~2 μm), aligning with *D. armatus*. In contrast, CCAH026/1 consisted of smaller, mostly solitary or paired cells (5–8 μm), ranging from elliptical to spherical, with no prominent spines, suggesting an affinity with *Scenedesmus obliquus*. CCAH027/1 formed short chains (2–4 cells) of elliptical cells (8–10 μm) without spines and contained large, dark-green chloroplasts, indicating its relationship with *Scenedesmus intermedius*.

Among the reference strains, morphological features were characteristic of the *Desmodesmus* and *Scenedesmus* genera. NIES-94 and NIES-2280 were identified as *S. obliquus* due to their lack of spines and round to elliptical cells (5–12 μm). NIES-97 was identified as *D. serratus* because of its chained, cylindrical-to-elliptical cells (6–8 μm) bearing prominent spines. NIES-685 exhibited elliptical cells (8–12 μm) with short spines, consistent with *D. abundans*, while UTEX 2551 presented chained elliptical cells (8–10 μm , with 4–6 cells per chain) and short spines, suggesting similarity to *D. armatus*.

This morphological diversity highlights the distinction between *Desmodesmus*, which typically features chained cells with prominent spines, and *Scenedesmus*, characterized by smoother or variably spined cells. These findings enhance the taxonomy and biodiversity data on *Desmodesmus* in Vietnam and provide a foundation for future studies of their ecological and biotechnological potential in dynamic environments, such as the Can Gio Biosphere Reserve.

3.2 Molecular Analysis

Molecular analyses of the five studied strains used two genetic markers: ITS and 18S. Examination of the ITS region, which consists of 563 nucleotides, revealed identical sequences between strains CCAH020/1 and CCAH024/1, as well as between CCAH026/1 and CCAH027/1, indicating close genetic relationships. In contrast, strain CCAH016/2 exhibited greater genetic distances (0.1998–0.2040) than the other strains, suggesting distinct genetic divergence. For the 18S region, which is 1029 nucleotides in most strains but 1425 nucleotides in CCAH026/1 and CCAH027/1 due to a unique insertion, the pairwise distances were minimal (0.0009–0.0069), confirming high conservation. Identical sequences were again observed between CCAH020/1 and CCAH024/1, as well as between CCAH026/1 and CCAH027/1. The genetic distances between these groups and CCAH016/2 were slightly higher (0.0427–0.0457), reflecting greater variability than the distances within each group in the 18S region.

BLAST analyses provided additional taxonomic clarification. For strain CCAH016/2, the ITS sequences matched *D. armatus* with 98.93–99.10% similarity, while the 18S region showed 100% identity to the same species. For CCAH020/1, the ITS sequences had 98.64–100% similarity to *D. armatus*, while the 18S region indicated 99.9–100% similarity to either *D. armatus* or *D. communis*. In the case of CCAH026/1, the ITS sequences showed 99.92–100% similarity to *D. intermedius*, while the 18S region demonstrated high similarity to *Desmodesmus* sp. and *Scenedesmus* sp.

Overall, the ITS region provided sufficient variability to distinguish genetic groups, highlighting the divergence of CCAH016/2 from the other strains. Conversely, the highly conserved 18S region confirmed genus-level relationships but offered limited resolution at the species level. These findings underscore the complementary roles of morphological and molecular data in accurately identifying and classifying strains of *Desmodesmus* and *Scenedesmus*.

3.3 Phylogenetic Analysis Based on ITS Sequences

A phylogenetic analysis of the ITS region (Figure 2) was performed to investigate the evolutionary relationships among the studied strains and reference species. The alignment included 68 sequences over 652 nucleotide positions, revealing two primary clusters: Cluster A, which consists of *Desmodesmus*, and Cluster B, comprising *Scenedesmus*, *Tetradasmus*, and *Acutodesmus*. High bootstrap values supported both clusters. Within Cluster A, strain CCAH016/2 was placed in Subcluster A5, showing a close relationship with *D. armatus*, but displayed an early divergence pattern, suggesting potential local variation. Strains CCAH020/1 and CCAH024/1 formed a sister clade to *D. armatus* in subcluster A3, indicating that they are genetically distinct yet closely related variants. Meanwhile, strains CCAH026/1 and CCAH027/1 were grouped in subcluster A2, consistent with their classification as *D. intermedius*.

In Cluster B, reference strains NIES-94 and NIES-2280 clustered alongside *S. obliquus*, highlighting a clear evolutionary divergence between *Desmodesmus* and *Scenedesmus*. Notably, NIES-97, initially classified as *Scenedesmus* sp., was reassigned to *D. brasiliensis* in subcluster A1. Additionally, UTEX 2551, originally labelled *Scenedesmus armatus*, was realigned with *D. armatus* in subcluster A5.

These findings support the molecular identifications of the studied strains and clarify taxonomic discrepancies in the reference strains. Specifically, the ITS region has proven highly effective in resolving species-level relationships, illustrating the genetic diversity within *D. armatus* and the distinct evolutionary separation between *Desmodesmus* and related genera.

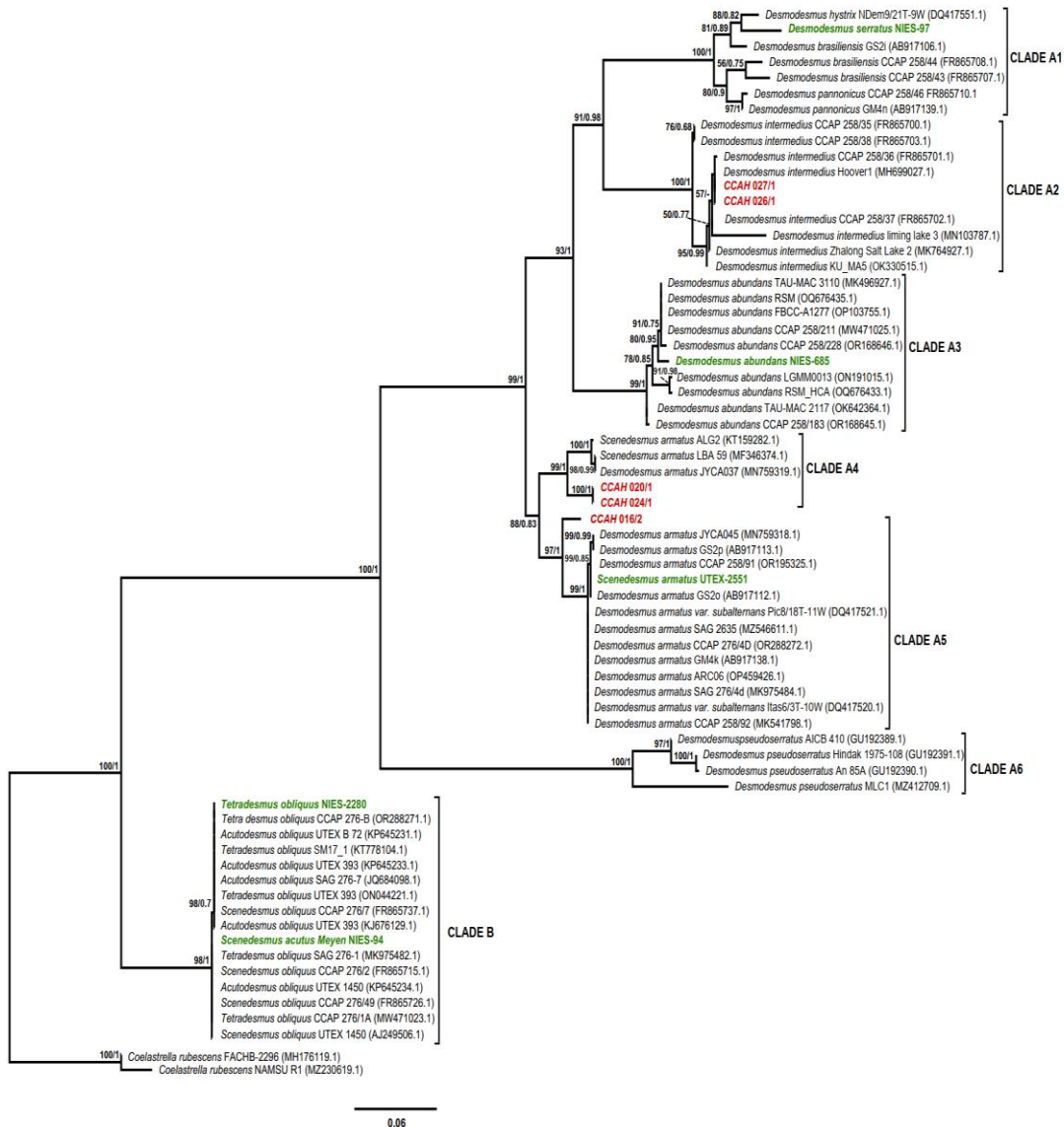


Figure 2 Phylogenetic Tree Based on the ITS Region, 68 ITS sequences, comprising 647 aligned positions, were analyzed to determine the evolutionary relationships among the studied and reference strains. Maximum Likelihood (ML) analysis was performed using IQ-TREE (SYM+G4) with 1,000 bootstrap replicates, while Bayesian Inference (BI) was conducted with MrBayes (SYM+G) for 100 million generations, accompanied by a 25% burn-in period. Branch support values, including ML bootstrap and BI posterior probabilities, are indicated at key nodes. The isolated strains are highlighted in red, and the reference strains are green. The analysis revealed two main clusters (*Desmodesmus* and *Scenedesmus*), with distinct subclusters reflecting genetic divergence within the *Desmodesmus* group.

3.4 Phylogenetic Analysis Based on 18S Sequences

Phylogenetic analysis of the 18S rRNA gene, based on 66 sequences aligned across 1,503 nucleotide positions, revealed two main clusters: Cluster C (*Desmodesmus*) and Cluster D (*Scenedesmus*) (Figure 3). Within Cluster C, the strain CCAH016/2 was grouped in Subcluster C1 alongside *D. armatus*, indicating its early divergence from other strains and highlighting its genetic distinctiveness. The strains CCAH020/1 and

CCAH024/1 clustered in C2, confirming their identification as variants of *D. armatus*. In contrast, CCAH026/1 and CCAH027/1 formed a separate group in C5, consistent with *D. intermedius*. Cluster D included reference strains NIES-94 and NIES-2280, aligning with *S. obliquus*. Strain NIES-97 was reassigned from *D. serratus* to *D. pannonicus*, while UTEX 2551 was originally identified as *Scenedesmus armatus* clustered with *D. armatus* in subcluster C3. Overall, this analysis confirmed the identities of the studied strains and highlighted the genetic variability within *D.*

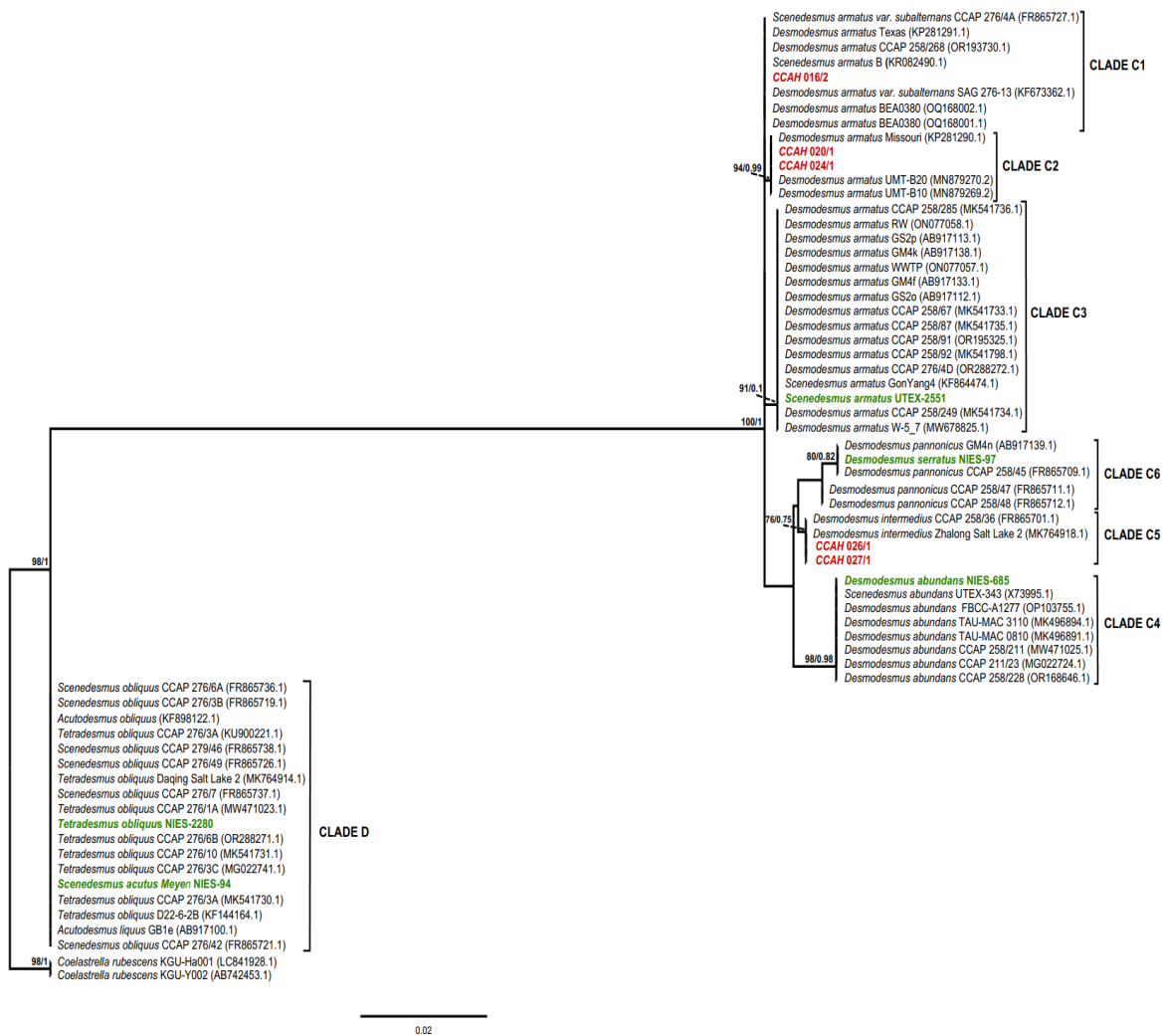


Figure 3 Phylogenetic Tree Based on the 18S Region, A total of 66 sequences, comprising 1503 aligned positions, were analyzed to assess their evolutionary relationships, maximum Likelihood (ML) analysis was conducted using IQ-TREE with the K2P+I model and included 1000 ultrafast bootstrap replicates, Bayesian Inference (BI) was performed in MrBayes using the K80+I model, running for 100 million generations with a 25% burn-in period, sampling every 1000 generations, branch support, indicated by ML bootstrap values and BI posterior probabilities, is shown at major nodes, isolated strains are represented in red, while reference strains are shown in green. The resulting tree reveals two main clusters: *Desmodesmus* (Cluster C) and *Scenedesmus* (Cluster D), with subclusters demonstrating genetic divergence within and between the genera.

armatus. However, due to the relatively conserved nature of the 18S rRNA gene, these findings emphasize the necessity for additional ITS data to achieve reliable species-level resolution.

Integrating morphological observations with molecular analyses enabled accurate identifications of the five studied strains. Morphologically, *D. armatus* was suggested for strains CCAH016/2, CCAH020/1, and CCAH024/1. In contrast, strains CCAH026/1 and CCAH027/1 were identified as either *S. obliquus* or *D. intermedius*. Molecular data confirmed these identifications, with ITS and 18S rRNA markers providing high-resolution, species-level classifications. Specifically, CCAH016/2 was

confirmed as *D. armatus*, while CCAH020/1 and CCAH024/1 were identified as closely related variants of *D. armatus*. Both CCAH026/1 and CCAH027/1 were consistently identified as *D. intermedius*. Although the 18S rRNA gene effectively established relationships at the genus level, the ITS marker offered superior resolution at the species level, particularly in distinguishing relationships at the species level, particularly in distinguishing CCAH016/2 from the other strains. Morphological inconsistencies, such as the initial misidentification of CCAH026/1 and CCAH027/1 as *Scenedesmus*, underscored the necessity for molecular validation. Table 1 summarizes these final identifications, integrating results from morphological, ITS, and 18S rRNA analyses. Overall, the combined approaches confirmed

Table 1 Summary of Morphological and Molecular Identification Results for Isolated and Reference Strains

Sample	Morphological ID	ITS Region ID	18S Region ID	Final Conclusion
CCAH016/2	<i>D. armatus</i>	<i>D. armatus</i>	<i>D. armatus</i>	<i>D. armatus</i>
CCAH020/1	<i>D. abundans</i>	<i>D. armatus</i>	<i>D. armatus</i>	<i>D. armatus</i>
CCAH024/1	<i>D. armatus</i>	<i>D. armatus</i>	<i>D. armatus</i>	<i>D. armatus</i>
CCAH026/1	<i>S. obliquus</i>	<i>D. intermedius</i>	<i>D. intermedius</i>	<i>D. intermedius</i>
CCAH027/1	<i>S. intermedius</i>	<i>D. intermedius</i>	<i>D. intermedius</i>	<i>D. intermedius</i>
NIES-94	<i>S. acutus</i>	<i>S. obliquus</i>	Similar to <i>S. acutus</i>	<i>S. obliquus</i>
NIES-97	<i>D. serratus</i>	<i>D. brasiliensis</i>	<i>D. serratus</i>	<i>D. serratus</i>
NIES-685	<i>D. abundans</i>	<i>D. abundans</i>	<i>D. abundans</i>	<i>D. abundans</i>
NIES-2280	<i>S. obliquus</i>	<i>S. obliquus</i>	<i>S. obliquus</i>	<i>S. obliquus</i>
UTEX 2551	<i>S. armatus</i>	<i>D. armatus</i>	<i>D. armatus</i>	<i>D. armatus</i>

the genetic variability within *D. armatus* and the distinct grouping of *D. intermedius*. These findings emphasize the importance of using both morphological and molecular methods for accurately identifying and classifying microalgae, especially in ecologically complex habitats like the Can Gio Biosphere Reserve.

4 Discussion

Combining morphological and molecular analyses was essential for achieving accurate species identification in this study. Although morphological traits, such as cell size, shape, and the presence of spines, initially suggested taxonomic affiliations for *Desmodesmus* and *Scenedesmus*, they ultimately proved insufficient for distinguishing closely related species (Mai et al. 2023; Nguyen et al. 2023). For instance, CCAH026/1 and CCAH027/1, initially identified morphologically as *Scenedesmus* due to their lack of spines, were reclassified as *D. intermedius* based on ITS and 18S data. These findings highlight the crucial role of molecular markers, particularly in ecologically complex and dynamic environments like the Can Gio Biosphere Reserve.

The ITS region was informative, providing high species-level resolution and serving as a common identifier for various algal taxa (Fawley and Fawley 2020; Kezlya et al. 2023; Nguyen et al. 2023). Its effectiveness is demonstrated by its ability to differentiate genetically distinct variants of *D. armatus*, such as CCAH016/2, which diverged early in phylogenetic trees, possibly indicating local adaptation or intraspecific genetic variation. Meanwhile, the highly conserved 18S region supported genus-level identifications and confirmed the relationships between *Desmodesmus* and *Scenedesmus*. Although some prior studies relied mainly on ITS for genus-level classification (Kezlya et al. 2023), the current findings highlight the complementary nature of using ITS and 18S to resolve species-level distinctions in *Desmodesmus*. Therefore, employing multiple molecular markers

alongside morphological data is critical, especially for complex or closely related taxa.

Phylogenetic analyses of the ITS and 18S regions also revealed distinct evolutionary boundaries between *Desmodesmus* and *Scenedesmus*, supporting the reclassification of several reference strains. For example, UTEX 2551, initially labelled as *S. armatus*, was reassigned to *D. armatus*, while NIES-97, formerly identified as *S. serratus*, was recognized as *D. pannonicus*. Such taxonomic revisions illustrate the reliability of molecular tools in addressing longstanding classification inconsistencies and emphasize the genetic diversity within *D. armatus* and *D. intermedius*. Identifying *D. intermedius* and genetically distinct variants of *D. armatus* in the Can Gio Biosphere Reserve points to the ecological adaptability of these species. Members of *Desmodesmus* are known to thrive in nutrient-rich, dynamic habitats (Abbas et al. 2024; Lin et al. 2020), a characteristic well suited to the transitional freshwater brackish conditions of Can Gio. The observed genetic variability within *Desmodesmus* could lead to the discovery of strains with specialized properties, such as enhanced lipid production for biofuels or strong stress tolerance for bioremediation. The co-occurrence of multiple *Desmodesmus* species further underscores Can Gio's role as a biodiversity hotspot, reinforcing the need for ongoing research and conservation initiatives. A key limitation of this study is the relatively small number of strains examined. Expanding the genetic dataset for *Desmodesmus* and *Scenedesmus* would refine taxonomic resolution and allow for broader phylogenetic comparisons. Future research should investigate how environmental parameters such as light intensity, nutrient availability, and salinity impact morphological plasticity to enhance traditional identification methods. Moreover, advanced sequencing approaches, such as whole-genome sequencing, could provide additional insights into these genera's evolutionary relationships and adaptive strategies. The implications for

biotechnology and conservation are significant. The documented genetic diversity of *Desmodesmus* strains suggests the potential for novel metabolic capabilities, ranging from increased lipid yields for biofuel production to pollutant degradation for environmental remediation. Additionally, the rich algal biodiversity within the Can Gio Biosphere Reserve highlights its importance as a natural resource, deserving of sustainable management and further investigation for both ecological and economic benefits.

Conclusion

This study integrated morphological and molecular approaches to accurately identify and characterize five microalgal strains isolated from the Can Gio Mangrove Biosphere Reserve. While the morphological observations provided preliminary insights, molecular markers, particularly the ITS region, were essential for achieving species-level identification. This confirmed the presence of *D. armatus* and *D. intermedius* and revealed genetic variability within *D. armatus*. Phylogenetic analyses clarified the evolutionary relationships within and between the genera *Desmodesmus* and *Scenedesmus*, addressing taxonomic ambiguities for several reference strains. These findings enhance our understanding of microalgal diversity in Vietnam and highlight the ecological importance of the Can Gio Biosphere Reserve as a habitat for diverse and resilient microalgae. Additionally, the study emphasizes the potential of *Desmodesmus* strains for future applications in biotechnology and environmental management. Ongoing research and conservation efforts are essential for fully realizing these valuable microorganisms' ecological and economic potential.

Acknowledgement of Funding

This research was funded by the Ho Chi Minh City Science and Technology Development Fund under Contract No. 18/2023/HD-QKHCN, focusing on genetic diversity and microalgal strain selection from the Can Gio Mangrove Biosphere Reserve. Financial support was crucial for advancing both the scientific understanding and practical applications of this study.

Conflicts of Interest

Authors declare that no conflicts exist.

Author contribution

Phuong-Nam Luu: collected samples, conducted laboratory studies, wrote reports and drafts for publication; Thanh-Cong Nguyen: collected and pre-processed experimental samples; Quoc-Dang Quan: compiled data, edited manuscript before publication; Duc-Hoan Huynh: performed preliminary morphological classification; Ngoc-Nam Trinh: adjusted the research and checked the research implementation process; Tuong-Lam Le-Nguyen: conducted laboratory studies, translated manuscript and grammar

edited; Hoang-Dung Tran: coordinated the entire research and edited the final manuscript.

References

- Abbas, M., Ni, L., & Du, C. (2024). Kinetic modelling and salinity tolerance in *Chlorella vulgaris* and *Desmodesmus communis* (Chlorophyta): insights into differential growth responses. *Aquatic Ecology*, 2024, 1-14. <https://doi.org/10.1007/s10452-024-10153-y>.
- Ajayi, O.O., Adekanmbi, A., Fagade, O. E., Dianda, M. (2022). Modified Methods for Quick and Safe Extraction of DNA from Microbiological Samples. *Journal of Microbiology and Pathology*, 6 (4), 1-5. DOI: 10.37421/2952-8119.6.158.
- Andersen, R. A., & Kawachi, L. (2005). Traditional microalgae isolation techniques. In R. A. Andersen (Ed.), *Algal culturing techniques*, (pp. 83-100). Elsevier Publication.
- DOST HCMC (2023). List of New Science and Technology Missions in the year 2023 using the Ho Chi Minh City budget provided by the DOST. Department of Science and Technology in Ho Chi Minh City. Retrieved from https://dost.hochiminhcity.gov.vn/documents/1961/Nhiem_vu_NCKH_moi_2023.xlsx (in Vietnamese).
- Fawley, M. W., & Fawley, K. P. (2020). Identification of Eukaryotic Microalgal Strains. *Journal of applied phycology*, 32(5), 2699–2709. <https://doi.org/10.1007/s10811-020-02190-5>
- Gouy, M., Guindon, S., & Gascuel, O. (2010). SeaView version 4: A multiplatform graphical user interface for sequence alignment and phylogenetic tree building. *Molecular Biology and Evolution*, 27(2), 221–224.
- Hegewald, E. (1979). Eine neue Unterteilung der Gattung *Scenedesmus* Meyen. *Nova Hedwigia*, 30, 343-376.
- Johnson, J.L., Fawley, M.W., & Fawley, K.P. (2007). The diversity of *Scenedesmus* and *Desmodesmus* (Chlorophyceae) in Itasca State Park, Minnesota, USA. *Phycologia*, 46(2), 214–229.
- Kessler, E., Schafer, M., Hummer, C., Kloboucek, A., & Huss, V.A. (1997). Physiological, Biochemical, and Molecular Characters for the Taxonomy of the Subgenera of *Scenedesmus* (Chlorococcales, Chlorophyta). *Botanica Acta*, 110(3), 244-250.
- Kezlya, E., Tseplik, N., & Kulikovskiy, M. (2023). Genetic Markers for Metabarcoding of Freshwater Microalgae: Review. *Biology*, 12, 1038.
- Khaw, Y. S., Khong, N. M. H., Shaharuddin, N. A., & Yusoff, F. M. (2020). A simple 18S rDNA approach for the identification of cultured eukaryotic microalgae with an emphasis on primers. *Journal of microbiological methods*, 172, 105890.

- Edgar, R. C. (2022) Muscle5: High-accuracy alignment ensembles enable unbiased assessments of sequence homology and phylogeny. *Nature Communications*, 13, 6968.
- Minh, B. Q., Schmidt, H. A., Chernomor, O., Schrempf, D., Woodhams, M. D., Von Haeseler, A., & Lanfear, R. (2020). IQ-TREE 2: new models and efficient methods for phylogenetic inference in the genomic era. *Molecular biology and evolution*, 37(5), 1530-1534.
- Lin, W. J., Ho, H. C., Chu, S. C., & Chou, J. Y. (2020). Effects of auxin derivatives on phenotypic plasticity and stress tolerance in five species of the green alga *Desmodesmus* (Chlorophyceae, Chlorophyta). *Peer J*, 8, e8623.
- Mai, X. C., Shen, C. R., Liu, C. L., Trinh, D. M., & Nguyen, M. L. (2023). "DNA signaturing" database construction for *Tetradesmus* species identification and phylogenetic relationships of Scenedesmus-like green microalgae (Scenedesmaceae, Chlorophyta). *Journal of Phycology*, 59(4), 775-784.
- Nguyen, M.L., Mai, X.C., Chu, N.H., Trinh, D.M., Liu, C.L., & Shen, C.R. (2023). DNA signaturing derived from the internal transcribed spacer 2 (ITS2): a novel tool for identifying *Desmodesmus* species (Scenedesmaceae, Chlorophyta). *Fottea Olomouc*, 23(1), 1-7.
- Pham, T. L. (2017). Environmental gradients regulate the spatio-temporal variability of phytoplankton assemblages in the Can Gio Mangrove Biosphere Reserve, Vietnam. *Ocean Science Journal*, 52, 537-547.
- Pham, T. L. (2019). Factors governing phytoplankton community in the Can Gio mangrove biosphere reserve, Vietnam. *Vietnam Journal of Marine Science and Technology*, 19(1), 67-78. <https://doi.org/10.15625/1859-3097/19/1/9179>
- Phung, B.T.M., Thanh, V.D., Chiem, N.H., & Nguyen, C.H. (2019). Diversity of benthic microalgal species in intensive rice cultivation, Cho Moi district, An Giang province Vietnam. *CTU Journal Of Science*, 55, 53-67.
- Rambaut, A. (2018). FigTree v1.4.4. Retrieved from <https://github.com/rambaut/figtree>
- Ronquist, F., Teslenko, M., Van Der Mark, P., Ayres, D. L., Darling, A., et al. (2012). MrBayes 3.2: efficient Bayesian phylogenetic inference and model choice across a large model space. *Systematic biology*, 61(3), 539-542.
- Sanger, F., Nicklen, S., & Coulson, A. R. (1977). DNA sequencing with chain-terminating inhibitors. *Proceedings of the National Academy of Sciences*, 74(12), 5463-5467.
- Shirora, A. (1966). *The plankton of south Viet Nam Fresh Water and Marine Plankton*. Overseas Technical Cooperation Agency Japan.
- White, T.J., Bruns, T.D., Lee, S.B., & Taylor, J.W.(1990). Amplification and direct sequencing of fungal ribosomal RNA genes for phylogenetics. In PCR Protocols: A Guide to Methods and App (pp. 315-322). *Academic Press, New York*.



Journal of Experimental Biology and Agricultural Sciences

<http://www.jebas.org>

ISSN No. 2320 – 8694

In-vitro antibacterial activity, Molecular docking, and MD Simulation Analysis of Phytoconstituents of *Nasturtium officinale*

Nitisha Negi^{1,2} , Sukirti Upadhyay¹ , Bhuwan Chandra Joshi² , Prinsa³ , Supriyo Saha^{4*} 

¹School of Pharmaceutical Sciences, IFTM University, Moradabad-244102, U.P., India

²Department of Pharmaceutical Sciences, Faculty of Technology, Sir J.C. Bose Technical Campus, Bhimtal, Kumaun University, Nainital-263136, Uttarakhand, India

³Department of Pharmaceutical Chemistry, Siddhartha Institute of Pharmacy, Near IT-Park, Sahastradhara Road, Dehradun-248001, Uttarakhand, India

⁴Department of Pharmaceutical Chemistry, Uttaranchal Institute of Pharmaceutical Sciences, Uttaranchal University, Dehradun-248007, Uttarakhand, India

Received – September 06, 2024; Revision – December 19, 2024; Accepted – December 30, 2024

Available Online – January 15, 2025

DOI: [http://dx.doi.org/10.18006/2024.12\(6\).838.849](http://dx.doi.org/10.18006/2024.12(6).838.849)

KEYWORDS

Nasturtium officinale
Staphylococcus aureus
 Antibacterial activity
 TLC fingerprint
 Molecular docking
 MD Simulation

ABSTRACT

Medicinal plants play a significant role in various traditional medicine systems worldwide. *Nasturtium officinale* W.T. Aiton, commonly known as ‘Halim,’ is a herbaceous perennial often used for its multiple health benefits. It serves as a depurative, diuretic, expectorant, hypoglycemic, hypolipidemic, and odontalgic agent and is utilized in the management of various ailments and disorders. This study aimed to evaluate the antimicrobial efficacy of different solvent extracts of *N. officinale* against *Staphylococcus aureus*. The antimicrobial activity was assessed through an in vitro assay using the disk diffusion method. Additionally, the minimum inhibitory concentration (MIC) was determined in comparison with standard reference compounds. Among the extracts tested, the chloroform extract of *N. officinale* (NOCE) exhibited the most potent inhibitory effect, demonstrating significant antibacterial activity. The high efficacy of the NOCE suggests that it may contain active phytoconstituents capable of targeting bacterial strains. Furthermore, molecular docking studies revealed that the phytoconstituents isorhamnetin, luteolin, and quercetin exhibited strong interactions with bacterial DNA gyrase. The molecular dynamics (MD) simulation of the best-docked compound, isorhamnetin, against bacterial DNA gyrase indicated that all parameters were within acceptable limits, and the compound effectively interacted with the receptor. These findings confirm that *N. officinale* possesses potential antibacterial activity, which may be attributed to the presence of isorhamnetin.

* Corresponding author

E-mail: supriyo9@gmail.com (Supriyo Saha)

Peer review under responsibility of Journal of Experimental Biology and Agricultural Sciences.

Production and Hosting by Horizon Publisher India [HPI]
 (<http://www.horizonpublisherindia.in/>).
 All rights reserved.

All the articles published by [Journal of Experimental Biology and Agricultural Sciences](#) are licensed under a [Creative Commons Attribution-NonCommercial 4.0 International License](#) Based on a work at www.jebas.org.



1 Introduction

Nasturtium officinale (*N. officinale*), also known as watercress, is a perennial herb that typically floats and creeps in water, commonly found near brooks, ditches, and ponds, especially in damp areas. This plant is native to Asia and North Africa and is rich in various vitamins, including vitamins A, C, and alpha-tocopherol (Shakerinasab et al. 2024). Additionally, *N. officinale* contains a high proportion of carotenoids, polyphenols, glucosinolates, and chlorophyll, according to previous reports. The herb is valued for both culinary and medicinal purposes. Traditionally, it has been used to treat respiratory conditions, diabetes, tuberculosis, and ailments affecting the kidneys, stomach, and liver (Negi et al. 2024a). Moreover, *N. officinale* is well-known for its anti-inflammatory, antimicrobial, antioxidant, anti-genotoxic, and cardioprotective properties (Klimek-Szczykutowicz et al. 2018). It is commonly used as a vegetable to enhance the flavor of various dishes and recipes (Mostafazadeh et al. 2022). This plant is composed of different phytochemicals, with phenolic compounds considered significant bioactive substances (Hibbert et al. 2023). The rich composition of *N. officinale* contributes to its nutritional and medicinal potential, making it a beneficial addition to a balanced diet (Klimek-Szczykutowicz et al. 2018). Various phytoconstituents exhibit different pharmacological activities, such as anti-inflammatory, anticancer, antioxidant, and antibacterial effects (Shakerinasab et al. 2024). The aerial parts of *N. officinale* are particularly notable for their medicinal significance, as they contain a higher concentration of phytoconstituents (Tabesh et al. 2022). These bioactive compounds act as a natural defense mechanism, aiding in the treatment of illnesses and protecting the human body from oxidative stress. Despite the numerous nutraceutical and ethnomedicinal uses of this plant, there have been no detailed analyses of molecular docking and molecular dynamics simulations related to its phytochemicals and pharmacological properties (Akbari Bazm et al. 2019). Consequently, the current study aims to evaluate the in vitro antibacterial properties of *N. officinale* and identify the phytoconstituents responsible for its antibacterial activity through computational studies.

2 Materials and Methods

2.1 Plant material

The plant material was collected from local areas in the Kumaun region of Bhimtal, Uttarakhand, India, at an altitude of 1,370 meters. It was authenticated by Dr. K. Madhava Chetty, Associate Professor in the Department of Botany at Sri Venkateshwara University, Tirupati, Andhra Pradesh, India (Voucher specimen no. 1243). The plant material was dried in the shade at a temperature of approximately 40°C, then ground into a coarse powder and stored in an airtight container.

2.2 Extraction

The dried plant material was coarsely powdered and then subjected to continuous hot extraction with petroleum ether using a Soxhlet apparatus (Jones and Kinghorn 2012). After extraction, the resulting extract was concentrated using a rotary evaporator and then dried in a vacuum desiccator. The concentrated extract was transferred to a previously weighed china dish (Priscilla et al. 2024). Following the defatting process, the remaining marc was air-dried and subsequently extracted again using chloroform, ethyl acetate, and ethanol. The percentage yields of the different extracts were calculated, and the prepared extracts were stored in a desiccator for further use (Zhao et al. 2014).

2.3 Phytochemical screening

For chemical testing, various solvent extracts of *N. officinale* were evaluated, including petroleum ether extract (NOPE), chloroform extract (NOCE), ethyl acetate extract (NOEE), and alcoholic extract (NOAE). The screening was conducted using standard methods established by previous researchers (Farnsworth 1966; Dubale et al. 2023; Joshi et al. 2024).

2.4 Antimicrobial Activity Assay

2.4.1 Inoculum preparation

Nutrient agar slants were used to store bacterial stock cultures of *S. aureus*, which were obtained from IMTECH Chandigarh at 4°C. A sterile loop was used to transfer cells from the stock cultures into test tubes containing nutrient agar media to prepare active cultures for testing. The inoculated test tubes were then incubated at 37°C for 24 hours under static conditions, which means without agitation, to promote bacterial growth. After incubation, the bacterial cultures were diluted with nutrient broth to achieve a standardized optical density corresponding to approximately 2.0×10^6 colony-forming units (CFU) per milliliter. This standardization ensured uniformity for subsequent tests (Biemer 1971).

2.4.2 Test for Antimicrobial Susceptibility and Determination of Minimum Inhibitory Concentration (MIC)

Prepared extracts were tested against *S. aureus* (MTCC 96) to evaluate their antibacterial activity using the disc diffusion method. Each bacterium was cultivated in 20 ml of sterilized nutritional agar medium within sterilized Petri plates. Once the medium solidified, the inoculum suspension was uniformly applied to the entire agar surface through a swabbing technique, spreading horizontally and then vertically to ensure even distribution of the bacteria across the agar (Ilieva et al. 2024; Kulathunga and Rubin 2017). Next, 6 mm filter paper discs infused with either 1 or 10 mg/ml solutions of the dry extract were placed on the agar plates (Huang et al. 2024). After allowing the extracts to diffuse for five

minutes, the plates were incubated at 37°C for 24 hours. Additionally, antibiotic discs (Hexa-G) were used as positive controls. The inhibition zones were measured using a Hi-media zone measuring ruler, and all experiments were conducted in duplicate (Hemeg et al. 2020; Dubale et al. 2023). To determine the minimum inhibitory concentration (MIC), fresh cultures were prepared in 5 ml nutrient broth tubes. Different concentrations (3, 5, 10, 15, 20, and 25 µg/ml) of the potent extract were added to the tubes (Hemeg et al. 2020). A 0.1 ml sample of the freshly cultured bacteria was introduced into each tube. Negative controls comprised tubes without any treatment, while positive controls contained tubes inoculated with bacteria and clindamycin. After incubating the tubes at 37°C, the cultures were examined at 24 and 48 hours. The minimum concentration that resulted in the least bacterial growth was recorded as the MIC (Barnes et al. 2023).

2.5 Thin Layer Chromatographic Profile (TLC) for Standardization

Thin Layer Chromatography (TLC) is often used as a reference or cross-validation technique for more complex analytical methods such as High-Performance Liquid Chromatography (HPLC) or Gas Chromatography (GC). It acts as a simple confirmatory test in laboratories, helping to identify compounds by comparing their retention factor (Rf) to that of standards. In this experiment, TLC was performed using a mixture of toluene and ethyl acetate as the eluent in an 8:2 ratio. The Camag Linomat 5 automated TLC applicator was employed to apply the sample in 6 mm-wide bands at a nitrogen flow rate of 90 nL/s. After the sample was applied, the plate was allowed to dry before being placed in a chromatographic tank, which was promptly covered. Once the solvent front reached the top of the plate, it was removed, labeled, and left to dry. Finally, the plate was examined under UV light at wavelengths of 254 nm and 366 nm (Mayasari et al. 2022).

2.6 Molecular Docking Studies of *N. officinale* Phytoconstituents

2.6.1 Collection of Phytoconstituents of *N. officinale* and Preparation of Ligand Molecules

After conducting an extensive literature search, it was found that *N. officinale* contains a variety of phytoconstituents, including apigenin, beta-carotene, caffeic acid, carvacrol, eucalyptol, gallic acid, isorhamnetin, kaempferol, lutein, luteolin, pulegone, quercetin, and rutin. A molecular docking study related to drug-receptor interactions indicates that biological activity is directly linked to these interactions. The significance of molecular docking lies in its ability to identify the phytoconstituents with the highest likelihood of effectiveness against microbes, suggesting potential antimicrobial activity. All molecular structures were prepared using Avogadro software and

AutoDock Tools (version 1.5.6). The ligand molecules were saved in .PDBQT format (Hanwell et al. 2012).

2.6.2 Procurement and Preparation of Receptor

In this manuscript, we focused on a topoisomerase ATPase inhibitor, specifically targeting DNA gyrase. This enzyme is selective for bacterial species, and its inhibition disrupts DNA synthesis, ultimately leading to cell death. The receptor discussed, identified as 3TTZ, is from *S. aureus*. The receptor comprises two chains, each consisting of 198 amino acids. Within the receptor, the complexed ligand, 2-[(3S,4R)-4-[(3,4-dichloro-5-methyl-1H-pyrrol-2-yl)carbonyl]amino]-3-fluoropiperidin-1-yl]-1,3-thiazole-5-carboxylic acid (07N), was detected (Sherer et al. 2011). This complexed ligand interacts with amino acids ARG 144, PRO 87, ASN 54, ILE 86, ILE 51, ILE 175, VAL 79, ARG 84, and GLU 58 (Paggi et al. 2024). After removing the complex ligand and water molecules, we added polar hydrogens and Gasteiger charges (Bisht et al. 2024). Finally, the receptor was saved in .PDBQT format. The grid box dimensions for the 3TTZ receptor were 7.751, 5.062, and 20.947 along the x, y, and z axes, respectively (Goodsell et al. 2021).

2.7 Molecular Dynamic (MD) Simulation of Selected Phytoconstituents of *N. officinale*

Molecular docking of the phytoconstituents revealed that isorhamnetin achieved the highest molecular docking score. While molecular docking is performed in a vacuum, molecular dynamics (MD) simulation is carried out in a realistic simulated environment using the best-docked isorhamnetin. Through MD simulation, the atomic-level interaction patterns of isorhamnetin with the receptor were identified in the presence of solvent, ions, temperature, pressure, and a CHARMM force field environment. TIP3 water was used for the simulation, conducted with GROMACS version 20.1 software. Prior to the simulation, the ligand-receptor complex underwent energy minimization (Kim et al. 2017). During the preparation of isorhamnetin for the simulation study, 8,701 water molecules and 11 sodium ions were incorporated into the system. The graphical representation of the simulation trajectories was created using Qtgrace software (Lemkul 2018).

2.8 Statistical Analysis

The results were presented as Mean ± SEM (Standard Error Mean) with n=3. The data were analyzed using ANOVA in GraphPad Prism 6.

3 Results and Discussion

3.1 Phytochemical Screening and Extraction Yield

The percentage yields (% w/w) of the extracts NOPE, NOEE, NOCE, and NOAE from *N. officinale* were found to be 20.37%,

Table 1 Phytochemical analysis of different extracts of *N. officinale*

Phytochemical	Tests (Dubale et al. 2023)	NOPE	NOCE	NOEE	NOAE
Amino acids	Ninhydrin test	+	-	-	+
Proteins	Biuret test	+	-	-	+
	Millon's test	+	-	-	+
Carbohydrates	Molisch's test	-	-	-	+
	Fehling's test	-	-	-	+
Steroids	Salkowski Reaction	-	-	-	-
Alkaloids	Mayer's test	-	+	-	-
	Dragendroff's test	-	+	-	-
	Hager's test	-	+	-	-
Glycosides	Legal	-	-	-	+
	Keller kiliani Test	-	-	-	+
	Borntrager's test	-	-	-	-
	Foam test	-	-	-	+
Flavonoids	Shinoda's test	-	+	+	-
Phenolic compounds	FeCl ₃ test	-	+	+	+
	Lead acetate solution test	-	+	+	+

+ positive; - negative

20.90%, 21.72%, and 18.69%, respectively. These findings indicate that the plant extracts contain various compounds, including proteins, alkaloids, tannins, polyphenols, flavanones, and reducing sugars (Ercan and Doğru 2023) (Table 1). *N. officinale* is a semi-aquatic plant known for its diverse array of chemical compounds and numerous therapeutic activities. The percentage yield of these extracts depends on the specific parts of the plant used, the species, and the solvent employed for extraction. Different parts of the plant contain varying concentrations of secondary metabolites, which contribute to many of the plant's beneficial properties. This suggests that *N. officinale* may serve as a valuable source of medicinal compounds, highlighting its significance in therapeutic applications. Furthermore, several solvent extracts were analyzed for specific chemical components, such as alkaloids, glycosides, flavonoids, and tannins, through phytochemical analysis. The anticancer potential of the phytochemicals found in *N. officinale* has been documented in previous studies (Negi et al. 2024b).

3.2 Antimicrobial activity of *N. officinale*

The antimicrobial properties of different extracts of *N. officinale* against *S. aureus* were evaluated using a disk diffusion method. The zones of inhibition for each tested extract were measured and are shown in Figure 1. Among the extracts evaluated, the NOCE exhibited the highest zones of inhibition, measuring 14.0

mm at a concentration of 1 mg/ml and 24.0 mm at 10 mg/ml. The NOEE demonstrated the second-highest zones of inhibition, with 12.0 mm at 1 mg/ml and 16.0 mm at 10 mg/ml. These results are comparable to the inhibition zones of the standard antibiotic clindamycin, which showed 16.0 mm and 29.0 mm at the same respective concentrations. All *N. officinale* extracts displayed observable zones of inhibition against *S. aureus* (Figure 2). Notably, NOCE exhibited the best antimicrobial activity across various dilutions during 4 hours (Tittikpina et al. 2018; Necedo-Mena et al. 2020). Additionally, the minimum inhibitory concentration (MIC) of the most effective extract (NOCE) was determined using different concentrations (3, 5, 10, 15, 20, 25 µg/ml). The potent MIC observed was 3 µg/ml, as shown in Table 2 (Mabhiza et al. 2016; Nair et al. 2017; Farhadi et al. 2019). Since the MIC represents the lowest concentration at which inhibition occurs, only this concentration is reported. Though inhibition was observed at 3 µg/mL, it is evident that higher concentrations also contributed to significant zones of inhibition. The findings of this investigation are consistent with the work of Jang et al. (2010), which indicated that *N. officinale* has a greater inhibitory effect on gram-positive bacteria, such as *S. aureus*, compared to gram-negative bacteria. Supporting evidence can also be found in the studies by Butnariu and Bostan (2011) and Mahdavi et al. (2019), which suggested that the antimicrobial activity of *N. officinale* has a bacteriostatic effect on *S. aureus*.

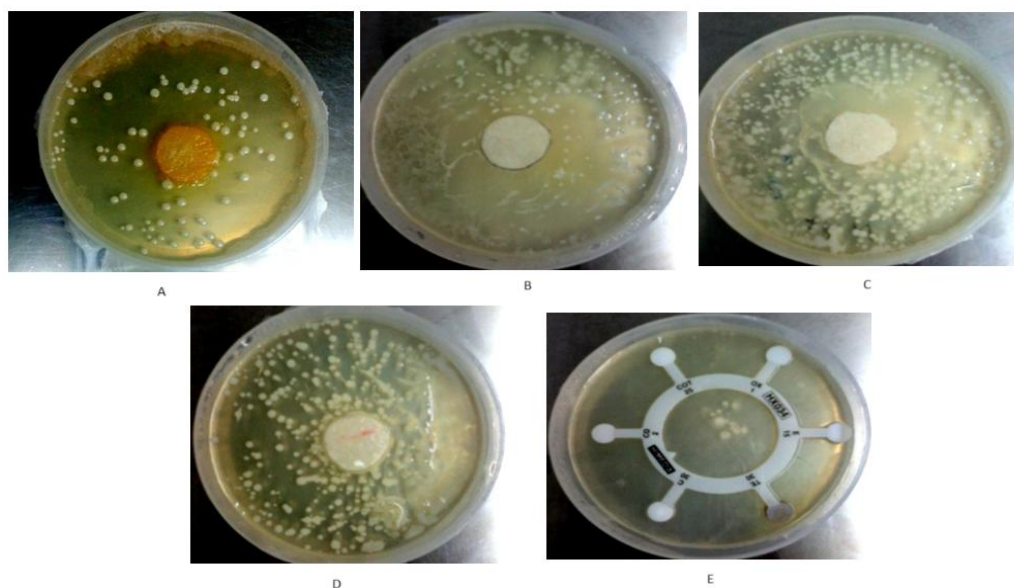


Figure 1 Antimicrobial activity of the different extracts of *N. officinale*; where A: NOCE, B: NOEE, C: NOAE, D: NOPE, E: HEXA G PLUS- 11 against *S. aureus*

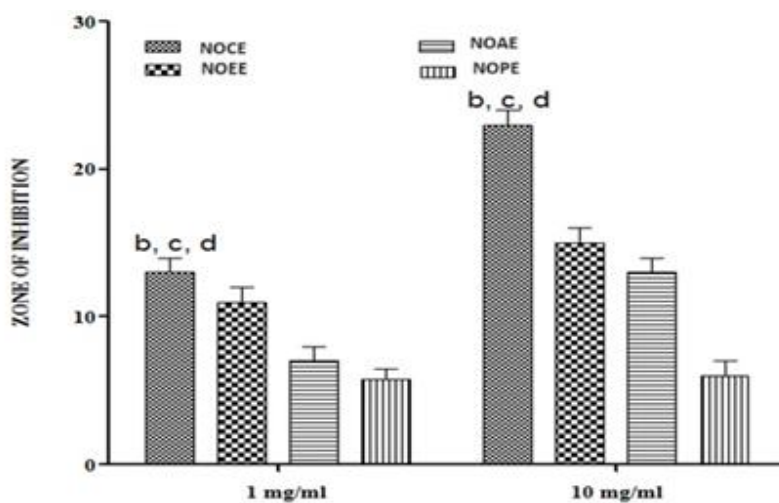


Figure 2 Bar diagram representing the antimicrobial activity of the different extracts of *N. officinale*. All the values expressed are Mean \pm SD (n=3), ^a P < 0.05 Vs NOCE; ^{b, c, d} P < 0.05 Vs NOEE, NOAE, NOPE.

Table 2 Result of zone of inhibition of potent antimicrobial extract (NOCE) at different concentrations

Extract	Concentration (μ g/ml)	Zone of inhibition (mm)
NOCE	3	26.0
	5	NA
	10	NA
	15	NA
	20	NA
	25	NA

NA: Not Applicable

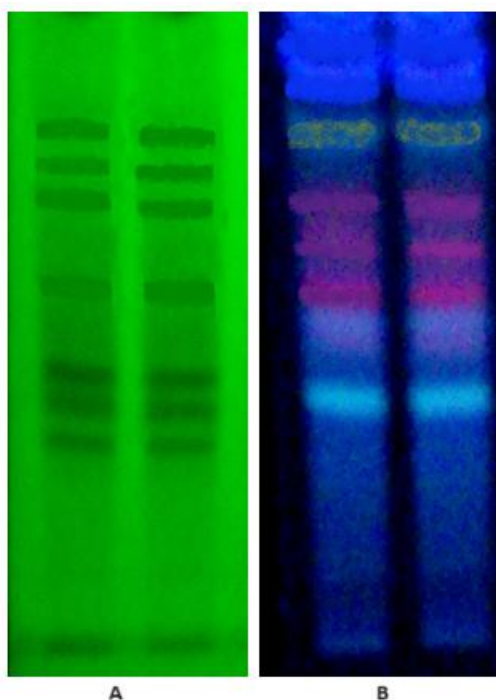


Figure 3 TLC fingerprinting profile of NOCE extract, where (A) under short and (B) long UV, respectively.

Table 3 Detail of the TLC profile of active extract (NOCE) under short UV (254 nm) and long UV (366 nm)

Extract	Rf in long UV (366 nm)	Rf in short UV (254 nm)
NOCE	0.20, 0.25, 0.31, 0.38, 0.44, 0.51, 0.61, 0.69, 0.73, 0.81	0.21, 0.28, 0.35, 0.40, 0.46, 0.51, 0.65, 0.82, 0.89

3.3 TLC fingerprinting profiles of NOCE

In the TLC (Thin Layer Chromatography) fingerprint profile, NOCE exhibited 10 spots in the long UV range and 9 spots in the short UV range, as shown in Figure 3 and Table 3. This study confirmed that NOCE contains a variety of phytoconstituents, indicated by the multiple spots observed at different RF (retention factor) values. Among the tested classes of compounds, the phytochemicals exhibiting the most significant color changes were flavonoids, alkaloids, and phenols (Ayele et al. 2015). The resulting chromatogram can serve as additional information for the identification and standardization of *N. officinale*.

3.4 Molecular Docking Analysis Data

The molecular docking study is focused on understanding drug-receptor interactions in a vacuum, which is directly related to the biological activity of drugs. The significance of this study lies in identifying which phytoconstituent has the highest probability of targeting microbes and contributing to antimicrobial activity. The molecular docking scores of the phytoconstituents from *N. officinale* against bacterial DNA gyrase ranged from -5.0 kcal/mol to -8.5 kcal/mol (Table 4). The top three phytoconstituents with the

highest docking scores were isorhamnetin (-8.5 kcal/mol), luteolin (-8.1 kcal/mol), and quercetin (-7.8 kcal/mol) (Kar et al. 2024). Isorhamnetin interacted with the receptor through several amino acids: ASN 54 (3.60 Å between interaction carbon atoms), ILE 86 (3.28 Å), and THR 173 (3.98 Å) via hydrophobic interactions. Additionally, it formed hydrogen bonds with ASN 54, GLU 58, ARG 84, GLY 85, and THR 173 (Yu et al. 2024). Luteolin interacted with the receptor through ILE 51 (3.68 Å), ILE 86 (3.58 Å), ILE 102 (3.33 Å), and LEU 103 (3.65 Å) via hydrophobic interactions. Its hydrogen bonds were formed with ASN 54, ARG 84, and GLY 85 (Rigby 2024). Quercetin interacted with the DNA gyrase receptor through ILE 51 (3.92 Å), ILE 86 (3.93 Å), THR 173 (3.74 Å), and ILE 175 (3.63 Å) via hydrophobic interactions. It also formed hydrogen bonds with GLU 58, ASP 81, and ARG 84 (Figure 4). The common amino acid residues shared between isorhamnetin and the complexed ligand include ASN 54, ILE 86, GLU 58, and ARG 84 (Lokhande et al. 2022). Luteolin and the complexed ligand share ILE 51, ILE 86, ASN 54, and ARG 84. Similarly, quercetin and the complexed ligand share ILE 51, ILE 86, GLU 58, and ARG 84. The docking scores and the active site residues suggest that isorhamnetin, luteolin, and quercetin interact effectively with the bacterial gyrase receptor, potentially contributing to their antibacterial activity (Notarte et al. 2023).

Table 4 Molecular docking interaction data of selected phytoconstituents of *N. officinale* against bacterial DNA gyrase

S. N.	Name	Dock score (kcal/mol)	Hydrophobic Interactions	Hydrogen bond Interactions
1.	Apigenin	-7.7	ASN 54 (distance between interaction carbon atoms 3.57 Å), ILE 86 (distance between interaction carbon atoms 3.31 Å), THR 173 (distance between interaction carbon atoms 3.84 Å).	ASN 54 (distance H-A 2.93 Å, D-A 3.64 Å), ARG84 (distance H-A 3.11 Å, D-A 3.67 Å), GLY 85 (distance H-A 2.66 Å, D-A 3.27Å), THR 173 (distance H-A 3.53 Å, D-A 3.87Å).
2.	Beta carotene	-6.9	GLU 68 (distance between interaction carbon atoms 3.54 Å), LYS 78 (distance between interaction carbon atoms 3.85 Å), THR 80 (distance between interaction carbon atoms 3.56 Å), TYR 141 (distance between interaction carbon atoms 3.76 Å), VAL 165 (distance between interaction carbon atoms 3.52 Å), VAL 174 (distance between interaction carbon atoms 3.58 Å).	None
3.	Caffeic acid	-6.7	ASN 54 (distance between interaction carbon atoms 3.45 Å), ILE 86 (distance between interaction carbon atoms 3.48 Å), THR 173 (distance between interaction carbon atoms 3.66 Å).	ASN 54 (distance H-A 3.58 Å, D-A 4.07Å), SER 55 (distance H-A 3.31 Å, D-A 3.74Å), GLU 58 (distance H-A 2.65 Å, D-A 2.94Å), ARG 84 (distance H-A 3.36 Å, D-A 3.90Å), GLY 85 (distance H-A 1.90 Å, D-A 2.83Å).
4.	Carvacrol	-5.9	ILE 51 (distance between interaction carbon atoms 3.60 Å), ASN 54 (distance between interaction carbon atoms 3.51 Å), ILE 86 (distance between interaction carbon atoms 3.66 Å), ILE 175 (distance between interaction carbon atoms 3.77 Å).	THR 173 (distance H-A 3.27Å, D-A 3.81Å).
5.	Eucalyptol	-5.0	ASN 54 (distance between interaction carbon atoms 3.66 Å), GLU 58 (distance between interaction carbon atoms 3.68 Å), ILE 102 (distance between interaction carbon atoms 3.77 Å).	None
6.	Gallic acid	-6.0	ARG 84 (salt bridge distance 4.19 Å).	ASN 54 (distance H-A 2.38 Å, D-A 3.23 Å), ASP 81 (distance H-A 2.17Å, D-A 3.06Å), GLY 85 (distance H-A 3.03 Å, D-A 3.87Å), ARG 144 (distance H-A 3.48 Å, D-A 4.08 Å).
7.	Isorhamnetin	-8.5	ASN 54 (distance between interaction carbon atoms 3.60 Å), ILE 86 (distance between interaction carbon atoms 3.28 Å), THR 173 (distance between interaction carbon atoms 3.98 Å).	ASN 54 (distance H-A 2.89 Å, D-A 3.63Å), GLU 58 (distance H-A 2.29Å, D-A 2.79Å), ARG 84 (distance H-A 3.18Å, D-A 3.74Å), GLY 85 (distance H-A 2.18Å, D-A 2.92Å), THR 173 (distance H-A 2.28 Å, D-A 2.79Å).
8.	Kaemferol	-7.5	ILE 51 (distance between interaction carbon atoms 3.74 Å), ILE 86 (distance between interaction carbon atoms 3.78 Å), THR 173 (distance between interaction carbon atoms 3.73 Å), ILE 175 (distance between interaction carbon atoms 3.48 Å).	None
9.	Lutein	-5.0	GLN 66 (distance between interaction carbon atoms 3.83 Å), GLU 68 (distance between interaction carbon atoms 3.64 Å), THR 80 (distance between interaction carbon atoms 3.64 Å), ILE 148 (distance between interaction carbon atoms 2.99 Å), LYS 163 (distance between interaction carbon atoms 3.68 Å), VAL 165 (distance between interaction carbon atoms 3.52 Å), VAL 174 (distance between interaction carbon atoms 3.36 Å).	GLN (distance H-A 1.74 Å, D-A 2.71Å), LYS 163 (distance H-A 3.32 Å, D-A 3.71Å), GLN 210 (distance H-A 3.18 Å, D-A 4.08Å).
10.	Luteolin	-8.1	ILE 51 (distance between interaction carbon atoms 3.68 Å), ILE 86 (distance between interaction carbon atoms 3.58 Å), ILE 102 (distance between interaction carbon atoms 3.33 Å), LEU 103 (distance between interaction carbon atoms 3.65 Å).	ASN 54 (distance H-A 3.41 Å, D-A 4.08Å), ARG 84 (distance H-A 2.90 Å, D-A 3.30Å), GLY 85 (distance H-A 2.33 Å, D-A 2.81Å).

S. N.	Name	Dock score (kcal/mol)	Hydrophobic Interactions	Hydrogen bond Interactions
11	Pulegone	-5.6	ASN 54 (distance between interaction carbon atoms 3.34 Å), ILE 86 (distance between interaction carbon atoms 3.58 Å), THR 173 (distance between interaction carbon atoms 3.76 Å), ILE 175 (distance between interaction carbon atoms 3.88 Å).	THR 173 (distance H-A 2.39 Å, D-A 3.15Å).
12	Quercetin	-7.8	ILE 51 (distance between interaction carbon atoms 3.92 Å), ILE 86 (distance between interaction carbon atoms 3.93 Å), THR 173 (distance between interaction carbon atoms 3.74 Å), ILE 175 (distance between interaction carbon atoms 3.63 Å).	GLU 58 (distance H-A 2.35 Å, D-A 2.95Å), ASP 81 (distance H-A 2.15 Å, D-A 3.00Å), ARG 84 (distance H-A 2.75 Å, D-A 3.27Å).
13	Rutin	-7.5	GLN 66 (distance between interaction carbon atoms 3.35 Å), THR 80 (distance between interaction carbon atoms 3.22 Å), TYR 141 (distance between interaction carbon atoms 3.72 Å), VAL 174 (distance between interaction carbon atoms 3.69 Å), LYS 170 (distance between interaction carbon atoms 3.51 Å).	ILE 67 (distance H-A 2.36 Å, D-A 2.84 Å), GLU 68 (distance H-A 2.56 Å, D-A 2.94 Å), HIS 143 (distance H-A 2.23 Å, D-A 3.06Å), LYS 170 (distance H-A 2.48 Å, D-A 2.90Å), GLN 210 (distance H-A 2.39Å, D-A 3.37Å), THR 212 (distance H-A 3.16 Å, D-A 3.81Å),

H-A= Distance between hydrogen and acceptor atom (Å); D-A= Distance between donor and acceptor atom (Å)

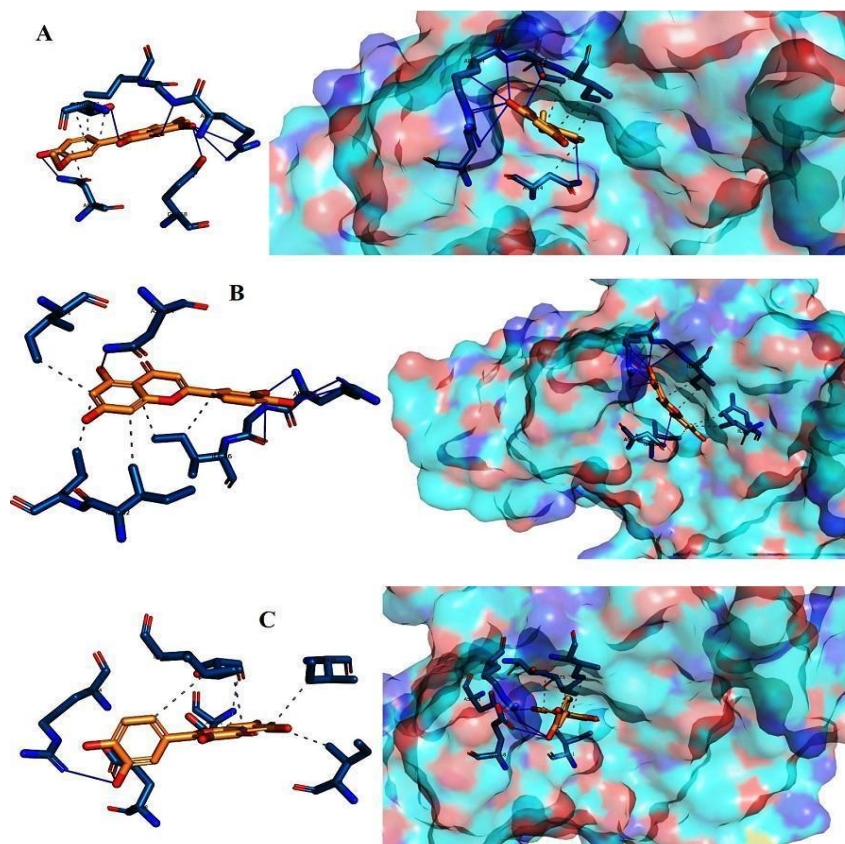


Figure 4 Molecular docking interactions data of Isorhamnetin (A), Luteolin (B), and Quercetin (C) against DNA gyrase

3.5 MD Simulation Analysis Data of Isorhamnetin with DNA gyrase

Molecular docking studies of the phytoconstituents indicated that isorhamnetin has the highest probability of interacting with bacterial gyrase, suggesting that the antibacterial activity of NOCE

may be attributed to isorhamnetin. Previous research has established the antibacterial effectiveness of isorhamnetin against *S. aureus* (Jiang et al. 2016; Suarez et al. 2021). As previously mentioned, molecular docking is conducted in a vacuum, whereas molecular dynamics (MD) simulations are performed in a realistically simulated environment using the best-docked structure

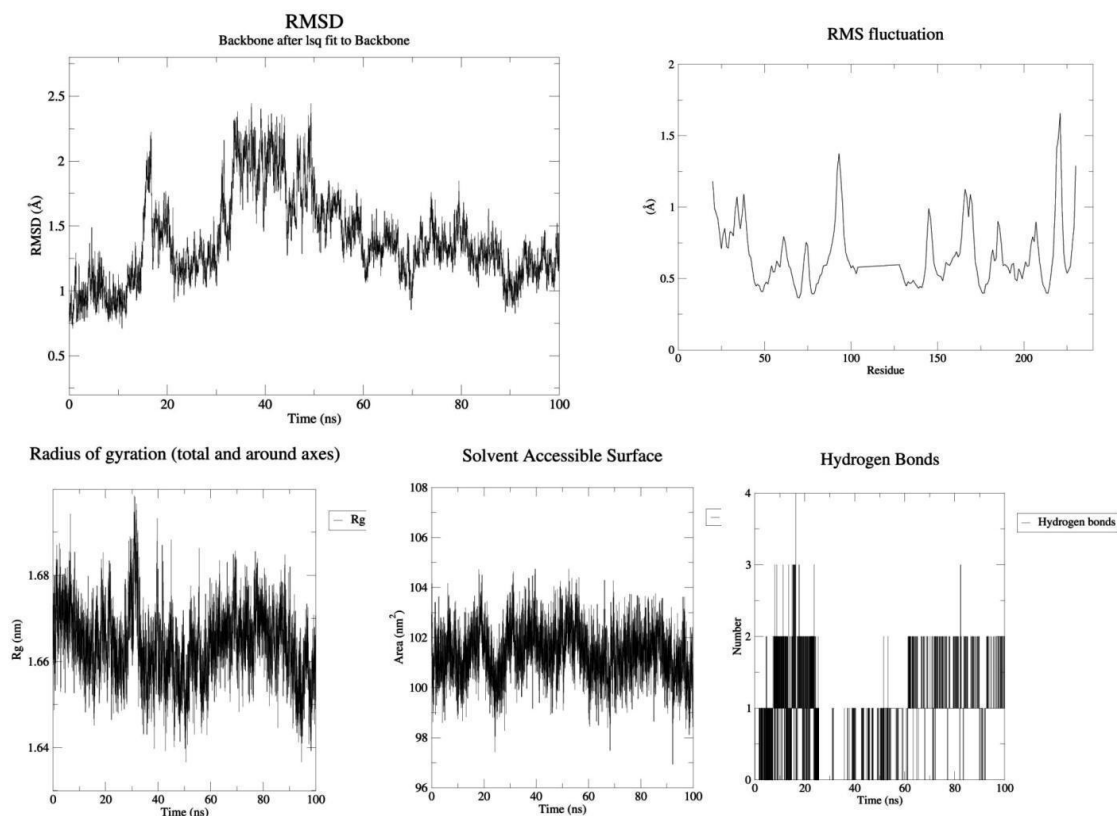


Figure 5 MD Simulation data of isorhamnetin interacted with DNA gyrase.

of isorhamnetin (Khan et al. 2024). Through MD simulations, we were able to identify atomic-level interaction patterns of isorhamnetin within the receptor in the presence of solvent, ions, temperature, pressure, and a CHARMM force field environment. The average root mean square deviation (RMSD) value for isorhamnetin was found to be 1.38 Å. The RMSD stabilized at 60 ns of simulation time, and during the simulation, both molecules maintained a similar interaction pattern (Dos Santos Nascimento and de Moura 2024). The root mean square fluctuation (RMSF) diagram indicated that fluctuations were generally limited to 1.6 Å during most of the simulation runs (Prinsa et al. 2024). Notably, isorhamnetin displayed considerable fluctuations near the 221st amino acid residue within the receptor and exhibited maximum fluctuations during the simulation, likely because these residues were either absent during interactions or located at a distance from the active site (Kushwaha et al. 2021). The average radius of gyration for the isorhamnetin complex with the receptor was measured at 1.66 nm, demonstrating a constant value without any significant fluctuation. The radius of gyration values remained within a lower range, indicating that the molecules were consistently contained within the receptor's active site throughout the simulation (Jalali et al. 2024). Additionally, the average solvent-accessible surface area (SASA) of the isorhamnetin complex with the bacterial DNA gyrase receptor was 101.38 nm²

(Zhong et al. 2024). The SASA values confirmed the formation of stable structures during the simulation (Kumari and Kumar 2014). The hydrogen bond interaction map confirmed that isorhamnetin remained complexed with the bacterial DNA gyrase receptor throughout the simulation, and the ligand molecule maintained contact with the active site amino acid residues, indicating a strong relationship between the ligand and receptor (Figure 5) (Kawsar et al. 2024).

Conclusion

In this manuscript, we demonstrate that the chloroform extract of *N. officinale* exhibits the most potent antibacterial activity. Molecular docking studies of the phytoconstituents of *N. officinale* against bacterial DNA gyrase indicated that isorhamnetin achieved the highest docking score. Molecular dynamics (MD) simulations of isorhamnetin interacting with bacterial DNA gyrase showed that all parameters remained within acceptable limits. These findings confirm that *N. officinale* has significant antibacterial properties, likely attributed to isorhamnetin.

Abbreviations

Nasturtium officinale petroleum ether extract (NOPE), *Nasturtium officinale* chloroform extract (NOCE), *Nasturtium officinale* ethyl

acetate extract (NOEE), and *Nasturtium officinale* alcoholic extract (NOAE)

Conflict of Interest

Nil

Ethical Clearance

No animal model was used in the study; therefore, ethical clearance is not required.

References

Akbari Bazm, M., Khazaei, M., Khazaei, F., & Naseri, L. (2019). *Nasturtium Officinale* L. hydroalcoholic extract improved oxymetholone-induced oxidative injury in mouse testis and sperm parameters. *Andrologia*, 51(7), e13294.

Ayele, T. T., Regasa, M. B., & Delesa, D. A. (2015). Antibacterial and antagonistic activity of selected traditional medicinal plants and herbs from East Wollega Zone against clinical isolated human pathogens. *Science, Technology and Arts Research Journal*, 4(3), 175-179.

Barnes, V.L., Heithoff, D.M., Mahan, S.P., House, J.K., & Mahan, M.J. (2023). Antimicrobial susceptibility testing to evaluate minimum inhibitory concentration values of clinically relevant antibiotics. *STAR Protocols*, 4(3), 102512.

Biemer, J.J. (1971). Antimicrobial susceptibility testing by the Kirby-Bauer disc diffusion method. *Annals of Clinical & Laboratory Science*, 3(2), 135-40.

Bisht, A., Tewari, D., Kumar, S., & Chandra, S. (2024). Network pharmacology, molecular docking, and molecular dynamics simulation to elucidate the mechanism of anti-aging action of *Tinospora cordifolia*. *Molecular Diversity*, 28(3), 1743-1763.

Butnariu, M., & Bostan, C. (2011). Antimicrobial and anti-inflammatory activities of the volatile oil compounds from *Tropaeolum majus* L.(*Nasturtium*). *African journal of biotechnology*, 10(31), 5900-5909.

Dos Santos Nascimento, I.J., & de Moura, R.O. (2024). Molecular Dynamics Simulations in Drug Discovery. *Mini Reviews in Medicinal Chemistry*, 24(11), 1061-1062.

Dubale, S., Kebebe, D., Zeynudin, A., Abdissa, N., & Suleman, S. (2023). Phytochemical screening and antimicrobial activity evaluation of selected medicinal plants in Ethiopia. *Journal of experimental pharmacology*, 15, 51-62.

Ercan, L., & Dođru, M. (2023). Determination of phenolic compounds in *Nasturtium Officinale* by LC-MS/MS using

different extraction methods and different solvents. *International Journal of Chemistry and Technology*, 7(2), 124-130.

Farhadi, F., Khameneh, B., Iranshahi, M., & Iranshahi, M. (2019). Antibacterial activity of flavonoids and their structure-activity relationship: An update review. *Phytotherapy Research*, 33(1), 13-40.

Farnsworth, N. R. (1966). Biological and phytochemical screening of plants. *Journal of Pharmaceutical Sciences*, 55(3), 225-276.

Goodsell D.S., Sanner M.F., Olson A.J., & Forli S. (2021). The AutoDock suite at 30. *Protein Science*, 30(1) 31-43.

Hanwell M.D., Curtis D.E., Lonie, D.C., Vandermeersch T., Zurek E., & Hutchison G.R. (2012). Avogadro: an advanced semantic chemical editor, visualization, and analysis platform. *Journal of Cheminformatics*, 4, 17.

Hemeg, H.A., Moussa, I.M., Ibrahim, S., Dawoud, T.M., Alhaji, J.H., et al. (2020). Antimicrobial effect of different herbal plant extracts against different microbial population. *Saudi Journal of Biological Sciences*, 27(12), 3221-3227.

Hibbert, L.E., Qian, Y., Smith, H.K., Milner, S., Katz, E., Kliebenstein, D.J., & Taylor, G. (2023). Making watercress (*Nasturtium officinale*) cropping sustainable: genomic insights into enhanced phosphorus use efficiency in an aquatic crop. *Frontiers in Plant Science*, 14, 1279823.

Huang, H., Zhang, Y., Du, Q., Zheng, C., Jin, C., & Li, S. (2024). Synthesis and Antimicrobial Activity of 3-Alkylidene-2-Indolone Derivatives. *Molecules*, 29(22), 5384.

Ilieva, Y., Zaharieva, M.M., Najdenski, H., & Kroumov, A.D. (2024). Antimicrobial Activity of *Arthrospira* (Former *Spirulina*) and *Dunaliella* Related to Recognized Antimicrobial Bioactive Compounds. *International Journal of Molecular Sciences*, 25(10), 5548.

Jalali, P., Nowroozi, A., Moradi, S., & Shahlaei, M. (2024). Exploration of lipid bilayer mechanical properties using molecular dynamics simulation. *Archives of Biochemistry and Biophysics*, 761, 110151.

Jang, M., Hong, E., & Kim, G. H. (2010). Evaluation of antibacterial activity of 3-butenyl, 4-pentenyl, 2-phenylethyl, and benzyl isothiocyanate in *Brassica vegetables*. *Journal of food science*, 75(7), M412-M416.

Jiang, L., Li, H., Wang, L., Song, Z., Shi, L., Li, W., Deng, X., & Wang, J. (2016). Isorhamnetin Attenuates *Staphylococcus aureus* Induced Lung Cell Injury by Inhibiting Alpha-Hemolysin Expression. *Journal of Microbiology and Biotechnology*, 26(3), 596-602.

- Jones, W.P., & Kinghorn, A.D. (2012). Extraction of plant secondary metabolites. *Methods in Molecular Biology*, 864, 341-66.
- Joshi, B.C., Juyal, V., & Sah, A.N. (2024). First Report on Pharmacognostic, Phytochemical Investigation and In vitro Radical Scavenging Efficacy of *Premna barbata* from Western Himalaya. *Proceedings of the National Academy of Sciences, India Section B: Biological Sciences*, 94, 685–695.
- Kar, P., Oriola, A.O., & Oyediji, A.O. (2024). Molecular Docking Approach for Biological Interaction of Green Synthesized Nanoparticles. *Molecules*, 29(11), 2428.
- Kawsar, S.M.A., Hossain, M.A., Saha, S., Abdallah, E.M., Bhat, A.R., Ahmed, S., Jamalis, J., & Ozeki Y. (2024). Nucleoside-Based Drug Target with General Antimicrobial Screening and Specific Computational Studies against SARS-CoV-2 Main Protease. *Chemistry Select*, 9, e202304774.
- Khan, M.I., Pathania, S., Al-Rabia, M.W., Ethayathulla, A.S., Khan, M.I., et al. (2024). MolDy: molecular dynamics simulation made easy. *Bioinformatics*, 40(6), btae313.
- Kim S., Lee J., Jo S., Brooks C.L. 3rd., Lee H.S., & Im W. (2017). CHARMM-GUI ligand reader and modeler for CHARMM force field generation of small molecules. *Journal of Computational Chemistry*, 38(21) 1879-1886.
- Klimek-Szczykutowicz, M., Szopa, A., & Ekiert, H. (2018). Chemical composition, traditional and professional use in medicine, application in environmental protection, position in food and cosmetics industries, and biotechnological studies of *Nasturtium officinale* (watercress) - a review. *Fitoterapia*, 129, 283-292.
- Kulathunga, D.G., & Rubin, J.E. (2017). A review of the current state of antimicrobial susceptibility test methods for Brachyspira. *Canadian Journal of Microbiology*, 63(6), 465-474.
- Kumari, R., & Kumar, R. (2014). Open Source Drug Discovery Consortium, Lynn A. g_mmpbsa-A GROMACS Tool for High-Throughput MM-PBSA Calculations. *Journal of Chemical Information and Modeling*, 54(7), 1951–1962.
- Kushwaha, P.P., Singh, A.K., Bansal, T., Yadav, A., Prajapati, K.S., Mohd, S., & Kumar, S. (2021). Identification of Natural Inhibitors Against SARSCoV-2 Drugable Targets Using Molecular Docking, Molecular Dynamics Simulation, and MM-PBSA Approach. *Frontier Cellular Infection Microbiology*, 11, 730288.
- Lemkul, J.A. (2018). From Proteins to Perturbed Hamiltonians: A Suite of Tutorials for the GROMACS-2018 Molecular Simulation Package, v1.0^o. *Living Journal of Computational Molecular Science*, 1(1), 5068.
- Lokhande, K., Nawani, N.K., Venkateswara, S., & Pawar, S. (2022). Biflavonoids from *Rhus succedanea* as probable natural inhibitors against SARS-CoV-2: a molecular docking and molecular dynamics approach. *Journal of Biomolecular Structure Dynamics*, 40(10), 4376-4388.
- Mabhiza, D., Chitemerere, T., & Mukanganyama, S. (2016). Antibacterial properties of alkaloid extracts from *Callistemon citrinus* and *Vernonia adoensis* against *Staphylococcus aureus* and *Pseudomonas aeruginosa*. *International Journal of Medicinal Chemistry*, 2016(1), 6304163.
- Mahdavi, S., Kheyrollahi, M., Sheikhlouei, H., & Isazadeh, A. (2019). Antibacterial and antioxidant activities of essential oil on food borne bacteria. *The Open Microbiology Journal*, 13(1), 81-85.
- Mayasari, D., Murti, Y.B., Pratiwi, S.U.T., Sudarsono, S., Hanna, G., & Hamann, M.T. (2022). TLC-Based Fingerprinting Analysis of the Geographical Variation of *Melastoma malabathricum* in Inland and Archipelago Regions: A Rapid and Easy-to-Use Tool for Field Metabolomics Studies. *Journal of Natural Products*, 85(1), 292-300.
- Mostafazadeh, M., Sadeghi, H., Sadeghi, H., Zarezade, V., Hadinia, A., & Panahi Kokhdan, E. (2022). Further evidence to support acute and chronic anti-inflammatory effects of *Nasturtium officinale*. *Research in Pharmaceutical Sciences*, 17(3), 305-314.
- Nair, J.J., Wilhelm, A., Bonnet, S.L., & van Staden, J. (2017). Antibacterial constituents of the plant family Amaryllidaceae. *Bioorganic & Medicinal Chemistry Letters*, 27(22), 4943-4951.
- Negi, N., Upadhyay, S., & Rana, M. (2024a). An Overview on Phytopharmacological Perspectives of a Potential plant Species: *Nasturtium officinale*. *Systematic Reviews in Pharmacy*, 15(8), 257-262.
- Negi, N., Upadhyay, S., & Rana, M. (2024b). Investigation of in vitro anticancer potential and phytochemical screening of *Nasturtium officinale*. *International Journal of Zoological Investigations*, 10(1), 537-544.
- Nocedo-Mena, D., Garza-González, E., González-Ferrara, M., & Del Rayo Camacho-Corona, M. (2020). Antibacterial Activity of *Cissus incisa* Extracts against Multidrug- Resistant Bacteria. *Current Topics in Medicinal Chemistry*, 20(4), 318-323.
- Notarte, K.I.R., Quimque, M.T.J., Macaranas, I.T., Khan, A., Pastrana, A.M., et al. (2023). Attenuation of Lipopolysaccharide-induced Inflammatory Responses through Inhibition of the NF-κB

- Pathway and the Increased NRF2 Level by a Flavonol-enriched n-Butanol Fraction from *Uvaria alba*. *ACS Omega*, 8(6), 5377–5392.
- Paggi, J.M., Pandit, A., & Dror, R.O. (2024). The Art and Science of Molecular Docking. *Annual Review of Biochemistry*, 93(1), 389-410.
- Prinsa., Saha, S., Bulbul, M.Z.H., Ozeki, Y., Alamri, M.A., & Kawsar, S.M.A. (2024). Flavonoids as potential KRAS inhibitors: DFT, molecular docking, molecular dynamics simulation and ADMET analyses. *Journal of Asian Natural Product Research*, 26(8), 955-992.
- Priscilla, K., Sharma, V., Gautam, A., Gupta, P., Dagar, R., Kishore, V., & Kumar, R. (2024). Carotenoid Extraction from Plant Tissues. *Methods in Molecular Biology*, 2788, 3-18.
- Rigby, S.P. (2024). Uses of Molecular Docking Simulations in Elucidating Synergistic, Additive, and/or Multi-Target (SAM) Effects of Herbal Medicines. *Molecules*, 29(22), 5406.
- Shakerinasab, N., Mottaghipisheh, J., Eftekhari, M., Sadeghi, H., Bazarganipour, F., Abbasi, R., Doustimotlagh, A.H. & Iriti, M. (2024). The hydroalcoholic extract of *Nasturtium officinale* reduces oxidative stress markers and increases total antioxidant capacity in patients with asthma. *Journal of Ethnopharmacology*, 318, 116862.
- Sherer, B.A., Hull, K., Green, O., Basarab, G., Hauck, S., et al. (2011). Pyrrolamide DNA gyrase inhibitors: Optimization of antibacterial activity and efficacy. *Bioorganic & medicinal chemistry letters*, 21(24), 7416-7420.
- Suarez, A.F.L., Tirador, A.D.G., Villorente, Z.M., Bagarinao, C.F., Sollesta, J.V.N., et al. (2021). The Isorhamnetin-Containing Fraction of Philippine Honey Produced by the Stingless Bee *Tetragonula biroi* Is an Antibiotic against Multidrug-Resistant *Staphylococcus aureus*. *Molecules*, 26(6), 1688.
- Tabesh, M., Sh, M.E., Etemadi, M., Naddaf, F., Heidari, F., & Alizargar, J. (2022). The antibacterial activity of *Nasturtium officinale* extract on common oral pathogenic bacteria. *Nigerian Journal of Clinical Practice*, 25(9), 1466-1475.
- Tittikpina, N.K., Nana, F., Fontanay, S., Philippot, S., Batawila, K., et al. (2018). Antibacterial activity and cytotoxicity of *Pterocarpus erinaceus* Poir extracts, fractions and isolated compounds. *Journal of Ethnopharmacology*, 212, 200-207.
- Yu, D., Li, H., Liu, Y., Yang, X., Yang, W., Fu, Y., Zuo, Y.A., & Huang, X. (2024). Application of the molecular dynamics simulation GROMACS in food science. *Food Research International*, 190, 114653.
- Zhao, S., Baik, O.D., Choi, Y.J., & Kim, S.M. (2014). Pretreatments for the efficient extraction of bioactive compounds from plant-based biomaterials. *Critical Reviews in Food Science and Nutrition*, 54(10), 1283-97.
- Zhong, H., Liu, H., & Liu, H. (2024). Molecular Mechanism of Tau Misfolding and Aggregation: Insights from Molecular Dynamics Simulation. *Current Medicinal Chemistry*, 31(20), 2855-2871.



Journal of Experimental Biology and Agricultural Sciences

<http://www.jebas.org>

ISSN No. 2320 – 8694

Gene action of yield and its contributing traits in wide-compatible elite rice (*Oryza sativa* L.) restorer lines

Kalpataru Nanda¹ , Nihar Ranjan Chakraborty¹ , Debarchana Jena²,
Diptibala Rout², Ramlakhan Verma^{2*} 

¹Visva-Bharati, Santiniketan, West Bengal, India

²ICAR-National Rice Research Institute, Cuttack, Odisha, India

Received – September 06, 2024; Revision – December 10, 2024; Accepted – December 27, 2024

Available Online – January 15, 2025

DOI: [http://dx.doi.org/10.18006/2024.12\(6\).850.859](http://dx.doi.org/10.18006/2024.12(6).850.859)

KEYWORDS

Wide compatibility
Generation mean analysis
Scaling test
Gene action
Genetic effects

ABSTRACT

Profiling the genetic architecture of quantitative traits, such as yield and its contributing factors, is essential for successful breeding programs. Understanding the genetic components of variation is key to maximizing genetic gains with precision in crop improvement programs. This study evaluated the genetics of yield and its contributing/attributing traits through generation mean analysis in six generations (P1, P2, F1, F2, B1, and B2) of crosses involving elite rice restorer lines. Results from the scaling tests indicated that epistatic interactions were present for all traits examined, except for effective tillers per plant in crosses I (CR 22-153-1 x Lemont) and II (CR 22-153-1 x CR 22-1-5-1). The six-parameter analysis showed a combination of additive, dominance, and epistatic gene effects, although their contributions varied. In both crosses, the additive or fixable variance was consistently lower than the non-additive variance for most yield-related traits. Among the genetic effects, the dominance effect and the dominance × dominance effect were significantly higher for most traits in both crosses. However, the values of these effects often exhibited opposite signs for different traits, underscoring the importance of duplicate epistasis in the inheritance and expression of these traits. The predominance of dominance, interaction effects, and duplicate epistasis across all studied traits and crosses limits the potential for early generation selection. Nevertheless, bi-parental matings between superior segregants may help disrupt undesirable linkages and produce favorable segregants with an accumulation of positive alleles for trait development.

* Corresponding author

E-mail: ram.pantvarsity@gmail.com (Ramlakhan Verma)

Peer review under responsibility of Journal of Experimental Biology and Agricultural Sciences.

Production and Hosting by Horizon Publisher India [HPI]
(<http://www.horizonpublisherindia.in/>).
All rights reserved.

All the articles published by [Journal of Experimental Biology and Agricultural Sciences](#) are licensed under a [Creative Commons Attribution-NonCommercial 4.0 International License](#) Based on a work at www.jebas.org.



1 Introduction

Rice is a crucial cereal crop that is grown and consumed on every inhabited continent. It serves as a staple food in Asia, where 90% of its production and consumption occurs (Kumar et al. 2023). However, as the global population continues to grow and arable land decreases due to rapid urbanization, there is an urgent need to increase rice production on the limited land available. Enhancing rice yields through genetic improvements is the most feasible solution for rice breeders to meet this demand. Although India has the largest area of rice cultivation in the world, it still lags behind China in terms of production due to lower productivity and the slow adoption of hybrid varieties (Das et al. 2022a). Since high-yielding intraspecific rice varieties and hybrids of the *indica* × *indica* type have reached a yield plateau in India, breeders must seek new sources of genetic variability, such as inter-subspecific hybrids (*indica* × *japonica*), to boost productivity (Revathi 2015). Studies demonstrate that *indica* × *japonica* hybrids exhibit high heterotic potential (Ikehashi and Araki 1984), but their commercial production is limited by partial hybrid sterility, a post-zygotic issue (Sundaram et al. 2010). This sterility is controlled by a tri-allelic system, known as the wide compatibility (WC) system, located at the S5 locus on chromosome 6. The system includes three alleles: 'S5i' *indica* allele, 'S5j' *japonica* allele, and 'S5n' neutral allele (Chen et al. 2008). The interaction between the S5i and S5j alleles leads to partial hybrid sterility in *indica* × *japonica* hybrids. However, when 'S5n' allele interacts with either the S5i or S5j allele, it produces fully fertile embryos (Sundaram et al. 2010). Therefore, wide-compatible varieties (WCVs) that carry 'S5n' allele (WC gene) can act as a bridge to facilitate *indica-japonica* hybridization (Kallugudi et al. 2022). When developing a breeding strategy, breeders need to understand the type and extent of gene action that influences yield-contributing traits and overall yield. Generation mean analysis is the most commonly used, straightforward, and reliable biometrical method for studying gene action in quantitative traits such as yield and its associated characters or traits (Lenka et al. 2021). First-degree statistics are used to estimate mean (m), additive (d), dominance (h), and epistatic gene effects, including additive × additive (i), additive × dominance (j), and dominance × dominance (l) effects (Mather and Jinks 1971). Understanding the nature and extent of gene action for yield and its contributing traits is crucial for selecting superior parents and evaluating the effectiveness of selection among progeny with varying genetic values (Kumar et al. 2019). The six-parameter model (Hayman 1958) of generation mean analysis is the only biometrical approach that can estimate the nature and magnitude of all types of epistatic gene effects (i, j, and l), which is essential for accurately maximizing genetic gain. The objective of this study was to use generation mean analysis to assess gene action on yield and associated traits in two distinct crosses between elite restorer lines of rice.

2 Materials and Methods

This study involved two crosses: CR 22-153-1 × Lemont and CR 22-153-1 × CR 22-1-5-1. These were developed using three elite restorer lines (Table 1), selected for their superior combining ability. The experiment took place during the Rabi season of 2022-23 at the ICAR-National Rice Research Institute in Cuttack. A Compact Family Block Design was employed, where six generations were grown: Parent 1 (P1), Parent 2 (P2), the first filial generation (F1), the second filial generation (F2), and backcross generations B1 and B2. Each generation was cultivated in three replications following a standard package of agricultural practices. Observations were recorded for fifteen quantitative traits: days to 50% flowering (DFF), days to maturity (DM), plant height (PH), flag leaf length (FLL), flag leaf width (FLW), effective tillers per plant (ETPP), panicle length (PL), grains per panicle (GPP), chaff per panicle (CPP), spikelet fertility percentage (SF%), test weight (TW), yield per plant (YPP), grain length (GL), grain breadth (GB), and the grain length-breadth ratio (GL/B ratio). For observations, 20 plants from both parental and F1 populations, 30 plants from the backcross (BC) generations, and 40 plants from the F2 population were randomly selected. To evaluate the adequacy of the additive-dominance model, the mean and variance of all six generations across replications were analyzed using the scaling tests (A, B, C, and D) proposed by Mather (1949). When epistatic interactions were detected, Hayman's six-parameter model (1958) was used to estimate gene effects and their interactions. In the absence of epistasis, the three-parameter model (Jinks and Jones 1958) was employed to assess gene effects alone. Scaling Tests formulas as devised by (Mather 1949):

$$\begin{aligned} A &= 2\bar{B}_1 + \bar{P}_1 - \bar{F}_1 & V_A &= 4V_{B_1} + V_{P_1} + V_{F_1} \\ B &= 2\bar{B}_2 - \bar{P}_2 - \bar{F}_1 & V_B &= 4V_{B_2} + V_{P_2} + V_{F_1} \\ C &= 4\bar{F}_2 - 2\bar{F}_1 - \bar{P}_1 - \bar{P}_2 & V_C &= 16V_{F_2} + 4V_{F_1} + V_{P_1} + V_{P_2} \\ D &= 2\bar{F}_2 - \bar{B}_1 - \bar{B}_2 & V_D &= 4V_{F_2} + V_{B_1} + V_{B_2} \end{aligned}$$

Standard errors and 't'-values of the above scales are calculated as follows:

$$\begin{aligned} \text{S.E.}_A &= (V_A)^{1/2} & t_A &= A / \text{S.E.}_A \\ \text{S.E.}_B &= (V_B)^{1/2} & t_B &= B / \text{S.E.}_B \\ \text{S.E.}_C &= (V_C)^{1/2} & t_C &= C / \text{S.E.}_C \\ \text{S.E.}_D &= (V_D)^{1/2} & t_D &= D / \text{S.E.}_D \end{aligned}$$

Where A, B, C, and D are the scales and $\bar{P}_1, \bar{P}_2, \bar{F}_1, \bar{F}_2, \bar{B}_1,$ and \bar{B}_2 are generated means of the trait. $V_A, V_B, V_C,$ and V_D are the corresponding variances of the scales and $V_{\bar{P}_1}, V_{\bar{P}_2}, V_{\bar{F}_1}, V_{\bar{F}_2}, V_{\bar{B}_1},$ and $V_{\bar{B}_2}$ are the variance of the sample means of respective generation.

Table 1 List of the elite restorer lines used in the study

S. N.	Parent genotype	Important feature
1	CR 22-153-1	Interspecific (<i>indica x japonica</i>) elite restorer –carrying fertility restorer genes, <i>Rf3</i> and <i>Rf4</i> but lacking <i>wc</i> gene
2	CR 22-1-5-1	Interspecific (<i>indica x japonica</i>) elite restorer possessing, <i>Rf3</i> , <i>Rf4</i> , and <i>WC</i> gene
3	Lemont	A <i>japonica</i> variety possessing <i>Rf3</i> , <i>Rf4</i> , and <i>WC</i> gene

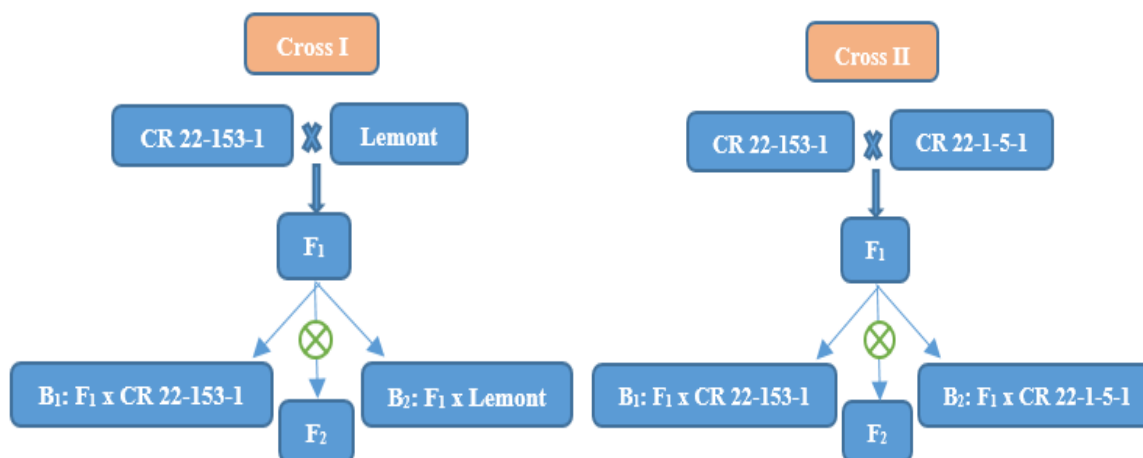


Figure 1 Two crosses made between the elite restorer lines

Estimation of the gene effects using the six-parameter model suggested by Hayman (1958) and Jinks and Jones (1958):

$$m = \bar{F}_2$$

$$d = \bar{B}_1 - \bar{B}_2$$

$$h = \bar{F}_1 - 4\bar{F}_2 - (\frac{1}{2})\bar{P}_1 - (\frac{1}{2})\bar{P}_2 + 2\bar{B}_1 + 2\bar{B}_2$$

$$i = 2\bar{B}_1 + 2\bar{B}_2 - 4\bar{F}_2$$

$$j = \bar{B}_1 - (\frac{1}{2})\bar{P}_1 + (\frac{1}{2})\bar{P}_2 - \bar{B}_2$$

$$l = \bar{P}_1 + \bar{P}_2 + 2\bar{F}_1 + 4\bar{F}_2 - 4\bar{B}_1 - 4\bar{B}_2$$

Where,

m = mean effect

d = additive effect

h = dominance effect

i = additive \times additive type of gene interaction

j = additive \times dominance type of gene interaction

l = dominance \times dominance type of gene interaction

\bar{P}_1 , \bar{P}_2 , \bar{F}_1 , \bar{F}_2 , \bar{B}_1 , and \bar{B}_2 are the mean values of different generations.

Variances of the above gene effects are:

$$V_m = V_{\bar{F}_2}$$

$$V_d = V_{\bar{B}_1} + V_{\bar{B}_2}$$

$$V_h = V_{\bar{F}_1} + 16V_{\bar{F}_2} + (\frac{1}{4})V_{\bar{P}_1} + (\frac{1}{4})V_{\bar{P}_2} + 4V_{\bar{B}_1} + 4V_{\bar{B}_2}$$

$$V_i = 4V_{\bar{B}_1} + 4V_{\bar{B}_2} + 16V_{\bar{F}_2}$$

$$V_j = V_{\bar{B}_1} + (\frac{1}{4})V_{\bar{P}_1} + (\frac{1}{4})V_{\bar{P}_2} + V_{\bar{B}_2}$$

$$V_l = V_{\bar{P}_1} + V_{\bar{P}_2} + 4V_{\bar{F}_1} + 16V_{\bar{F}_2} + 16V_{\bar{B}_1} + 16V_{\bar{B}_2}$$

Where, $V_{\bar{P}_1}$, $V_{\bar{P}_2}$, $V_{\bar{F}_1}$, $V_{\bar{F}_2}$, $V_{\bar{B}_1}$, and $V_{\bar{B}_2}$ are the mean variances of the sample mean of the respective generation

Standard errors and 't'-values for the above gene effects are calculated as follows:

$$S.E. m = (V_m)^{1/2} \quad t_m = m / S.E. m$$

$$S.E. d = (V_d)^{1/2} \quad t_d = d / S.E. d$$

$$S.E. h = (V_h)^{1/2} \quad t_h = h / S.E. h$$

$$S.E. i = (V_i)^{1/2} \quad t_i = i / S.E. i$$

$$S.E. j = (V_j)^{1/2} \quad t_j = j / S.E. j$$

$$S.E. l = (V_l)^{1/2} \quad t_l = l / S.E. l$$

3 Results and Discussion

The suitability of the additive-dominance model for estimating genetic components was evaluated using the A, B, C, and D scales. The results from both crosses showed significance for at least one

of the scales for nearly every trait examined, except for the effective tillers per plant in Cross I (CR 22-153-1 x Lemont) and Cross II (CR 22-153-1 x CR 22-1-5-1). The scaling test results (Table 2) indicated significant epistatic interactions for nearly all traits, rendering the additive-dominance model ineffective for

Table 2 Scaling test of fifteen quantitative traits for Cross-I and Cross-II

Traits	Cross	A ± SeA	B ± SeB	C ± SeC	D ± SeD
DFF	I	-7.60±0.82**	0.9±0.95	-3.40±1.46*	1.65±0.77*
	II	2.00±1.02*	4.25±1.07**	-12.25±2.00**	-9.25±0.82**
DM	I	-7.15±1.08**	0.2±1.06	-3.35±1.63*	1.8±0.90*
	II	2.55±1.11*	5.55±1.07**	-10.00±2.16**	-9.05±0.94**
PH	I	6.50±3.08*	0.23±3.06	-11.26±5.45*	-8.99±2.84**
	II	2.05±3.34	4.2±3.30	-11.85±6.00*	-9.05±2.98**
FLL	I	-18.70±2.41**	-1.35±1.64	-27.55±2.81**	-3.75±1.64*
	II	4.71±2.13*	4.15±1.93*	-7.20±3.40*	-8.03±1.61**
FLW	I	-0.30±0.10**	-0.18±0.09*	-1.09±0.15**	-0.31±0.07**
	II	-0.19±0.09*	-0.20±0.08*	-0.65±0.13**	-0.13±0.06*
ETPP	I	-0.6±0.53	-1.15±0.62	-2.25±1.31	-0.25±0.65
	II	0.5±0.45	0.05±0.50	-0.25±1.13	-0.4±0.55
PL	I	-4.20±1.25**	-5.39±0.70**	-10.27±1.20**	-0.34±0.82
	II	4.39±1.03**	2.38±1.20*	0.7±2.19	-3.03±1.24**
GPP	I	-48.50±18.37**	-17.85±16.08	-305.85 ± 22.66**	-119.75±10.42**
	II	65.50±29.86*	-23.1±24.59	-133.40±66.74*	-87.9±36.98**
CPP	I	6.25±22.01	43.70±14.13**	-33.55±13.74*	-41.75±13.20**
	II	59.15±19.84**	121.85±15.82**	289.20±43.47**	54.1±23.64*
SF%	I	-3.54±4.51	-14.45±4.43**	-17.40±4.10**	0.3±3.45
	II	-8.26±3.74*	-29.66±3.17**	-65.61±7.14**	-13.84±3.92**
TW	I	0.1±0.07	0.26±0.08**	0.29±0.18	0.02±0.09
	II	0.20±0.08**	-0.14±0.07*	-0.26±0.13*	-0.16±0.07*
YPP	I	-2.07±1.37	3.26±0.96**	-11.05±1.78**	-6.12±0.82**
	II	4.24±1.51**	-1.51±1.11	-8.20±3.45*	-5.47±1.70**
GL	I	0.775±0.227**	0.571±0.236*	1.296±0.429**	-0.025±0.23
	II	-0.05±0.160	0.748±0.315*	-0.392±0.511	-0.54±0.27*
GB	I	-0.191±0.068**	0.221±0.054**	-0.314± 0.116**	-0.17±0.06**
	II	0.276±0.100**	-0.256±0.129*	0.758±0.174**	0.37±0.11**
G. L/B ratio	I	0.522±0.135**	-0.143±0.100	0.867±0.239**	0.24±0.13*
	II	-0.341±0.103**	0.872±0.338**	-1.149±0.341**	-0.84±0.23**

** -Significant at $P = 0.01$, * - Significant at $P = 0.05$, days to fifty percent flowering (DFF), days to maturity (DM), plant height (PH), flag leaf length (FLL), flag leaf width (FLW), effective tillers per plant (ETPP), panicle length (PL), grains per panicle (GPP), chaff per panicle (CPP), spikelet fertility % (SF%), test-weight (TW), yield per plant (YPP), grain length (GL), breadth (GB), and grain length-breadth ratio (G L/B ratio),

assessing all the genetic components. To comprehensively evaluate all genetic components, the six-parameter model of generation mean analysis was used to analyze the mean and variance data for each trait in both crosses, with the exception of effective tillers per plant. For this specific trait, a three-parameter model was applied to estimate only the gene effects in both crosses. These findings are consistent with previous studies (Gobu et al. 2021; Arsode et al. 2022; Sharma et al. 2024). The breakdown of the generation mean into six distinct genetic components revealed that the mean effect (m) had a significant positive influence, with a greater magnitude than other genetic effects for nearly every trait in both crosses tested (Table 3). This suggests that these traits exhibited significant variation across generations and were quantitatively inherited. However, in Cross I, the magnitude of the genetic components (h and i) surpassed the mean effect for grains per plant (GPP), while the components (l, h, and i) exceeded the mean effect for chaffs per plant (CPP). Similar results were reported by Das et al. (2022b) and Ganapati et al. (2020).

Our findings indicated that all gene and interaction effects were significant for days to fifty percent flowering (DFF) in both crosses. Among the genetic components measured, the magnitude of 'h' (-13.0**) was highest in Cross I, whereas 'l' (-24.75**) was highest in Cross II. This suggests that the nature and magnitude of the interaction components are specific to each cross. The significant values of 'h' and 'l' with opposing signs in both crosses indicate the presence of duplicate epistasis in the inheritance and expression of this trait. The stronger dominance effect, combined with duplicate epistasis, suggests that plant selection should be postponed to later generations, with the intermating of segregants followed by recurrent selection to enhance the trait. Similar findings have been reported in previous studies (Lingaiyah et al. 2020; Das et al. 2022a; Sakr et al. 2024). The negative dominance gene effect 'h' in Cross I (-13.0**) indicates that Lemont contributed more to the expression of the trait. Both crosses exhibited significant genetic effects for days to maturity (DM). Among all genetic components, the 'l' (-26.2**) component had the highest value in Cross II, while 'h' (-13.78**) was the highest in Cross I. The negative values for 'l' indicated ambidirectional dominance between the parents. Both 'h' and 'l' showed significant values with opposite signs in both crosses, further suggesting the presence of duplicate epistasis in the inheritance and expression of the trait. Similar results were reported by Gobu et al. (2021), Sreelakshmi and Babu (2022), and Arsode et al. (2022). The presence of a strong dominance effect and duplicate epistasis limited the potential for early generation selection. The negative dominance gene effect 'h' in Cross I (-13.78**) indicates that Lemont contributed dominant genes for the expression of DM.

All genetic components, except for 'j', were significant for plant height (PH) in both crosses, with 'l' demonstrating the highest value. Plant height exhibited ambidirectional dominance between

the parents, as indicated by the negative values for 'l' in both Cross-I (-24.71**) and Cross-II (-24.35**). The positive and high values of 'i' in both Cross-I (17.98**) and Cross-II (18.1**) suggested a strong association of alleles in the parents. The opposite signs for 'h' and 'l' in both crosses indicated the presence of duplicate epistasis in the inheritance and expression of the trait. These findings align with those reported by Solanke et al. (2019), Kumar et al. (2024), and Nofal and Gaballah (2024). The dominance of interaction effects, coupled with duplicate epistasis, suggests that selection should be postponed until more advanced generations. The negative values for the additive gene effects 'd' in both Cross-I (-3.5*) and Cross-II (-4.25*) indicated significant contributions from Lemont and CR 22-1-5-1 to the expression of the trait in their respective crosses.

For flag leaf length (FLL), the magnitude of all genetic components was substantial in Cross-I, while all components except 'j' were significant in Cross-II. The 'j' component (-17.35**) had the largest magnitude among all components in Cross-I, while 'l' (-24.92**) showed the highest value in Cross-II. In Cross-I, both 'h' and 'l' had identical signs (both positive), indicating complementary epistasis. However, in Cross-II, they had opposing signs, suggesting duplicate epistasis in the inheritance and expression of the trait. These findings highlight the complexities involved in the trait's inheritance and expression, as well as the influence of the cross combination on improvement. These results are consistent with those of Arsode et al. (2022), Kathiresan et al. (2024), and Sakr et al. (2024). The negative value of the additive gene effect 'd' in Cross-I (-2.75*) suggests that Lemont is the major contributor to the expression of this trait.

For flag leaf width (FLW), the genetic components 'd', 'h', and 'i' were significant in both Crosses-I and II, with 'h' showing the highest magnitude in both cases. The additive genetic components ('d' and 'i') were positive, and their sum exceeded the non-additive dominance component 'h' in both crosses. This suggests that selection should be postponed to later generations until the epistatic effect is reduced. Similar observations for flag leaf width were reported by Kumar et al. (2024), Kathiresan et al. (2024), and Gobu et al. (2021).

For effective tillers per plant (ETPP), the non-significant values for all four scales necessitated the use of the three-parameter model to estimate gene effects in both crosses. In both crosses, only the dominance gene effect 'd' showed a significant value, indicating the involvement of additive gene action in the inheritance and expression of the trait. Similar findings for effective tillers per plant were reported by Gajanan (2015) and Ganapati et al. (2020). Simple selection in early generations or a pedigree breeding strategy would be effective in exploiting the additive gene action present in this trait. However, such results are likely to occur only in specific crosses, as observed in this experiment. The negative additive effect 'd' in

Table 3 Genetic effects of fifteen quantitative traits for Cross I and II

Trait	Cross	$m \pm \text{Sem}$	$d \pm \text{Sed}$	$h \pm \text{Seh}$	$i \pm \text{Sei}$	$j \pm \text{Sej}$	$l \pm \text{Sel}$	Epistasis Type
DFF	I	105.90±0.29**	2.05±0.51**	-13.00±1.61**	-3.30±1.55*	-8.50±1.13**	10.00±4.57*	Duplicate
	II	109.05±0.33**	3.05±0.49**	15.28±1.80**	18.50±1.63**	-2.25±1.07*	-24.75±4.72**	Duplicate
DM	I	132.45±0.32**	3.30±0.64**	-13.78±1.88**	-3.60±1.81*	-7.35±1.39**	10.55±4.71*	Duplicate
	II	135.75±0.39**	3.75±0.53**	14.40±2.03**	18.10±1.88**	-3.00±1.18**	-26.20±4.81**	Duplicate
PH	I	97.26±1.11**	-3.50±1.76*	16.44±5.89**	17.98±5.67**	6.27±3.93	-24.71±8.26**	Duplicate
	II	99.70±1.17**	-4.25±1.86*	19.78±6.26**	18.10±5.97**	-2.15±4.02	-24.35±8.94**	Duplicate
FLL	I	33.00±0.54**	-2.75±1.24*	7.13±3.40*	7.50±3.28*	-17.35±2.75**	12.55±5.66*	Complementary
	II	41.00±0.59**	2.63±1.09**	16.16±3.45**	16.06±3.22**	0.56±2.42	-24.92±6.04**	Duplicate
FLW	I	1.79±0.03**	0.13±0.05*	0.73±0.15**	0.61±0.14**	-0.13±0.11	-0.13±4.00	-
	II	2.01±0.02**	0.10 ±0.05*	0.32±0.14*	0.26±0.13*	0±0.11	0.13±4.00	-
ETPP	I	6.63±1.32**	-1.02±0.16*	-0.97±30.42	-	-	-	No Epistasis
	II	5.83±1.10**	-0.53±0.15**	1.73±30.23	-	-	-	No Epistasis
PL	I	26.41±0.24**	1.61±0.66**	3.32±1.68*	0.67±1.64	1.19±1.38	8.93±4.38*	Complementary
	II	28.14±0.50**	1.41±0.72*	5.46±2.51*	6.06±2.48**	2.01±1.49	-12.82±5.09**	Duplicate
GPP	I	191.85±2.31**	55.15±9.34**	206.28±23.27**	239.50±20.84**	-30.65±20.37	-173.15±34.23**	Duplicate
	II	281.45±16.12**	99.80±18.12**	205.60±74.46**	175.80±73.96*	88.60±37.17*	-218.20±82.26**	Duplicate

Trait	Cross	$m \pm \text{Sem}$	$d \pm \text{Sed}$	$h \pm \text{Seh}$	$i \pm \text{Sei}$	$j \pm \text{Sej}$	$l \pm \text{Sel}$	Epistasis Type
CPP	I	51.95±2.36**	29.55±12.33*	64.03±26.88*	83.50±26.41**	-37.45±25.68	-133.45±32.46**	Duplicate
	II	138.30±10.34**	14.3±11.48	-121.60±47.76**	-108.20±47.29*	-62.70±24.09**	-72.8±53.33	-
SF%	I	78.77±0.83**	-2.34±3.01	-0.34±6.99	-0.59±6.89	10.91±6.15*	18.58±10.51	-
	II	67.31±1.63**	3.27±2.17	29.87±7.97**	27.69±7.83**	21.40±4.53**	10.24±10.07	-
TW	I	1.98±0.04**	0.17±0.05**	-0.05±0.19	-0.04±0.19	-0.26±0.10**	-0.21±4.01	-
	II	2.08±0.03**	0.25±0.04**	0.37±0.15**	0.32±0.14*	0.34±0.10**	-0.37±4.00	-
YPP	I	22.15±0.28**	2.20±0.59**	11.55±1.78**	12.25±1.64**	-5.32±1.51**	-13.44±4.64**	Duplicate
	II	25.79±0.78**	5.36±0.69**	11.30±3.48**	10.93±3.40**	5.75±1.68**	-13.66±5.58**	Duplicate
GL	I	8.450±0.091**	0.284±0.135*	0.981±0.466*	0.05±0.452	0.204±0.298	-1.396±0.689*	Duplicate
	II	8.400±0.115**	-0.954±0.149**	1.290±0.559*	1.089±0.547*	-0.798±0.331**	-1.786±0.786**	Duplicate
GB	I	2.322±0.026**	0.209±0.037**	0.430±0.131**	0.344±0.128**	-0.412±0.083**	-0.373±0.189*	Duplicate
	II	2.700±0.040**	0.516±0.077**	-0.761±0.226**	-0.738±0.22**	0.532±0.160**	0.719±0.354*	Duplicate
G. L/B ratio	I	3.647±0.053**	-0.179±0.071**	-0.314±0.263	-0.488±0.257	0.664±0.157**	0.109±0.372	-
	II	3.131±0.079**	-1.166±0.169**	1.731±0.468**	1.679±0.464**	-1.213±0.348**	-2.210±0.757**	Duplicate

** -Significant at $P = 0.01$, * - Significant at $P = 0.05$, days to fifty percent flowering (DFF), days to maturity (DM), plant height (PH), flag leaf length (FLL), flag leaf width (FLW), effective tillers per plant (ETPP), panicle length (PL), grains per panicle (GPP), chaff per panicle (CPP), spikelet fertility % (SF%), test-weight (TW), yield per plant (YPP), grain length (GL), breadth (GB), and grain length-breadth ratio (G L/B ratio)

Cross-I (-1.02*) and Cross-II (-0.53**) indicated that Lemont and CR 22-1-5-1 made significant contributions to the expression of the trait in their respective crosses.

For panicle length (PL), all genetic components except for 'j' were significant in cross II, while 'i' and 'j' were insignificant in cross I. In cross I, the largest value was for 'l' (8.93*), followed by 'h' (3.32*) and 'd' (1.61**). In cross II, 'l' had the highest value (-12.82**), followed by 'i' (6.06**), 'h' (5.46**), and 'd' (1.41*). The magnitudes of both 'h' and 'l' in cross I had similar signs, indicating complementary interactions. In contrast, in cross II, they had opposite signs, suggesting the presence of duplicate interactions in the inheritance and expression of the trait. This highlights the complexities involved in trait inheritance and expression, as well as the influence of cross-combinations on trait improvement. Similar findings regarding panicle length have been reported by Sahoo et al. (2022), Kathiresan et al. (2024), and Sakr et al. (2024). Cross I has the potential to benefit from heterosis breeding due to the significant dominance effects present. The negative value of 'l' in cross II indicates ambidirectional dominance, which, along with duplicate epistasis, limits the potential for early-generation selection to enhance this trait.

In terms of grains per panicle (GPP), all genetic components were significant in cross II, while all except 'j' were significant in cross I. In cross I, 'i' had the highest value (239.5**), followed by 'h' (206.28**), 'l' (-173.15**), and 'd' (55.15**). In cross II, 'l' had the highest value (-218.2**), followed by 'h' (205.6**), 'i' (175.8*), 'd' (99.8**), and 'j' (88.6*). The positive and high magnitude of 'i' indicates a strong association of alleles in the parents. The influence of duplicate epistasis on the inheritance and expression of this trait was evident from the opposing signs of 'h' and 'l'. Similar results have been found in previous research (Arsode et al. 2022; Kumar et al. 2024; Kathiresan et al. 2024). The negative signs for 'l' in both crosses indicate ambidirectional dominance between the parents, which, together with duplicate epistasis, reduces the potential for early generation selection to improve the trait. The majority of the genetic components displayed nearly equal magnitudes, suggesting that population improvement could lead to the development of superior lines carrying several desirable genes.

In terms of chaff per panicle (CPP), the significant genetic components identified in cross I included 'd', 'h', 'i', and 'l'. Meanwhile, in Cross II, the significant components were 'h', 'i', and 'j'. Cross I recorded the largest magnitude for the genetic component 'l' (-133.45**), whereas Cross II showed the largest magnitude for 'h' (-121.6**). The contrasting signs for 'h' and 'l' in cross I suggest that there are duplicate interactions involved in the inheritance and expression of this trait. Similar findings for CPP have been reported by Ganapati et al. (2020), Gobu et al. (2021), and Sreelakshmi and Babu (2022).

For test weight (TW), all genetic components except for 'l' were significant in Cross II, while only 'd' and 'j' were significant in Cross I. In Cross II, the largest magnitude was observed for 'h' (0.37**), while in Cross I, the largest magnitude was recorded for 'j' (-0.26**). These results are consistent with previous studies (Solanke et al. 2019; Gobu et al. 2021; Kathiresan et al. 2024).

When examining yield per plant (YPP), all genetic components were significant in both crosses. In Cross I, the highest magnitude was recorded for 'l' (-13.44**), followed by 'i' (12.25**), 'h' (11.55**), 'j' (-5.32**), and 'd' (2.2**). In Cross II, the highest magnitude was also for 'l' (-13.66**), followed by 'h' (11.30**), 'i' (10.93**), 'j' (5.75**), and 'd' (5.36**). The negative values for 'l' indicate ambidirectional dominance, while the substantial positive dominance gene effect for 'h' and the highly significant negative dominance \times dominance effect for 'l' suggest duplicate epistasis in the inheritance and expression of this trait. These results align with the findings of Arsode et al. (2022), Sakr et al. (2024), Kumar et al. (2024), and Nofal and Gaballah (2024) regarding per plant yield. These observations suggest that selection may be delayed until the dominance and epistatic effects dissipate in advanced generations. Additionally, biparental mating of superior segregants, along with recurrent selection, might be effective in producing desirable segregants.

In the case of grain length (GL), all genetic components were found to be significant in Cross II. However, in Cross I, all the components except for 'i' and 'j' were significant. The highest value for the parameter 'l' was observed in both crosses, measuring -1.4* in Cross I and -1.79** in Cross II. Grain length demonstrated ambidirectional dominance, as indicated by the negative value of 'l'. The contrasting signs of 'h' and 'l' in both crosses suggested duplicate interactions in how the trait is inherited and expressed. Consequently, it is advisable to defer selection to advanced generations. Strategies such as biparental matings or recurrent selection could be employed to obtain desirable early segregants. Similar findings were reported by Sharma et al. (2024) and Kour et al. (2019). Furthermore, the negative value of the additive gene effect 'd' in Cross II (-0.95**) indicated that the genotype CR 22-1-5-1 played a significant role in the expression of this trait.

For grain breadth (GB), all genetic components were significant in both crosses. Among these, the highest values were observed for 'h', with measurements of 0.43** in Cross I and -0.76** in Cross II. The contrasting signs of 'h' and 'l' in both crosses suggested the presence of duplicate-type interactions in the trait's inheritance and expression. Non-allelic interactions with duplicate-type epistasis can be effectively utilized in pedigree breeding by delaying selection until advanced generations. These results align with the findings reported by Sharma et al. (2024) and Kamara et al. (2017).

Additionally, the negative dominance effect 'h' in Cross II suggested that the genotype CR 22-1-5-1 harbors dominant genes influencing trait expression.

Regarding the grain length-breadth ratio (GL/B ratio), all genetic components were significant in Cross II, while only 'd' and 'j' were significant in Cross I. The highest magnitude was recorded for 'l' in Cross II at -2.21** and for 'j' in Cross I at 0.66**. In Cross II, the contrasting signs of 'h' and 'l' indicated the presence of duplicate-type interactions for the inheritance and expression of this trait. These findings are consistent with those of Kour et al. (2019). The negative values for the additive gene effect 'd' in both crosses suggested that the male parent significantly contributed to the expression of the trait in their respective crosses.

Conclusion

The analysis of yield and its contributing traits in both crosses indicated that a combination of additive, dominance, and epistatic gene effects influenced most traits. Generally, non-additive effects outweighed additive ones, except for effective tillers per plant and flag leaf width, where additive effects were significant. The dominance effect ('h') was greater than the additive effect ('d') for most traits, suggesting substantial genetic variation between the parental lines. The dominance \times dominance ('l') effect was the strongest interaction, followed by additive \times additive ('i') and additive \times dominance ('j') effects. These interactions often showed opposing directions, indicating the presence of duplicate epistasis, which can reduce the effectiveness of early-generation selection. Notably, dominance \times dominance interactions had the highest frequency of negative values. Contrasting signs in interactions for traits such as days to fifty percent flowering (DFF), days to maturity (DM), plant height (PH), grain per plant (GPP), yield per plant (YPP), grain length (GL), grain breadth (GB), and grain length to breadth ratio (GL/B) suggested that there are dispersed alleles in the interacting loci. These findings highlight the significance of dominance and interaction effects in the genetic control of yield-related traits. It is recommended to use biparental mating of superior segregants to break undesirable linkages and concentrate favorable alleles for improved yield.

Conflict of interest

The authors declare that they have no conflict of interest.

Funding

The authors did not receive funding from any organization for the submitted work.

Ethical Clearance

No ethical clearance required for this study.

References

- Arsode, P. B., Singh, R. P., Singh, S., Kumar, M., Namrata, et al. (2022). Genetics of grain yield and its component traits in drought tolerance rice. *Oryza-An International Journal on Rice*, 59(2), 150–156. <https://doi.org/10.35709/ory.2022.59.2.2>
- Chen, J., Ding, J., Ouyang, Y., Du, H., Yang, J., et al. (2008). A triallelic system of *S5* is a major regulator of the reproductive barrier and compatibility of *indica-japonica* hybrids in rice. *Proceedings of the National Academy of Sciences*, 105(32), 11436–11441. <https://doi.org/10.1073/pnas.0804761105>
- Das, G., Pradhan, B., Bastia, D., Samantaray, S., Jena, D., et al. (2022a). Pyramiding Submergence Tolerance and Three Bacterial Blight Resistance Genes in Popular Rice Variety Hasanta through Marker-Assisted Backcross Breeding. *Agriculture*, 12, 1815. <https://doi.org/10.3390/agriculture12111815>.
- Das, G., Pradhan, B., Bastia, D. N., & Verma, R. (2022b). Generation mean analysis for submergence tolerant and yield traits in rice. *The Pharma Innovation Journal*, 11(3), 1022–1026.
- Gajanan, K. A. (2015). *Generation mean analysis in rice (Oryza sativa L.)* Ph.D. Dissertation submitted to the Navsari Agricultural University, Gujarat, India.
- Ganapati, R. K., Rasul, M. G., Sarker, U., Singha, A., & Faruquee, M. (2020). Gene action of yield and yield contributing traits of submergence tolerant rice (*Oryza sativa L.*) in Bangladesh. *Bulletin of the National Research Centre*, 44(1), 1-7. <https://doi.org/10.1186/s42269-019-0261-0>
- Gobu, R., Lal, J. P., & Anandan, A. (2021). Generation Mean Analysis for Yield and Drought Tolerant Traits under Rainfed and Irrigated Conditions in Rice (*Oryza sativa L.*). *International Journal of Environment and Climate Change*, 11(11), 170–178. <https://doi.org/10.9734/ijecc/2021/v11i1130530>
- Hayman, B. I. (1958). The separation of epistatic from additive and dominance variation in generation means. *Heredity*, 12(3), 371-390. <https://doi.org/10.1038/hdy.1958.36>
- Ikehashi, H., & Araki, H. (1984). Varietal Screening of Compatibility Types Revealed in F₁ Fertility of Distant Crosses in Rice. *Japanese Journal of Breeding*, 34(3), 304–313. <https://doi.org/10.1270/jsbbs1951.34.304>
- Jinks, J. L., & Jones, R. M. (1958). Estimation of the components of heterosis. *Genetics*, 43(2), 223–234. <https://doi.org/10.1093/genetics/43.2.223>
- Kallugudi, J., Singh, V. J., Vinod, K. K., Krishnan, S. G., Nandakumar, S., et al. (2022). Population Dynamics of Wide

- Compatibility System and Evaluation of Intersubspecific Hybrids by indica-japonica Hybridization in Rice. *Plants*, 11(15), 1930. <https://doi.org/10.3390/plants11151930>
- Kamara, N., Asante, M. D., & Akromah, R. (2017). Inheritance studies of aroma and yield attributes in rice (*Oryza sativa* L.) genotypes. *African journal of agricultural research*, 12(50), 3461–3469. <https://doi.org/10.5897/AJAR2017.12583>
- Kathiresan, P. K., Ramamoorthy, P., & Subramanian, S. (2024). Generation mean analysis reveals insights into yield attributing traits in rice (*Oryza sativa* L.) under drought and irrigated environments. *Vegetos*, 1-8. <https://doi.org/10.1007/s42535-024-00958-5>
- Kour, A., Kumar, B., Singh, B., Attri, H., & Bangarwa, S. K. (2019). Generation mean analysis for yield and grain quality traits in rice (*Oryza sativa* L.). *Electronic Journal of Plant Breeding*, 10(1), 289–292. <https://doi.org/10.5958/0975-928X.2019.00035.8>
- Kumar, K. P., Pushpam, R., Manonmani, S., Raveendran, M., & Senthil, A. (2024). Deciphering gene action for traits contributing to submergence tolerance and yield in rice (*Oryza sativa* L.). *Electronic Journal of Plant Breeding*, 15(1), 63-69.
- Kumar, M., Singh, R.P., Jena, D., Singh, V., Rout, D., et al. (2023). Marker-Assisted Improvement for Durable Bacterial Blight Resistance in Aromatic Rice Cultivar HUR 917 Popular in Eastern Parts of India. *Plants*, 12, 1363. <https://doi.org/10.3390/plants12061363>.
- Kumar, M., Singh, R. P., Singh, O. N., Singh, P., Arsode, P., Jena, D., Samantaray, S., & Verma, R. (2019). Generation mean analysis for bacterial blight resistance and yield traits in rice. *Journal of Pharmacognosy and Phytochemistry*, 8(4), 2120–2124.
- Lenka, B., Baisakh, B., Dash, M., Lenka, D., & Tripathy, S. K. (2021). Gene Action Studies for Yield and its Related Traits by using Generation Mean Analysis in Mungbean [*Vigna radiata* (L.) Wilczek]. *Legume Research*, 45(2): 149-153. <https://doi.org/10.18805/LR-4715>
- Lingaiah, N., Raju, C. S., Radhika, K., Sarla, N., Venkanna, V., & Reddy, D. V. V. (2020). Estimation of gene effects through generation mean analysis in elite rice (*Oryza sativa* L.) crosses. *Journal of Experimental Biology and Agricultural Sciences*, 8(1), 15–20. [https://doi.org/10.18006/2020.8\(1\).15.20](https://doi.org/10.18006/2020.8(1).15.20)
- Mather, K. (1949). *Biometrical Genetics: The Study of Continuous Variation by K. Mather: Very Good Plus (1949) 1st Edition. Tarrington Books.* <https://www.abebooks.com/first-edition/Biometrical-Genetics-Study-Continuous-Variation-Mather/30685509296/bd>
- Mather, K., & Jinks, J. L. (1971). *Biometrical Genetics*. Springer US. <https://doi.org/10.1007/978-1-4899-3404-8>
- Nofal, R. S., & Gaballah, M. M. (2024). Determining the Gene Action Type for Grain Yield and its Components using Generation Mean Analysis in Rice (*Oryza sativa* L.). *Journal of Plant Production*, 15(4), 139-144.
- Revathi, S. (2015). *Marker-assisted introgression of wide compatibility gene into restorer parents for exploitation of heterosis in indica/japonica crosses of rice (Oryza sativa L.)* Ph.D. Dissertation submitted to the Tamil Nadu Agricultural University, Tamil Nadu, India.
- Sahoo, B., Nair, S. K., Jena, D., Rout, D., Singh, V., et al. (2022). Genetic analysis of yield and quality traits in improved parental lines of the rice hybrid Rajalaxmi. *Journal of Emerging Technologies and Innovative Research*, 9(3), 366-373.
- Sakr, S. M., Gaballah, M. M., Ghidan, W. F., & Talha, I. A. (2024). Inheritance Analysis of Grain Yield and Contributing Traits in Rice Through Six Populations Under Normal and Water Deficit Conditions. *Journal of Plant Production*, 15(12), 803-812.
- Sharma, A., Kumawat, S., Kumar, A., & Jaiswal, H. K. (2024). Generation mean analysis for yield and quality traits in basmati rice (*Oryza sativa* L.). *Electronic Journal of Plant Breeding*, 15(1), 138-146.
- Solanke, A. C., Patel, P. B., & Patel, P. K. (2019). Generation mean analysis for yield and its contributing traits in aromatic rice (*Oryza sativa* L.). *The Pharma Innovation Journal*, 8(8), 05-09.
- Sreelakshmi, C., & Babu, P. R. (2022). Study of genetic architecture of grain yield and quality traits through generation mean analysis in rice (*Oryza sativa* L.). *Electronic Journal of Plant Breeding*, 13(2), 325-333.
- Sundaram, R. M., Sakthivel, K., Hariprasad, A. S., Ramesha, M. S., Viraktamath, B. C., et al. (2010). Development and validation of a PCR-based functional marker system for the major wide-compatible gene locus S5 in rice. *Molecular Breeding*, 26(4), 719–727. <https://doi.org/10.1007/s11032-010-9482-5>













Journal of Experimental Biology and Agricultural Sciences

<http://www.jebas.org>

ISSN No. 2320 – 8694

Soil erosion assessment in the Ranganadi watershed of Lakhimpur district, Assam, using GIS techniques and Revised Universal Soil Loss Equation model

Tilak Prasad Panika¹ , D.K. Patgiri¹ , Bipul Deka² , Prem Kumar Bharteey^{3*} ,
Marami Dutta¹ , Sumit Rai⁴ , Ashish Rai⁵ , Surajyoti Pradhan⁶ , Ayush Bahuguna³ ,
Maneesh Kumar⁷, Rituparna Saikia⁸ 

¹Department of Soil Science, Assam Agricultural University, Jorhat-85 013, Assam, India

²AICRP on Irrigation Water Management, Assam Agricultural University, Jorhat-785 013, Assam, India

³Department of Agricultural Chemistry & Soil Science, C.C.R (P.G.) College, Muzaffarnagar-251 001, Uttar Pradesh, India

⁴Centre for Environment Assessment & Climate Change GB Pant National Institute of Himalayan Environment Kosi-Katarmal, Almora-263643, Uttarakhand, India

⁵Krishi Vigyan Kendra, Parsauni, East Champaran, Dr RPCAU, Pusa Bihar, India

⁶Department of Agronomy, Krishi Vigyan Kendra (OUAT), Mayurbhanj-2, Orissa, India

⁷Subject Matter Specialist (Soil Science) Krishi Vigyan Kendra, Kaimur, Bihar -8221102

⁸Krishi Vigyan Kendra, Kamrup, Guwahati-781 017, Assam, India

Received – September 17, 2024; Revision – December 08, 2024; Accepted – December 28, 2024

Available Online – January 15, 2025

DOI: [http://dx.doi.org/10.18006/2024.12\(6\).860.875](http://dx.doi.org/10.18006/2024.12(6).860.875)

KEYWORDS

Soil loss

RUSLE model

GPS

GIS

Watershed

ABSTRACT

The loss of soil due to erosion is one of the most critical land degradation issues globally, representing a vital asset for both the economy and the environment. To effectively manage and regulate such a global issue, it is imperative to estimate the loss. With technological advancements, methodologies such as Geographic Information Systems (GIS) and Remote Sensing (RS) are crucial in addressing these difficulties. The primary objective of this study was to employ the Revised Universal Soil Loss Equation (RUSLE) model inside a GIS framework to quantify soil loss in the Ranganadi river basin of Assam, providing a more rapid and accurate estimate. Three distinct physiographic units, *i.e.*, Piedmont Plain, Alluvial Plain, and Flood Plain, were delineated. Collected 60 GPS-based soil samples from distinct physiographic units were collected and analyzed for different soil physico-chemical properties, in addition to taking into account a variety of criteria, such as rainfall erosivity factor (R), soil erodibility factor (K), topography factor (LS), cover and management factor (C), and conservation practices factor (P), the RUSLE approach is based on the evaluation of soil loss per unit area. Five basic RUSLE factors,

* Corresponding author

E-mail: premcrcd@gmail.com (Prem Kumar Bharteey)

Peer review under responsibility of Journal of Experimental Biology and Agricultural Sciences.

Production and Hosting by Horizon Publisher India [HPI]
(<http://www.horizonpublisherindia.in/>).
All rights reserved.

All the articles published by [Journal of Experimental Biology and Agricultural Sciences](#) are licensed under a [Creative Commons Attribution-NonCommercial 4.0 International License](#) Based on a work at www.jebas.org.



viz., R factor, K factor, LS factor, C factor, and P factor, were used to determine soil erosion. Further, erosion ratio, dispersion ratio, and erosion index are the basic examples of erodibility indicators that were taken into consideration while used to evaluating the erodibility of the soil. The anticipated soil erosion in the above-said area varied from minimal to severe, with values between 0.01 and 27.38 t ha⁻¹ yr⁻¹. Among the physiographic units, alluvial plain soils had the greatest mean soil erosion value of 8.52 t ha⁻¹ yr⁻¹, whereas floodplain landscapes indicated the lowest average value of 3.39 t ha⁻¹ yr⁻¹. The dispersion ratio varied between 0.08 and 0.33, with soils exhibiting a dispersion ratio exceeding 0.15, signifying their vulnerability to erosion. The erosion ratio varied between 0.04 and 0.61, whereas the erosion index fluctuated from 0.06 to 0.84. As a result, this model is particularly useful in anticipating soil loss in an area, allowing community members, legislatures, and other linked agencies to plan ahead of time for future efforts to mitigate the degradation.

1 Introduction

We all know that all living organisms that live on Earth need clean water, air, and nutrients, which all come from soil (Katsuyuki 2009; Keesstra et al. 2016). Because of the population's heavy reliance on soil resources, overexploitation causes soil degradation. In India, erosion hazards impact approximately 147 million hectares, comprising 94 million hectares of submerged erosion and 9 million hectares of wind erosion. Annually, a reduction of 1 mm of topsoil leads to a decrease of 5,334 MT in production attributable to soil erosion (Bhattacharyya et al. 2015). According to Meena et al. (2017), soil loss is a severe environmental problem that affects water body siltation, nutrient loss, and soil productivity. It adversely affects public health and the lives of marginalized communities dependent on agriculture, especially in the Eastern Indian Himalayas (Pimental 2006). The area is experiencing considerable soil erosion, with rivers transporting substantial quantities of sediment into the Bay of Bengal. The Himalayan and Tibetan regions contribute approximately 25% of the dissolved load to the world's oceans (Raymo and Ruddiman 1992). The Himalayan foothills in northeastern India, including Arunachal Pradesh, Nagaland, Manipur, Mizoram, Meghalaya, and Assam, are no exception to soil loss. However, the Himalayan rivers' sediment load has grown due to loss of forest cover, indiscriminate exploitation of natural resources, strong monsoon precipitation, and vulnerable river catchments with inadequate water retention capacity (Valdai 1985; Rawat and Rawat 1994). Thus, soil erosion needs immediate analysis since it is a significant obstacle to the long-term preservation of the environment and natural resources. The efficacy of various land management strategies, therefore, depends on measuring and evaluating the mean amount of soil erosion in arable and pastoral lands (Prasuhn et al. 2013). Soil attrition in any region may be quantified using several formulas and equations found in the literature. These have been produced during an extensive period of global experimentation. The Universal Soil Loss Equation (USLE) (Wischmeier and Smith 1978; Singh and Panda 2017) and RUSLE are the most commonly used methods for the computation of soil degradation (Renard et al. 1997; Fernandez

et al. 2003; Srinivasan et al. 2019). The idea of associating available data sources employed with RUSLE and GIS technology is a reliable solution for computing the extent of soil erosion (Bez and Krishna 2014; Pham et al. 2018). These techniques have been widely incorporated and applied in many types of research; the RUSLE model can effectively estimate the erosion susceptibility of a watershed (Shinde et al. 2010; Ganasri and Ramesh 2016). Furthermore, GIS skills, in conjunction with satellite imaging techniques, are highly effective in modeling areas that are prone to soil erosion (Parveen and Kumar 2012). Molla and Sisheber (2017) estimated soil loss and conservation strategies under different slope classes and land uses in the Koga watershed in the upper part of the Blue Nile basin. Balakrishna and Balakrishna (2019) evaluated soil erosion and identified critical sub-watersheds. Soil erosion is instrumental in land degradation in mountain regions, with increased rainfall and surface water runoffs on bare lands, which increase soil erosion in India's northernmost region (Thapa 2020). Kandpal et al. (2018) carried out soil erodibility assessments in three forest divisions of Shivalik Hills, Punjab. They found that the Dasuya forest division exhibited maximum soil loss (31.78%), followed by the moderately dense forest of Gurdaspur (29.20%) and Garshnkar (11.28%). The Brahmaputra Valley in Assam is characterized by significant undulation, resulting in serious soil erosion issues. The depletion of soil due to runoff from the ground is one of the most prevalent types of soil damage in Assam, especially during times of heavy and prolonged rains that have a negative impact on agricultural output. According to the State Department of Soil Conservation, Assam, the Ranganadi basin, which is found in Assam's northern bank plains, is most susceptible to erosion. This watershed has many physiographic units, and the specific soils in this region exhibit numerous fundamental characteristics. Still, the knowledge about the characteristics of the soils that erode inside the watersheds is limited. The purpose of this work was to use the model developed by RUSLE and GIS analysis to explore the Ranganadi watershed's deteriorating soil features to enable the policymakers to devise strategies for watershed management to minimize soil erosion in the area.

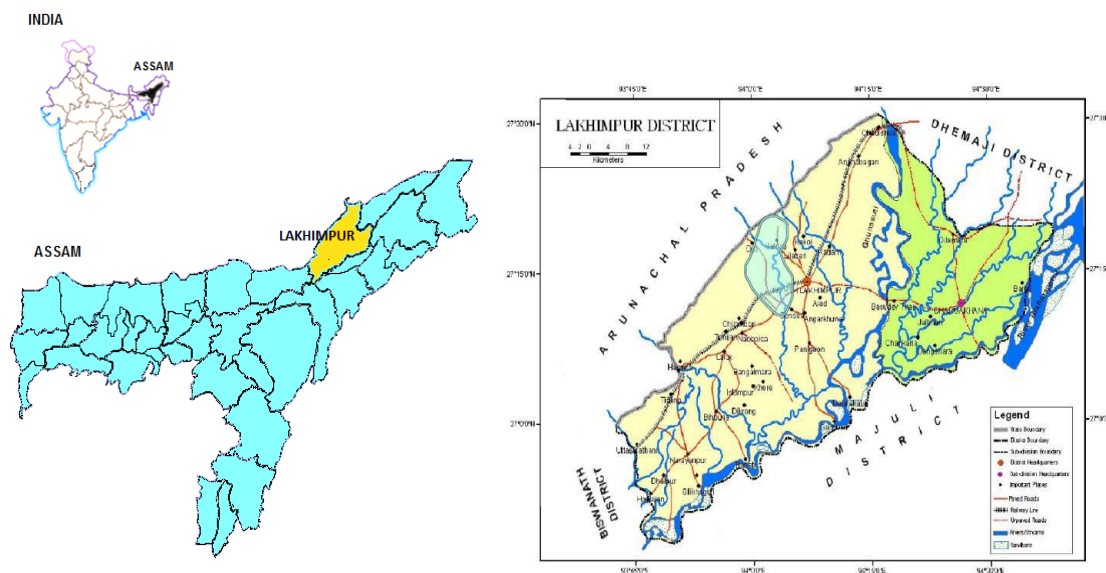


Figure 1 Location map of the study area

2 Materials and Methods

2.1 Site description and climate

The Ranganadi catchment is situated in the Lakhimpur district, in the North Bank Plain Zone of Assam. The Ranganadi watershed lies between $93^{\circ}59'06.18''\text{E}$ and $94^{\circ}05'08.55''\text{E}$ longitude and between $27^{\circ}10'36.40''\text{N}$ and $27^{\circ}20'33.68''\text{N}$ latitude (Figure 1). The climate in the scrutinized field is a humid sub-tropical one, with an average annual rainfall of 3194 mm, an average annual temperature of more than 22°C and the difference between the average summer temperature of 27.3°C and means winter temperature of 18°C are 5°C . Consequently, the studied area can be considered to have a hyperthermic soil temperature regime. The climate of the said field has equal concentrations of soil moisture.

2.2 Delineation of watershed

They visually interpreted the geocoded FCC of the Resourcesat-1 LISS-III data of 2015 and prepared the physiographic map in consultation with the Survey of India toposheets of scale 1:50,000. The physiographic units that have been identified following visual discernment of colour, tones, and texture differences include the Piedmont Plain, which occupied 4192 ha; the Alluvial Plain, which occupied 4808 ha; and Flood Plain, which occupied 3174 ha (Figure 2). The satellite map of the transect of the Ranganadi watershed is illustrated in Figure 3.

2.3 Soil collection and analysis

With the help of the GPS, 60 locations were selected as sampling sites in physiographic units, i.e., Piedmont Plain (soil sample 16), Alluvial Plain (soil sample 19), and Flood Plain (soil sample 25).

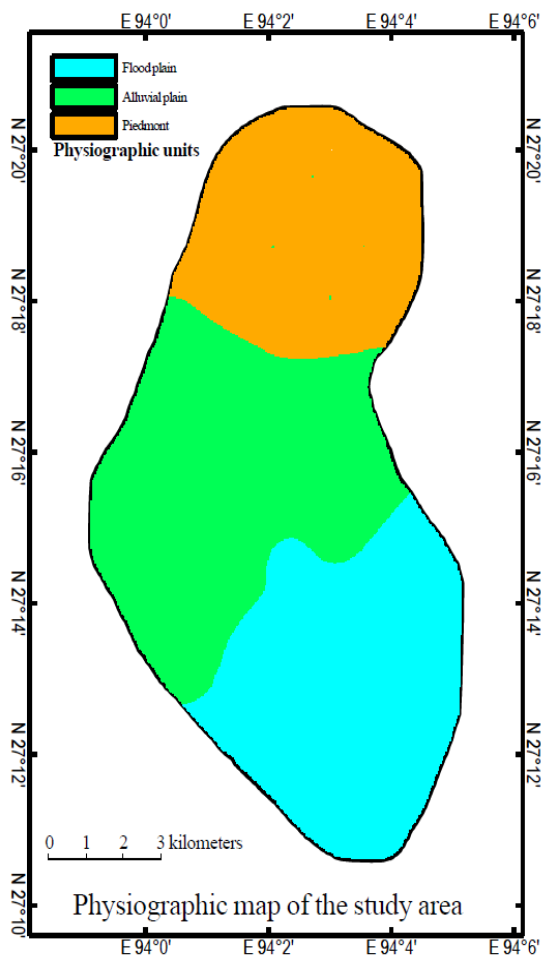


Figure 2 Physiographic delineation map

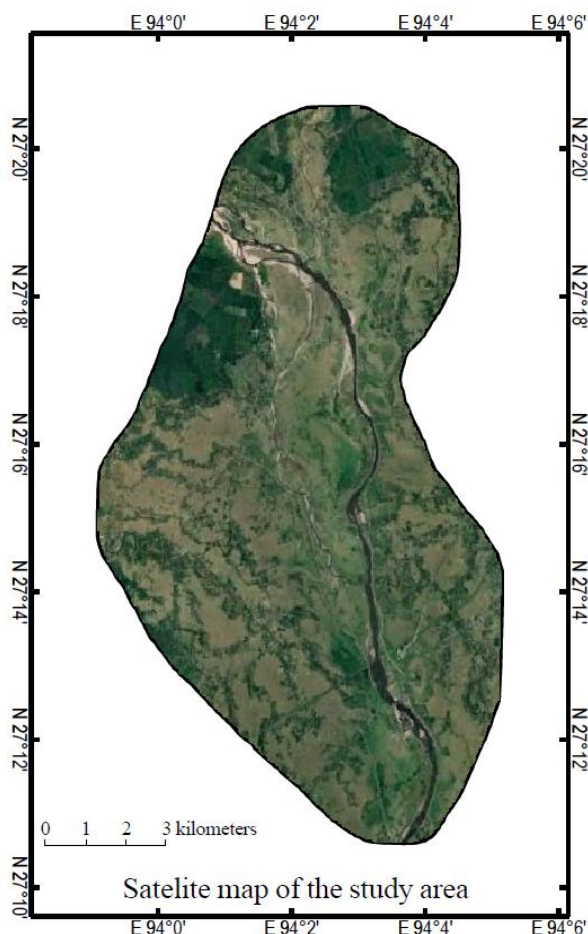


Figure 3 Satellite map of Ranganadi watershed

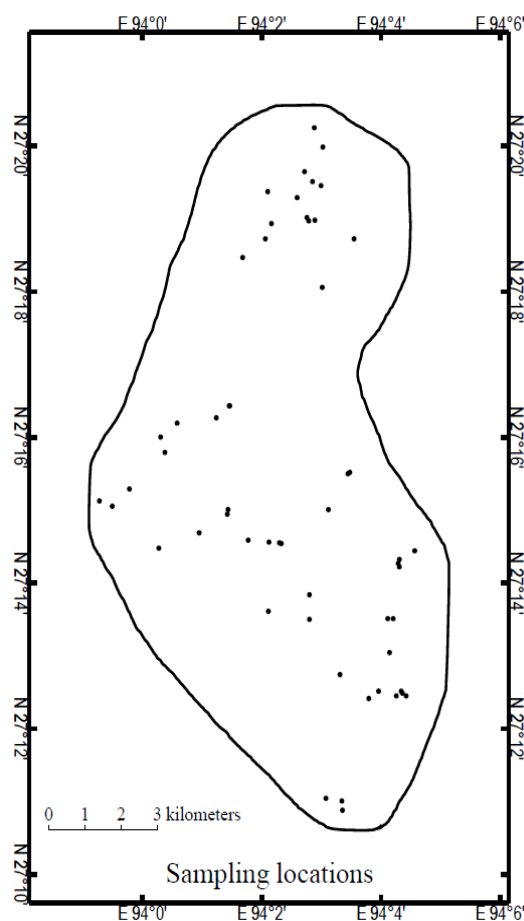


Figure 4 Sampling site map

The places that were sampled within the examined field are shown in the following figure 4. Therefore, bulk and core samples were taken from all the detected locations. The collected soil samples in bulk were dried by air, thereafter mixed and ground using a wooden mortar and pestle, and then separated using a 2mm sieve. These samples were also taken to examine some of the physical features of the soil samples obtained through the core samples, including particle size distribution by the International pipette procedure (Piper 1966), constant head approach for assessing Hydraulic Conductivity (Klute 1965), Water Holding Capacity (Piper 1966), Organic Carbon (Walkley and Black 1934), Available Water Content (Richards 1948), and Soil Aggregate (Yoder 1936).

2.4 RUSLE Parameters Analysis

Renard et al. (1997) developed the Revised Universal Soil Loss Equation (RUSLE) model (Figure 5), which was used to evaluate annual soil loss in the Ranganadi watershed region. When assessing soil loss, this model has the advantage of taking into account all important input variables, including land use or land

cover, soil erodibility, rainfall intensity and volume, and conservation practices. The Revised Universal Soil Loss Equation (RUSLE) is represented as:

$$\text{Soil loss (A)} = R, K, LS, C, P$$

Where, A = the mean annual soil loss ($\text{t ha}^{-1} \text{ yr}^{-1}$), R = rainfall erosivity factor (MJ mm ha yr), K = soil erodibility factor ($\text{t ha MJ}^{-1} \text{ mm}^{-1}$), LS = slope length/steepness factor, C = cover and management factor, and P = conservation practice factor

2.4.1 Rainfall erosivity factor (R)

The rainfall erosivity factor (R) was computed using the formula provided by Bergsma (1980). The established equation is:

$$R = 0.1059a \cdot b \cdot c + 52$$

Where a = average yearly precipitation, b = maximum 24-hour precipitation with a recurrence interval of two years, and c = one-hour maximum precipitation with a recurrence frequency of two years.

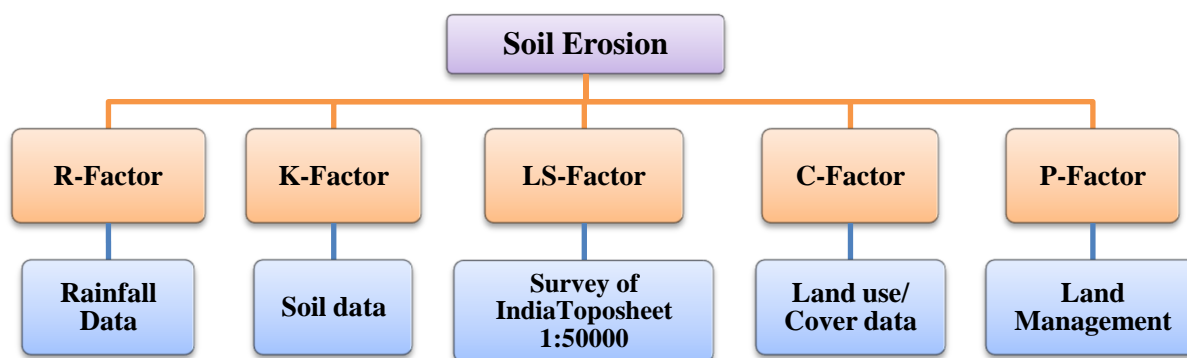


Figure 5 Flow diagram for investigation of soil erosion using the RUSLE model

2.4.2 Soil erodibility factor (K)

By measuring the rate at which soil deteriorates due to surface runoff or raindrop contact, the erodibility factor captures the variation in soil erosion per unit area as a result of external pressures. This element is profoundly influenced by soil texture, structure, permeability, and organic matter content. The volume written by Wischmeier et al. (1971) was essential in determining K values in the study area using the following equation:

$$100 K = 2.1 \times 10^4 - 4 \times M^{1.14} (12 - a) + 3.25 (b - 2) + 2.5 (c - 3)$$

Where K = soil erodibility factor, M = percent of silt + percent of very fine sand, a = percentage of organic matter, b = soil structure code, and c = soil permeability code.

2.4.3 Slope length/steepness factor (LS)

Wischmeier and Smith's 1978 monographs and the Survey of India Topographical Map of 1:50000 were used to calculate the LS factor of each physiographic unit.

2.4.4 Cover management factor (C)

Cover management factor (C) factors were calculated using the primary crop growth/land use data gathered during the field survey.

2.4.5 The conservation practice factors (P)

The P factors employed in conservation practice were determined using information gathered during field surveys. Previous studies provided the 'P' cut-off values for various land usage categories (Potdar et al. 2003).

2.5 Erodibility indices & geostatistical analysis

The erodibility of soils was assessed by calculating the erodibility indices: (i) Dispersion ratio (Middleton 1930) = [% Undispersed (silt + clay) / % Dispersed (silt + clay)]; (ii) Erosion ratio

(Middleton 1930) = Dispersion ratio / [Clay (%) / Available water]
(iii) Erosion index (Sahi et al. 1977) = Dispersion ratio / [Clay (%) / 0.5 Water holding capacity].

2.6 Geostatistical analysis

Using these data, a GIS environment constructed the map showing soil loss. The values obtained from each sample location were extracted from the location map utilizing ArcMap 10.4. The soil parameter values at the unsampled site were determined through the application of the Inverse Distance Weighted (IDW) method, following the methodology outlined by Jensen (1986). The study employed the IDW interpolation methodology, a geostatistical method commonly utilized by several authors for estimating surface maps and forecasting soil parameters (Abdelrahman et al. 2020). The interpolated maps were reclassified to get the map units and legends displayed here. The watershed border of Ranganadi was superimposed on the interpolated maps to get the final map. The analysis of eight quantitative soil erosion variables, linked to three indices of erodibility and soil loss, was conducted using the statistical program SPSS-21 and Xlstat. The investigation yielded significant statistical parameters, including the correlation matrix, variance-covariance matrix, and Eigenvalues with corresponding Eigenvectors and loading. Each sample was assigned a 'Score', which is the computed value of the factor at that site and is referred to as 'Factor score'. The samples were graded according to the factor concerned.

3 Results and Discussion

3.1 Soil erosion related characters:

The eight soil erosional characteristics of the Ranganadi watershed for estimating soil erosion are depicted in Table 1. Various box plots were developed, as shown in Figure 6.

The watershed under study comprises a range of soil types, *i.e.*, from clayey loam to sandy soil. Single grains and subangular blocky shapes were among the different soil structures. Sand and

Table 1 Physiographic distribution soil erosional properties of Ranganadi watershed

Parameter	Piedmont plain			Alluvial plain			Flood plain		
	Range	Mean	CV (%)	Range	Mean	CV (%)	Range	Mean	CV (%)
Total sand (%)	22-82.40	62.79	34.93	26.30-89.36	57.36	30.70	32.21-90.08	59.17	29.76
Very fine sand (%)	11.12-26.23	18.79	31.37	10.12-33.34	20.33	29.96	11.12-31.12	18.77	33.16
Silt (%)	9.72-60.28	26.13	69.28	5.68-56.80	25.28	42.24	5.44-53.83	25.09	46.69
Clay (%)	5.09-18	11.08	40.14	4.96-35.56	17.36	60.41	4.48-33.14	15.74	53.74
HC (cm hr ⁻¹)	0.42-5.87	3.06	69.61	0.43-6.24	2.51	87.28	0.48-6.17	2.32	86.27
WHC (%)	15.25-42.35	25.49	30.24	16.85-53.70	30.38	32.33	14.21-52.34	32.92	36.99
AWC (%)	5.25-13.19	8.32	39.23	4.36-17.97	11.59	34.99	4.64-18.33	10.53	35.84
OM (g kg ⁻¹)	0.88-2.02	1.45	24.71	0.53-2.83	1.53	40.97	0.28-2.97	1.49	42.79

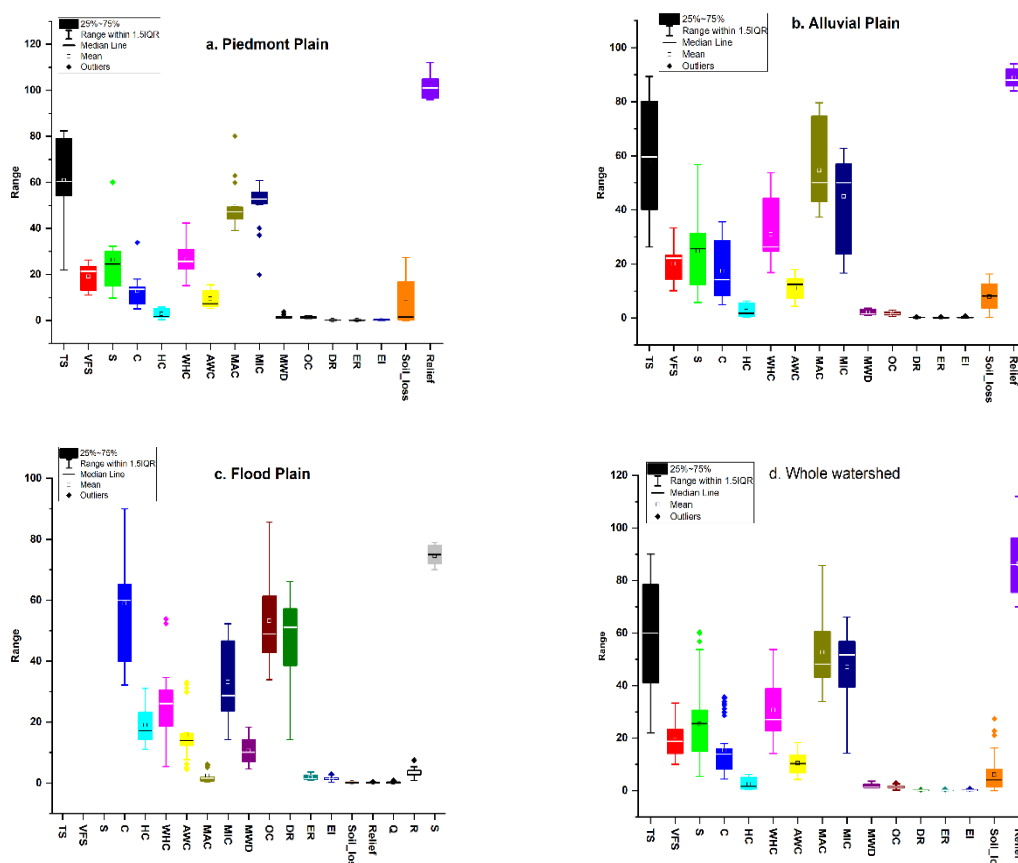


Figure 6 Box plots showing soil erosional properties of Ranganadi Watershed (a) Piedmont Plain (b) Alluvial Plain (c) Flood Plain (d) Whole watershed

fine sand contents in the examined soils ranged from 22.00 to 90.08% and 10.12 to 33.34%, respectively (Table 1). Similarly, Table 1 shows that the concentrations of silt and clay varied from 5.44 to 60.28% and 4.48 to 35.56%, respectively. The alluvial plain had the lowest percentage of sand (Mean 57.36) among the

physiographic units, while the piedmont plain had the greatest percentage (Mean 62.79). The highest silt percentage (Mean 26.13) was found on the Piedmont Plain. Conversely, the highest concentrations of clay (Mean 17.36) and extremely very fine sand (Mean 20.33) are found in the alluvial plain area. The faster transit

of finer materials from the Piedmont Plain to the alluvial plain and flood plain is caused by erosion, which carries these materials downstream from the Piedmont Plain and dumps them in these areas. Soil degradation is influenced by factors such as sensitivity to degradative processes, land use, duration, and management. Shifting farming has been a long-standing practice in Assam. Apart from that, the river Subansiri shows evidence of large amounts of sediment being deposited and overflowing the flood area, which leads to significant wearing away of the river bank (Sasang Guite and Bora 2016). From the results, it is seen that the area experiences soil erosion because of high slope angles. High braiding, huge water flow, and the rising of the river bottom owing to silt deposition are the main causes of the river's significant instability at numerous reaches. Recurring floods every year owing to heavy rainfall during long monsoons in the study area have led to breaches of embankments and developed areas of bars, which cause erosion. In the north bank plain of Assam, Deka et al. (2009) found that the texture of the soils is finer at lower elevations than at higher elevations. Sand's coefficient of variation is lowest in flood zones (CV = 29.76%), middle in alluvial regions (30.70%), and highest in piedmont plains (34.93%). While the amount of clay differed considerably among the alluvial, flood, and piedmont plains, the silt fraction varied significantly among the piedmont basin (CV = 69.28%), Flood plain (CV = 46.69%), and Flood plain (CV = 42.24%). These findings are supported by the results of Oku et al. (2010). The presence of a substantial positive link between relief and sand, as well as a large negative correlation with silt and clay, supports the experimental finding. Bharatey et al. (2023) observed similar findings. The hydraulic conductivity of the watershed ranged from 0.42 to 6.24 cm hr⁻¹ (Table 1). Of all the physiographic units, the Piedmont Plain had the highest hydraulic conductivity, with an average of 3.06 cm hr⁻¹. The strong negative correlation ($r = -0.735^{**}$) (Figure 11) between hydraulic conductivity and clay concentration can be explained by the dispersion and movement of smaller particles into the pores that allow for conductivity. Dutta and Barkakoty (1996) discovered such associations in multiple soils in Assam. The studied soils had water-holding capacities ranging from 19.88% to 63.12% (Table 1). Among the physiographic units, the Piedmont plain soils have the lowest water-holding capacity, averaging 29.14%. This could be due to the greater sand content in certain soils, which supported the gradual increases in water holding capacity of the particular area soil.

From the upper Piedmont plain to the flood plain, finer materials provide more capillary holes and a bigger surface area to store water. A considerable positive connection was found between water-holding capacity and silt ($r = 0.502^{**}$), clay content ($r = 0.716^{**}$), porosity ($r = 0.741^{**}$), and organic matter ($r = 0.381^{**}$) (Figure 11). The soil type is also an important factor in determining erosional activity. Silty soils are extremely sensitive to

water and wind erosion, whereas clayey soil is least prone to soil erosion (Brady and Weil 2012). Deka et al. (2017) found comparable correlations in the soil of Assam's North Bank Plains. The measured soils had available water ranging from 1.0% to 22.5% (Table 1). The alluvial plain has the highest available (mean 11.59%) among all physiographic units, owing mostly to the presence of finer materials. In contrast, the Piedmont Plain had the lowest water holding capacity (mean 8.32%). There was a considerable negative association ($r = -0.663^{**}$) between the amount of water that could be stored in the soil and the sand content. However, there was a strong positive association ($r = 0.764^{**}$) between the amount of water that could be stored in the soil and the concentration of clay. Borgohain et al. (2021) found a similar link between the Pabho watershed. The organic matter content of the watershed ranged from 0.28 to 2.97 grams per kilogram (Table 1). Among the physiographic units, the alluvial plain soil contained the most organic matter, with a mean of 1.53 g kg⁻¹, while the piedmont plain had the least (mean 1.45 g kg⁻¹). The floodplain soils have higher organic matter content as a result of farmers' extensive crop cultivation using organic manures. Furthermore, the migration of bases and clay particles from higher to lower elevations via transportation and leaching contributed to the increase. Debnath et al. (2009) reported higher organic matter levels in rice production soils in the West Bengal Terai region. This conclusion is ascribed to farmers in the area who use more organic manure.

3.2 Principal Component Analysis of Soil Parameters

Variations in 11 soil hydro physical parameters besides relief, erodibility indices, and soil loss were successfully accounted for by the two major components whose Eigenvalues were more than 1.5, which accounts for 65% variation in the soil parameters (Table 2). The screen plot (Figure 7) shows the relation of the Eigenvalues with the principal component's numbers. From the factor loading matrix of the soil parameters, it is seen that silt, clay, water holding capacity, available water content, macroaggregate, mean weight diameter, Organic carbon, and soil loss had a positive factor on P1. In contrast, sand, very fine sand, hydraulic conductivity, and microaggregate had a negative factor on P1. The common P1 component that had compositions bearing a strong relationship with the inherited mechanical components was given the name of the 'Inherent Potentiality Factor'. Three parameters, such as dispersion ratio, erosion ratio, and erosion index, loaded positively in the second principal component (P2). All these erodibility parameters were more or less related to each other, and a group of parameters was therefore defined with reference to soil erosion. Thus, this second factor was termed the 'Erosion Factor'. Table 2 shows the factor loading of the soil parameters in P1 and P2; the studied parameters were distributed in all four quadrants. The PCA biplot in Figure 8 shows both the PC scores of samples and the loading of

Table 2 Eigenvalues, variance (%), cumulative variance (%), and matrix factor loading of soil parameters

Rotated Component Matrix		
Parameters	PCA 1	PCA 2
Eigenvalue	8.52	1.93
% of Variance	53.25	12.11
Cumulative variance (%)	53.25	65.36
Coarse Sand	-0.950	0.067
Very fine sand	-0.306	0.348
Silt	0.744	-0.295
Clay	0.898	0.277
Hydraulic conductivity	-0.866	0.165
Water holding capacity	0.769	0.396
Available water content	0.712	0.260
Macroaggregate	0.919	0.303
Microaggregate	-0.916	-0.321
Mean weight diameter	0.895	0.334
Organic carbon	0.367	0.239
Dispersion ratio	-0.592	0.646
Erosion ratio	-0.708	0.539
Erosion index	-0.739	0.535
Soil loss	0.527	-0.059
Elevation	-0.142	-0.186

variables. The first quadrant revealed positive loading on both the PCs, and the second quadrant had negative loadings on P1 and positive loadings on P2. Deka and Dutta (2016) also found similar findings in the Northern Brahmaputra plains of Assam.

3.3 Soil Erosion Rate Assessment

To assess soil erosion in the Ranganadi watershed, the parameters associated with the RUSLE model were initially calculated. The specifics of the assessment of the components are shown in Table 3.

3.3.1 Rainfall erosivity factor (R):

The R-factor quantifies the impact of precipitation on soil erosion. Average yearly rainfall data is necessary for calculating the R-factor. Rainfall data from 2000 to 2019 was obtained from the Regional Meteorological Centre in Northeast India. The analyzed region experienced an annual precipitation of 319.40 cm, a maximum 24-hour precipitation of 10.36 cm, and a one-hour maximum precipitation of 2.55 cm. The rainy erosivity factor (R) for the whole watershed was determined to be 945.57 mm (Table 3), and it was identified as a significant contributor to soil erosion processes in the study area. Northeast India has a higher rate of soil loss compared to the rest of the country, possibly due to excessive rainfall. Severe rainfall in the region causes acidification and loss of critical metallic minerals, including calcium, magnesium, potassium, and sodium, which are necessary for agricultural productivity. Barman et al. (2020) also got similar results in Meghalaya.

3.3.2 Soil erodibility factor (K)

The K-factor for each location was determined using field and laboratory estimates of texture, organic matter content, structure,

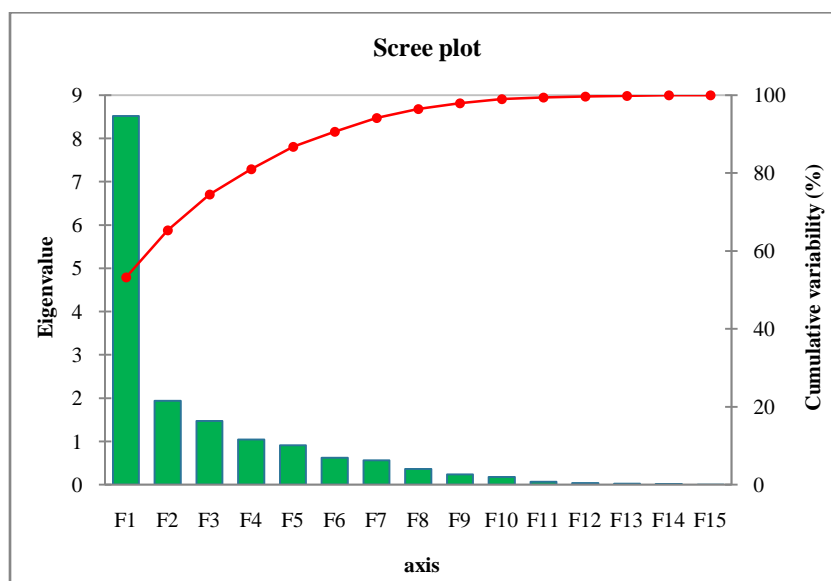


Figure 7 Screen Plot showing the relation between Eigenvalues and PC numbers

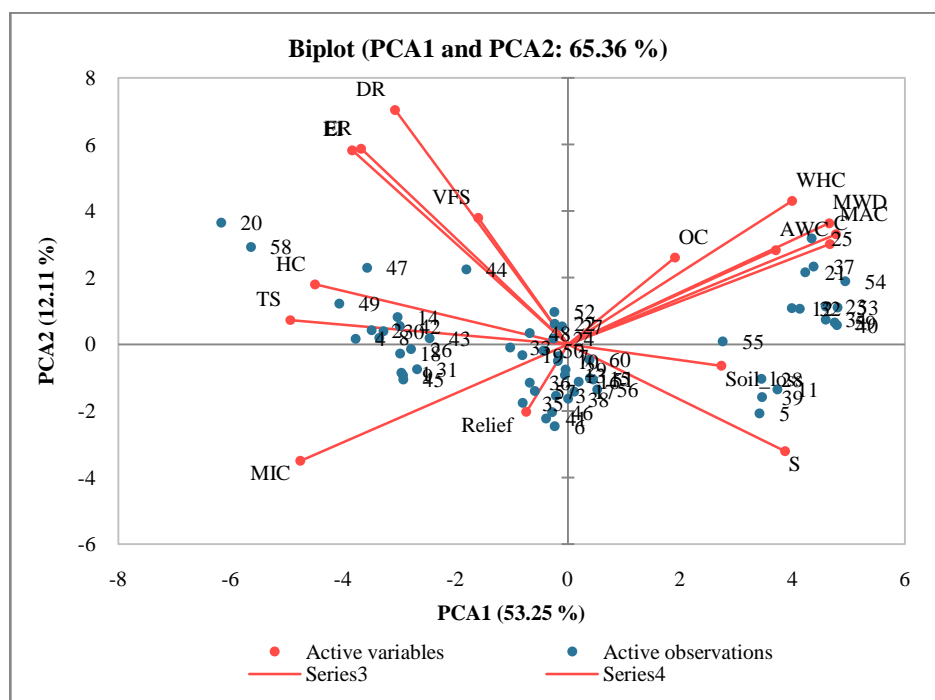


Figure 8 PCA Biplot showing factor loading of soil parameters

Table 3 Range, mean, and CV (%) values of RUSLE factors, soil loss, and elevation in diverse physiographic units of the Ranganadi watershed

Parameters	Piedmont plain			Alluvial plain			Flood plain		
	Range	Mean	CV (%)	Range	Mean	CV (%)	Range	Mean	CV(%)
R	-	945.57	-	-	945.57	-	-	945.57	-
K	0.001-0.118	0.06	88.73	0.001-0.118	0.06	51.25	0.026-0.12	0.07	37.55
LS	1.63-1.63	1.63	-	0.97-0.97	0.97	-	0.32-0.32	0.32	-
C	0.02-0.50	0.24	105.24	0.02-0.50	0.44	35.55	0.10-0.50	0.47	23.17
P	0.30-0.54	0.43	29.09	0.30-0.54	0.34	27.22	0.30-0.54	0.35	27.87
Soil loss (t ha ⁻¹ yr ⁻¹)	0.01-27.38	7.37	157.85	0.33-22.77	8.52	67.76	0.53-12.61	3.39	58.02
Elevation	96-112	104.18	4.76	81-94	86.74	4.71	70-79	74.88	4.39

and permeability of surface soil samples in accordance with the monograms provided by Wischmeier and Smith (1978). The erodibility factor (K) for the examined watershed area varied from 0.001 to 0.12 (Table 3). The K value demonstrated moderate fluctuation, with a coefficient of variation of 51.94 percent. The flood plain has the greatest soil erodibility factor (Mean=0.07), succeeded by the piedmont and alluvial regions, each with a mean value of 0.06. The K factor exhibited the greatest variability (CV= 88.73%) in piedmont soils and the least variability (CV= 37.55%) in floodplain soils. A higher value of 0.51 on the basin's K factor map indicates increased susceptibility to erosion. Fine-loamy, coarse-loamy, and fine-loamy textures with a higher K value are more susceptible to erosion. Soil with a loose texture and little

organic matter is especially susceptible to erosion. If the sandy Alfisol is devoid of natural surface litter, it is prone to erosion from heavy rain (Brady and Weil 2012). This K factor is mostly influenced by the amount of humus present in the soil and its texture (Getu et al. 2022).

3.3.3 Slope length and slope percentage factor (LS)

The LS factor was calculated according to the methodology established by Wischmeier and Smith (1978) using nomographic computation. The LS factor in the soils of the examined watershed varied from 0.32 to 1.63, exhibiting moderate variability (CV = 60.68%) (Table 3). Erosion and landslides are strongly influenced

by topography. The topographic factor (LS) reflects the impacts of topography on erosion and includes the slope's length and steepness, which influence surface runoff speed (Beskow et al. 2009; Pradhan et al. 2012).

3.3.4 Crop cover and management factor (C)

The C-factor values designated for various land use/land cover types are as follows: 0.5 for Paddy, Pineapple, Okra, and Cabbage; 0.02 for Tea cultivation; and 0.1 for Arecanut and Lemon Garden. The values were ascertained using land use/land cover data provided by Potdar et al. (2003). The crop cover and management factor (C) of the Ranganadi watershed varied from 0.02 to 0.50. The C component exhibited the greatest variability (CV= 105.24 %) in piedmont area soils and the least variability (CV= 23.17 %) in floodplain soils (Table 3). Soil erosion rate is primarily influenced by terrain and crop cover; however, other factors also have a role (Wolka et al. 2018). Crop cover acts as a barrier to land degradation, and soil loss due to excess rainfall is minimized up to a greater extent. Plant cover protects soil by enhancing infiltration, physical and chemical characteristics, and material cohesion (Tiruwa et al. 2021). Additionally, it cuts up raindrop kinetic energy and intercepts some precipitation.

3.3.5 Conservation Practice Factor (P)

The P-factor values were assigned based on field survey data. Paddy (0.5), Pineapple (0.8), Arecanut, Vegetables, and Lemon Garden (0.4) were designated. The 'P' value for tea plantations was designated as 0.8, as the cultivation of plantation crops is a form of conservation practice. The conservation practice factor (P) of the examined watershed area ranged from 0.30 to 0.54. The P component exhibited the greatest variability (CV = 29.09%) in Piedmont area soils and the least variability (CV = 27.22%) in alluvial plain soils (Table 3).

3.3.6 Estimation of Soil Loss

Assessed the input parameters for the RUSLE (R, K, LS, C, and P) and subsequently multiplied all components to compute the total soil loss (A). The soil erosion in the examined watershed ranged from a minimum of $0.01 \text{ t ha}^{-1} \text{ yr}^{-1}$ to a maximum of $27.38 \text{ t ha}^{-1} \text{ yr}^{-1}$, with an average of $13.50 \text{ t ha}^{-1} \text{ yr}^{-1}$, in comparison to the moderate range ($10\text{-}15 \text{ t ha}^{-1} \text{ yr}^{-1}$) identified by Potdar et al. 2003 (Table 3). Annual soil loss was highest in alluvial plain soils (Mean = $8.52 \text{ t ha}^{-1} \text{ yr}^{-1}$) and lowest in flood plain soils (Mean = $3.39 \text{ t ha}^{-1} \text{ yr}^{-1}$) across the physiographic groups (Table 3). Potdar et al. (2003) categorize soil loss into several erosion classes: weak ($<5 \text{ t ha}^{-1} \text{ yr}^{-1}$), fairly slight ($5\text{-}10 \text{ t ha}^{-1} \text{ yr}^{-1}$), moderate ($10\text{-}15 \text{ t ha}^{-1} \text{ yr}^{-1}$), moderately severe ($15\text{-}20 \text{ t ha}^{-1} \text{ yr}^{-1}$), severe ($20\text{-}40 \text{ t ha}^{-1} \text{ yr}^{-1}$), and extremely severe ($>40 \text{ t ha}^{-1} \text{ yr}^{-1}$). We saw soil erosion varying from little to severe in both the piedmont and alluvial plains. Consequently, the piedmont and alluvial regions exhibited

greater vulnerability to soil erosion than lower-elevation locations. The positive association between height and soil loss is also noticeable ($r = 0.166$). Approximately 22 hectares (0.18%) are vulnerable to significant soil erosion, ranging from 20 to 40 tonnes per hectare per year. A total area of 50 hectares (0.41%) fell under the moderately severe classification, while 1047 hectares (8.60%) were categorized as moderate. The largest area of 5550 hectares (45.59%) exhibited moderate soil loss of $5\text{-}10 \text{ t ha}^{-1} \text{ yr}^{-1}$, whereas the 5505 hectares (45.22%) had a minor erosion issue of less than $5 \text{ t ha}^{-1} \text{ yr}^{-1}$. While it may not experience severe soil loss, it is likely to incur significant soil loss owing to erosion issues. Thus, it is essential to put measures to preserve soil into practice promptly to avert future degradation of soil quality in the region. Figure 9 illustrates the distribution of soil erosion classifications among the three distinct physiographic units. The negative correlation ($r = -0.609^{**}$) (Figure 11) between sand concentration and soil loss indicates that increased sand content decreases soil loss. Sand particles possessing elevated potential energy can displace raindrops by surpassing their kinetic energy. The kinetic energy of raindrops more readily displaces tiny silt and clay particles, resulting in heightened soil loss ($r = 0.610^{**}$, 0.389^{**} for silt and clay, respectively) (Figure 11). The inverse connection of HC ($r = -0.494^{**}$) with soil loss indicates that increased water transfer rates facilitate more water absorption, hence mitigating soil loss. Elevated water retention exacerbates soil erosion ($r = 0.323$) due to the increased weight of water-saturated soil. Similar results were also reported by Deka et al. (2011) and Das et al. (2020). A relationship between soil erosion with relief and Erodibility indices (Figure 10) smaller aggregates possess less potential energy. The positive link between soil loss and relief showed that increased removal of soil was correlated with longer and steeper slopes.

3.4 Soil erodibility indices

Soil erodibility mainly depends on the specific physical characteristics of the soil, such as the structure of the soil, which may include the elements of soil aggregates, the nature and intensity of organic matter content in the soil, and the distribution of the particle size. It is worth pointing out that the land use system significantly affects most of these physical characteristics of soils. Therefore, the diverse erodibility indices, including water-stable aggregates, dispersion ratio, erosion ratio, and erosion index under different land use systems, were predicted in this study with the aid of data on basic soil properties and by applying different empirical formulas (Table 4).

3.4.1 Aggregate status

In the Ranganadi watershed, soil macroaggregates ranged from 33.94 to 85.72 percent. Similarly, the percentage of microaggregates varied from 14.28 to 66.06 percent (Mean 47.14 percent). The mean weight diameter of the soil particles in the studied watershed ranged from

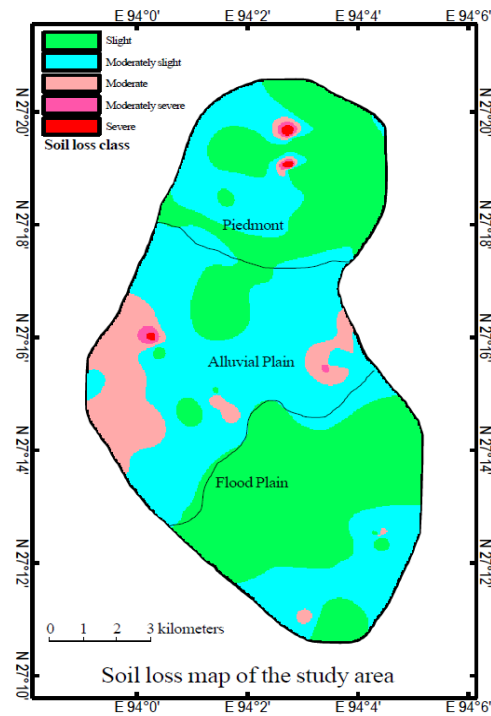


Figure 9 Distribution of soil loss in Ranganadi watershed

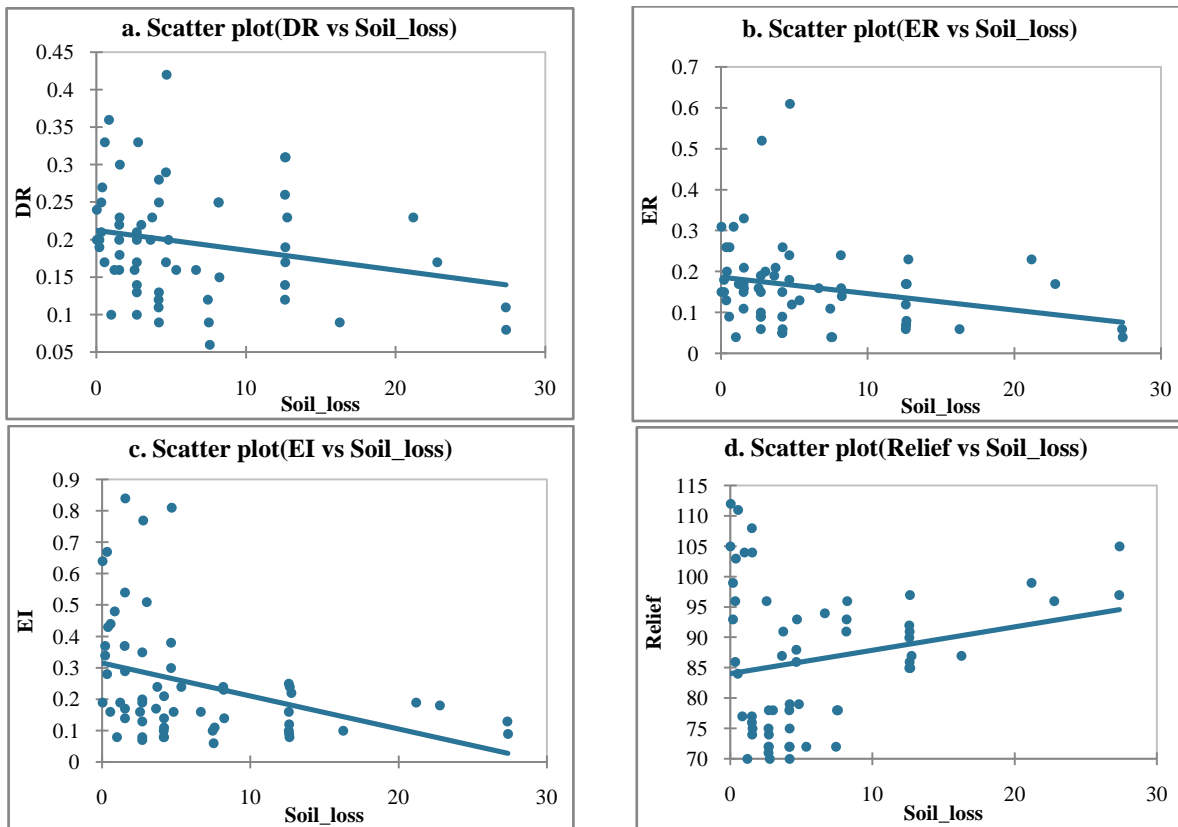


Figure 10 Relation between soil loss and dispersion ratio, erosion ratio, erosion index, and relief

Table 4 Physiographic distribution of Erodibility indices soils of Ranganadi watershed

Parameters	Piedmont plain			Alluvial plain			Flood plain		
	Range	Mean	CV (%)	Range	Mean	CV (%)	Range	Mean	CV (%)
Dispersion ratio	0.08-0.33	0.19	39.49	0.09-0.42	0.21	34.16	0.06-0.36	0.18	42.40
Erosion ratio	0.04-0.31	0.16	54.28	0.06-0.61	0.17	64.76	0.04-0.52	0.15	72.85
Erosion index	0.08-0.64	0.26	69.33	0.08-0.81	0.25	71.99	0.06-0.84	0.25	84.64
Macroaggregate (%)	39.18-62.94	47.81	15.65	37.28-80.14	54.92	26.79	33.94-85.72	52.84	29.65
Microaggregate(%)	37.06-60.82	52.19	14.34	16.59-62.72	44.70	34.33	14.28-66.06	47.16	33.22
Mean Weight Diameter(mm)	1.06-2.58	1.55	33.83	1.07-3.69	1.96	50.55	1.03-3.58	1.84	48.09

1.03 mm to 3.69 mm. Among the physiographic units, the value of macroaggregates was highest in the alluvial plain area (Mean 54.92%) and lowest in the piedmont plain area (mean 47.81%). On the other hand, the microaggregate percentage was highest in the Piedmont Plain (Mean 52.19%) and lowest in the Alluvial Plain (Mean 44.70%). The mean weight diameter was found to be highest in the Alluvial Plain area (Mean 1.96 mm) and lowest in the Piedmont Plain area (Mean 1.55 mm). An increasing trend of macroaggregate was observed in the Piedmont plain (Mean 47.81 percent), flood plain (Mean 52.84 percent), and alluvial plain soils (Mean 54.92 percent). In the case of microaggregate, the reverse trend was followed by the alluvial plain (Mean 44.70 %), flood plain (Mean value 47.16 %), and Piedmont plain areas (Mean value 52.19 %). Mean weight diameter also exhibited a trend similar to that of macroaggregates from the Piedmont plain (Mean 1.55 mm), floodplain soils (Mean 1.84 mm), and alluvial plain (Mean 1.96 mm). The rising trend of mean weight diameter with declining elevation suggests improved aggregation due to a greater concentration of finer particles (clay and organic materials) in lower elevation regions. Furthermore, correlation analysis indicated that MWD was favorably correlated with clay ($r=0.94^{**}$) and SOM content ($r=0.42^{**}$) (Figure 11). This is evident from the chemical inactivity of sand particles, their lack of cation exchange capacity, and their bigger particle size. Consequently, MWD predominantly reflects macro-aggregation in soil due to the predominance of macroaggregate-size classes over microaggregate-size classes in its calculation. The results align with the findings of Das et al. (2020) across several watersheds in Assam.

3.4.2 Dispersion ratio (DR)

In the soils of the studied watershed, a high dispersion ratio was observed (Mean = 0.20), and the ratio varied from 0.06-0.42 (Table 4). Among the physiographic units, alluvial plain soils (Mean 0.21) were found to have a higher dispersion ratio, and floodplain soils had the lowest dispersion ratio (Mean 0.18). According to Middleton, a DR > 0.15 is categorized as erodible. From the analysis, it was observed that about 71.6 percent of the total

studied area falls under the erodible group (DR > 0.15), out of which 72.7 percent of the soil samples from piedmont plain, 86.3 percent from the alluvial plain and 64 percent from the flood plain areas had DR values greater than 0.15, indicating its susceptibility to erosion. The DR exhibited a significant positive correlation with sand ($r = 0.545^{**}$). At the same time, it had a significant negative correlation with silt ($r = -0.560^{**}$) and clay ($r = -0.327^*$) (Figure 11), indicating that the smaller the particles, the greater the dispersion, leading to increased vulnerability of the soils to erosion, positive relationship with HC ($r = 0.503^{**}$) and a negative relationship with water retention parameters ($r = -0.276^*$ for WHC). This indicates that a higher DR will reduce porosity and, thus, water retention, leading to a higher surface flow of water and increasing the erodibility of soils. Therefore, it corroborates that a higher clay content will reduce DR ($r = -0.327^*$) due to aggregate formation, as indicated by a significant negative correlation with MWD ($r = -0.359^{**}$) (Figure 11). Similarly, it had significant positive relations with ER ($r = 0.819^{**}$), EI ($r = 0.726^{**}$), and soil loss ($r = 0.232$) (Figure 11), indicating that with higher DR, there will be more soil loss. Dabral et al. (2016) also reported similar findings in Nirjuli of Arunachal Pradesh.

3.4.3 Erosion ratio (ER)

The soil erosion ratios in the studied watershed area varied widely. The soil erosion ratio in the Ranganadi watershed varied between 0.04-0.61 (Table 4). The erosion ratio was found to be highest in the alluvial plain (Mean 0.17) and relatively lower in the flood plain (Mean 0.15) soils. The presence of a high amount of sand and a low amount of silt and clay in the alluvial plain soils may be the reason for the highest erosion ratio. The results demonstrate a strong positive association with sand ($r = 0.640^{**}$) and a high negative association with silt ($r = -0.554^{**}$) and clay ($r = -0.531^{**}$) (Figure 11), respectively. Hydraulic conductivity has a significant negative role ($r = -0.588^{**}$) on ER, i.e., higher HC will reduce ER. Similarly, water retention parameters also have a negative role on ER ($r = -0.396^{**}$ for WHC) in reducing ER. Increased soil aggregation lowers ER ($r = -0.526^{**}$), while all other erosion indices have a significant positive influence on ER ($r = 0.819^{**}$

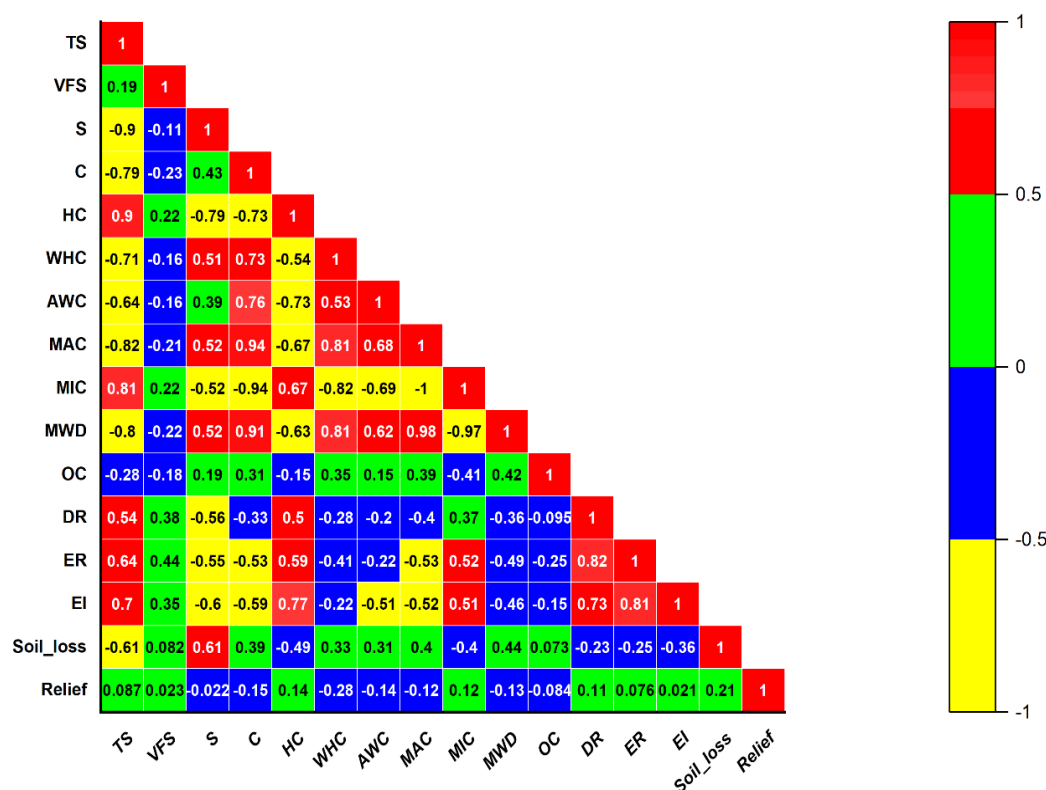


Figure 11 Correlation of soil physicochemical and soil loss ($p \leq 0.05$)

and 0.811** for DR and EI, respectively) (Figure 11). The present investigation observes a positive effect ($r = 0.250$) on soil loss, indicating that ER induces soil loss. Similar findings were also reported by Singh and Khera (2008) in the submountaneous of Panjab.

3.4.4 Erosion Index (EI)

It became apparent that the investigated soils' erosion indices ranged widely, from 0.06 to 0.84 (Table 4). The Piedmont plain soils had the highest value of the erosion index (Mean 0.26), whereas the alluvial plain and floodplain soils had equal mean values of 0.25. The erosion index of the studied watershed was nearly the same in all the physiographic units (EI = 0.26 in Piedmont and 0.25 in both alluvial and flood plains). The dominance of medium to lighter soil textures in the study area could be the reason for the high erosion index. The sand content had a significant positive influence on EI ($r = 0.698^{**}$), while finer particles, especially clay ($r = -0.588^{**}$), had a negative role. These findings followed Deka et al. (2017), which stated that the erodibility of soil varied directly with sand content. Similar to other indices, water transmission properties have a significant positive role on EI ($r = 0.770^{**}$), while retention properties ($r = -0.190$ and -0.521^{**} for WHC and AW, respectively) (Figure 11) have negative implications. Higher MWD reduces EI ($r = -$

0.460^{**}). EI had a significant positive relationship with all other erosion indices ($r = 0.726^{**}$ and 0.811^{**} for DR and ER, respectively) (Figure 11), indicating that it is also on par in predicting soil erosivity. Higher EI leads to increased soil loss, as is evident from a positive correlation ($r = 0.358$) with soil loss. Saha et al. (2011) also reported similar findings in the hilly ecosystem of Meghalaya.

3.5 Suggested erosion control measures

Taking into account the severity of the extent of soil erosion in the discussed area, it can be assumed that the area requires the implementation of serious soil conservation measures to decrease the impact of soil loss downstream. The Piedmont plain soils indicated low to very high levels of erosion rate. This is due to high elevation, low organic matter, coarse-textured soils, and lower clay. For such conditions, vegetative bunds, contour bunds, terracing, mulching, use of farmyard manure, intercropping, and growing nitrogen-fixing crops with fibrous root systems would help reduce erosion and improve the productivity of these soils. Moreover, these soils may be used for bamboo cultivation as bamboo has a strong potential to reduce soil loss as well as to improve the economic status of the farmers. The alluvial plain soils were affected by slight to severe erosion. Good agronomic practices can be adopted to reduce probable soil loss in these soils,

such as conservation tillage, crop rotation, mulching, farmyard manure, cover crops, leguminous crops, etc. The floodplain soils showed slight to moderately slight erosion, and as such, the adoption of selective agronomic practices in a location-specific manner would help reduce soil loss.

Conclusions

It was also found that the RUSLE model and the GIS were effective in estimating the extent of soil abrasion and identifying areas vulnerable to erosion. The variables that were estimated include different parameters affecting water erosion. Some of the studies employed spatial information data on physiographic, slope, land use/land cover, and soils obtained from satellite remote sensing and supporting data. The study also showed that the whole watershed was found to moderate soil erosion and, among the physiographic units, is subject to various levels of soil erosion. Soils of the Piedmont plain and alluvial plain, which are on relatively higher slopes, show a spectrum of erosion ranging from moderately to slightly eroded. Measures that should be put into practice to minimize the extent of soil erosion involve vegetative bunds, contour bunds, terracing, mulching and the use of farmyard manure, intercropping, and adoption of crops with nitrogen-fixing capability that have fibrous root systems. On the other hand, downslope landforms such as alluvial plains have varied to some extent in terms of erosion. Finally, for such conditions, it is possible to apply conservation tillage, crop rotation, mulching, farmyard manure, and the cultivation of cover crops and leguminous crops. Likewise, the floodplain soils with an almost gentle slope possess slight to moderate FF deterioration. Those limited and special forms of tillage and other management practices applied at particular places would be favorable in checking the soil loss, noting that the intensity of soil erosion is least in the low-lying areas, which have low elevation.

Acknowledgments

This study was carried out with the assistance of the Indian Space Research Organization, the Department of Space and the Government of India under the RESPOND program.

Funding

Not Applicable

Ethical approval and consent to participate

The work does not contain any studies involving human and animal subjects.

Conflict of interest

The authors declare no competing interests.

References

- Abdelrahman, M.A., Zakarya, Y.M., Metwaly, M.M., & Koubouris, G. (2020). Deciphering soil spatial variability through geostatistics and interpolation techniques. *Sustainability*, 13, 194.
- Balakrishna, K., & Balakrishna, B.H.D. (2019). Assessment of soil erosion by USLE model using remote sensing and GIS of Hemavathy basin. *International Journal of Scientific Engineering and Research*, 10, 106-116.
- Barman, B. K., Rao, K. S., Sonowal, K., Prasad, N. S. R., & Sahoo, U. K. (2020). Soil erosion assessment using revised universal soil loss equation model and geo-spatial technology: A case study of upper Tuirial river basin, Mizoram, India. *AIMS Geosciences*, 6(4), 525-545.
- Bergsma, E. (1980). Provisional rain-erosivity map of Netherlands: In: M. Deboodt, & D. Gabriels (Eds.) *Assessment of Erosion* (pp. 121-126). *John Wiley and Sons*.
- Beskow, S., Mello, C.R., Norton, L.D., Cur, N., Viola, M.N., & Avanzi, J.C. (2009). Soil erosion prediction in the Grande River Basin, Brazil using distributed modeling. *Catena*, 79, 49-59
- Bez, P.K., & Krishna, A.P. (2014). Geospatial assessment of erosional behaviour of a watershed in Angara block of Ranchi district, Jharkhand. *Indian Journal of Soil Conservation*, 42(1), 107-113.
- Bharteey, P.K., Deka, B., Dutta, M., Goswami, J., & Saikia, R. (2023). Geospatial variability of soil physico-chemical properties of Moridhal watershed in Dhemaji district of Assam, India using remote sensing and GIS. *Annals of Plant and Soil Research*, 25(1): 99-109.
- Bhattacharyya, R., Ghosh, B. N., Mishra, P. K., Mandal, B., Rao, C. S., et al. (2015). Soil Degradation in India: Challenges and Potential Solutions. *Sustainability*, 7(4), 3528-3570. <https://doi.org/10.3390/su7043528>.
- Borgohain, S., Deka, B., Dutta, M., Thakuria, R.K., & Patgiri, D.K. (2021). Geospatial assessment of water induced soil and nutrient erosion in Pabho watershed of Assam, India using USLE model. *Journal of Environmental Biology*, 42, 406-413.
- Brady, N.C., & Weil, R.C. (2012). *The nature and properties of soils*. Pearson education, New Delhi
- Dabral, R., Choudhury, A., Barman, M., & Pandey, P. K. (2016). Determination of erodibility under different land uses in the vicinity of Nirjuli, Arunachal Pradesh. *Journal of Soil Water Conservation*, 15(4), 292-295.

- Das, R., Gogoi, B., & Jaiswal, M. K. (2020). Soil loss assessment in Sadiya Region, Assam, India using remote sensing and GIS. *Indian Journal Science Technology*, 13(23), 2319–2327.
- Debnath, P., Mahanta, M., & Ghosh, S.K. (2009). Distribution of available boron in the selected surface and subsurface soils of Terai zone of West Bengal in relation to physico-chemical properties. *Journal of Maharashtra Agriculture University*, 3, 357–358.
- Deka, B., & Dutta, M. (2016). Principal component analysis of soil properties in assessing erodibility indices in the Northern Brahmaputra plains of Assam. *Journal of Soil Water Conservation*, 15, 277–283.
- Deka, B., Barua, T.C., Dutta, M., & Patgiri, D.K. (2009). Landscape soil relationship and pedogenic evaluation of soils in Ghiladhari watershed of the Brahmaputra Valley of Assam. *Journal of Indian Society of Soil Science*, 60, 92–100.
- Deka, B., Baruah, T.C., Dutta, M., & Neog, P. (2011). Soil loss estimation on RS data and GIS techniques in Ghiladhari Watershed of Northern Brahmaputra Valley in Assam. *Journal of Soil Water Conservation*, 10, 123–128.
- Deka, B., Maruthi, Sankar, G.R., Dutta, M., Baruah, T.C., Pushpanjali, et al. (2017). Assessment of fertility potential for the soils of Northern Brahmaputra valley zone using Principal Component Analysis. *Indian Journal of Soil Conservation*, 45, 1–11.
- Dutta, M., & Barkakoty, P.K. (1996). Evaluation of some physical characteristics of Charaipani irrigation project command area. *Journal of Agriculture Science Society North East India*, 9, 135–140.
- Fernandez, C., Wu, J.Q., McCool, D.K., & Stöckle, C.O. (2003). Estimating water erosion and sediment yield with GIS, RUSLE, and SEDD. *Journal of Soil Water Conservation*, 58(3), 128–136.
- Ganasri, B.P., & Ramesh, H. (2016). Assessment of soil erosion by RUSLE model using remote sensing and GIS: A case study of Nethravathi Basin. *Geoscience Frontiers*, 7(6), 953–961.
- Getu, L. A., Nagy, A., & Addis, H. K. (2022). Soil loss estimation and severity mapping using the RUSLE model 625 and GIS in Megech watershed, Ethiopia. *Environmental Challenges*, 8, 100560. <https://doi.org/10.1016/j.envc.2022.100560>
- Jensen, J.R. (1986). *Introductory Digital Image Processing – A Remote Sensing Perspective*. Prentice Hall, Englewood Cliff, New Jersey, USA.
- Kandpal, H., Kumar, A., Reddy, C.P., & Malik, A. (2018). Geomorphologic parameters-based prioritization of hilly sub-watersheds using remote sensing and geographical information system. *Journal of Soil Water Conservation*, 17(3), 232–240.
- Katsuyuki, M. (2009). Soil and humanity: Culture, civilization, livelihood and health. *Soil Science Plant Nutrition*, 55, 603–615.
- Keesstra, S., Pereira, P., Novara, A., Brevik, E. C., Azorin-Molina, C., et al. (2016). Effects of soil management techniques on soil water erosion in apricot orchards. *Science Total Environment*, 551, 357–366.
- Klute, A. (1965). Laboratory measurement of hydraulic conductivity of unsaturated soil. In C.A. Black, D.D. Evans, L. E. Ensminger, J.L. White, F. E. Clark (Eds.) *Methods of Soil Analysis, Mono. 9, Part 1* (pp. 253–261). American Society of Agronomy, Madison, WI.
- Meena, N.K., Gautam, R., Tiwari, P., & Sharma, P. (2017). Nutrient losses due to soil erosion. *Journal of Pharmacognosy Phytochemistry*, 2017 (SP 1), 1009–1011.
- Middleton, H.E. (1930). Properties of soils which influence erosion. *U.S. Department of Agriculture Technical Bulletin*, 178, 1–16.
- Molla, T., & Sisheber, B. (2017). Estimating soil erosion risk and evaluating erosion control measures for soil conservation planning at Koga watershed in the highlands of Ethiopia. *Solid Earth*, 8(1), 13–25.
- Oku, E., Essoka, A., & Thomas, E. (2010). Variability in soil properties along an udalf toposequence in the humid forest Zone of Nigeria. *Kasetsart Journal (Natural Science)*, 44, 564–573.
- Parveen, R., & Kumar, U. (2012). Integrated approach of Universal Soil Loss Equation (USLE) and Geographical Information System (GIS) for soil loss risk assessment in Upper South Koel Basin, Jharkhand. *Journal of Geographical Systems*, 4, 588–596.
- Pham, T.G., Nguyen, H.T., & Kappas, M. (2018). Assessment of soil quality indicators under different agricultural land use and topographic aspects in Central Vietnam. *International Soil and Water Conservation Research*, 6(4), 280–288.
- Pimental, D. (2006). Soil erosion: A food and environmental threat. *Environ Dev Sustainability* 8, 119–137.
- Piper, C.S. (1966). *Soil and Plant Analysis*. University of Adelaide, Australia.
- Potdar, S.S., Srivastava, R., Nagaraju, M.S.S., Prasad, J., & Saxena R.K. (2003). Mapping of erosional soil loss in Nanda-Khairi watershed of Nagpur district of Maharashtra using remotely sensed data and GIS techniques. *Agropedology*, 13, 10–18.

- Pradhan, B., Chaudhari, A., Adinarayana, J., & Buchroithner, M.F. (2012). Soil erosion assessment and its correlation with landslide events using remote sensing data and GIS: a case study at Penang Island, Malaysia. *Environment Monitoring Assessment*, 184(2), 715-727.
- Prasuhn, V., Liniger, H., Gisler, S., Herweg, K., Candinas, A., & Clément, J.P. (2013). A high-resolution soil erosion risk map of Switzerland as strategic policy support system. *Land Use Policy*, 32, 281-291.
- Rawat, J.S., & Rawat, M.S. (1994). Accelerated erosion and denudation in the Nana kosi watershed, Central Himalaya, India, Part I: Sediment load. *Mountain Research and Development*, 14 (1), 25-38
- Raymo, M.E., & Ruddiman, W.F. (1992). Tectonic forcing of Late Cenozoic climate. *Nature*, 359, 117- 122.
- Renard, K.G., Foster, G.R., Weesies, G.A., McCool, D.K., & Yoder, D.C. (1997). Predicting soil erosion by water - a guide to conservation planning with the Revised Universal Soil Loss Equation (RUSLE). *USDA-ARS Handbook No. 703*, United States Government Printing Office, Washington, DC.
- Richards, L.A. (1948). Pressure membrane apparatus, construction and use. *Agriculture Engineering*, 28, 451-454.
- Saha, R., Mishra, K. V., & Khan, K. S. (2011). Soil erodibility characteristics under modified land-use systems as against shifting cultivation in hilly ecosystems of Meghalaya, India. *Journal of Sustainable Forestry*, 30, 301-312
- Sahi, B.P., Singh, S.N., Sinha, A.C., & Acharya, B. (1977). Erosion Index – A new index of soil erodibility. *Journal of Indian Society Soil Society*, 25, 7-10.
- Sasang Guite, L., & Bora, A. (2016). Impact of River Bank Erosion on Land Cover in Lower Subansiri River 701 Flood Plain. *International Journal of Scientific and Research Publications*, 6(5), 480-486.
- Shinde, V., Tiwari, K.N., & Singh, M. (2010). Prioritization of micro watersheds on the basis of soil erosion hazard using remote sensing and geographic information systems. *Journal of Water Resources Planning and Management*, 2(3), 130-136.
- Singh, G., & Panda, R.K. (2017). Grid-cell based assessment of soil erosion potential for identification of critical erosion-prone areas using USLE, GIS and remote sensing: A case study in the Kapgari watershed, India. *International Journal of Soil Water Conservation Research*, 5(3), 202-211.
- Singh, M. J., & Khera, K. L. (2008). Soil erodibility indices under different land uses in lower Shiwaliks. *Tropical Ecology*, 49(2), 113-119.
- Srinivasan, R., Singh, S.K., Nayak, D.C., Hegde, R., & Ramesh, M. (2019). Estimation of soil loss by USLE Model using Remote Sensing and GIS Techniques - A Case study of Coastal Odisha, India. *European Journal of Soil Science*, 8(4), 321-328.
- Thapa, P. (2020). Spatial estimation of soil erosion using RUSLE modeling: a case study of Dolakha district, Nepal. *Environmental System Research*, 9(1), 15.
- Tiruwa, D.B., Khanal, B.R., Lamichhane, S., & Acharya, B.S. (2021). Soil erosion estimation using Geographic Information System (GIS) and Revised Universal Soil Loss Equation (RUSLE) in the Siwalik Hills of Nawalparasi, Nepal. *Journal of Water and Climate Change*, 12(5), 1958-1974. doi: 10.2166/wcc.2021.198.
- Valdiya, K.S. (1985). Accelerated erosion and landslide-prone zones in the central Himalaya. In J.S. Singh (Eds.) *Environmental regeneration in Himalaya: concepts and strategies* (pp. 12-38). Nainital: Central Himalayan Environmental Association and Gynodaya Prakashan.
- Walkey, A., & Black, I.A. (1934). Determination of organic matter in soil. *Soil Science*, 37, 549-556.
- Wolka, K., Mulder, J., & Biazin, B. (2018). Effects of soil and water conservation techniques on crop yield, runoff and soil loss in Sub-Saharan Africa: A review. *Agricultural Water Management*, 207, 67-79. doi: 10.1016/j.agwat.2018.05.016.
- Wischmeier, W.H., & Smith, D.D. (1978). *Predicting rainfall erosion losses - a guide to conservation planning*. Agriculture Handbook No. 537, U.S. Department of Agriculture.
- Wischmeier, W.H., Johnson, C.G., & Cross, B.V. (1971). Soil Erodibility monograph for farm land conservation sites. *Journal of Soil Water Conservation*, 26, 189-193.
- Yoder, R.E. (1936). A direct method of aggregate analysis and a study of the physical nature of erosion losses. *Journal of American Society*, 28, 337-351.







Journal of Experimental Biology and Agricultural Sciences

<http://www.jebas.org>

ISSN No. 2320 – 8694

Dehydrogenase: A key soil health indicator for Thar Desert, India

Akhilesh Chaurasiya¹ , Neelam Jain^{2*} , Ram Pyare³ , G.K. Aseri^{1*} 

¹Amity Institute of Microbial Technology, Amity University Rajasthan, Jaipur India (303002)

²Amity Institute of Biotechnology, Amity University Rajasthan, Jaipur India (303002)

³C.S.A. University of Agriculture & Technology Kanpur, Uttar Pradesh, India (208002)

Received – October 12, 2024; Revision – November 14, 2024; Accepted – December 30, 2024

Available Online – January 15, 2025

DOI: [http://dx.doi.org/10.18006/2024.12\(6\).876.886](http://dx.doi.org/10.18006/2024.12(6).876.886)

KEYWORDS

Soil biology
 Micronutrients
 Soil fertility
 Rhizosphere
 Nutrient uptake

ABSTRACT

A field study was conducted to identify a potential fertility indicator for the soils of the Thar Desert. The study area included eight districts, covering a total of 156,580 km². This region experiences a wide range of climatic conditions, with annual rainfall varying from 177 mm to 409 mm and temperatures fluctuating between 8°C and 46°C. Surface soil samples (0-10 cm depth) were collected from agricultural fields across the region, representing various soil properties and cropping patterns. The soil texture varied from sandy loam to loamy sand, and the wet colour ranged from dark reddish-brown to dark yellowish-brown. The physicochemical and biological properties of the soil samples from different areas of the Thar Desert were as follows: moisture content ranged from 2.19% to 8.73%, bulk density from 1.18 to 1.33 Mg/m³, particle density from 1.82 to 4.11 Mg/m³, pore space percentage from 26.74% to 68.53%, solid space percentage from 31.47% to 73.26%, pH values from 7.69 to 8.43, and electrical conductivity from 0.12 to 0.17 dS/m. Furthermore, the soil organic carbon content ranged from 0.82% to 1.21%, while organic matter content varied between 1.41% and 2.09%. The available nitrogen was found to be between 285.69 and 365.87 kg/ha, phosphorus ranged from 19.84 to 24.77 kg/ha, potassium levels ranged from 214.29 to 314.72 kg/ha, and sulfur levels varied between 16.08 and 23.62 ppm. Additionally, nitrogenase retention time was recorded at 1.391 to 1.547 minutes, phosphatase activity ranged from 269.44 to 343.15 µg p-nitrophenol g⁻¹ h⁻¹, and dehydrogenase enzyme activity ranged from 250.33 to 309.34 µg TPF/g/24 h. The results demonstrated that soil properties varied across the Thar Desert. This study provided valuable insights into the physicochemical and biological characteristics of

* Corresponding author

E-mail: gkaseri@jpr.amity.edu (G.K. Aseri);

njain1@jpr.amity.edu (Neelam Jain)

Peer review under responsibility of Journal of Experimental Biology and Agricultural Sciences.

Production and Hosting by Horizon Publisher India [HPI]
 (<http://www.horizonpublisherindia.in/>).
 All rights reserved.

All the articles published by [Journal of Experimental Biology and Agricultural Sciences](#) are licensed under a [Creative Commons Attribution-NonCommercial 4.0 International License](#) Based on a work at www.jebas.org.



the soil in the Thar Desert of Rajasthan, India. Notably, a significant positive correlation (r^2 value of 0.95) was found between dehydrogenase enzyme activity and various soil fertility parameters, suggesting that dehydrogenase could serve as a potential biological indicator of soil fertility.

1 Introduction

The Thar Desert, also known as the Great Indian Desert, covers about 70% of Rajasthan's total landmass, earning it the nickname "Desert State of India." The desert spans approximately 446,000 square kilometres, with around 208,110 square kilometres of this area in India. The annual rainfall in the region ranges from 177 to 409 mm, while temperatures can vary from 8 to 46°C. Geographically, Rajasthan is situated between 23.30° to 30.120° North latitude and 69.300° to 78.170° East longitude (Kumari et al. 2021). Since immemorial, soil has been one of our most fundamental natural resources, used by humans and other living beings, alongside water and plants. However, improper management of these resources has disrupted ecological balance, agricultural productivity, and biodiversity (Rajshri et al. 2021). Soil is a valuable resource crucial in fulfilling our food and fibre needs by providing a medium for plant growth (Naphade et al. 2021). Factors such as soil fertility, management techniques, and climate can significantly impact agricultural yield. While natural elements influence soil fertility, they can often be controlled to enhance the soil's ability to provide essential nutrients to plants (Av and Ghabane 2018).

Its texture and structure influence soil fertility, affecting water retention, aeration, and root penetration. Soils with good structure and texture foster root development and plant nutrient uptake. Organic matter is vital for productive soil, as it contributes nutrients, enhances soil structure, improves water retention, and encourages beneficial microbial activity. Decomposed organic matter gradually releases nutrients that improve soil fertility over time (Wolf et al. 2023). Fertile soil contains adequate amounts of critical macronutrients and micronutrients, such as nitrogen, phosphorus, potassium (NPK), and sulfur. Soil fertility is affected by various microorganisms, including bacteria, fungi, earthworms, and decomposers. These organisms play essential roles in nutrient cycling, organic matter decomposition, and soil aggregation, all contributing to soil health and fertility (Tale and Ingole 2015).

Enzymes present in the soil have been widely studied for their significant contributions to soil fertility, as they facilitate biochemical processes necessary for nutrient cycling, organic matter decomposition, and overall soil health (Meena and Rao 2021). Soil microorganisms, plant roots, and decomposing organic matter produce these enzymes. Notably, phosphatase enzymes hydrolyze organic phosphorus compounds into inorganic phosphate, making phosphorus available for plant uptake. Phosphatase activity is critical for releasing phosphorus from organic matter (Margalef et al. 2017). Nitrogenase enzymes play a vital role in biological nitrogen fixation,

converting atmospheric nitrogen (N_2) into ammonia (NH_3) or ammonium (NH_4^+). This process provides an essential nitrogen source for plant nutrition while enhancing soil fertility by increasing nitrogen levels (Threatt and Rees 2023).

Dehydrogenase activity indicates microbial metabolic activity in the soil and is frequently used to assess soil microbial health. Dehydrogenase enzymes are involved in oxidation-reduction reactions within microbial cells; higher activity levels in fertile soil indicate a robust microbial community, contributing to improved soil fertility (Aseri and Tarafdar 2006). The future of sustainable agriculture relies on maintaining long-term soil fertility, environmental conservation, and global food security amid challenges such as climate change, population growth, and land degradation. This study assesses soils' physicochemical and biological characteristics from various regions within the Thar Desert, Rajasthan. Understanding soil health indicators that reflect overall soil fertility is vital for comprehending the soil ecosystem and predicting future agricultural productivity.

2 Materials and methods

2.1 Soil sampling

Soil samples were collected from eight locations in the Thar Desert, spanning Rajasthan, India. The selected areas include (1) Sikar, (2) Jhunjhunu, (3) Churu, (4) Nagaur, (5) Bikaner, (6) Barmer, (7) Jodhpur, and (8) Jaisalmer (Figure 1). Samples were taken from a depth of 0-10 cm. The locations of the soil samples were recorded using a GIS system on a portable mobile app (Table 1). After collection, the samples were processed and analyzed for their physicochemical and biological properties using standard laboratory techniques.

2.2 Field History

A field history of cultivation practices and rainfall data for 2022-2023 has been recorded in Table 1.

2.3 Characterization of physical properties of soil

The soil samples were sieved through a 2mm mesh to analyze their physical properties. This included determining soil texture using the Bouyoucos hydrometer method (1927), assessing soil colour with the Munsell soil colour chart (1954), and measuring soil moisture using the gravimetric method outlined by Taylor (1955). Additionally, we determined bulk density, particle density, percent pore space, and percent solid space using a 100 ml graduated measuring cylinder, following the method described by Muthuvel et al. (1992).

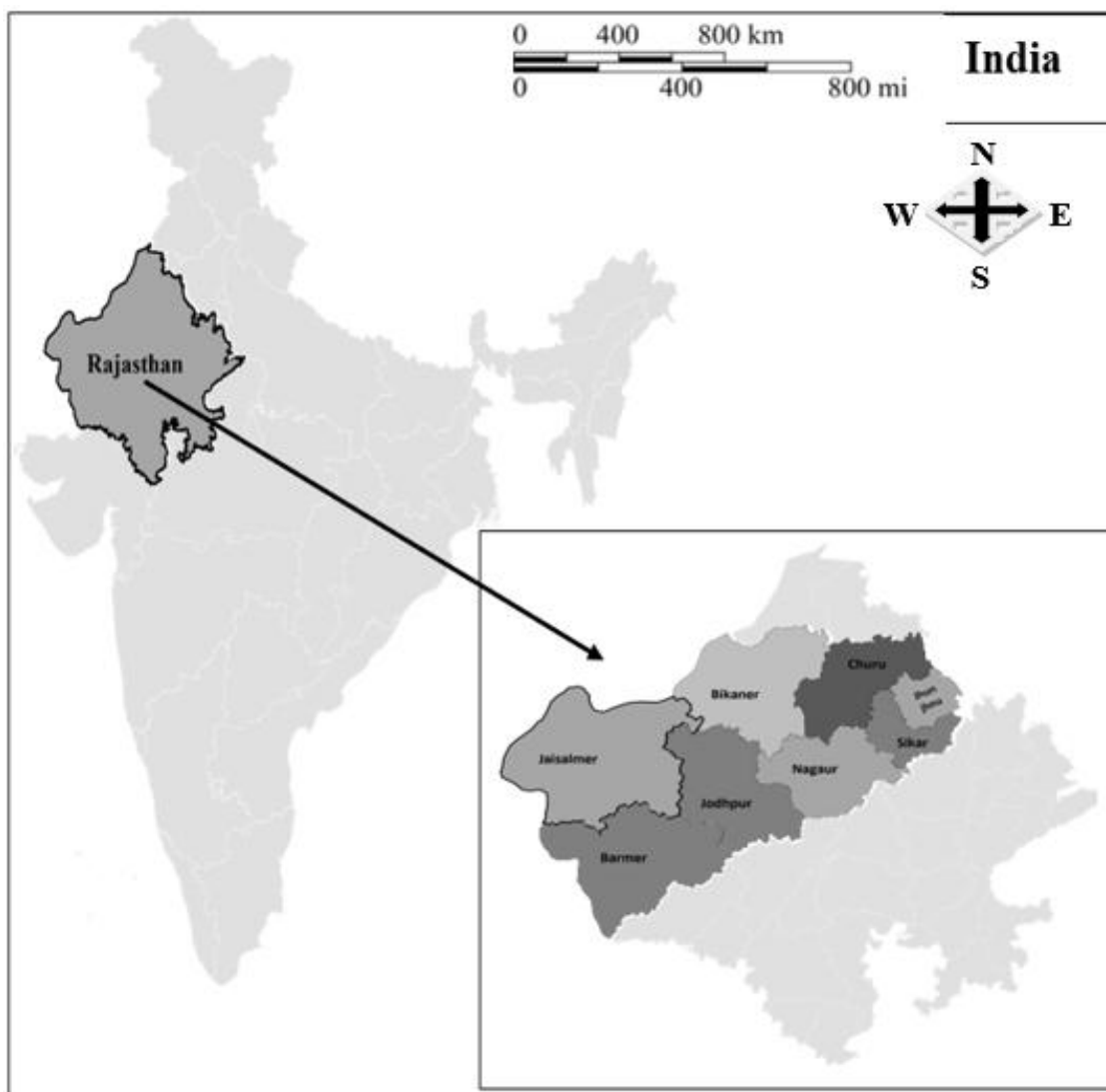


Figure 1 Map showing the soil sample locations from various regions of the Thar Desert, Rajasthan

Table 1 Soil field history of various regions of the Thar Desert, Rajasthan District's

S. No	Area	Field history of Thar Desert soil			
		Latitude(N)	Longitude (E)	Rainfall (mm)	Temperature (°C)
1.	Sikar	27.6094° N	75.1398° E	407.1	10-36
2.	Jhunjhunu	28.1317° N	75.4022° E	408.8	9-37
3.	Churu	28.2925° N	74.9707° E	334.2	8-38
4.	Nagaur	27.1983° N	73.7493° E	369.5	9-38
5.	Bikaner	28.0229° N	73.3119° E	247.2	9-42
6.	Barmer	25.7521° N	71.3967° E	272.7	12-43
7.	Jodhpur	26.2389° N	73.0243° E	292.6	12-40
8.	Jaisalmer	26.9157° N	70.9083° E	176.9	12-46

2.4 Characterization of chemical properties of soil

The chemical properties of soil, including pH (Jackson 1958) and electrical conductivity (EC), are measured using a digital EC meter (Wilcox 1950). Organic carbon (OC) and organic matter (OM) are determined by the wet-oxidation method or rapid titration method (Walkley 1947). Available nitrogen is assessed using the Kjeldahl method (Subbiah and Asija 1956). The amount of accessible phosphorus is calculated using a spectrophotometer with the colourimetric technique (Olsen et al. 1954). Potassium is measured with a flame photometer (Toth and Prince 1949). The turbidometric approach estimates the available sulfur (Chesnin and Yien 1950).

2.5 Characterization of biological properties of soil

The biological properties of soil, such as nitrogenase activity, were measured using the gas chromatography (GC) method (Dilworth 1966). The soil's dehydrogenase activity (Casida et al. 1964) and phosphatase activity (Tabatabai and Bremner 1969) were determined using a spectrophotometer.

2.6 Statistical analysis

Statistical analysis of the data was performed using Microsoft Excel 365, including calculations for standard error and the creation of bar graphs.

3 Results & Discussion

3.1 Physical parameters of Thar desert soil

The observed soil texture in the Thar Desert of Rajasthan ranged from sandy loam to loamy sand. In wet conditions, the soil colour varied from dark reddish-brown (2.5YR2/3) to dark yellowish-brown (10YR4/4), while in dry conditions, it changed from reddish-brown (2.5YR4/3) to yellowish-brown (10YR5/4). Soil moisture at different depths ranged from 2.19% to 8.73% (Table 2). The bulk density of the soil samples varied across different areas of the Thar Desert, ranging from 1.18 to 1.33 Mg m⁻³ (Table 3), and it was observed to increase with depth. Additionally, the particle density ranged from 1.82 to 4.11 Mg m⁻³ (Table 3),

Table 2 Physical properties of Soil from various regions of Thar Desert, Rajasthan

S. No	Area	Physical properties of soil at 0-10 cm depth			
		Soil Texture	Soil Colour		Soil Moisture (%) [*]
			Wet condition	Dry condition	
1.	Sikar	Sandy loam	Dark reddish brown	Reddish brown	8.00 ± 0.83
2.	Jhunjhunu	Sandy loam	Dark reddish brown	Reddish brown	7.06 ± 0.87
3.	Churu	Sandy loam	Dark reddish brown	Reddish brown	8.73 ± 0.24
4.	Nagaur	Sandy loam	Dark reddish brown	Reddish brown	7.65 ± 0.91
5.	Bikaner	Loamy sand	Dark yellowish brown	Yellowish brown	2.65 ± 0.86
6.	Barmer	Loamy sand	Dark yellowish brown	Yellowish brown	2.19 ± 0.91
7.	Jodhpur	Loamy sand	Dark yellowish brown	Yellowish brown	3.47 ± 1.01
8.	Jaisalmer	Loamy sand	Dark yellowish brown	Yellowish brown	4.28 ± 1.50

^{*}Data are mean of replicates, ± Standard Error of mean

Table 3 Physical properties of Soil from various regions of Thar Desert, Rajasthan

S. No	Area	Physical properties of soil at 0-10 cm depth			
		BD (Mg m-3)	PD (Mg m-3)	Pore Space (%)	Solid Space (%)
1.	Sikar	1.30 ± 0.02	4.11 ± 0.49	67.50 ± 3.15	32.50 ± 3.15
2.	Jhunjhunu	1.25 ± 0.04	4.11 ± 0.49	68.53 ± 4.45	31.47 ± 4.45
3.	Churu	1.18 ± 0.04	2.17 ± 0.17	45.20 ± 2.58	54.80 ± 2.58
4.	Nagaur	1.25 ± 0.04	2.89 ± 0.24	56.40 ± 2.04	43.60 ± 2.04
5.	Bikaner	1.33 ± 0.04	4.11 ± 0.49	66.43 ± 4.46	33.57 ± 4.46
6.	Barmer	1.33 ± 0.04	2.89 ± 0.24	53.33 ± 3.33	46.67 ± 3.33
7.	Jodhpur	1.30 ± 0.02	2.24 ± 0.14	41.11 ± 4.84	58.89 ± 4.84
8.	Jaisalmer	1.33 ± 0.04	1.82 ± 0.10	26.74 ± 1.03	73.26 ± 1.03

Data are mean of replicates, ± Standard Error of mean

increasing with soil depth. The increase in particle density was linked to factors including soil depth, water quality, and their interaction (Kumar et al., 2018).

These variations were primarily attributed to differences in clay, silt, and organic carbon and the low water holding capacity (WHC) typical of sandy soils due to their high sand concentration and low clay content. An uneven pattern emerged across different soil strata, with increased clay concentration at certain sites improving water-holding capacity. Similar findings were reported by Sharma et al. (2010). The percentage of pore space in the soil varied from 26.74% to 68.53%, while the percentage of solid space ranged from 31.47% to 73.26% (Table 3). Soils with high organic matter content exhibited increased porosity. However, the percentage of pore space decreased with increasing soil depth, a trend consistent with the study conducted by Choudhary et al. (2020).

3.2 Chemical parameters of Thar desert soil

3.2.1 Soil pH

The Thar Desert of Rajasthan soil is primarily neutral to alkaline, with a pH range of 7.69 to 8.43. This finding aligns with studies conducted in the Kanpur region (Saxena et al. 2021). Research shows that the pH of soil in most villages of the Kanpur Nagar district in India ranges from 7.03 to 9.75, indicating that the soil is neutral to alkaline in nature (Ladwani et al. 2012; Saxena et al. 2021). Soil pH is crucial for regulating the solubility and mobility of heavy metals. At acidic pH levels, heavy metals such as nickel, lead, and cadmium become more soluble and bioavailable to plants, as noted by Wang et al. (2018). However, the slightly alkaline pH found in the uncultivated soil of this study is not likely to significantly affect overall soil fertility since these pH values remain close to neutral (Dewangan et al. 2023). Generally, pH values tend to increase with soil depth (Rajshri et al. 2021). Low pH levels may result from a lack of organic matter or insufficient

bacterial activity during nitrification processes in the soil, which produces acids (Ladwani et al. 2012).

3.2.2 Electrical Conductivity (ds m^{-1})

The surface soil samples' electrical conductivity (EC) in the study area ranged from 0.12 to 0.17 dS/m, below one (Table 4). These findings are consistent with those reported by Saxena et al. (2021), who observed similar EC values in most areas of the Kanpur Nagar district in India, ranging from 0.07 to 0.35 dS/m. This suggests that the soil contains safe soluble salts for crop production. Additionally, the decline in electrical conductivity (EC) may be due to the complex precipitation of salts and their subsequent plant uptake. This decrease in EC in cultivated soils agrees with the findings of Geetha et al. (2017). The low EC levels can likely be attributed to good drainage conditions, which facilitate the removal of released bases through percolation, as noted by Ladwani et al. (2012). In summary, the soil in the study area is suitable for crop cultivation due to its low soluble salt content, resulting from effective drainage.

3.2.3 Organic Carbon (%)

The study revealed significant soil organic carbon content variations across different fields and depths. Organic carbon percentages ranged from 0.82% to 1.21% (Table 4). Generally, arid soils in Rajasthan exhibit low organic carbon (OC) content, ranging from 0.01% to 0.84%, with a mean of 0.16%. Most of these soils are deficient in OC, primarily due to high temperatures, low rainfall, sparse vegetation, and sandy texture, which promote rapid oxidation, as reported by several researchers (Singh et al. 2007; Kumar et al. 2011, 2019). These findings align with those of Gautam et al. (2018), who reported organic carbon percentages of 0.10% to 0.59% in the red sandy soils of the Mirzapur district in India. A decline in organic carbon concentration with increasing soil depth was observed, consistent with previous research by

Table 4 Chemical properties of soil from various regions of Thar Desert, Rajasthan

S. No	Area	Chemical properties of soil at 0-10 cm depth			
		Soil pH	Soil EC (ds m^{-1})	Soil OC (%)	Soil OM (%)
1.	Sikar	8.34 ± 0.11	0.14 ± 0.009	0.82 ± 0.01	1.41 ± 0.03
2.	Jhunjhunu	8.43 ± 0.12	0.14 ± 0.009	0.94 ± 0.01	1.62 ± 0.01
3.	Churu	8.39 ± 0.15	0.14 ± 0.006	0.82 ± 0.01	1.41 ± 0.03
4.	Nagaur	7.98 ± 0.09	0.12 ± 0.003	1.04 ± 0.01	1.79 ± 0.01
5.	Bikaner	8.12 ± 0.12	0.15 ± 0.003	1.10 ± 0.01	1.90 ± 0.02
6.	Barmer	7.69 ± 0.10	0.17 ± 0.006	1.06 ± 0.01	1.83 ± 0.02
7.	Jodhpur	8.03 ± 0.06	0.12 ± 0.007	1.21 ± 0.01	2.09 ± 0.02
8.	Jaisalmer	8.33 ± 0.12	0.17 ± 0.006	1.15 ± 0.01	1.99 ± 0.02

Data are mean of replicates, ± Standard Error of mean

Bhatti et al. (2016). This trend is likely due to the higher application of farmyard manure (FYM) and plant residues on the soil surface compared to deeper layers. The study demonstrated that soil organic carbon content varies spatially and vertically, with higher levels typically found in surface soils.

3.2.4 Organic matter (%)

The study revealed significant soil organic matter content variation across different fields and depths. The percentages of organic matter ranged from 1.41% to 2.09% (Table 4). Low organic matter content in soil can be detrimental, as it decreases the soil's ability to absorb heavy metals. A decline in organic matter concentration was observed with increasing soil depth, consistent with previous research conducted by Bhatti et al. (2016).

3.2.5 Available Nitrogen (kg/ha)

The available nitrogen (N) content in soil samples from the Thar Desert ranged from 285.69 to 370.02 kg/ha (Table 5). These findings are consistent with previous research conducted by Bhavya et al. (2018). In contrast, the available nitrogen levels in Bengaluru, Karnataka, ranged from 101.62 to 122.85 kg/ha. The results indicate a significant decrease in enzyme activity in forest soils compared to desert soils. This difference may be attributed to excess nitrogen deposition and soil acidification in forest ecosystems, as Zhong et al. (2022) reported. The nitrogen levels indicate low availability in the soil, which decreases with increasing soil depth. Additionally, these values are below the recommended limits established by Jaiswal (2014), suggesting nitrogen deficiency in the soil. Like the Thar Desert, nitrogen content decreases with increasing soil depth.

3.2.6 Available Phosphorus (kg/ha)

Available phosphorus (P) levels in soil samples varied from 19.84 to 24.77 kg/ha across different fields and depths (Table 5). Similar

findings were reported in a previous study, which indicated that available phosphorus in soils showed significant variability, ranging from 1.19 to 96.6 kg/ha, with a mean of 13.3 kg/ha. This suggests a low to medium phosphorus status. Notably, 48.7% of the area had low P levels, while 46.9% exhibited medium P content. The deficiency of phosphorus in arid soils can be attributed to their inherently low P status, low organic matter content, and the formation of calcium phosphate (Ca-P) in soils with high calcium carbonate (CaCO₃) concentrations (Kumar et al. 2021). The phosphorus levels observed fall within the suggested upper limit provided by Jaiswal (2014), indicating sufficient phosphorus for optimal crop growth. Higher phosphorus concentrations were recorded in the topsoil layers. These findings are consistent with the previous research conducted by Bhavya et al. (2018). Similarly, in Bengaluru, Karnataka, available phosphorus in the soil ranged from 24.51 to 26.56 kg/ha, decreasing with soil depth. These levels were classified as medium, suggesting suitable soil conditions for crop production. The variation in phosphorus content across different mound segments likely correlates with the clay content of the mound soil, as reported by Lopez Hernandez et al. (2006). As observed in the study area, phosphorus concentrations were highest in the surface layer and decreased with increased depth.

3.2.7 Available Potassium (kg/ha)

The available potassium (K) concentrations in soil samples ranged from 214.29 to 314.72 kg/ha (Table 5). These findings align with previous research by Khanday et al. (2018) and Abba et al. (2014), which reported available potassium levels between 290.03 and 397.45 kg/ha in the Ganderbal district of Kashmir Valley, India. Several factors likely contribute to the higher available potassium observed in the surface layers, including the intense weathering of potassium-bearing minerals, the release of readily available potassium from decomposing organic materials, the application of potassium fertilizers, and the upward movement of potassium from

Table 5 Available N, P, K, and S from soils of various regions of Thar desert, Rajasthan

S. No	Area	Soil macronutrients (at 0-10 cm depth)			
		Available N (kg/ha)	Available P (kg/ha)	Available K (kg/ha)	Available S (ppm)
1.	Sikar	285.69 ± 3.07	19.87 ± 0.37	214.29 ± 1.35	16.12 ± 0.45
2.	Jhunjhunu	317.73 ± 1.37	22.52 ± 0.21	265.81 ± 2.61	17.21 ± 0.40
3.	Churu	292.51 ± 7.05	19.84 ± 0.33	226.24 ± 1.71	16.08 ± 0.30
4.	Nagaur	338.34 ± 3.66	23.74 ± 0.13	228.48 ± 2.33	16.62 ± 0.33
5.	Bikaner	348.04 ± 4.27	24.67 ± 0.10	284.11 ± 2.92	21.08 ± 0.25
6.	Barmer	347.58 ± 2.60	23.43 ± 0.16	238.19 ± 2.27	19.16 ± 0.33
7.	Jodhpur	370.02 ± 9.11	24.77 ± 0.12	314.72 ± 1.29	23.62 ± 0.29
8.	Jaisalmer	365.87 ± 8.12	24.73 ± 0.13	288.96 ± 2.96	22.50 ± 0.26

Data are mean of replicates, ± Standard Error of mean

lower depths through the capillary rise of groundwater. The study revealed that the available potassium status was adequate across the entire study area at various depths. Notably, potassium availability was highest in the topsoil and decreased rapidly with increasing depth (Bhavya et al. 2018).

3.2.8 Available Sulphur (ppm)

The available sulfur (S) levels in soil samples were sufficient, ranging from 16.08 to 23.62 ppm across various fields and depths (Table 5). These levels indicate an adequate supply of sulfur in the soil, which aligns with the findings of Kour and Jalali (2008) regarding sulfur availability in different agro-climatic zones of the Jammu Region, India. The high sulfur content observed in the surface horizons is likely due to increased organic matter. The highest concentration of available sulfur was found in the topsoil, with a gradual decrease noted as soil depth increased (Saxena et al. 2021).

3.3 Biological Parameters

3.3.1 Dehydrogenase activity

Soil dehydrogenase activity (DHA) was measured spectrophotometrically, ranging from 250.33 to 309.34 $\mu\text{g TPF/g/24h}$ (Table 6). These results are consistent with previous research by Adak et al. (2014), which examined dehydrogenase activity in typical Ustocrepts soil under subtropical conditions in Lucknow, India. In contrast to their typically nutrient-limited state, desert soils with increased nitrogen (N) levels may have overcome these limitations. The potential abundance of nitrogen could support the survival and reproduction of a broader range of bacteria, thereby promoting greater bacterial diversity (Chen et al. 2024). Additionally, increased dehydrogenase activity and microbial biomass were associated with higher nutrient inputs. Furthermore, soil management practices influence soil

dehydrogenase activity and strongly correlate with organic matter content (Kaur and Kaur 2021).

3.3.2 Phosphatase activity

Soil phosphatase activity was measured spectrophotometrically, with values ranging from 269.44 to 343.15 $\mu\text{g p-nitrophenol g}^{-1} \text{h}^{-1}$ (Table 6). These results are consistent with those reported by Margalef et al. (2017) and align with global patterns of phosphatase activity observed in natural soils. It is important to note that various factors, such as soil type and climate across different biomes, influence phosphatase activity. A strong correlation between phosphatase activity and indicators like precipitation suggests that ecosystem productivity significantly affects phosphate cycling.

3.3.3 Nitrogenase activity

Nitrogenase activity was assessed by measuring the conversion of acetylene (C_2H_2) to ethylene (C_2H_4) using gas chromatography, with retention times ranging from 1.391 to 1.547 minutes (Table 6). These results are consistent with those reported by Wu et al. (2009) regarding nitrogenase activity in the biological soil crusts of the Gurbantunggut Desert in Northwestern China. Nitrogen fixation in all crusts is vital in maintaining soil fertility in sparsely vegetated areas and provides fixed nitrogen to nearby plants. These findings indicate that species composition should be considered when estimating nitrogen inputs in desert ecosystems.

Dehydrogenase activity (DHA) shows a strong positive correlation (r) with other parameters, and its regression r^2 value is 0.95 (Table 7). This indicates that DHA is a reliable indicator of other soil health parameters, making it an excellent measure for assessing healthy soils (Figure 2). It is well established that the excessive use of fertilizers in recent years has led to the degradation of many productive fields. Identifying and measuring soil qualities has

Table 6 Dehydrogenase, Phosphatase, and Nitrogenase activity from soils of various regions of Thar desert, Rajasthan

S. No	Areas	Biological properties of soil at 0-10 cm depth.		
		Dehydrogenase (Conc.) ($\mu\text{g TPF g}^{-1}24\text{h}^{-1}$)	Phosphatase (Conc.) ($\mu\text{g p-nitrophenol gh}^{-1}$)	Nitrogenase (Conc.) ($\text{nmol C}_2\text{H}_4 \text{ m}^{-2}\text{h}^{-1}$)
1.	Sikar	250.33 \pm 2.84	268.02 \pm 0.82	1.391 \pm 0.04
2.	Jhunjhunu	270.00 \pm 1.42	293.54 \pm 0.96	1.425 \pm 0.03
3.	Churu	260.16 \pm 1.42	277.84 \pm 0.84	1.403 \pm 0.04
4.	Nagaur	278.20 \pm 0.82	300.19 \pm 0.57	1.449 \pm 0.03
5.	Bikaner	291.31 \pm 2.17	329.36 \pm 0.27	1.515 \pm 0.03
6.	Barmer	288.03 \pm 0.82	313.83 \pm 0.57	1.516 \pm 0.02
7.	Jodhpur	309.34 \pm 1.42	342.36 \pm 0.57	1.547 \pm 0.03
8.	Jaisalmer	301.97 \pm 1.42	333.80 \pm 0.42	1.513 \pm 0.02

Data are mean of replicates, \pm Standard Error of mean

Table 7 Matrix of linear correlation (r) between enzymes with chemical parameters of Thar desert, Rajasthan

S. No	Parameters	Dehydrogenase	Phosphatase
1.	pH	0.455	0.418
2.	EC	0.155	0.178
3.	Organic Carbon	0.982**	0.976**
4.	Organic Matter	0.983**	0.977**
5.	Available Nitrogen	0.983**	0.970**
6.	Available Phosphorus	0.926**	0.937**
7.	Available Potassium	0.853**	0.881**
8.	Available Sulfur	0.936**	0.951**

$p < 0.05$; ** $p < 0.01$; EC – Electrical conductivity

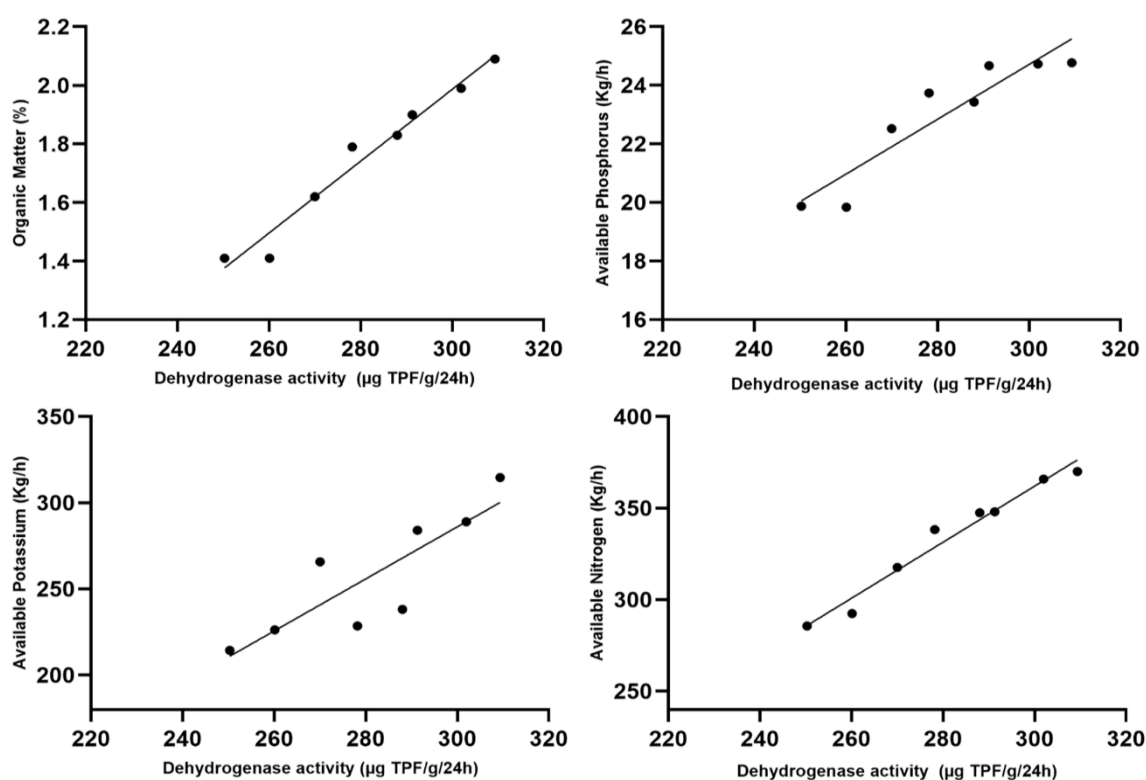


Figure 2 Linear regression equation between dehydrogenase activity and organic matter, available (N, P, K)

become increasingly important to prevent further deterioration. Robust soil health data is essential for providing farmers with reliable recommendations to restore soil fertility.

To maintain ecosystem sustainability and stability, it is crucial to implement appropriate actions, including rigorous soil health monitoring, particularly in degraded agricultural lands. Dehydrogenase as an indicator can help us understand the soil ecosystem and its ability to support cultivation, which will, in turn, enhance the agricultural economy.

Soil dehydrogenase activity is a critical aspect of overall soil enzymatic activity and serves as a sensitive indicator of various environmental factors, both biotic and abiotic. It reflects the health of soil microorganisms, and any deviations from normal activity may indicate ecosystem disturbances or the presence of toxic substances. By assessing dehydrogenase activity, we gain valuable insights into soil health. Healthy soils with high dehydrogenase activity are often associated with elevated levels of other enzymes, such as phosphatase and nitrogenase, as well as readily available nutrients, including nitrogen, phosphorus, potassium, and sulfur.

This information can guide sustainable agricultural practices and improve crop yields. A deeper understanding of the role of this enzyme can further enhance its use as a diagnostic tool for soil health management.

The Thar Desert, also known as the Great Indian Desert, is a vast arid region in the northwestern part of the Indian subcontinent. Although the soil fertility in the Thar Desert is generally considered medium, there can be significant variations across different areas. The activity of the dehydrogenase enzyme serves as a valuable indicator of soil health and fertility. By measuring this enzyme's activity, scientists and farmers can gain important insights into the overall microbial health of the soil. However, it is essential to recognize that the effectiveness of dehydrogenase activity as a soil health indicator may vary based on specific soil and environmental conditions.

Conclusions

This study concluded that soil fertility, nutrient concentrations, and enzymatic activities, specifically dehydrogenase, are important indicators of soil health. Soil microbial biomass significantly influences various soil enzymes, including phosphatase, nitrogenase, and dehydrogenase, along with organic carbon and the availability of nutrients such as nitrogen (N), phosphorus (P), potassium (K), and sulfur. Analysis of soil parameters in selected areas of the Thar Desert, particularly Jodhpur and Jaisalmer, revealed favourable conditions for crop growth. The soil in these regions exhibited a texture ranging from sandy loam to loamy sand, a neutral to alkaline pH, and normal electrical conductivity. While sufficient sulfur was present in the topsoil, organic carbon, organic matter, and nitrogen levels were moderate. Additionally, potassium and phosphorus levels were in the medium range. A decrease in bulk density was inversely correlated with organic matter content. The correlation of dehydrogenase with various soil fertility parameters was positive, indicating that dehydrogenase activity strongly indicates biological activity and soil fertility. Combining organic inputs, such as farmyard manure, with inorganic nutrient sources is recommended to maintain soil fertility. Given its favourable fertility status and productivity, the soil in the Thar Desert is suitable for cultivating various crops, including legumes, cotton, maize, mustard, and wheat. Furthermore, dehydrogenase activity can be a reliable indicator for assessing soil health. Monitoring this activity provides valuable insights into soil quality, allows for evaluating the impact of different management practices, and aids farmers and researchers in making informed decisions to promote sustainable agricultural practices.

Acknowledgement

The authors are thankful to the Department of Soil Science and Agricultural Chemistry at Chandra Shekhar Azad University of

Agriculture, Technology, and Sciences in Kanpur, Uttar Pradesh. They are also grateful to DST-FIST (SR/FST/LS-1/2019/502) for enhancing the department's research infrastructure supporting this study.

Conflict of interest

The authors declare no conflict of interest.

References

- Abba, H.M., Sawa, F.B.J., Gani, A.M., Abdul, S. D., & Iliyaches, M. (2014). Soil Physico Chemical Characteristics of Kanawa Forest Reserve (KFR), Gombe State, Nigeria. *IOSR Journal of Environmental Science, Toxicology and Food Technology*, 10(2), 68-75.
- Adak, T., Singha, A., Kumar, K., Shukla, S.K., Singh, A., & Singh, V.K. (2014). Soil organic carbon, dehydrogenase activity, nutrient availability, and leaf nutrient content as affected by organic and inorganic sources of nutrients in mango orchard soil. *Journal of Soil Science and Plant Nutrition*, 14(2), 394-402. <http://dx.doi.org/10.4067/s0718-95162014005000031>
- Aseri, G.K., & Tarafdar, J.C. (2006). Fluorescein diacetate: a potential biological indicator for arid soils. *Arid Land Research and Management*, 20(2), 87-99. <https://doi.org/10.1080/15324980500544473>.
- Av, P., & Ghabane, V.V. (2018). Assessment of available soil nutrient status in black soils of Akola district, Maharashtra. *Journal of Pharmacognosy and Phytochemistry*, 7(5), 1124-1129.
- Bhatti, S.S., Kumar, V., Singh, N., Sambyal, V., Singh, J., Katnoria, J.K., & Nagpal, A.K. (2016). Physico-chemical properties and heavy metals contents of soils and Kharif crops of Punjab, India. *Procedia Environmental Sciences*, 35, 801-808.
- Bhavya, V.P., Kumar, A.S., Alur, A., Shivkumar, K.M., & Shivanna, M. (2018). Soil chemical properties under different horticultural cropping systems with different depths. *Indian Journal of Pure & Applied Biosciences*, 6(1), 1645-1651. <http://dx.doi.org/10.18782/2320-7051.6115>
- Bouyoucos, G.J. (1927). The hydrometer is a new method for the mechanical analysis of soil. *Soil science*, 23, 343- 353. <http://dx.doi.org/10.1097/00010694-192705000-00002>
- Casida, L., Klein, D., & Santoro, T. (1964). Soil dehydrogenase activity. *Soil science*, 98, 371-376. DOI: 10.1097/00010694-196412000-00004
- Chen, L., Li, C., Zhang, Z., Feng, Q., Xi, H., Guo, R., & Et, A.L. (2024). Landscape differentiation of soil bacteria and bacteria-soil-

- vegetation interactions in desert-oasis ecosystems. *Global and Planetary Change*, 232, 104323 <https://doi.org/10.1016/j.gloplacha.2023.104323>
- Chesnin, L., & Yien, C. (1950). Turbidimetric determination of available sulfates. *Proceedings of the Soil Science Society of America*, 14, 149-151. <http://dx.doi.org/10.2136/sssaj1951.036159950015000c0032x>
- Choudhary, S., Swaroop, N., & Thomas, T. (2020). Assessment on physico-chemical properties of soil from different blocks of Rajsamand district of Rajasthan, India. *International Journal of Current Microbiology and Applied Sciences*, 9(9), 1718-1722.
- Dewangan, S. K., Kumari, L., Minj, P., Kumari, J., & Sahu, R. (2023). The effects of soil pH on soil health and environmental sustainability: a review. *Journal of Emerging Technologies and Innovative Research*, 10 (6), 611-616.
- Dilworth, M.J. (1966). Acetylene reduction by nitrogen-fixing preparations from *Clostridium pasteurianum*. *Biochimica et Biophysica Acta*, 127, 285-294. [https://doi.org/10.1016/0304-4165\(66\)90383-7](https://doi.org/10.1016/0304-4165(66)90383-7)
- Gautam, M.K., Ghosh, A.K., Latore, A.M., Singh, R.K., Singh, U.P., & Maurya, A. (2018). Characterization of Physico-chemical properties of red soil in Mirzapur district of Uttar Pradesh. *International Journal of Chemical Studies*, 6(3), 1067-1073.
- Geetha, S., Reddy, B., & Hemalatha, K.P.J. (2017). Physico-chemical analysis of selected agricultural soil samples in Kommangipanchyathi, Chintapalli mandal, Visakhapatnam. *International Journal of Information Retrieval Research*, 4 (1), 3530-3532.
- Jackson, M. (1958). *The pH was determined in 1:2 soil water suspensions using a digital pH meter. Soil chemical analysis*. Prentice Hall India, New Delhi.
- Jaiswal, P.C. (2014). *Soil plant and water analysis*. Edn 3, Kalyani publisher, New Delhi, pp. 120.
- Kaur, J., & Kaur, G. (2021). Dehydrogenase Activity as a Biological Indicator of Soil Health. *Chemical Science Review and Letters*, 10 (39), 326-329. [10.37273/chesci.cs205205338](https://doi.org/10.37273/chesci.cs205205338).
- Khanday, M.D., Wani, J.A., Ram, D., & Kumar, S. (2018). Depth-wise distribution of available nutrients of soils of horticultural growing areas of ganderbal district of Kashmir valley. *Journal of Pharmacognosy and Phytochemistry*, 7(1), 19-22.
- Kour, S., & Jalali, V.K. (2008). Forms of sulfur and their relationship in soils of different agro-climatic zones of Jammu region. *Journal of the Indian Society of Soil Science*, 56, 309-312.
- Kumar, M., Kar, A., Raina, P., Singh, S.K., Moharana, P. C., & Chauhan, J.S. (2021). Assessment and mapping of available soil nutrients using GIS for nutrient management in hot arid regions of Northwestern India. *Journal of the Indian Society of Soil Science*, 69 (2), 119-132. [10.5958/0974-0228.2021.00035.9](https://doi.org/10.5958/0974-0228.2021.00035.9)
- Kumar, M., Kar, A., Raina, P., Singh, S.K., Moharana, P.C., & Chauhan, J.C. (2019). Spatial variability of available nutrients in the Shekhawati region of Thar Desert, India. *Journal of the Indian Society of Soil Science*, 67, 21-33.
- Kumar, M., Kumar, N., Bharose, R., & Kumar, R. (2018). Morphology, physicochemical properties, and classification of salt-affected soils of Rudauli block, Faizabad, Uttar Pradesh. *Annals of Plant Sciences*, 20(1), 26-30.
- Kumar, M., Singh, S.K., Raina, P., & Sharma, B.K. (2011). Status of available major and micronutrients in arid soils of Churu district of western Rajasthan. *Journal of the Indian Society of Soil Science*, 59, 188-192.
- Kumari, N., Singh, A.K., Agarwal, S., & Thomas, T. (2021). Assessment of physico-chemical properties of soil from different blocks of Jhunjhunu district, Rajasthan. *The Pharma Innovation Journal*, 10(12), 2247-2254.
- Ladwani, K.D., Ladwani, K.D., Manik, V.S., & Ramteke, D. S. (2012). Impact of Domestic Wastewater Irrigation on soil properties and crop yield. *International Journal of Scientific and Research Publications*, 2(10), 2250-3153.
- López-Hernández, D., Brossard, M., Fardeau, J.C., & Lepage, M. (2006). Effect of different termite feeding groups on P sorption and P availability in African and South American savannas. *Biology and Fertility of Soils*, 42, 207-214. <https://doi.org/10.1007/s00374-005-0017-x>
- Margalef, O., Sardans, J., Fernández-Martínez, M., Molowny-Horas, R., Janssens, I. A., et al. (2017). Global patterns of phosphatase activity in natural soils. *Scientific reports*, 7(1), 1337. <https://doi.org/10.1038/s41598-017-01418-8>
- Meena, A., & Rao, K.S. (2021). Assessment of soil microbial and enzyme activity in the rhizosphere zone under different land use/cover of a semiarid region, India. *Ecological Processes*, 10, 16. <https://doi.org/10.1186/s13717-021-00288-3>
- Munsell, A. (1954). *Munsell soil color chart*. First edition. Munsell Color Company Inc. 2441 n, Baltimore, Maryland.
- Muthuvel, P., Udayasoorian, C., Natesan, R., & Ramaswami, P. (1992). *Introduction to soil analysis*. First edition. Tamil Nadu Agricultural University, Coimbatore.

- Naphade, M., Sidhu, G.S., Patil, V.D., & Shinde, R. (2021). Assessment of physico-chemical properties and micronutrient status of Jalgaon district, Maharashtra states, India. *International Journal of Current Microbiology and Applied Sciences*, 10(03), 52–59. DOI: <https://doi.org/10.20546/ijcmas.2021.1003.009>
- Olsen, S.R., Cole, C.V., & Watanabe, F.S. (1954). *Estimation of Available Phosphorus in Soils by Extraction with Sodium Bicarbonate*. USDA Circular No. 939, US Government Printing Office, Washington DC.
- Rajshri, S., Sidhu, G. S., Patil, V. D., & Naphade, M. (2021). Evaluation of physicochemical properties in hot semi-arid eco-region of Beed district, Maharashtra India. *International Journal of Current Microbiology and Applied Sciences*, 10(03), 45–51. <https://doi.org/10.20546/ijcmas.2021.1003.008>
- Saxena, A., Thomas, T., Nandan, R., & Khatana, S. (2021). Evaluation of physico-chemical properties of soil from different blocks of Kanpur Nagar district, Uttar Pradesh. *The Pharma Innovation Journal*, 10 (10), 252-259.
- Sharma, C.M., Gairola, S., Ghildiyal, S.K., & Suyal, S. (2010). Physical properties of soils about forest composition in moist temperate valley slopes of the central western Himalaya. *Journal of Forest Science*, 26(2), 117-129.
- Singh, S.K., Kumar, M., Sharma, B.K., & Tarafdar, J.C. (2007). Depletion of organic carbon, phosphorus, and potassium under pearl millet-based cropping system in the arid region of India. *Arid Land Research and Management*, 21, 119-131.
- Subbiah, B.V., & Asija, C.L. (1956). A rapid procedure for the estimation of available nitrogen in soils. *Current Science*, 25, 259-260.
- Tabatabai, M.A., & Bremner, J.M. (1969). Use of p-nitrophenyl phosphate for assay of soil phosphatase activity. *Soil Biology & Biochemistry*, 1(4), 301-307. [http://dx.doi.org/10.1016/0038-0717\(69\)90012-1](http://dx.doi.org/10.1016/0038-0717(69)90012-1)
- Tale, K.S., & Ingole, S. (2015). Chemical science review and letters a review on the role of physicochemical properties in soil quality. *Chemical Science Review and Letters*, 13, 57–66.
- Taylor, S. A. (1955). Field determinations of soil moisture. *Agricultural engineering*, 36, 654-659.
- Threatt, S.D., & Rees, D.C. (2023). Biological nitrogen fixation in theory, practice, and reality: a perspective on the molybdenum nitrogenase system. *FEBS Letters*, 597(1), 45-58. DOI: 10.1002/1873-3468.14534.
- Toth, S.J., & Prince, A.L. (1949). Estimation of cation exchange capacity and exchangeable Ca, K, and Na content of soil by flame photometer technique. *Soil Science*, 67, 439-445. <https://doi.org/10.1097/00010694-194906000-00003>
- Walkley, A. (1947). A critical examination of a rapid method for determining organic carbon in soils—effect of variations in digestion conditions and of inorganic soil constituents. *Soil Science*, 63 (4), 251-264. <http://dx.doi.org/10.1097/00010694-194704000-00001>
- Wang, Y., Zhong, B., Shafi, M., Ma, J., Guo, J., et al. (2018). Effects of biochar on growth, and heavy metals accumulation of Moso bamboo soil physical properties, and heavy metals solubility in soil. *Chemosphere*, 219, 510–516.
- Wilcox, L.V. (1950). Electrical conductivity. *Journal American Water Works Association*, 42, 775-776.
- Wolf, M.K., Wiesmeier, M., & Macholdt, J. (2023). Importance of soil fertility for climate-resilient cropping systems: The farmer's perspective. *Soil Security*, 13, 100119. DOI: <https://doi.org/10.1016/j.soisec.2023.100119>.
- Wu, N., Zhang, Y.M., & Downing, A. (2009). Comparative study of nitrogenase activity in different types of biological soil crusts in the Gurbantunggut desert, northwestern China. *Journal of Arid Environments*, 73(9), 828–833. <https://doi.org/10.1016/j.jaridenv.2009.04.002>.
- Zhong, Y., Yan, W., Canisares, L.P., Wang, S., Brodie, E.L., & Schrodt, F. (2022). Alterations in soil pH emerge as a key driver of the impact of global change on soil microbial nitrogen cycling: evidence from a global meta-analysis. *Global Ecology and Biogeography*, 32, 145–165. <https://doi.org/10.1111/geb.13616>.








Journal of Experimental Biology and Agricultural Sciences

<http://www.jebas.org>

ISSN No. 2320 – 8694

Influence of Zinc Oxide Nanoparticles on the Productivity, Mineral Element Accumulation, and Fruit Quality of Tomato (*Solanum lycopersicum* L.)

Razu Ahmed^{1*} , Md. Abdul Quddus¹ , Md. Kamal Uddin^{2*} , Susilawati Binti Kasim²,
 Khairul Hafiz bin MohdYusoff², M. A. Motalib Hossain³ , Zakaria Solaiman⁴,
 Ahmad Numery Ashfaql Haque⁵ 

¹Soil and Water Management Section, HRC, Bangladesh Agricultural Research Institute, Gazipur-1701, Bangladesh

²Department of Land Management, Faculty of Agriculture, Universiti Putra Malaysia, Serdang 43200, Malaysia

³Institute of Sustainable Energy, Universiti Tenaga Nasional, 43000, Kajang, Malaysia

⁴The UWA Institute of Agriculture, UWA School of Agriculture and Environment, The University of Western Australia, Perth, WA 6009, Australia

⁵Bangladesh Agricultural Research Council(BARC), Dhaka, Bangladesh

Received – October 12, 2024; Revision – November 19, 2024; Accepted – December 30, 2024

Available Online – January 15, 2025

DOI: [http://dx.doi.org/10.18006/2024.12\(6\).887.904](http://dx.doi.org/10.18006/2024.12(6).887.904)

KEYWORDS

Growth

Nutrient uptake

Profitability

Solanum lycopersicum

Yield traits

ABSTRACT

Foliar application of zinc oxide nanoparticles (ZnO-NPs) is a promising strategy in modern agriculture. This method has shown significant potential in enhancing tomato yields, improving fruit quality, and increasing nutrient uptake. An experiment was conducted in cocopeat media under glasshouse conditions at Ladang 15, Universiti Putra Malaysia (UPM) in 2020 to evaluate the effectiveness of various doses of ZnO-NPs on plant growth, yield, nutrient uptake, and fruit quality in terms of profitability. A total of ten treatments were evaluated, consisting of five levels of ZnO-NPs (0 ppm, 25 ppm, 50 ppm, 75 ppm, and 100 ppm) and two tomato varieties (MARDI Tomato 1 and MARDI Tomato 3). The experiment utilized a split-plot design with four replications. The results indicated that the application of 100 ppm ZnO-NPs produced the maximum measures of plant growth and fruit quality, including the highest number of primary branches per plant (27.75), leaf area (27.80 cm²), photosynthetic rate (33.05 μmol/m²/s), stomatal conductance (1.01 mol/m²/s), fruit length (4.55 cm), fruit diameter (4.33 cm), number of fruits per plant (52.75), fruit yield (53.85 t/ha), ascorbic acid content (26.13 mg/100 g), zinc content in fruits (52.25 mg/kg), total zinc uptake (102.34 mg/plant), and a benefit-cost ratio of 3.39. Moreover, among the tested varieties, MT3 outperformed MT1. Therefore, a foliar application of 100 ppm ZnO-NPs is recommended as the optimal dose for tomato cultivation. This

* Corresponding author

E-mail: razuahmed52@yahoo.com (Razu Ahmed);
mkuddin07@gmail.com (Md. Kamal Uddin)

Peer review under responsibility of Journal of Experimental Biology and Agricultural Sciences.

Production and Hosting by Horizon Publisher India [HPI]
 (<http://www.horizonpublisherindia.in/>).
 All rights reserved.

All the articles published by [Journal of Experimental Biology and Agricultural Sciences](http://www.jebas.org) are licensed under a [Creative Commons Attribution-NonCommercial 4.0 International License](https://creativecommons.org/licenses/by/4.0/) Based on a work at www.jebas.org.



approach promotes healthier plants and superior fruit quality and supports more sustainable and productive agricultural practices while minimizing environmental harm. Additionally, further research is necessary to explore higher dosages of ZnO-NPs in tomato production to establish the best dose for optimizing output.

1 Introduction

Tomato (*Solanum lycopersicum* L.) is one of the most widely cultivated and consumed vegetables globally. It is renowned for its high yield and substantial contribution to human nutrition (Hanif et al. 2023). The fruit is rich in vitamins (B, C, K, A, and E), carotenoids, and essential minerals such as potassium and phosphorus, making it a valuable source of nutrients (Ali et al. 2021). Additionally, widespread tomato cultivation and consumption significantly contribute to economic growth in many regions worldwide (Angyu and Kwon-Ndung 2024). However, tomato production faces numerous challenges, both biological and environmental. Among these, nutrient deficiencies stand out as a major factor that can adversely affect plant growth, fruit quality, and yield (Fu et al. 2020; Wang et al. 2023). Nanotechnology has brought revolutionary changes across various fields, including agriculture. Nanoparticles (NPs), which have at least one dimension in the nanoscale (1 to 100 nanometers), exhibit unique properties due to their increased surface area and significant effects (Kwon-Ndung et al. 2019; Ahsan et al. 2025).

Among these nanoparticles, zinc oxide nanoparticles (ZnO-NPs) have garnered considerable attention for their potential to enhance plant growth, nutrient uptake, and stress tolerance (Pinela et al. 2022; Wang et al. 2023). Zinc (Zn) is a vital micronutrient for plants, playing crucial roles in numerous physiological processes, including enzyme activation, protein synthesis, chlorophyll formation, pollen development, and the maintenance of biological membrane integrity (Quddus et al. 2020; Kondak et al. 2022). Zinc deficiency can lead to stunted growth, reduced yield, and diminished fruit quality in crops like tomatoes (Quddus et al. 2022a). ZnO-NPs have emerged as a promising solution to overcome Zn deficiency in plants (Wang et al. 2023). Their unique properties, such as high surface area and reactivity, facilitate efficient Zn delivery to plants (Ahmed et al. 2023).

Several studies have reported that ZnO-NPs can improve plant growth, nutrient uptake, and yield in various crops (Chanu and Upadhyaya 2019; Su et al. 2019; Huang et al. 2020; Khan et al. 2021; Wang et al. 2023; Ahsan et al. 2025). Using zinc oxide nanoparticles presents a significant opportunity to address challenges posed by a rapidly growing global population (Jampílek and Král'ová 2021). Continued research and development are key to realizing the full economic benefits of ZnO-NPs while ensuring their safe and responsible usage, paving the way for innovative

applications and sustainable growth (Ahsan et al. 2025). Studies have shown that ZnO-NPs positively impact tomato plants, leading to increased growth, improved fruit quality, and enhanced stress tolerance. Pérez Velasco et al. (2020) reported significant plant height, stem diameter, and fruit weight improvements. Furthermore, ZnO-NPs have been found to increase protein content and mitigate the negative effects of salt stress. However, it is crucial to consider factors like plant age, nanoparticle dose, and type, as these can influence the extent of benefits (Faizan et al. 2021). For instance, ZnO-NPs at 50 ppm significantly enhanced the nutritional quality of tomatoes by increasing antioxidant enzyme activities and total soluble solids by 26.92%. They also showed potential in mitigating tomato mosaic virus through improved growth, photosynthesis, and antioxidant production (Gutiérrez-Miceli et al. 2021; Sofy et al. 2021). Foliar spraying with 100 ppm ZnO-NPs significantly improved tomato plant growth, as evidenced by increased fresh and dry weights of leaves and roots, along with enhanced levels of sucrose, starch, and glucose (Sun et al. 2020). Foliar applications of ZnO-NPs are preferred over soil applications because they can rapidly correct deficiencies, minimize toxicity, and prevent nutrient immobilization within the soil, as highlighted by Abdelaziz et al. (2021). While high concentrations of ZnO-NPs (400-800 mg/L) can adversely affect seed germination and plant growth, lower concentrations (up to 200 mg/L) have been shown to enhance growth and stimulate antioxidant enzyme activity (Tondey et al. 2021; Włodarczyk and Smolińska 2022). Consequently, ZnO-NPs are pivotal in boosting tomato productivity and promoting sustainable agricultural practices by reducing soil degradation and minimizing the environmental and economic risks associated with excessive fertilizer use (Benavides-Mendoza et al. 2023). Nevertheless, the specific effects of ZnO-NPs on tomato growth, productivity, mineral element accumulation, and fruit quality remain an active area of research (Pérez Velasco et al. 2020; Sofy et al. 2021). Given the circumstances, choosing the ideal foliar dose of zinc oxide nanoparticles (ZnO-NPs) is necessary to enhance tomato growth, yield, and quality. This study conducts comprehensive research on how ZnO-NPs influence various aspects of tomato growth, fruit quality, yield, and the accumulation of essential minerals. By understanding these effects, we can better assess the potential benefits of using ZnO-NPs in tomato cultivation, ultimately contributing to sustainable agriculture and a secure food supply. Therefore, this study aims to evaluate the influence of zinc oxide nanoparticles on the productivity, mineral element accumulation, and fruit quality of selected tomato varieties.

2 Materials and Methods

2.1 Experimental site and design

The experiment was conducted in cocopeat media at the glasshouse (8D) in the Agro-Tech Unit, Ladang 15, Faculty of Agriculture, Universiti Putra Malaysia (UPM), Serdang, Selangor, from March 2020 to August 2020. The experimental site is located in Malaysia's lowlands at a latitude of 2059'22.6" N and a longitude of 101042'82.2" E. The average daytime temperature was 30.28°C (33.38°C inside the glasshouse), and the relative humidity averaged 88.58% (83.92% inside the glasshouse), indicating high ambient temperatures and humidity levels (Shamshuddin et al. 2020; Ahmed et al. 2023). The experiment utilized a split-plot design with four replications. It involved 10 treatments consisting of five levels of zinc oxide nanoparticles (ZnO-NPs): 0 ppm, 25 ppm, 50 ppm, 75 ppm, and 100 ppm, in combination with two tomato varieties, MARDI Tomato 1 and MARDI Tomato 3. The selected varieties were V1 (MT 1) and V2 (MT 3). The treatments were labeled as T1 (0 ppm), T2 (25 ppm), T3 (50 ppm), T4 (75 ppm), and T5 (100 ppm). Tomato varieties were allocated to the main plots, while the zinc oxide nanoparticles were applied to each variety as sub-plot treatments.

2.2 Plant and planting materials

High-yielding tomato varieties MT-1 and MT-3 were sourced from the Malaysian Agricultural Research and Development Institute (MARDI). The seeds were initially germinated in trays filled with a mixture of peat moss and bio-soil in a 3:1 ratio. After three weeks, the healthiest seedlings were carefully transplanted into black poly bags measuring 18 inches by 18 inches, each filled with 3 Kg of coco peat. Each bag was equipped with 32 drainage holes to ensure optimal water management. The seedlings were placed 60 cm apart within rows and 75 cm between adjacent rows to maintain adequate spacing. The initial nutrient composition of the planting medium was methodically assessed using the methodology established by Keeney and Nelson (1982), and the results are presented in Table 1.

2.3 Agronomic management

In this study, tomato plants received three liquid fertilizers applied at different growth stages: seedling, vegetative, and fruiting. A 20g fertilizer blend composed of N (13%), P (40%), K (13%), B

(0.01%), Cu (0.003%), Fe (0.025%), Mn (0.013%), Mo (0.0018%), and Zn (0.004%) was dissolved in 20 liters of water. This initial solution was applied twice weekly at 250 mL per plant during seedling. A second fertilizer blend, with the same NPK and micronutrient content as the seedling stage, was also prepared at 20g per 20 liters. This solution was applied twice weekly at 300 mL per plant during the vegetative stage. At the fruiting stage, a third fertilizer blend was created, containing N (13%), P (7%), K (20%), Ca (8%), Mg (2%), B (0.025%), Cu (0.01%), Fe (0.085%), Mn (0.045%), Mo (0.0038%), and Zn (0.025%). This blend was prepared at a rate of 35g per 20 liters and was applied twice weekly at 500 mL per plant. The tomato plants were vertically staked with plastic sticks to minimize root disturbance and prevent damage. Regular weeding and irrigation were performed as needed, and notably, the study period was free from any disease outbreaks or insect infestations.

2.4 Synthesis method of zinc oxide nanoparticles (ZnO-NPs)

To synthesize zinc oxide (ZnO) nanoparticles, we added 2 ml of 0.01% Polyvinyl Alcohol (PVA) to a 1 M zinc sulfate heptahydrate solution. This was followed by a dropwise addition of 2 M sodium hydroxide. The mixture was stirred for 18 hours, resulting in the formation of a white precipitate. This precipitate was filtered, washed, dried at 100°C, and calcined for three hours at 450°C. The structural properties of the ZnO nanoparticles were analyzed using Field Emission Scanning Electron Microscopy (FESEM) (Figure 1a) and X-ray diffraction (XRD) (Figure 1b), as described by Mohan and Renjanadevi (2016). For the foliar treatments, we applied various doses of ZnO nanoparticle fertilizer at three stages of tomato growth: (i) before flower initiation, (ii) after fruit set (when the fruit reached the marble size), and (iii) 20 days after the second spray. Each plant received 1000 ml of water, divided into three sprays: 300 ml for the first two stages and 400 ml for the third spray.

2.5 Measurement of growth and yield parameters

After the experiment, plant height was measured using a wooden meter ruler, and leaf area was calculated with a leaf area meter (LI-3000, Li-COR) in cm². The number of branches and total fruits were counted weekly. We recorded the total fruit weight per plant (in kg) and total yield (in t/ha) up to the final harvest (Cox 1995). Chlorophyll content was measured at the vegetative, flowering, and mature stages using a SPAD meter (SPAD-502, Konica Minolta). The experimental plot setup is illustrated in Figure 2.

Table 1 Initial nutrient status of the media in the experimental pot

Properties and Unit	pH	Total C (%)	Total N (%)	Total S (%)	K	Ca	Mg	Cu	Mn	B	Zn
								mg/kg			
Value	6.8	41.06	0.28	0.09	2917	603	205	0.8	24.9	11.4	14.7

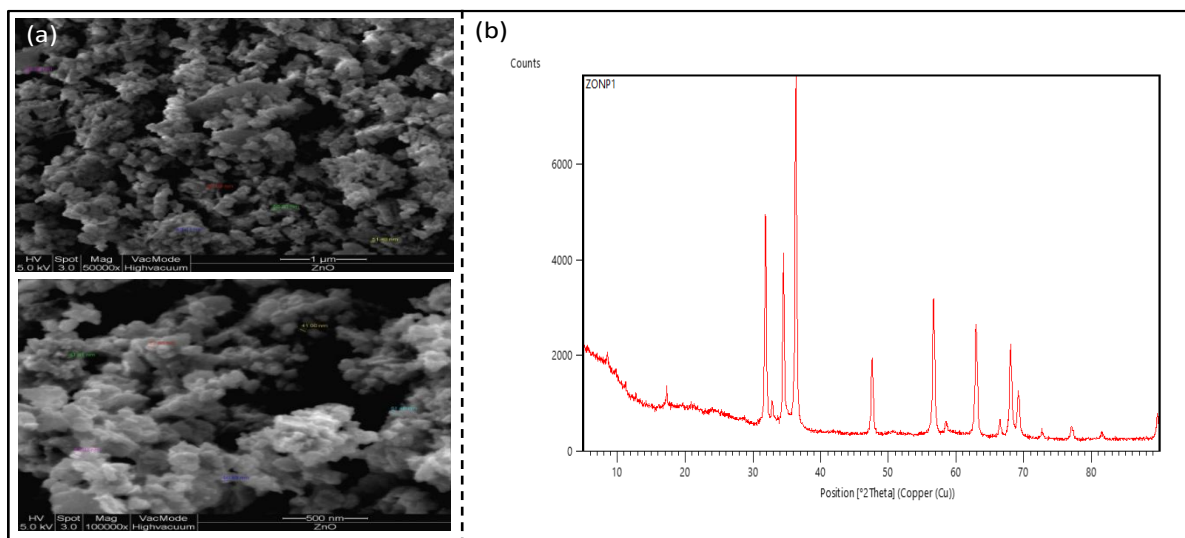


Figure 1 (a) Represent the Scanning Electron Microscope (SEM) image of the zinc oxide nanoparticles (ZnO-NPs)' size (40-55 nm), (b) XRD spectrum of zinc oxide nanoparticle prepared using Poly Vinyl Alcohol (PVA).



Figure 2 The image of the experimental plot

2.6 Measurement of photosynthetic parameters

The gross photosynthetic rate (PN), leaf stomatal conductance (GS), and transpiration rate of 5-week-old plant leaves were measured in the morning using a portable gas exchange system (LI-6400, LI-COR, Lincoln, NE, USA).

2.7 Determination of total carbon, total N, and sulfur in leaves and fruits of tomatoes

Samples of tomato fruits and leaves were collected from various pots and stored separately in paper bags. The paper bags containing the samples were placed in an oven set to 70°C for 72 hours or until they reached a constant weight. After drying, the plant samples were crushed and sieved through a 4 mm sieve. The total amounts of carbon, nitrogen, and sulfur were measured using a Leco TruMac CNS analyzer. For the analysis, 0.2–0.3 g of the air-dried sample was placed in a ceramic boat and combusted at

1350°C with helium, compressed air, and 99.99% pure oxygen. The gases produced, CO₂, NO₂, and SO₂, were used to identify the total carbon, nitrogen, and sulfur contents, respectively. The total carbon and nitrogen contents were recorded as percentages (Ahmed et al. 2023).

2.8 Determination of P, K, Mg, B, Fe, and Zn in leaves and fruits of tomatoes

The total concentrations of phosphorus (P), potassium (K), magnesium (Mg), boron (B), iron (Fe), and zinc (Zn) were determined using an ICP-Optical Emission Spectrometer, following the dry ashing method based on Cottenie's theory (Cottenie 1980). A 2–3 g air-dried sample was dried at 60°C for 24 hours, then ashed at 300°C for 1 hour and at 550°C for 8–9 hours. After cooling, 2 mL of concentrated hydrochloric acid (HCl) and water were added, and the sample was heated for 15–20 minutes. Once cooled, 10 mL of 20% nitric acid (HNO₃) was added, and the

sample was placed in a water bath for 1 hour. Finally, the sample was filtered through Whatman filter paper No. 2, diluted to a final volume of 100 mL with distilled water, and analyzed for P, K, Mg, B, Fe, and Zn concentrations using the PerkinElmer Optima 8300 ICP-Optical Emission Spectrometer.

2.9 Determination of quality parameters

Tomato fruits were manually harvested at the red ripe stage to assess their quality performance. For the experiment, we selected fruits of uniform size and colour that were undamaged and free from disease and bruises, following the guidelines established by Beckles (2012). Total Soluble Solids (TSS), firmness, and Titratable Acidity (TA) were measured immediately in the fresh fruit, while the physicochemical properties were analyzed in refrigerated samples (Ahmed et al. 2023).

2.9.1 Total Soluble Solid (TSS)

A digital pocket refractometer (model PAL1, ATAGO, Tokyo, Japan) was used to measure tomato fruits' soluble solids. Fresh tomato juice was placed on the refractometer's glass lens using a garlic pestle, a kitchen tool. The total soluble solids (TSS) were expressed as a percentage of Brix (% Brix) (Nirupama Pila et al. 2010).

2.9.2 Firmness

The firmness of the tomato fruits was measured using a Universal Testing Machine (Model 5543, load frame, Instron Corp., Norwood, MA, USA). The machine was equipped with a 6 mm diameter cylindrical probe and operated at a 20 mm/min speed. The measurements were recorded in Newtons (N) using Instron Merlin software, version M12-13664-EN (Kumah et al. 2011).

2.9.3 Titratable Acidity (TA)

Titrate acidity was measured using a titration method. To prepare the sample, 10g of tomato fruit pulp was homogenized with 20 mL of distilled water. This mixture was then filtered and combined with phenolphthalein. The solution was titrated with 0.1 N NaOH until a persistent pink colour, indicating a pH of 8.1, was achieved. As Mohammadi-Aylar et al. (2010) described, the volume of NaOH used was recorded, and the results were expressed as the percentage of citric acid per 100 g of fresh weight.

$$\begin{aligned} \text{Titrate acidity (\%)} &= (\text{Titer vol. (ml)} \times \text{normality NaOH}(0.1) \\ &\times \text{vol. made up (20 ml)} \\ &\times 64 \text{ g(equivalent wt. of citric acid)} \\ &\times 100)/(\text{Wt. of sample (5 g)} \\ &\times \text{vol. of sample for titration (5 ml)} \\ &\times 1000) \end{aligned}$$

2.9.4 Antioxidant properties

2.9.4.1 Ascorbic acid

The ascorbic acid content was measured using a direct colourimetric method with 2,6-dichlorophenol-indophenol (DCPIP) dye, as Ding and Mashah (2016) outlined. To extract the ascorbic acid, 2 grams of tomato fruit were mixed with 20 mL of 2% metaphosphoric acid (HPO₃). The mixture was then filtered, and the volume was adjusted by adding more 2% HPO₃. An aliquot of 0.5 mL of the extract was combined with 3 mL of 2% HPO₃ and 2 mL of DCPIP dye. The absorbance was measured at 518 nm using a UV spectrophotometer. Based on a standard curve, the ascorbic acid content in the tomato fruit was expressed as mg/g of fresh weight.

$$\text{AA (in mg/g FM)} = \frac{\text{C}_{\text{ppm}} \times \text{V}}{\text{W}}$$

Here, C_{ppm} = Conc. of sample soln. as ppm computed from the standard curve

V = Final vol. made up in liter (0.04 L)

W = Fresh wt. of the samples (g)

2.9.4.2 Lycopene

Lycopene content was measured using slightly modified techniques developed by Nagata and Yamashita (1992). Approximately 1g of the sample was dissolved in a mixture of 10 to 20 mL of acetone and hexane in a 4:6 ratio. The pigments were extracted and homogenized with a mortar and pestle, after which the supernatant was separated. The optical density of the supernatant was measured using a UV spectrophotometer at wavelengths of 663, 645, 505, and 453 nm. The amount of lycopene was then calculated using the following equation:

$$\text{Lycopene (mg/100g)} = -0.0458A_{663} + 0.204A_{645} + 0.372A_{505} - 0.0806A_{453}$$

A₆₆₃, A₆₄₅, A₅₀₅, and A₄₅₃ are the absorbance at 663 nm, 645 nm, 505 nm, and 453 nm of each other. Data obtained as mg/100 mL were converted as data mg/100 mL × sample volume = data mg/100 g.

The total N contents of the tomato dry fruit were multiplied by the constant food factor of 6.25 to estimate the protein content (Hiller et al. 1948).

2.10 Calculation of nutrient uptake

The nutrient content was multiplied by the dry weight of the tomato plant portion (oven-dry weight) to calculate nutrient uptake (Sharma et al. 2012):

$$\text{Nutrient uptake} = \frac{\text{Nutrient concentration (\%)} \times \text{Dry weight (g)}}{100}$$

2.11 Calculation of apparent zinc recovery efficiency (AZnR)

Baligar et al. (2001) calculated the apparent zinc recovery efficiency based on dry weight. The following equation is provided:

$$\text{AZnR} = \frac{\text{Nutrient uptake (mg/plant)} - \text{control value}}{\text{Applied zinc (mg/plant)}} \times 100$$

2.12 Cost and Return Analysis

In the experiment, the variable cost for each treatment was calculated by adding the costs of labour and inputs. Each treatment's tomato fruit yield was expressed in tons per hectare (t ha⁻¹). To determine the gross return, we multiplied the yield by the current unit price of tomatoes. It is important to note that the net house and experimental land rent were excluded from this calculation. Subsequently, we calculated the gross margin by subtracting the variable cost from the gross return. The benefit-cost ratio (BCR) was then calculated using the formula provided by Quddus et al. (2023): BCR = GR ÷ TVC, Where GR= Gross return and TVC= Total variable cost

2.13 Statistical analysis

The statistical analysis focused on growth, yield, yield-contributing characteristics, quality attributes, and nutrient content data. This

analysis was conducted using SAS software (version 9.4) and ANOVA. A significance level of 0.05 (p < 0.05) was set for Tukey's Honestly Significant Difference (HSD) test, which was employed to compare the means.

3 Results and Discussion

3.1 The growth parameters

3.1.1 Varietal effect on growth traits

Growth traits, such as the number of primary branches per plant and leaf area, showed significant variation among different tomato varieties, while plant height did not exhibit any notable differences (Table 2). The MT3 variety demonstrated superior characteristics, with an average of 24.05 branches per plant and a leaf area of 22.91 cm² compared to the MT1 variety. The greater number of branches and larger leaf area in MT3 may be attributed to genetic differences and favourable environmental conditions, which enhance nutrient uptake. Tujuba and Ayana (2020) similarly observed that the number of branches varies among different tomato cultivars, linking this variation to genetic differences.

3.1.2 Effect of ZnO-NPs on growth parameters

The growth parameters of plant height, number of primary branches per plant, and leaf area were significantly influenced by

Table 2 Effects of foliar application of zinc oxide nanoparticles on growth parameters of tomato varieties

Treatment	Plant height (cm)	No. of primary branch/plant	Leaf area (cm ²)
MT1	116.40 ±2.62 ^a	20.75 ±1.05 ^b	19.49 ±1.19 ^b
MT3	119.25 ±2.72 ^a	24.05 ±1.48 ^a	22.91 ±1.53 ^a
Level of sig.	ns	*	**
MSD value	11.99	3.13	1.54
CV (%)	8.06	12.00	8.53
T ₁	105.13 ±2.55 ^b	14.00 ±0.53 ^c	12.58 ±0.37 ^d
T ₂	112.75 ±2.85 ^{ab}	19.63 ±0.82 ^b	16.61 ±0.58 ^c
T ₃	121.25 ±4.25 ^a	24.63 ±1.13 ^a	23.54 ±1.41 ^b
T ₄	124.00 ±4.13 ^a	26.00 ±1.38 ^a	25.48 ±0.89 ^{ab}
T ₅	126.00 ±2.27 ^a	27.75 ±1.52 ^a	27.80 ±1.07 ^a
Level of sig.	**	**	**
MSD value	13.99	3.96	2.66
CV (%)	8.06	12.00	8.53
(V*T)	ns	ns	ns

Means in a column that includes the same letters are not statistically different at the 5% level using Tukey's HSD test, MSD = Minimum significant difference, CV = Coefficient of variation, sig.= significance, T₁: 0 ppm, T₂: 25 ppm, T₃: 50 ppm, T₄: 75 ppm and T₅: 100 ppm of ZnO-NPs. ns indicated non-significant at p>0.05, *indicated significant at p≤0.05 and ** indicated significant at p≤0.01, ± standard error mean (n=4) according to ANOVA.

various levels of foliar-applied zinc oxide nanoparticles (ZnO-NPs) (Table 2). The maximum plant height of 126.00 cm was achieved with a treatment of 100 ppm ZnO-NPs (T₅), representing a 20% increase over the control group. This height was superior to the results from treatments T₁ and T₂ but similar to those from T₃ and T₄. Zinc oxide nanoparticles (ZnO-NPs) may enhance plant growth, particularly height, by potentially releasing essential nutrients crucial for crop development, increasing chlorophyll content, and promoting active photosynthesis (Khanm et al. 2018; Mi et al. 2023). This finding aligns with Sun et al. (2020), who reported the highest plant height with 100 mg/L ZnO-NPs. Additionally, 50 ppm ZnO-NPs led to a 30.1% increase in shoot length (Faizan and Hayat 2019), while treatment of 100 ppm ZnO-NPs resulted in a 16% increase in wheat plant height (Munir et al. 2018; Ahmed et al. 2023). Plants treated with 100 ppm ZnO-NPs (T₅) showed the most vigorous branching, with an average of 27.75 branches per plant, followed closely by those treated with 75 ppm (T₄) and 50 ppm (T₃). In contrast, the control treatment resulted in the fewest branches, averaging just 14 per plant. This significant increase in branching among the ZnO-NPs-treated plants suggests that these nanoparticles stimulate new branch development by interacting with the plant's growth-regulating tissues and triggering important metabolic processes, as previously noted by Faizan and Hayat (2019) and Wang et al. (2024).

Moreover, leaf area also showed significant variation among the different treatments. Plants treated with 100 ppm ZnO-NPs exhibited the largest leaf area (27.80 cm²), followed closely by those treated with 75 ppm ZnO-NPs (T₄). The control group demonstrated the smallest leaf area at 12.58 cm². This increase in leaf area can be attributed to the vital role of zinc in plant growth. Zinc is actively involved in essential metabolic processes, including carbohydrate and protein synthesis, as well as the production of auxin, a plant hormone that stimulates cell expansion and differentiation, ultimately resulting in larger leaf size (Vasconcelos et al. 2011; Saleem et al. 2022; Kondak et al. 2022; Ahsan et al. 2025). These findings mirror the observations of Faizan and Hayat (2019), who reported a substantial 24.1% increase in leaf area when plants were treated with 50 ppm ZnO-NPs compared to the control treatment.

3.2 The physiological characteristics

3.2.1 Varietal effect on physiological traits

Physiological traits, such as leaf stomatal conductance, varied significantly among the different tomato varieties, while chlorophyll content, photosynthetic rate, and transpiration rate did not show any significant differences (Table 3). The variety MT3 exhibited higher stomatal conductance (0.86 mol/m²/s) than MT1

Table 3 Effects of foliar application of zinc oxide nanoparticles on physiological growth of tomato varieties

Treatment	Chlorophyll content in leaf (SPAD)	Photosynthesis rate (μmol/m ² /s)	Stomatal conductance (mol/m ² /s)	Transpiration rate (mmol/m ² /s)
MT1	46.00 ± 1.32 ^a	26.44 ± 1.09 ^a	0.78 ± 0.04 ^b	12.43 ± 0.58 ^a
MT3	49.69 ± 1.69 ^a	28.95 ± 1.38 ^a	0.86 ± 0.04 ^a	13.37 ± 0.60 ^a
Level of sig.	ns	Ns	**	ns
MSD value	6.10	2.55	0.02	1.51
CV (%)	7.40	10.68	8.98	8.35
T ₁	38.94 ± 1.01 ^c	20.12 ± 0.55 ^c	0.56 ± 0.02 ^d	8.70 ± 0.27 ^c
T ₂	44.25 ± 1.71 ^b	24.66 ± 0.79 ^b	0.72 ± 0.03 ^c	11.85 ± 0.37 ^b
T ₃	49.55 ± 1.74 ^a	29.22 ± 0.82 ^a	0.89 ± 0.03 ^b	14.25 ± 0.39 ^a
T ₄	51.85 ± 1.52 ^a	31.45 ± 0.96 ^a	0.94 ± 0.03 ^{ab}	14.48 ± 0.48 ^a
T ₅	54.63 ± 1.40 ^a	33.05 ± 1.87 ^a	1.01 ± 0.04 ^a	15.22 ± 0.45 ^a
Level of sig.	**	**	**	**
MSD value	5.22	4.36	0.11	1.59
CV (%)	7.40	10.68	8.98	8.35
(V*T)	ns	Ns	ns	ns

Means in a column that include the same letters are not statistically different at the 5% level using Tukey's HSD test, MSD = Minimum significant difference, CV = Coefficient of variation, sig.= significance, T₁: 0 ppm, T₂: 25 ppm, T₃: 50 ppm, T₄: 75 ppm and T₅: 100 ppm of ZnO-NPs, ns indicated non-significant at p>0.05, * indicated significant at p≤0.05 and ** indicated significant at p≤0.01, ± standard error mean (n=4) according to ANOVA.

(0.78 mol/m²/s). This difference may reflect variations in growth and yield potential due to genetic and environmental factors (Ben-Rouina et al. 2006; Isah et al. 2014; Dong et al. 2025). Additionally, the variety MT3 demonstrated superior nutrient uptake compared to MT1. This finding is consistent with Olaniyi et al. (2010) and Ahmed et al. (2023), who noted enhanced physiological growth attributes in the UC82B variety.

3.2.2 Effect of ZnO-NPs on physiological parameters

Physiological parameters such as leaf chlorophyll content, photosynthetic rate, stomatal conductance, and transpiration rate in tomatoes were significantly influenced by the foliar application of various levels of ZnO nanoparticles.

3.2.2.1 Chlorophyll Content

The highest chlorophyll content observed was 54.63 SPAD in the treatment with 100 ppm ZnO-NPs (T₅). This was comparable to the 75 ppm treatment (T₄) and the 50 ppm treatment (T₃) but significantly higher than the control group, which had a chlorophyll content of 38.94 SPAD. These results are consistent with previous research by Sun et al. (2020) and Faizan and Hayat (2019), who found a 32.1% increase in chlorophyll content with 50 ppm ZnO-NPs compared to the control group.

3.2.2.2 Photosynthetic Rate

The highest photosynthetic rate recorded was 33.05 μmol/m²/s with the application of 100 ppm ZnO nanoparticles (ZnO-NPs). This rate was statistically similar to those observed at 75 ppm and 50 ppm but significantly higher than the rates at 25 ppm and the control group, which had a rate of 20.12 μmol/m²/s. This improvement aligns with the findings of Sofy et al. (2021), who noted that nanoparticles enhance key processes such as carbohydrate and protein metabolism and cell wall development (Jabri et al. 2022). However, the results of this study contradict those of Faizan and Hayat (2019), who observed a substantial 35% increase in the photosynthetic rate with the application of 50 ppm ZnO-NPs, followed by 100 ppm ZnO-NPs. Munir et al. (2018) also reported a significant 58% improvement in the photosynthetic rate in wheat plants treated with 100 mg/L ZnO-NPs. Rehman et al. (2023) also corroborated similar findings in tomatoes.

3.2.2.3 Stomatal Conductance

The maximum stomatal conductance of 1.01 mol/m²/s was achieved with 100 ppm of ZnO nanoparticles (T₅). This level was comparable to that observed with 75 ppm (T₄) but was significantly higher than the measurements taken with 50 ppm (T₃) and the control group (T₁). This finding is consistent with the research conducted by Munir et al. (2018), which reported a 102% increase in stomatal conductance in wheat treated with 100 mg/L of ZnO nanoparticles.

3.2.2.4 Transpiration Rate

The highest transpiration rate recorded was 15.22 mmol/m²/s with the application of 100 ppm ZnO nanoparticles (T₅), while the control group (T₁) exhibited the lowest transpiration rate. This result supports the established role of zinc in enhancing the production of carbonic anhydrase, an essential enzyme for CO₂ transport during photosynthesis (Saleem et al. 2022; Alloway 2008). The improvement in transpiration is likely due to increased nitrogen accumulation, higher stomatal density, and greater leaf area, all of which are positively influenced by zinc (Jabri et al. 2022; Rehman et al. 2023). Additionally, this finding is supported by Munir et al. (2018), who reported a 62% increase in transpiration in wheat treated with 100 mg/L ZnO nanoparticles.

3.3 The yield and yield contributing characters

3.3.1 Varietal effect on yield and yield contributing characters

Tomato yield and characteristics, such as fruit length, individual fruit weight, and total yield, varied significantly among the varieties, with no differences in fruit diameter or the number of fruits per plant (Table 4). The MT3 variety had the highest fruit length (4.14 cm), individual fruit weight (43.79 g), number of fruits per plant (46.10g), and total yield (2.09 kg per plant), representing a 22.2% increase over MT1. These differences likely stem from genetic factors and better nutrient uptake (Quddus et al. 2022b). Similar results were noted by Razzaque et al. (2016) in mungbean varieties.

3.3.2 Effect of ZnO-NPs on yield and yield contributing characters

Tomato yield and yield contributing characters were significantly enhanced by the different levels of ZnO-NPs (Table 4). ZnO-NPs in previous research were demonstrating their positive influence on plant growth and development (Ahsan et al. 2025; Wang et al. 2023).

3.3.2.1 Fruit length and diameter

The treatment with 100 ppm ZnO nanoparticles (T₅) resulted in the largest fruits, measuring 4.55 cm in length and 4.33 cm in diameter. This size was statistically comparable to the fruits from the 75 ppm ZnO nanoparticles treatment (T₄). In contrast, the control treatment (T₁) produced the smallest fruits, with a length of 3.16 cm and a diameter of 3.02 cm. Zinc is essential for various plant processes, including RNA metabolism, carbohydrate and protein synthesis, DNA replication, fruit set, and the development of fruit characteristics (Quddus et al. 2020). This finding is consistent with the observation by Kumar et al. (2017), which noted that combining 150 ppm ZnO and FeO nanoparticles resulted in the largest fruit sizes.

Table 4 Effects of foliar application of zinc oxide nanoparticles on yield and yield attributes of tomato varieties

Treatment	Fruit length (cm)	Fruit diameter (cm)	Individual fruit weight (g)	No. of fruits/plant	Yield (kg/plant)	Yield (t/ha)
MT1	3.69 ±0.10 ^b	3.70 ±0.11 ^a	39.30 ±1.83 ^b	42.20 ±1.77 ^a	1.71 ±0.14 ^b	34.28 ±2.77 ^b
MT3	4.14 ±0.17 ^a	3.94 ±0.13 ^a	43.79 ±2.22 ^a	46.10 ±1.99 ^a	2.09 ±0.18 ^a	41.87 ±3.51 ^a
Level of sig.	**	ns	**	ns	*	**
MSD value	0.22	0.34	1.58	4.03	0.24	4.89
CV (%)	7.49	7.06	7.04	7.55	10.81	10.07
T ₁	3.16 ±0.10 ^c	3.02 ±0.07 ^c	27.23 ±0.72 ^d	31.75 ±1.03 ^d	0.87 ±0.04 ^d	17.33 ±0.80 ^d
T ₂	3.48 ±0.09 ^c	3.55 ±0.09 ^b	37.33 ±0.98 ^c	39.50 ±1.31 ^c	1.48 ±0.08 ^c	29.53 ±1.51 ^c
T ₃	4.05 ±0.12 ^b	4.05 ±0.12 ^a	45.26 ±1.50 ^b	47.50 ±1.21 ^b	2.16 ±0.12 ^b	43.18 ±2.33 ^b
T ₄	4.35 ±0.18 ^{ab}	4.16 ±0.11 ^a	47.14 ±1.69 ^{ab}	49.25 ±1.71 ^{ab}	2.33 ±0.12 ^b	46.50 ±2.43 ^b
T ₅	4.55 ±0.19 ^a	4.33 ±0.11 ^a	50.77 ±1.65 ^a	52.75 ±1.68 ^a	2.69 ±0.16 ^a	53.85 ±3.20 ^a
Level of sig.	**	**	**	**	**	**
MSD value	0.43	0.40	4.31	4.91	0.30	6.06
CV (%)	7.49	7.06	7.04	7.55	10.81	10.07
(V*T)	ns	ns	ns	ns	ns	ns

Means in a column that includes the same letters are not statistically different at the 5% level using Tukey's HSD test, MSD = Minimum significant difference, CV = Coefficient of variation, sig.= significance, T₁: 0 ppm, T₂: 25 ppm, T₃: 50 ppm, T₄: 75 ppm and T₅: 100 ppm of ZnO-NPs. ns indicated non-significant at p>0.05, * indicated significant at p≤0.05 and ** indicated significant at p≤0.01, ± standard error mean (n=4) according to ANOVA.

3.3.2.2 Individual fruit weight

Applying 100 ppm ZnO nanoparticles (ZnO-NPs) resulted in the heaviest individual fruit, weighing 50.77 grams. This weight was significantly greater than that of other treatments and closely matched the 75 ppm ZnO-NPs treatment results. This finding is consistent with previous research highlighting the positive effects of ZnO-NPs on fruit weight. For instance, Ahmed et al. (2023) reported the highest fruit weight in tomatoes treated with 100 ppm ZnO-NPs, while Kumar et al. (2017) observed similar results with a combination of 150 ppm ZnO-NPs and FeO-NPs. Prasad et al. (2012) also found that 125 ppm ZnO-NPs significantly enhanced peanut shoot growth, pod size, and overall yield compared to chelated zinc sulfate.

3.3.2.3 Number of fruits per plant

The highest number of fruits per plant (52.75) was achieved by applying 100 ppm ZnO-NPs (T₅). This result was significantly higher than those from other treatments and was comparable to the 75 ppm ZnO-NPs treatment (T₄). In contrast, the control treatment (T₁) had the lowest fruit count, recording only 31.75 fruits. These findings align with previous studies. For instance, Faizan and Hayat (2019) reported a 21.1% increase in fruit numbers with

sequential foliar sprays of 50 ppm and 100 ppm ZnO-NPs. Additionally, Kumar et al. (2017) found the highest fruit count per plant using 150 ppm ZnO-NPs in combination with FeO-NPs. Similarly, Ahmed et al. (2023) observed comparable results with 100 ppm ZnO-NPs in tomato plants.

3.3.2.4 Overall yield

The foliar application of 100 ppm ZnO nanoparticles (T₅) produced the highest yield, averaging 2.69 kg per plant and 53.85 tons per hectare. This yield was significantly greater than all other treatments, with a remarkable 210% increase. This finding is consistent with the research by Seleiman et al. (2023), which reported optimal maize yields at a concentration of 100 mg/L ZnO nanoparticles. Zinc plays a critical role in various metabolic processes, as highlighted by Qudus et al. (2022b), and positively influences fruit set, number, length, diameter, and dry fruit weight, as noted by Mubashir et al. (2023). Meanwhile, foliar spraying with 50 ppm resulted in a 19.4% yield increase over the control. Faizan and Hayat (2019) concluded that combining 150 ppm ZnO nanoparticles with FeO nanoparticles enhanced fruit yield. However, the 100 ppm concentration consistently demonstrated the most significant impact, resulting in a 185% increase in wheat grain yield compared to the control, as documented by Munir et al. (2018).

Table 5 Effects of foliar application of zinc oxide nanoparticles on the quality attributes of tomato varieties

Treatment	TSS (^o Brix)	Firmness (N)	Titrateable acidity (%)	Ascorbic acid (mg/100g)	Lycopene content(μ g/100g)	Protein content (%)
MT1	6.58 \pm 0.21 ^a	11.45 \pm 0.56 ^b	0.64 \pm 0.03 ^a	21.30 \pm 0.86 ^a	211.50 \pm 7.77 ^b	13.55 \pm 0.61 ^a
MT3	6.87 \pm 0.23 ^a	12.86 \pm 0.57 ^a	0.67 \pm 0.04 ^a	23.20 \pm 1.02 ^a	232.55 \pm 10.87 ^a	13.96 \pm 0.66 ^a
Level of sig.	ns	**	ns	ns	*	ns
MSD value	0.48	0.52	0.05	3.35	15.14	1.04
CV (%)	6.82	7.48	10.69	9.45	8.65	8.28
T ₁	5.25 \pm 0.13 ^c	8.25 \pm 0.35 ^d	0.83 \pm 0.03 ^a	16.00 \pm 0.46 ^c	167.63 \pm 5.11 ^c	8.75 \pm 0.23 ^c
T ₂	6.35 \pm 0.18 ^b	11.17 \pm 0.40 ^c	0.77 \pm 0.03 ^{ab}	20.50 \pm 0.71 ^b	195.88 \pm 4.53 ^c	14.00 \pm 0.41 ^b
T ₃	7.10 \pm 0.19 ^a	13.15 \pm 0.42 ^b	0.67 \pm 0.03 ^{bc}	24.00 \pm 0.85 ^a	227.00 \pm 7.17 ^b	14.63 \pm 0.38 ^{ab}
T ₄	7.35 \pm 0.21 ^a	13.61 \pm 0.64 ^{ab}	0.59 \pm 0.02 ^c	24.63 \pm 0.92 ^a	245.38 \pm 8.76 ^b	15.47 \pm 0.39 ^{ab}
T ₅	7.58 \pm 0.18 ^a	14.62 \pm 0.46 ^a	0.45 \pm 0.02 ^d	26.13 \pm 1.04 ^a	274.25 \pm 11.14 ^a	15.94 \pm 0.41 ^a
Level of sig.	**	**	**	**	**	**
MSD value	0.68	1.34	0.10	3.10	28.30	1.68
CV (%)	6.82	7.48	10.69	9.45	8.65	8.28
(V*T)	ns	ns	ns	ns	ns	ns

Means in a column that includes the same letters are not statistically different at the 5% level using Tukey's HSD test, MSD = Minimum significant difference, CV = Coefficient of variation, sig.= significance, T₁: 0 ppm, T₂: 25 ppm, T₃: 50 ppm, T₄: 75 ppm and T₅: 100 ppm of ZnO-NPs. ns indicated non-significant at $p > 0.05$, * indicated significant at $p \leq 0.05$ and ** indicated significant at $p \leq 0.01$, \pm standard error mean (n=4) according to ANOVA.

3.4 Quality parameters

3.4.1 Varietal effect on quality traits

The quality traits of tomatoes, such as fruit firmness and lycopene content, showed significant variations between the two varieties examined. However, no significant differences were observed in total soluble solids (TSS), titrateable acidity, ascorbic acid, and protein content (Table 5). The tomato variety MT3 had higher fruit firmness, measuring 12.82 N, and a greater lycopene content of 232.55 μ g/100 g than the MT1 variety. MT3 displayed superior nutritional characteristics, likely due to genetic and environmental factors. Similar findings were reported by Quddus et al. (2020) and Razzaque et al. (2016) in their studies on mungbean varieties.

3.4.2 ZnO-NPs effect on quality traits

The foliar application of ZnO-NPs significantly affected the total soluble solids (TSS), firmness, titrateable acidity, ascorbic acid, lycopene, and protein content of tomatoes (Table 5).

3.4.2.1 Total soluble solids (TSS)

The highest total soluble solids (TSS) value of 7.58 was achieved with 100 ppm ZnO nanoparticles (T₅). This result was similar to other treatments, except for the 25 ppm ZnO nanoparticles (T₂) and the control (T₁), which recorded the lowest TSS at 5.25. Zinc

enhances photosynthesis and sugar content while reducing acidity (Ahmed et al. 2023; Włodarczyk et al. 2024). Additionally, Gutiérrez-Miceli et al. (2021) found that ZnO nanoparticles at a concentration of 50 ppm improved TSS by 26.92% compared to the control.

3.4.2.2 Fruit firmness

The highest fruit firmness, measured at 14.62 N, was observed in the treatment with 100 ppm ZnO nanoparticles (T₅). This significantly differed from the treatments with 50 ppm ZnO nanoparticles (T₃) and 25 ppm ZnO nanoparticles (T₂). The control treatment (T₁) exhibited the lowest firmness at 8.25 N. It is suggested that zinc may play a role in the synthesis of cell wall components, which could enhance tomato fruits' firmness and shelf life. This observation is supported by Siva Prasad et al. (2021).

3.4.2.3 Titrateable acidity

Titrateable acidity decreased as the levels of ZnO nanoparticles (ZnO-NPs) increased. The lowest acidity (0.45%) was recorded with 100 ppm of ZnO-NPs (T₅), while the control group (T₁) exhibited the highest acidity at 0.83%. These results are consistent with the findings of previous researchers (Ahmed et al. 2021; Ahmed et al. 2023; Włodarczyk et al. 2024).

3.4.2.4 Ascorbic acid

The highest ascorbic acid (26.13 mg/100 g) was found in the treatment with 100 ppm ZnO-NPs (T₅). This level was not significantly different from the other treatments, except for the one with 25 ppm ZnO-NPs (T₂). The control group (T₁) had the lowest ascorbic acid content, at 16.00 mg/100 g. Włodarczyk et al. (2024) reported that foliar application of ZnO-NPs at 150 ppm could increase the amount of ascorbic acid in tomato fruits.

3.4.2.5 Lycopene content

The maximum lycopene content recorded was 274.25 µg/100 g, achieved with 100 ppm ZnO-NPs (T₅), significantly higher than in other treatments. The second highest content was 245.38 µg/100 g, observed with 75 ppm ZnO-NPs (T₄), closely followed by 50 ppm ZnO-NPs (T₃). The control group (T₁) had the lowest lycopene content at 167.63 µg/100 g. Zinc is critical for photosynthesis and associated enzymatic activities, which help increase sugar content and reduce acidity (Jabri et al. 2022; Włodarczyk et al. 2024). Applying ZnO-NPs at 100 ppm led to a 113.1% increase in lycopene content (Raliya et al. 2015). Additionally, ZnO-NPs at 150 ppm also exhibited the highest levels of lycopene and beta-carotene compared to the control (Włodarczyk et al. 2024). Sofy et al. (2021) observed significant

improvements in growth indices, quality traits, and antioxidant levels by applying 100 ppm ZnO-NPs.

3.4.2.6 Protein content

The highest protein content (15.94%) was observed in the treatment with 100 ppm of ZnO nanoparticles (T₅), which was significantly different from the treatment with 25 ppm of ZnO nanoparticles (T₂). In contrast, the control treatment (T₁) showed the lowest protein content at 8.75%. The presence of zinc nutrition played a significant role in enhancing the protein levels in tomatoes, a conclusion supported by the findings of Quddus et al. (2020).

3.5 Nutrient contents in leaves

Significant differences in macronutrient content in tomato leaves were observed between plants treated with zinc oxide nanoparticles (ZnO-NPs) and those not (Table 6). While no significant differences were found among the various tomato varieties, the MT3 variety consistently showed higher nutrient levels, followed by the MT1 variety. In the case of ZnO-NPs, the highest nitrogen content (29.15 g/kg) was recorded at a concentration of 100 ppm (T₅), significantly greater than all other treatments. The control group (T₁) had the lowest nitrogen content. Similarly, higher levels

Table 6 Effects of foliar application of zinc oxide nanoparticles on nutrient contents in leaves of tomato varieties

Treatment	Nitrogen (N)	Phosphorus (P)	Potassium (K)	Sulphur(S)	Boron (B)	Zinc (Zn)
	(g/kg)				(mg/kg)	
MT1	23.30 ±1.24 ^a	9.52 ±0.72 ^a	22.11 ±1.27 ^a	10.72 ±0.52 ^b	54.12 ±2.46 ^a	503.02 ±57.03 ^a
MT3	23.68 ±1.22 ^a	10.05 ±0.76 ^a	23.15 ±1.24 ^a	11.07 ±0.55 ^a	55.36 ±2.27 ^a	515.52 ±58.82 ^a
Level of sig.	ns	ns	ns	**	ns	ns
MSD value	1.82	0.71	2.21	0.20	3.93	53.53
CV (%)	8.24	8.97	8.62	8.40	8.75	7.51
T ₁	14.05 ±0.41 ^c	4.95 ±0.13 ^e	13.63 ±0.41 ^d	7.02 ±0.28 ^d	39.95 ±1.26 ^d	20.10 ±0.58 ^d
T ₂	23.90 ±0.63 ^b	7.97 ±0.22 ^d	21.00 ±0.93 ^c	11.03 ±0.45 ^c	51.95 ±1.49 ^c	551.10 ±13.55 ^c
T ₃	24.35 ±0.75 ^b	10.05 ±0.30 ^c	23.71 ±0.68 ^{bc}	11.63 ±0.46 ^b	52.70 ±1.42 ^c	625.65 ±15.78 ^b
T ₄	26.00 ±0.73 ^b	11.99 ±0.38 ^b	26.08 ±0.74 ^{ab}	11.94 ±0.48 ^b	61.00 ±1.74 ^b	636.90 ±14.53 ^b
T ₅	29.15 ±0.81 ^a	13.97 ±0.38 ^a	28.72 ±0.73 ^a	12.87 ±0.48 ^a	68.10 ±1.83 ^a	712.60 ±18.12 ^a
Level of sig.	**	**	**	**	**	**
MSD value	2.85	1.29	2.87	0.46	7.06	54.20
CV (%)	8.24	8.97	8.62	8.40	8.75	7.51
(V*T)	ns	ns	ns	ns	ns	ns

Means in a column that includes the same letters are not statistically different at the 5% level using Tukey's HSD test, MSD = Minimum significant difference, CV = Coefficient of variation, sig.= significance, T1: 0 ppm, T2: 25 ppm, T3: 50 ppm, T4: 75 ppm and T5: 100 ppm of ZnO-NPs. ns indicated non-significant at p>0.05, * indicated significant at p≤0.05 and ** indicated significant at p≤0.01, ± standard error mean (n=4) according to ANOVA.

of phosphorus (13.97 g/kg), potassium (28.72 g/kg), boron (68.10 mg/kg), and zinc (712.60 mg/kg) were also observed in the 100 ppm ZnO-NPs treatment (T₅), while the control had the lowest values for these nutrients. Regarding sulfur content, the highest level (12.87 g/kg) was found in plants treated with 75 ppm ZnO-NPs (T₄), 83% higher than in the control group. Ahmed et al. (2023) obtained similar findings with 100 ppm zinc oxide nanoparticles, reporting the highest contents of nitrogen, phosphorus, potassium, sulfur, boron, and zinc.

3.6 Nutrient contents in fruits

The macronutrient content, specifically nitrogen (N), phosphorus (P), potassium (K), and sulfur (S) in the fruits of two tomato varieties was significantly affected by the foliar application of zinc oxide nanoparticles (ZnO-NPs) (Table 7). The highest nitrogen content (25.50 g/kg) was observed with the application of 100 ppm ZnO-NPs (T₅). This result was similar to those obtained with 75 ppm ZnO-NPs (T₄) and 50 ppm ZnO-NPs (T₃). In contrast, the control group (T₁) exhibited the lowest nitrogen content. A similar trend was noted for phosphorus, potassium, and sulfur content. The highest levels were recorded with the 100 ppm ZnO-NPs treatment (T₅), and it was reported that 12.29 g/kg phosphorus, 25.53 g/kg potassium, and 11.14 g/kg sulphur. These values were statistically similar to those from the 75 ppm ZnO-NPs treatment (T₄), while

the control group showed the lowest levels. Micronutrient content in the tomato fruits was also significantly influenced by varying levels of zinc oxide nanoparticles (Table 7). The highest zinc content at 52.25 mg/kg was recorded with the 100 ppm ZnO-NPs treatment (T₅), which was significantly greater than other treatments, except for the 75 ppm ZnO-NPs treatment (T₄). The control group had the lowest zinc content at 18.68 mg/kg. Previous studies have indicated that increased application of zinc can lead to higher phosphorus content in tomato leaves and fruits. Additionally, higher zinc levels may influence potassium levels (Islam et al. 2018; Kaya and Higgs 2002; Quddus et al. 2020). Adequate zinc application also enhances boron uptake, helping to mitigate deficiencies (Jabri et al. 2022; Rengel et al. 1998).

3.7 Total Nutrient uptake by plant

A significant difference was observed in the macronutrient content of two tomato varieties following the foliar application of ZnO nanoparticles (ZnO-NPs) (Figure 3a). The maximum nitrogen uptake by the plants measured 7.18 g per plant with the application of 100 ppm ZnO-NPs (T₅), significantly higher than all other treatments. In contrast, the minimum nitrogen uptake of 1.70 g per plant was recorded in the control treatment (T₁). The foliar application of zinc improved nitrogen uptake and accumulation, ultimately increasing plant production (Grzebisz et al. 2008; Jabri

Table 7 Effects of foliar application of zinc oxide nanoparticles on nutrient contents in fruits of tomato varieties

Treatment	Nitrogen (N)	Phosphorus (P)	Potassium (K)	Sulphur(S)	Boron (B)	Zinc (Zn)
MT1	21.68 ±0.97 ^a	9.03 ±0.62 ^a	19.83 ±1.16 ^a	9.24 ±0.53 ^b	26.84 ±1.71 ^a	42.65 ±2.86 ^a
MT3	22.34 ±1.05 ^a	9.24 ±0.65 ^a	20.49 ±1.18 ^a	9.57 ±0.53 ^a	27.82 ±1.75 ^a	42.93 ±2.95 ^a
Level of sig.	ns	ns	ns	**	ns	ns
MSD value	1.66	0.89	1.47	0.04	3.00	3.17
CV (%)	8.28	10.37	9.13	8.98	8.50	7.32
T ₁	14.00 ±0.37 ^c	5.80 ±0.15 ^c	11.19 ±0.33 ^d	5.35 ±0.21 ^d	13.65 ±0.38 ^d	18.68 ±0.44 ^d
T ₂	22.40 ±0.66 ^b	6.36 ±0.16 ^c	19.81 ±0.54 ^c	9.75 ±0.43 ^c	26.80 ±0.77 ^c	45.40 ±1.15 ^c
T ₃	23.40 ±0.62 ^{ab}	9.61 ±0.46 ^b	21.30 ±0.66 ^{bc}	10.23 ±0.41 ^{bc}	30.00 ±0.89 ^{bc}	46.53 ±1.21 ^{bc}
T ₄	24.75 ±0.62 ^{ab}	11.62 ±0.33 ^a	22.96 ±0.62 ^{ab}	10.58 ±0.44 ^b	32.20 ±0.93 ^{ab}	51.10 ±1.20 ^{ab}
T ₅	25.50 ±0.65 ^a	12.29 ±0.33 ^a	25.53 ±0.70 ^a	11.14 ±0.45 ^a	34.00 ±0.96 ^a	52.25 ±1.20 ^a
Level of sig.	**	**	**	**	**	**
MSD value	2.68	1.40	2.64	0.50	3.42	4.62
CV (%)	8.28	10.37	9.13	8.98	8.50	7.32
(V*T)	ns	ns	ns	ns	ns	ns

Means in a column that includes the same letters are not statistically different at the 5% level using Tukey's HSD test, MSD = Minimum significant difference, CV = Coefficient of variation, sig.= significance, T₁: 0 ppm, T₂: 25 ppm, T₃: 50 ppm, T₄: 75 ppm and T₅: 100 ppm of ZnO-NPs. ns indicated non-significant at p>0.05, * indicated significant at p≤0.05 and ** indicated significant at p≤0.01, ± standard error mean (n=4) according to ANOVA.

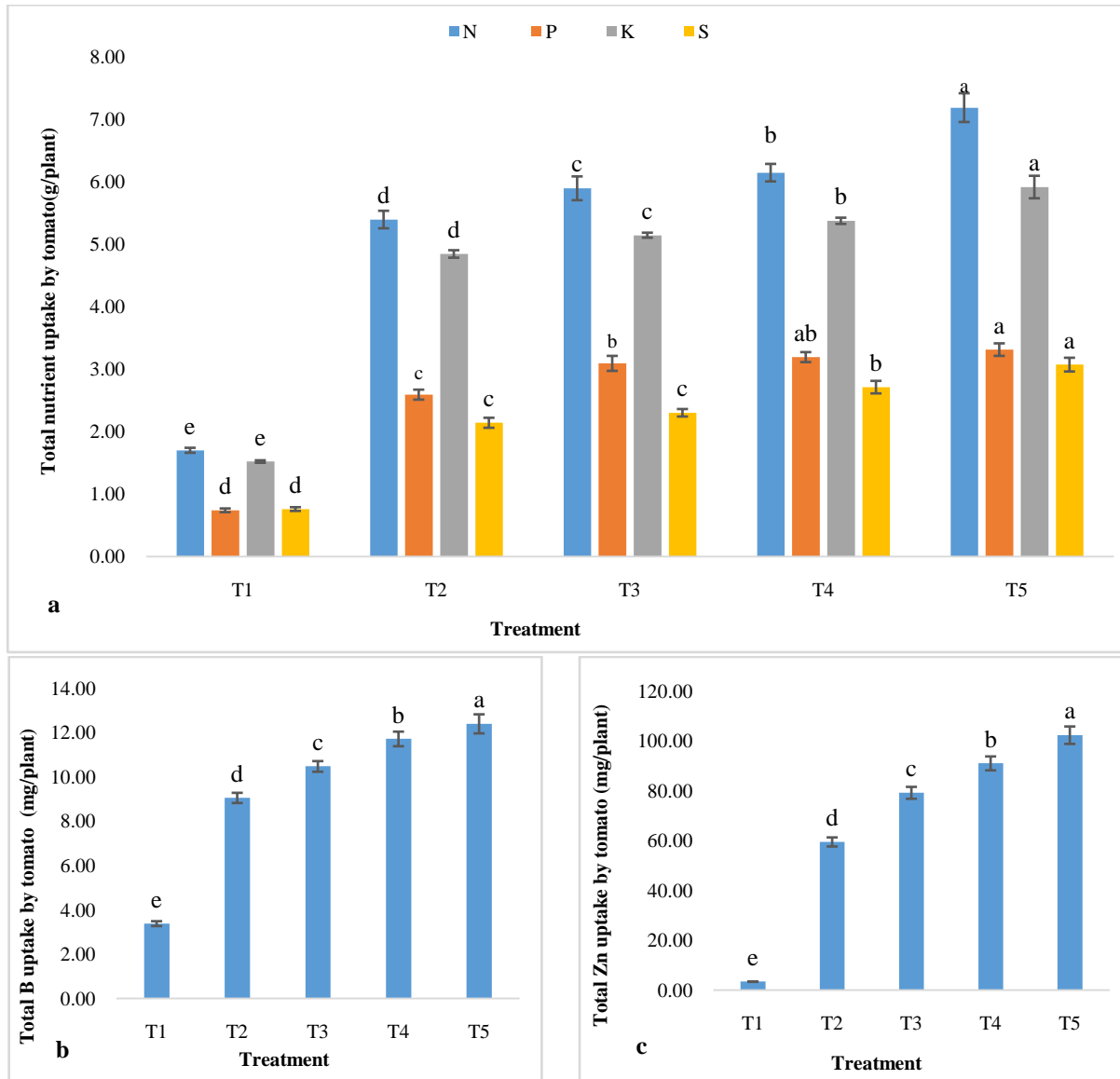


Figure 3 Effects of zinc oxide nanoparticles on (a) total uptake of N, P, K, S, (b) total B uptake, and (c) total Zn uptake by tomato, Error bar represents the \pm standard error mean ($n=4$). Mean values on the bar followed by a different letter (s) are significantly different from each other at a 5% level of significance by Tukey's HSD test, T₁: 0 ppm, T₂: 25 ppm, T₃: 50 ppm, T₄: 75 ppm and T₅: 100 ppm of ZnO-NPs.

et al. 2022). Regarding phosphorus uptake, the highest level was also found in the 100 ppm ZnO-NPs treatment (T₅), and it was reported at 3.31 g per plant, similar to the 75 ppm ZnO-NPs treatment (T₄). The lowest phosphorus uptake (0.74 g per plant) was noted in the control treatment (T₁). Similarly, the highest total potassium and sulfur uptake was seen in the T₅ treatment (100 ppm ZnO-NPs), with values significantly different from all other treatments, while the control group (T₁) exhibited the lowest results. The highest boron uptake of 12.39 mg per plant also occurred in the T₅ treatment (100 ppm ZnO-NPs) and was significantly higher than all other treatments, with the control group again showing the lowest uptake. Additionally, zinc uptake

peaked in the T₅ treatment at 102.34 mg per plant, significantly different from the other treatments. The lowest zinc uptake (1.32 mg per plant) was recorded in the control (T₁). Ahmed et al. (2023) similarly reported the highest uptake of zinc and boron from applying 100 ppm ZnO-NPs to tomatoes.

3.8 Apparent zinc recovery efficiency of tomato

Tomatoes' apparent zinc recovery efficiency was affected by the foliar application of zinc oxide nanoparticles (ZnO-NPs) (Figure 4). Applying 75 ppm ZnO-NPs (T₄) resulted in the highest apparent zinc recovery efficiency at 7.05%, while the treatment

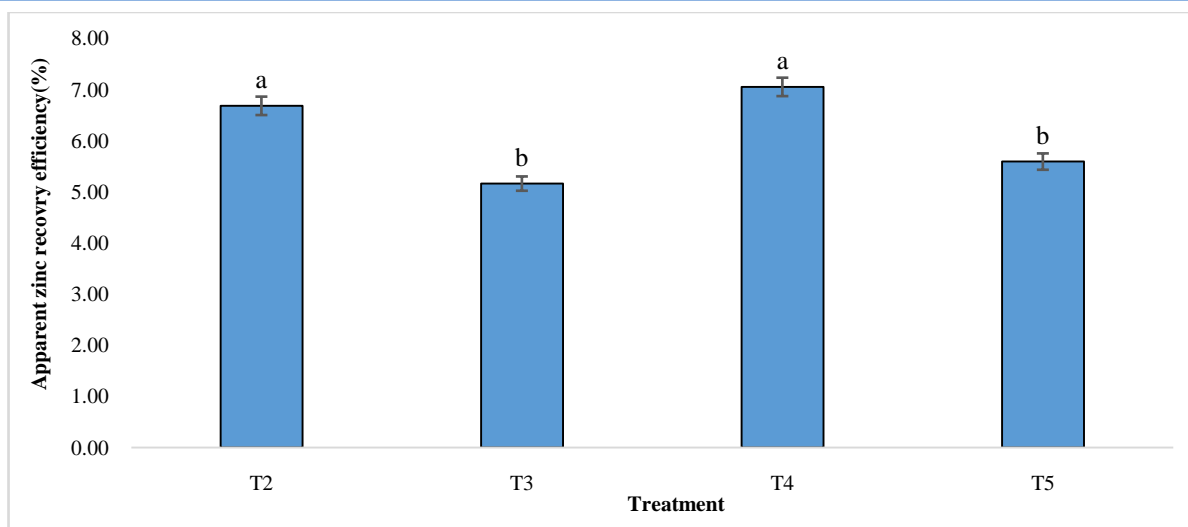


Figure 4 Effect of zinc oxide nanoparticles on apparent zinc recovery efficiency of tomato, error bar represents the \pm standard error mean (n=4), Mean values on bar followed by uncommon letter (s) are significantly different from each other at 5% level of significance by Tukey's HSD test, T₁: 0 ppm, T₂: 25 ppm, T₃: 50 ppm, T₄: 75 ppm and T₅: 100 ppm of ZnO-NPs.

Table 8 Effect of different doses of zinc oxide nanoparticles on the cost and return of tomato

Treatment	Gross return (US Dollar/ha)	Total variable cost (US Dollar/ha)	Gross margin (US Dollar/ha)	Benefit-cost ratio(BCR)	% increased of BCR over control
T ₁	20,796	17,045	3,751	1.22	-
T ₂	35,436	17,545	17,891	2.02	65.57
T ₃	51,816	18,045	33,771	2.87	135.25
T ₄	55,800	18,545	37,255	3.01	146.72
T ₅	64,620	19,045	45,575	3.39	177.87

T₁: 0 ppm, T₂: 25 ppm, T₃: 50 ppm, T₄: 75 ppm and T₅: 100 ppm of ZnO-NPs, Output: Price of fresh tomato fruit = 1.2 dollar/kg, Input: Seed price = 300 dollar/kg, cost of other fertilizer = 650 \$, total cost for seed germination tray = 595 \$/ha, price of bio soil + peat moss = 600 \$/ha, price of coco peat = 125 dollar/ton (total need 60 ton), total cost of Poly bag = 1200 \$/ha, Labour cost =1200 \$/ha, price of plastic stick= 5000 \$/ha, price of zinc oxide nanoparticles = 1000 US dollar/kg, 1 US dollar = 4.16 Ringgit (Malaysian currency), Fresh tomato price was considered based on current farm gate price.

with 50 ppm ZnO-NPs (T₃) yielded the lowest efficiency. As the supply of nutrients like zinc increases, nutrient usage efficiency often decreases (Saleem et al. 2022; Elia and Conversa 2012). Biological factors and varying nutrient recovery rates may influence tomatoes' absorption capacity for nutrients. Several factors significantly affect crop productivity, including seasonal variability, the growing environment, and fertilizer management practices. These factors can interact in complex ways, leading to apparent nutrient recovery efficiency inconsistencies. Consequently, the amount of fertilizer applied to a crop does not always result in increased yields. Other elements, such as weather conditions, soil type, and the timing and method of fertilizer application, also play crucial roles in determining how much of the applied nutrients are absorbed and utilized by the plants. This variability in nutrient recovery efficiency underscores the importance of considering multiple factors when deciding fertilizer management practices (Baligar et al. 2001). The high apparent zinc

recovery efficiency observed in tomatoes at 75 ppm ZnO-NPs is attributed to increased zinc absorption. However, it is necessary to acknowledge that nutrient use efficiency (NUE) in crops can be influenced by various factors, including environmental conditions and the fertilizer application rate, as demonstrated by Quddus et al. (2022b).

3.9 Cost and return analysis

Cost and return analysis is a crucial factor in determining farmers' technology adoption, as Maroušek and Maroušková (2021) emphasized. The foliar application of 100 ppm ZnO nanoparticles (T₅) yielded the highest gross return of US\$64,620 per hectare, followed by the application of 75 ppm ZnO nanoparticles (T₄) (Table 8). This gross return was 211% higher than the control treatment (T₁). Additionally, the benefit-cost ratio of 3.39 achieved with the 100 ppm ZnO nanoparticles application was 177.78%

higher than that of the control. The observed increase in gross return and the favourable benefit-cost ratio can likely be attributed to the positive effects of the ZnO nanoparticles application, although the exact mechanisms remain unidentified.

Conclusion

The foliar application of zinc oxide nanoparticles (ZnO-NPs) has shown significant positive effects on tomato plants' growth, yield, quality, and nutrient uptake. The experiment indicated that applying 100 ppm of ZnO-NPs resulted in the highest values for key growth and yield parameters, such as the number of primary branches, leaf area, photosynthetic rate, fruit size, number of fruits per plant, and overall fruit yield. Additionally, this treatment led to increased nutrient content and enhanced nutrient uptake. The nutritional quality of tomato fruit, including ascorbic acid levels, was most positively impacted by the 100 ppm ZnO-NPs application. This treatment also resulted in a better benefit-to-cost ratio. Moreover, the MARDI Tomato-3 (MT3) variety outperformed MARDI Tomato-1 (MT1) in most of the evaluated parameters. These findings suggest that a concentration of 100 ppm ZnO-NPs is optimal for improving both the productivity and quality of tomatoes and providing a potential alternative to excessive chemical fertilizer use. This approach could help minimize environmental impacts and contribute to food security and nutritional enhancement. Further research is necessary to investigate the effects of higher doses of ZnO-NPs on tomato fruit yield to determine the optimal dosage for maximizing production.

Author Contributions

Conceptualization, R.A., M.K.U., M.A.Q., and M.A.M.H.; methodology, R.A., M.A.Q., M.K.U. and M.A.M.H.; formal analysis, R.A., M.K.U. and M.A.Q.; data curation: R.A. and M.A.Q.; statistical analysis, R.A., M.A.Q. and M.K.U.; writing—original draft preparation, R.A. and M.A.Q.; writing—review and editing, M.K.U., M.A.Q. and M.A.M.H.; visualization: R.A., M.A.M.H. and M.A.Q.; supervision, M.K.U., M.A.Q. and M.A.M.H. All authors have read and agreed to the published version of the manuscript.

Acknowledgements

The Bangladesh Agricultural Research Institute (BARI), the Bangladesh Agricultural Research Council (NATP Phase-II Project), the Ministry of Agriculture, Bangladesh for financial support, and Universiti Putra Malaysia, Selangor, Darul Ehsan, Malaysia for research facilities are all acknowledged by the authors.

Conflict of interest

The authors have no conflict of interest.

References

- Abdelaziz, A. M., Dacrory, S., Hashem, A. H., Attia, M., Hasanin, M., Fouda, H. M., Kamel, S., & Elsaied, H. (2021). Protective role of zinc oxide nanoparticles based hydrogel against wilt disease of pepper plant. *Biocatalysis and Agricultural Biotechnology*, 35(1–2), 083.
- Ahmed, R., Uddin, M. K., Quddus, M. A., Samad, M. Y. A., Hosain, M. A. M., & Haque, A. N. A. (2023). Impact of Foliar Application of Zinc and Zinc Oxide Nanoparticles on Growth, Yield, Nutrient Uptake and Quality of Tomato. *Horticulturae*, 9(2), 162.
- Ahmed, R., Yusoff Abd Samad, M., Uddin, M.K., Quddus, M.A., & Hossain, M.A.M. (2021). Recent Trends in the Foliar Spraying of Zinc Nutrient and Zinc Oxide Nanoparticles in Tomato Production. *Agronomy*, 11, 2074.
- Ahsan, T., Li, B., Khalil, A., Zafar, T., & Razzaq, M. (2025). Impact of Alkalescent Nucleoside Antibiotic Loaded ZnONPs, on Enzymes, Hormones, Fatty Acids, and Metabolites in Rice Plant. *Iranian Journal of Science*, <https://doi.org/10.1007/s40995-024-01743-4>.
- Ali, M.Y., Sina, A.A.I., Khandker, S.S., Neesa, L., Tanvir, E. M., Kabir, A., Khalil, M.I., & Gan, S.H. (2021). Nutritional Composition and Bioactive Compounds in Tomatoes and Their Impact on Human Health and Disease: A Review. *Foods*, 10, 45.
- Alloway, B. J. (2008). Zinc in soils and crop nutrition. published by IZA and IFA. *Brussels, Belgium and Paris, France*, pp. 139.
- Angyu, A. E., & Kwon-Ndung, E. H. (2024). Alpha-Spin-Mediated Growth Improvement for Tomato (*Lycopersicon esculentum* Mill.) Varieties in Jauro Yinu, Ardo-Kola LGA, Taraba State. *Lafia Journal of Scientific & Industrial Research*, 2(2), 96-100.
- Baligar, V. C., Fageria, N. K., & He, Z. L. (2001). Nutrient use efficiency in plants. *Communication in Soil Science and Plant Analysis*, 32(7&8), 921–950.
- Beckles, D.M. (2012). Factors affecting the postharvest soluble solids and sugar content of tomato (*Solanum lycopersicum* L.) fruit. *Postharvest Biology and Technology*, 63 (1), 129-140. DOI: <https://doi.org/10.1016/j.postharvbio.2011.05.016>.
- Benavides-Mendoza, A., Betancourt-Galindo, R., & Francisco-Francisco, N. (2023) Impact of ZnSO₄- and ZnO Nanoparticles on Seed Germination and Seedling Growth of Lettuce. *Phyton-International Journal of Experimental Botany*, 92(6), 1831-1840.
- Ben-Rouina, B., Ben-Ahmed, C., Athar, H.U.R., & Boukhriss, M. (2006). Water relations, proline accumulation and photosynthetic

- activity in olive tree (*Olea europaea* L. CV" Chemlali") in response to salt stress. *Pakistan Journal of Botany*, 38(5 SPEC. ISS.), 1397-1406.
- Chanu, T.T., & Upadhyaya, H. (2019). Zinc oxide nanoparticle-induced responses on plants: A physiological perspective. *Nanomaterials in Plants, Algae and Microorganisms*, 2, 43–64.
- Cottenie, A. (1980) Soil and Plant Testing as a Basis of Fertilizer Recommendations. FAO Soil Bulletin 38/2. Food and Agriculture Organization of the United Nations, Rome.
- Cox, D. (1995). Water quality: pH and alkalinity. *University of Massachusetts Extension, Department of Plant and Soil Science, Massa*.
- Ding, P., & Mashah, N. C. (2016). Growth, maturation and ripening of underutilized *Carissa congesta* fruit. *Fruits*, 71(3), 171-176.
- Dong, H., Li, F., Xuan, X., Ahiakpa, J. K., Tao, J., Zhang, X., Ge, P., Wang, Y., Gai, W., & Zhang, Y. (2025). The genetic basis and improvement of photosynthesis in tomato. *Horticultural Plant Journal*, 11 (1) 69-84.
- Elia, A., & Conversa, G.(2012). Agronomic and physiological responses of a tomato crop to nitrogen input. *European Journal of Agronomy*, 40, 64-74.
- Faizan, M., Bhat, J. A., Chen, C., Alyemini, M. N., Wijaya, L., Ahmad, P., & Yu, F. (2021). Zinc oxide nanoparticles (ZnO-NPs) induce salt tolerance by improving the antioxidant system and photosynthetic machinery in tomato. *Plant Physiology and Biochemistry*, 161, 122-130.
- Faizan, M., & Hayat, S. (2019). Effect of foliar spray of ZnO-NPs on the physiological parameters and antioxidant systems of *Lycopersicon esculentum*. *Polish Journal of Natural Sciences*, 34(6), 87-105.
- Fu, L., Wang, Z., Dhankher, O. P., & Xing, B. (2020). Nanotechnology as a new sustainable approach for controlling crop diseases and increasing agricultural production. *Journal of Experimental Botany*, 71(2), 507–519.
- Grzebisz, W., Wrońska, M., Diatta, J. B., & Dullin, P. (2008). Effect of zinc foliar application at early stages of maize growth on patterns of nutrients and dry matter accumulation by the canopy. Part I. Zinc uptake patterns and its redistribution among maize organs. *Journal of Elementology*, 13, 17–28.
- Gutiérrez-Miceli, F. A., Oliva-Llaven, M. Á., Luján-Hidalgo, M. C., Velázquez-Gamboa, M. C., González-Mendoza, D., & Sánchez-Roque, Y. (2021). Zinc oxide Phytonanoparticles' effects on yield and mineral contents in fruits of tomato (*Solanum lycopersicum* L. cv. Cherry) under field conditions. *The Scientific World Journal*, 2021(1), 5561930.
- Hanif, M., Munir, N., Abideen, Z., Dias, D. A., Hessini, K., & El-Keblawy, A. (2023). Enhancing tomato plant growth in a saline environment through the eco-friendly synthesis and optimization of nanoparticles derived from halophytic sources. *Environmental Science and Pollution Research*, 30(56), 118830–118854.
- Hiller, A., Plazin, J., & Vanslyke, D.D. (1948). A study of conditions of Kjeldhal determination of nitrogen inproteins. *Journal of Biological Chemistry*, 176(3), 1401-1420.
- Huang, Z., Xie, W., Wang, M., Liu, X., Ashraf, U., et al. (2020). Response of rice genotypes with differential nitrate reductase-dependent NO synthesis to melatonin under ZnO nanoparticles' (NPs) stress. *Chemosphere*, 250, 126337.
- Isah, A., Amans, E., Odion, E., & Yusuf, A. (2014). Growth rate and yield of two tomato varieties (*Lycopersicon esculentum* Mill) under green manure and NPK fertilizer rate Samaru Northern Guinea Savanna. *International Journal of Agronomy*, 2014(1), 932759.
- Islam, M. M., Karim, M. R., Oliver, M. M. H., Urmi, T. A., Hossain, M. A., & Haque, M. M. (2018). Impacts of trace element addition on lentil (*Lens culinaris* L.) agronomy. *Agronomy*, 8(7), 100.
- Jabri, H. A., Saleem, M. H., Rizwan, M., Hussain, I., Usman, K., & Alsafan, M. (2022). Zinc Oxide Nanoparticles and Their Biosynthesis: Overview. *Life*, 12, 594.
- Jampi'lek, J., & Kra'l'ova, K. (2021). Nanoparticles for improving and augmenting plant functions. In: S. Jogaiyah, B. Singh, L.F., Fraceto, & R, de Lima (eds) *Woodhead Publishing series in food science, technology and nutrition, advances in nano-fertilizers and nanopesticides in agriculture* (pp. 171-227). Woodhead Publishing, India.
- Kaya, C., & Higgs, D. (2002). Response of tomato (*Lycopersicon esculentum* L.) cultivars to foliar application of zinc when grown in sand culture at low zinc. *Scientia Horticulturae*, 93(1), 53-64.
- Keeney, D. R., & Nelson, D. W. (1982). Nitrogen—inorganic forms. *Methods of soil analysis: Part 2 chemical and microbiological properties*, 9, 643-698.
- Khan, M., Khan, M.S.A., Borah, K.K., Goswami, Y., Hakeem, K.R., & Chakrabarty, I. (2021). The potential exposure and hazards of metal-based nanoparticles on plants and environment, with special emphasis on ZnO NPs, TiO₂ NPs, and AgNPs: A review. *Environmental Advances*, 6(80), 100128.

- Khanm, H., Vaishnavi, B., & Shankar, A. (2018). Raise of Nano-fertilizer ERA: Effect of nano scale zinc oxide particles on the germination, growth and yield of tomato (*Solanum lycopersicum*). *International Journal of Current Microbiology and Applied Sciences*, 7(5), 1861-1871.
- Kondak, S., Molnar, A., Olah, D., & Kolbert, Z. (2022). The role of nitric oxide (NO) in plant responses to disturbed zinc homeostasis. *Plant Stress*, 4(1), 100068.
- Kumah, P., Olympio, N., & Tayviah, C. (2011). Sensitivity of three tomato (*Lycopersicon esculentum*) cultivars-Akoma, Pectomech and power-to chilling injury. *Agriculture and Biology Journal of North America*, 2, 799-805.
- Kumar, U. J., Bahadur, V., Prasad, V., Mishra, S., & Shukla, P. (2017). Effect of different concentrations of iron oxide and zinc oxide nanoparticles on growth and yield of strawberry (*Fragaria x ananassa* Duch) cv. Chandler. *International Journal of Current Microbiology and Applied Sciences*, 6(8), 2440-2445.
- Kwon-Ndung, E., Joseph, C., Goler, E. E., Kana, H., & Paul, T. T. (2019). Promising use of Alpha-Spin(r) nano particles bombardment for selection of useful variations in *Moringa oleifera* seedlings in Nigeria. *International Journal of Innovative Approaches in Agricultural Research*, 3(2), 202–209.
- Maroušek, J., & Maroušková, A. (2021). Economic considerations on nutrient utilization in wastewater management. *Energies*, 14(12), 3468.
- Mi, K., Yuan, X., Wang, Q., Dun, C., Wang, R., et al. (2023). Zinc oxide nanoparticles enhanced rice yield, quality, and zinc content of edible grain fraction synergistically. *Frontiers in Plant Science*, 14, 1196201.
- Mohammadi-Aylar, S., Jamaati-e-Somarin, S., & Azimi, J. (2010). Effect of stage of ripening on mechanical damage in tomato fruits. *American-Eurasian Journal of Agricultural & Environmental Science*, 9, 297–302.
- Mohan, A. C., & Renjanadevi, B. (2016). Preparation of zinc oxide nanoparticles and its characterization using scanning electron microscopy (SEM) and X-ray diffraction (XRD). *Procedia Technology*, 24, 761-766.
- Mubashir, A., Nisa, Z., Shah, A. A., Kiran, M., Hussain, I., et al. (2023). Effect of foliar application of nano-nutrients solution on growth and biochemical attributes of tomato (*Solanum lycopersicum*) under drought stress. *Frontiers in Plant Science*, 13, 1066790.
- Munir, T., Rizwan, M., Kashif, M., Shahzad, A., Ali, S., & Amin, N. (2018). Effect of zinc oxide nanoparticles on the growth and zn uptake in wheat (*Triticum aestivum* L.) by seed priming method. *Digest Journal of Nanomaterials & Biostructures*, 13(1), 315-323.
- Nagata, M., & Yamashita, I. (1992). Simple method for simultaneous determination of chlorophyll and carotenoids in tomato fruit. *Nippon shokuhin kogyo gakkaiishi*, 39(10), 925-928.
- Nirupama Pila, N. P., Gol, N. B., & Rao, T. R. (2010). Effect of post harvest treatments on physicochemical characteristics and shelf life of tomato (*Lycopersicon esculentum* Mill.) fruits during storage. *American-Eurasian Journal of Agricultural & Environmental Sciences*, 9(5), 470–479.
- Olaniyi, J., Akanbi, W., Adejumo, T., & Akande, O. (2010). Growth, fruit yield and nutritional quality of tomato varieties. *African journal of food science*, 4(6), 398-402.
- Pérez Velasco, E. A., Betancourt Galindo, R., Valdez Aguilar, L. A., Gonzalez Fuentes, J. A., Puente Urbina, B. A., Lozano Morales, S. A., & Sánchez Valdés, S. (2020). Effects of the morphology, surface modification and application methods of ZnO-NPs on the growth and biomass of tomato plants. *Molecules*, 25(6), 1282.
- Pinela, J., Petropoulos, S. A., & Barros, L. (2022). Editorial: Advances in tomato and tomato compounds research and technology. *Frontiers in Nutrition*, 9, 1018498.
- Prasad, T., Sudhakar, P., Sreenivasulu, Y., Latha, P., Munaswamy, V., Reddy, K. R., et al. (2012). Effect of nanoscale zinc oxide particles on the germination, growth and yield of peanut. *Journal of plant nutrition*, 35(6), 905-927.
- Quddus, M. A., Ahmed, R., Islam, M. S., Siddiky, M. A., & Rahman, M. A. (2023). Evaluation of potassium nutrition in productivity, quality and potassium use efficiency of garden pea in terrace soils. *Bangladesh Journal of Agricultural Research*, 48(3), 307-323.
- Quddus, M.A., Siddiky, M.A., Ali, M.R., Ahmed, R., Sarker, K.K., & Arfin, M.S. (2022a). Influence of boron and zinc on yield, nutrient uptake and quality of strawberry. *Journal of Plant Nutrition*, 45 (6), 866-882.
- Quddus, M. A., Siddiky, M. A., Hussain, M. J., Rahman, M. A., Ali, M. R., & Masud, M. A. T. (2022b). Magnesium influences growth, yield, nutrient uptake, and fruit quality of tomato. *International Journal of Vegetable Science*, 28(5), 441-464.
- Quddus, M. A., Anwar, M. B., Naser, H. M., Siddiky, M. A., Hussain, M. J., et al. (2020). Impact of zinc, boron and molybdenum addition in soil on mungbean productivity, nutrient uptake and economics. *Journal of Agricultural Science*, 12 (9), 115-129.

- Raliya, R., Nair, R., Chavalmane, S., Wang, W.N., & Biswas, P. (2015). Mechanistic evaluation of translocation and physiological impact of titanium dioxide and zinc oxide nanoparticles on the tomato (*Solanum lycopersicum* L.) plant. *Metallomics*, 7(12), 1584-1594.
- Razzaque, M., Haque, M., Rahman, M., Bazzaz, M., & Khan, M. (2016). Screening of mungbean (*Vigna radiata* L. Wilczek) genotypes under nutrient stress in soil. *Bangladesh Journal. Agricultural Research*, 41, 377-386.
- Rehman, F., Paker, N. P., Khan, M., Zainab, N., Ali, N., Munis, M. F. H., Iftikhar, M., & Chaudhary, H. J. (2023). Assessment of application of ZnO nanoparticles on physiological profile, root architecture and antioxidant potential of *Solanum lycopersicum*. *Biocatalysis and Agricultural Biotechnology*, 53, 102874.
- Rengel, Z., Römheld, V., & Marschner, H. (1998). Uptake of zinc and iron by wheat genotypes differing in tolerance to zinc deficiency. *Journal of Plant Physiology*, 152(4-5), 433-438.
- Saleem, M. H., Usman, K., Rizwan, M., Jabri, H. A., & Alsafran, M. (2022). Functions and strategies for enhancing zinc availability in plants for sustainable agriculture. *Frontiers in Plant Science*, 13, 1033092.
- Seleiman, M. F., Ahmad, A., Alhammad, B. A., & Tola, E. (2023). Exogenous Application of Zinc Oxide Nanoparticles Improved Antioxidants, Photosynthetic, and Yield Traits in Salt-Stressed Maize. *Agronomy*, 13(10), 2645.
- Shamshuddin, J., Rabileh, M. A., & Fauziah, C. I. (2020). Can the Acidic Ultisols in Peninsular Malaysia Be Alleviated by Biochar Treatment for Corn Cultivation? *Malaysian Journal of Soil Science*, 24, 1-10.
- Sharma, N. K., Singh, R. J., & Kumar, K. (2012). Dry matter accumulation and nutrient uptake by wheat under poplar based agroforestry system. *Agronomy*, 2012(1), 1-7.
- Siva Prasad, P. N., Subbarayappa, C. T., Sathish, A., & Ramamurthy, V. (2021). Impact of zinc fertilization on tomato (*Solanum lycopersicum* L.) yield, zinc use efficiency, growth and quality parameters in Eastern Dry Zone (EDZ) soils of Karnataka, India. *International Journal of Plant & Soil Science*, 33, 20-38.
- Sofy, A. R., Sofy, M. R., Hmed, A. A., Dawoud, R. A., Alnaggar, A. E.A. M., Soliman, A. M., & El-DougDoug, N. K. (2021). Ameliorating the adverse effects of tomato mosaic tobamovirus infecting tomato plants in Egypt by boosting immunity in tomato plants using zinc oxide nanoparticles. *Molecules*, 26(5), 1337.
- Su, Y., Ashworth, V., Kim, C., Adeleye, A.S., Rolshausen, P., Roper, C., White, J., & Jassby, D. (2019). Delivery, uptake, fate, and transport of engineered nanoparticles in plants: A critical review and data analysis. *Environmental Science. Nano*, 6(8), 2311-2331.
- Sun, L., Wang, Y., Wang, R., Wang, R., Zhang, P., Ju, Q., & Xu, J. (2020). Physiological, transcriptomic, and metabolomic analyses reveal zinc oxide nanoparticles modulate plant growth in tomato. *Environmental Science: Nano*, 7(11), 3587-3604.
- Tondey, M., Kalia, A., Singh, A., Dheri, G. S., Taggar, M. S., Neovimova, E., Krejcar, O., & Kuca, K. (2021). Seed priming and coating by nanoscale zinc oxide particles improved vegetative growth, yield and quality of fodder maize (*Zea mays*). *Agronomy*, 11(4), 729.
- Tujuba, M., & Ayana, N. G. (2020). Evaluation of released tomato (*Lycopersicon Esculentum* Mill.) varieties for fruit yield quality parameters in Western Ethiopia. *Journal of Agricultural and Biological Science*, 6(2), 100-113.
- Vasconcelos, A. D., Nascimento, C. W. A., & Cunha Filho, F. D. (2011). Distribution of zinc in maize plants as a function of soil and foliar Zn supply. *International Research Journal of Agricultural Science and Soil Science*, 1(1), 1-5.
- Wang, J., Xu, J., Xie, R., Chen, N., Yang, M., Tian, X., & Shi, D. (2024). Effects of nano oxide particles on the growth and photosynthetic characteristics of okra plant under water deficiency. *Folia Horticulturae*, 36(3), 1-13.
- Wang, Q., Xu, S., Zhong, L., Zhao, X., & Wang, L. (2023). Effects of Zinc Oxide Nanoparticles on Growth, Development, and Flavonoid Synthesis in *Ginkgo biloba*. *International Journal of Molecular Sciences*, 24(21), 15775.
- Włodarczyk, K., Smolińska, B., & Majak, I. (2024). How Nano-ZnO Affect Tomato Fruits (*Solanum lycopersicum* L.)? Analysis of Selected Fruit Parameters. *International Journal of Molecular Science*, 25, 8522.
- Włodarczyk, K., & Smolińska, B. (2022). The Effect of Nano-ZnO on Seeds Germination Parameters of Different Tomatoes (*Solanum lycopersicum* L.) Cultivars. *Molecules*, 27(15), 4963.